

# Solitary Internal Waves in Marsdiep Tidal Channel

Using ADCP measurements

By: Sjoerd Groeskamp

Supervisor: Prof. Dr. L.R.M. Maas

## **Master Thesis**

Utrecht University

Master Meteorology, Physical Oceanography and Climate

**Institute for Marine and Atmospheric Research Utrecht (IMAU)**

The research for the Master Thesis was carried out on the:

**Royal Netherlands Institute for Sea Research (NIOZ)**

The cover is designed by Malou Zuidema

# Contents

<b>1</b>	<b>Introduction</b>	<b>4</b>
1.1	General introduction . . . . .	4
1.2	Internal Solitons . . . . .	7
1.3	Study area . . . . .	8
1.3.1	The Marsdiep as barrier tidal inlet . . . . .	12
1.3.2	The Marsdiep as an estuary . . . . .	16
1.3.3	Expected (secondary) effects on the currents in the Marsdiep . . . . .	17
<b>2</b>	<b>The Deployment</b>	<b>21</b>
2.1	Requirements and circumstances . . . . .	21
2.2	Design of the deployment . . . . .	21
2.3	The second deployment . . . . .	23
2.4	Recommendations for future deployments . . . . .	30
<b>3</b>	<b>Data Collection and Processing</b>	<b>36</b>
3.1	General collection and processing . . . . .	36
3.2	Specific processing: The depth measurements . . . . .	36
3.3	Specific processing: The acoustic backscatter intensity measurements . . . . .	37
3.4	Specific processing: The velocity measurements . . . . .	37
3.4.1	Determining the along stream direction . . . . .	42
3.5	Discussing the obtained data . . . . .	43
<b>4</b>	<b>The Velocity Triangle</b>	<b>49</b>
4.1	The Harmonic analysis . . . . .	49
4.1.1	Derivations . . . . .	50
4.1.2	Restrictions . . . . .	54
4.1.3	The explained variance . . . . .	55
4.1.4	Overtides and compound tides . . . . .	57
4.1.5	Discussing the LSHA results using Fourier analysis . . . . .	62
4.2	The clockwise and anti-clockwise phases and amplitudes . . . . .	64
4.3	The ellipse parameters . . . . .	68
4.4	Discussing the results of the velocity triangle . . . . .	70
4.4.1	Velocity triangle parameters and bottom friction . . . . .	70
4.4.2	Velocity triangle parameters and effects near the surface; The wind induced effects and attachment chain interference. . . . .	72
4.4.3	Eccentricity, mean currents and concluding notes. . . . .	76
<b>5</b>	<b>Barotropic Model</b>	<b>80</b>
5.1	The governing equations . . . . .	80
5.2	Rewriting the governing equations . . . . .	81
5.3	Solving the governing equation . . . . .	83
5.3.1	Finding an expression for $w_1(t)$ . . . . .	83
5.3.2	Finding an expression for $w_2(t, z)$ . . . . .	84
5.3.3	Constructing $w(t, z)$ . . . . .	85
5.3.4	Applying the boundary conditions to $w(t, z)$ . . . . .	85
5.4	Determining the forcing term . . . . .	88

5.4.1	Scaling with the input amplitude and obtaining the final expression . . . . .	90
5.5	Rewriting the model to obtain the clockwise and anti-clockwise phases and amplitudes	91
5.6	Fitting the model with the measurements. . . . .	92
5.6.1	Combining the model with the measurements . . . . .	92
5.6.2	Method to fit $\nu$ and $s$ . . . . .	93
5.7	Comparing the coherent velocity with the barotropic model . . . . .	94
5.7.1	The cross stream phase . . . . .	96
5.7.2	All physical parameters and concluding notes . . . . .	97
<b>6</b>	<b>The Residual Signal</b>	<b>104</b>
6.1	Proof of vertical shear and stratification in the Marsdiep from a different source . .	104
6.1.1	Navicula data. A general description . . . . .	104
6.1.2	Navicula data. The search for shear, using the barotropic model . . . . .	107
6.1.3	Navicula data. Anchor Station 55, a special case . . . . .	108
6.2	Residual Buoy signal . . . . .	109
6.2.1	Ebb slack - Example One . . . . .	113
6.2.2	Ebb slack - Example Two . . . . .	115
6.2.3	Ebb slack - Example Three . . . . .	118
6.2.4	Ebb slacks in general . . . . .	120
6.3	Internal Waves or Internal Solitons? . . . . .	123
6.3.1	General comparison of the observed wave events . . . . .	131
6.3.2	Combining observations and theory. . . . .	131
6.3.3	Concluding discussion of the observations . . . . .	135
<b>7</b>	<b>Conclusions</b>	<b>139</b>
<b>8</b>	<b>Appendix</b>	<b>142</b>
8.1	Velocity triangle calculations . . . . .	142
8.2	List of abbreviations . . . . .	144
8.3	People that worked on the project . . . . .	144

# 1 Introduction

The idea for the research described in this master thesis started when my supervisor L.R.M Maas spotted a phenomenon that might possibly indicate the existence of a certain type of wave in the Marsdiep. Where the Marsdiep is located, what kind of wave we are dealing with and if they are indeed present will be explained in this thesis. Before going into details it is nice to give a short introduction using the first paragraph of a proposal I had submitted to claim a price which would provide with aperture to measure the waves we were looking for. Though I did not get the instruments, the research was carried out with equipment from the NIOZ (Royal Netherlands Institute for Sea Research). The first paragraph clearly indicates the heart of the research. From there I will start to describe the research performed in this thesis in more detail.

The main purpose of our research is to verify the possible existence of Internal Solitons (ISs) in the Marsdiep. ISs are nonlinear internal gravity waves propagating with speeds that depend on their amplitudes. Their occurrence in the Marsdiep was unexpected, but ISs were coincidentally spotted there by Internal Waves scientist Prof. Dr. L. Maas (NIOZ/University of Utrecht) on 27-07-08 when he crossed the Marsdiep with the ferry Dokter Wagemaker (DW, see figure 1). The phenomenon he saw had characteristics that are typical surface manifestations of ISs, namely: elongated bands of deviant surface roughness extending in cross channel direction that slowly propagate out to the North Sea. This observation suggests ISs exist in the Marsdiep. A photograph taken by an astronaut from the International Space Shuttle (ISS) taken on another day supports the idea of possible multiple occurrences of ISs in the Marsdiep (see figure 2). Also, captains of the DW have seen this pattern in the water more often and claimed that they could sense its impact on the ship. This is an indication of the strong (vertically sheared) subsurface currents that are typical for ISs [23, 14]. The surface currents due to ISs are such that at some parts (where there is convergence) surface wind waves will steepen enough to see a difference with 'normal' surface wind waves (see also figure 1 and 2). These typical current patterns make it possible to locate ISs with ADCP measurements [26]. The research proposed here will be the topic of my master thesis to graduate as M. Sc. Meteorology, Physical Oceanography and Climate at the University of Utrecht and will be performed at NIOZ.

## 1.1 General introduction

In this Master Thesis I discuss the measurement of currents and temperature, obtained using an Acoustic Doppler Current Profiler (ADCP), in an estuarine tidal inlet system. The measurements are decomposed in tidally forced barotropic currents (associated with long surface gravity waves) and baroclinic currents (forced by density gradients). The presence of topographic variations and stratification makes it feasible to find Internal Solitons (ISs) in the baroclinic part of the collected data set. To be able to decompose the data set into a barotropic and baroclinic part, an analytical model (forced by the tide, including Coriolis force and bottom frictional effects) that represents the barotropic currents is derived. The model is tested with the measurements and can then be used to obtain and subtract the barotropic currents from several data sets obtained at different locations and times. The resulting baroclinic currents of all the data sets are then analyzed for the existence of ISs. The model is tested with data retrieved with a downward looking ADCP mounted in a buoy that was deployed in the Marsdiep tidal inlet for 19.8 days from 09-04-09 until 29-04-09. The ADCP measured the whole water column with a frequency of  $\frac{1}{3}Hz$  with a vertical resolution of  $0.5m$ . In this section an introduction about ISs, the circumstances of the study area and an overall set-up of the experiment is described. In section (2) the technical description and the design of the deployment is presented. As a new on-line data sampling technique was used and problems were encountered while doing so, a detailed description of the deployment techniques is given. In section 3 the details on data collection and criteria for data rejection are given and the quality of the obtained data is discussed. In section 4 an analysis of the vertical structure of the measured currents is given and the basic input for the barotropic model is obtained. The barotropic model is derived and discussed in section 5.



Figure 1: Surface manifestation of internal Solitons seen as long bands of 'rougher' water. At 08:40 UTC at least 3 bands are clearly seen on this picture. The view is towards Den Helder, taken on the ferry Dokter Wagemaker. Other bands were visible at the Wadden Sea side of the ferry. The wavelength of the phenomenon was estimated to be approximately 30-50 meters and the bands move towards the North Sea with an estimated speed of approximately 0.2 m/s. When these waves were seen the currents were directed into the Marsdiep (flood) and they could not be due to the wind because they moved in the opposite direction.

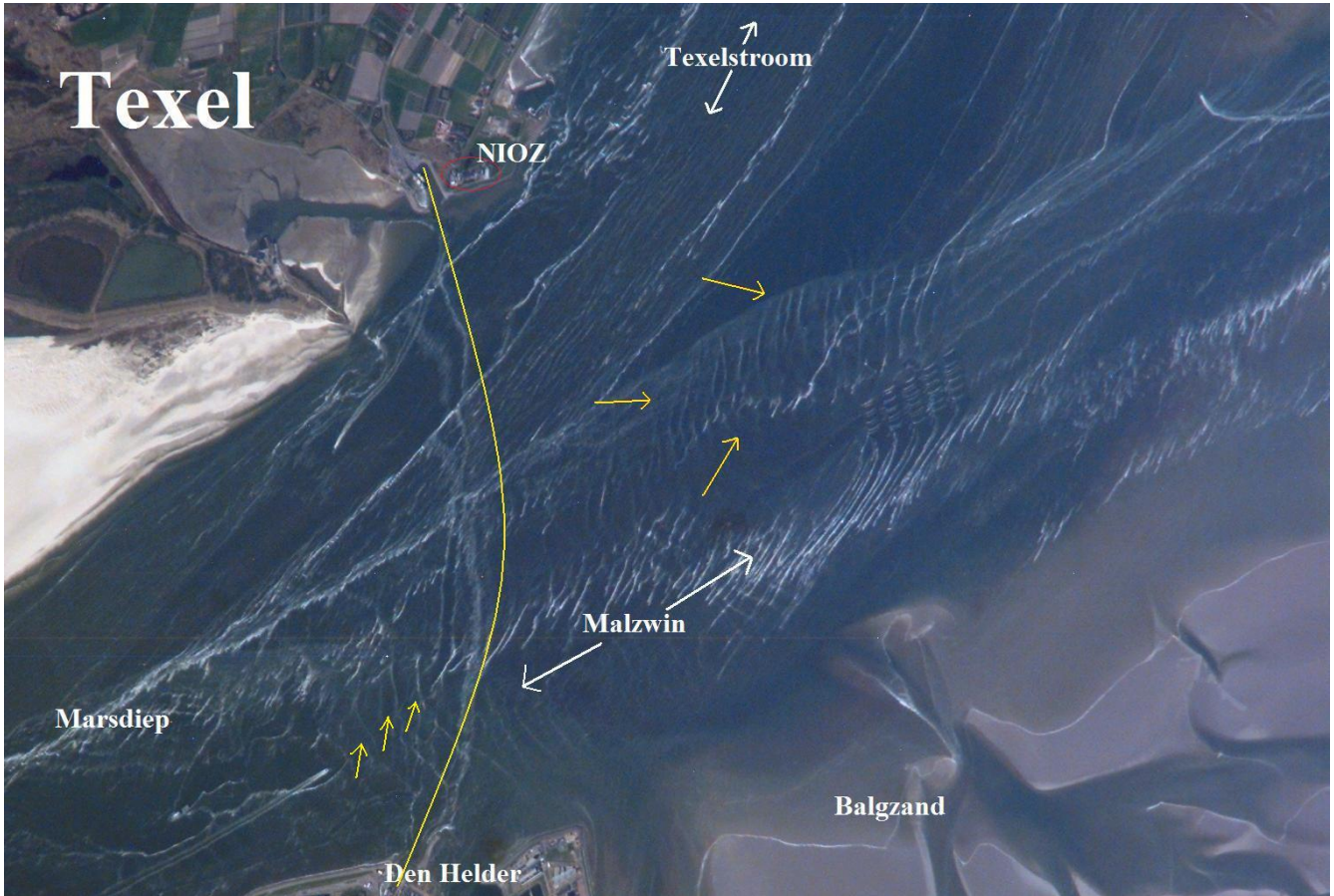


Figure 2: A photograph of the Marsdiep taken by an astronaut onboard ISS, on 1 May 2007 during ebb currents. The Marsdiep is located between Texel and Den Helder and bifurcates into the Texelstroom and Malzwin, which are the two main stream directions. More details of the location are described in section (1.3). The yellow line is the approximated track of the TESO ferry, Dokter Wagemaker and the red circle indicates the location of the NIOZ. The yellow arrows indicate the locations where certain wave phenomena are seen. These wave phenomena might be surface expressions of ISs.

## 1.2 Internal Solitons

An internal wave (IW) is a wave beneath the sea surface propagating in the interior of the ocean. An IW of interfacial type is located at the interface of fluids with different density (internal gravity waves) or different angular velocity due to the earth's rotation (internal inertial waves). Note that surface waves are also (gravity) waves between two interfaces, but because the density difference between these interfaces (ocean and atmosphere) is so large, surface waves have different physical dimensions than IWs. The IWs that maybe exist in the Marsdiep are on time and length scales that are not under influence of the earth's rotation and must therefore be considered pure interfacial internal gravity waves. Since the beginning of the 20<sup>th</sup> century until recently many examples of IW observations are available from locations all around the world [18, 6, 11, 10, 16]. Because of the vertical movement of the interface on which IWs propagate pressure differences are created that cause currents. The dynamics of linear IWs on an interface is well known linear theory. A simple example of current structures associated with IWs are those governed by a mode 1 IW and is illustrated in figure (3), based on [12] which gives a very clear derivation to obtain equations describing IWs. Published derivations leading to the equation describing velocities due to IWs can be found in [17, 36]. Important to note is that even one of the most simple forms of IW motion already contains vertical shear of horizontal currents.

Internal Solitons (ISs) are nonlinear variants of IWs and have also been observed in the ocean [27, 21, 23, 14, 24]. The velocity profiles associated with ISs are in first approximation the same as that of IWs, but due to (strong) nonlinearities the velocity profiles might differ from that of IWs. The nonlinear aspect of ISs is indicated by the shape of the isopycnals altered by a passing IS. There are several solutions known for the complex nonlinear equation describing ISs, which illustrates this nonlinearity. The most well known solution is the Korteweg-de Vries (KdV) solution. A derivation leading to the KdV equation can again be found in [12]. Published papers which have the KdV are for example that of [24, 23]. The KdV solution results in waves with shapes as described in figure (4). There are some important properties of ISs resulting from the KdV solutions:

- If an IS propagates in a two layered system and  $h_1$  and  $h_2$  are the depths of respectively the upper and lower layer and  $h_1 < h_2$ , then the IS manifest, itself as a depression.
- The larger the amplitude the faster the propagation speed of the IS. As a result ISs emanating from the same source are ordered in amplitude, with the Solitons with the largest amplitude at front.
- The larger the amplitude the shorter the IS.

It is also known that IWs but also ISs can transport sediments, nutrients and can cause mixing of different water masses [33]. Therefore the existence of ISs in the Marsdiep can be of great importance for sediment and nutrient transport between the North Sea and Wadden Sea, and for the mixing of both waters. Fresh supply of silt and nutrients is crucial for biological activity in this area, which is seen as one of the most special ecological areas of the Netherlands. Therefore it is of great importance to understand the processes that give this area its unique features. This is also one of the goals of research that is done by the Royal Netherlands Institute for Sea Research (NIOZ) on Texel, situated right next to the Marsdiep. Taking this into account it is worthwhile to take effort to exam the first indication of the existence of ISs in the Marsdiep in more detail.

To be able to manifest IWs or ISs the Marsdiep needs an interface and therefore the water column must at least contain two layers of water with different densities. On the interface between these layers the IWs or ISs can propagate. In general the Marsdiep is assumed to be vertically well

mixed due wind in combination with its shallowness and strong tidal motion which interacts with the bottom causing turbulence [38, 39]. Internal waves and related transports are not possible in that case. Nevertheless, it is expected that in combination with the right meteorological and tidal circumstances, the vertical density stratification in the Marsdiep will be such that ISs can exist. 'Right circumstances' here refers to the absence of vigorous wind and tidal mixing, so that the water column is not completely mixed.

Not discussed above is the generation mechanism of IWs. The two main generation mechanism of IWs are wind and tidal currents interacting with bottom topography. In the Marsdiep it is expected that the wind is not an option, because if there are strong wind, then also mixing of the water column is expected and therefore no stratification is available, hence no interface for the IWs to propagate on. As a result the mechanism must be found in the interaction between the tidal current and bottom topography. If the fluid is stratified and the barotropic tidal current moves over a bottom topography, than lines of constant density (isopycnals) are bend in approximately the same shape as the topography, as illustrated in figure (5). The isopycnals cause pressure differences that needs to be restored. As a result waves move from this source, with phase speed  $c$ , in both directions. This can be compared when a stretched rope is lifted in the middle and then relaxed again. From the middle of the rope, waves will propagate in both directions. The same happens with waves on the isopycnals leading to propagating waves in both direction from the source. As a result on the side toward which the current is directed (down current) nothing prevents the waves from propagating away from the source. On the contrary at the up current side, the barotropic current itself prevents the waves from propagating up current as long as the velocity of the barotropic current ( $u$ ) is higher than that of the phase speed of the waves ( $c$ ). Therefore waves will only propagate in the up current direction when  $c > u$  with a speed that is approximately  $c + u$  (note that  $u$  has opposite sign) [10, 9]. One can imagine that in the beginning the waves will propagate very slowly, only to become faster when the current slackens even more.

### 1.3 Study area

The measurements are obtained in an estuarine tidal inlet called the Marsdiep, which is about  $8km$  long and whose width increases from west to east from  $3km$  tot  $4.5km$ . The Marsdiep has maximum depths of approximately  $55m$  and is located in the northwest of the Netherlands, between Den Helder and the island of Texel and can be crossed with a ferry. The currents in the Marsdiep area can reach values up to  $2ms^{-1}$ . This is relatively high compared with the amplitudes of the sea surface height variations that are normally within  $2m$ . The reason is that the length of the inlet is artificially decreased in 1933 by the construction of the 'Enclosure Dam'. As a result the channel came closer to resonance resulting in increased velocities [19]. Wind is a variable but common feature in the Marsdiep area and reaches values of  $8Bft$  or higher several times per year. Due to the winds surface waves can be generated in the area itself or move inward from the North Sea into the Marsdiep inlet. The waves are sometimes steep and reach heights of several meters. In the spring and summer algae blooms and barnacles may grow quickly in the area and therefore also on the instruments leading to biofouling. The buoy that was mounted with the ADCP was placed at  $52^{\circ}59'N$  and  $4^{\circ}49'E$ . At this location it was approximately  $18m$  deep. The location of the buoy and details of the bathymetry are shown in figure (6), it also displays the location of the NIOZ institute from which the research was carried out, the route of the TESO ferries and the location where R.V. Navicula has done additional measurements. The main direction of the currents in this area is denoted by red arrows together with the main site of the measurements indicated by 'Buoy'. Two yellow lines are cross stream and along stream paths of depth measurements taken



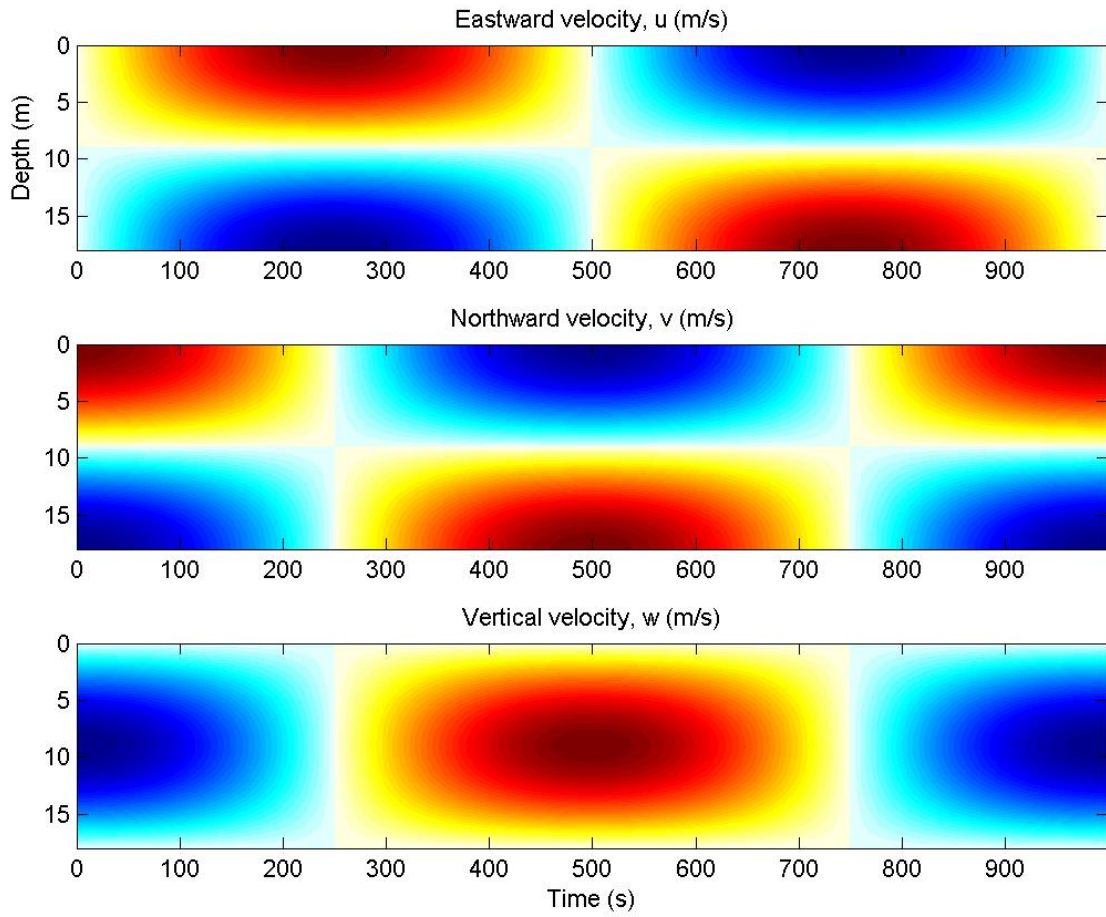


Figure 3: The velocity profiles for east, north and vertical velocities associated with IWs modified from [12]. Red (blue) values indicate positive (negative) values. The used parameters are amplitude  $a = 1$ , Coriolis frequency  $f = 1.6 * 10^{-4}$ , wave period  $T = 750s$ , at time  $t = 0$ , with wavelength  $\lambda = 100$ , wave number  $k = \frac{2\pi}{\lambda}$ , depth  $H = 18m$  and distance travelled  $x \in [0, \lambda]$ .

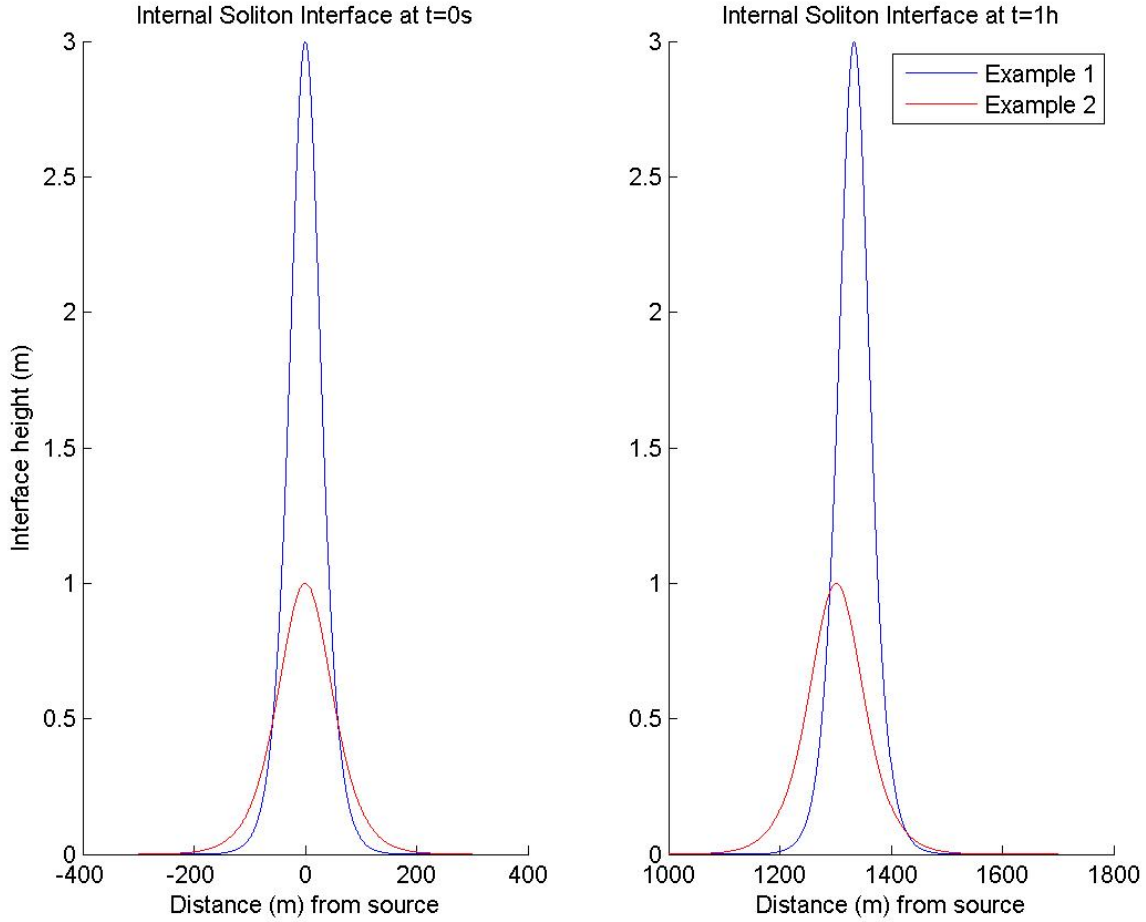


Figure 4: The shape of the interface between two layers of different densities due to IS. The left panel is calculated at  $t = 0s$ , the right panel is calculated at  $t = 3600s$ . Density of surface and bottom layer of  $\rho_0 = 1026kgm^{-3}$ ,  $\rho_s = 1024kgm^{-3}$ ,  $\rho_b = 1027kgm^{-3}$ ,  $g = 9.81ms^{-2}$ ,  $h_s = 10m$ ,  $h_b = 8m$ . Amplitudes of both examples  $a_1 = 1.5m$  and  $a_2 = 3m$ . Note the increased width with decreasing amplitude and that this is a soliton of elevation obtained by taking a surface layer that is thicker than the bottom layer. By comparing the left and the right panel it is clear that a larger amplitude soliton travels faster than a smaller amplitude soliton.

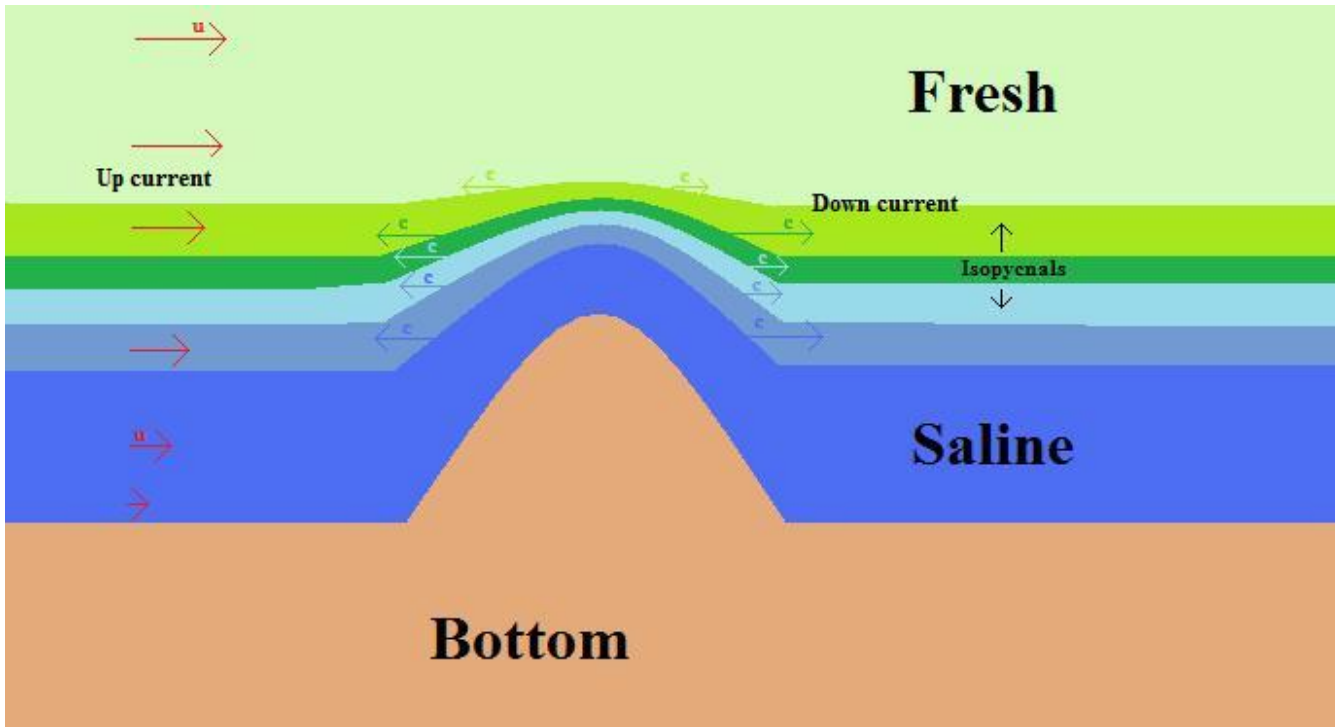


Figure 5: Here layers of different densities are indicated with a different color. Because of a current  $u$  (red arrows), a stratified water column is pushed over a bottom topography. As a result the isopycnals indicating the lines of equal density, must bend. The resulting pressure difference will be restored by waves propagating from the source to both sides. On the down current side nothing prevents the waves from propagating, on the up current direction propagation is only possible if the phase speed of the waves (indicated with  $c$ ) is larger than that of the current ( $u$ ).

from a cruise on made with the R.V. *Navicula* on 28-04-10. The results are shown in figure (7). The asymmetrical shape of the basin in the cross stream direction and the 'Deep of Helsdeur' in the along channel transect is clearly visible. On the one hand the Marsdiep shows features that are common for an estuary due to fresh water inflow from Lake IJssel. On the other hand it has features typically found in barrier tidal inlets because of the tidal waves running in and out the Wadden Sea Basin through the Marsdiep inlet. To be able to fully understand the observed water motion in this area, a general description of the expected motions in an estuarine and tidal inlet is necessary.

### 1.3.1 The Marsdiep as barrier tidal inlet

A tidal inlet is a (narrow) channel that connects the ocean with a shallow basin in which tidal currents maintain the connection and cause transport of water, nutrients and sediment. Tidal inlets worldwide have many useful economical and natural purposes. The Marsdiep tidal inlet connects the North Sea with the Wadden Sea which is, for various reasons, an important touristic, economical and natural area. As a result much research has been performed in and around the Wadden Sea and especially the Marsdiep tidal inlet [38, 39, 32, 31, 4, 5, 3]. The Marsdiep tidal inlet can be classified as a barrier tidal inlet. A barrier tidal inlet is normally created after barriers are breached due to storms or due to transgression of coastal plains due to sea level rise. Due to the tidal currents the channels connecting the flooded area and the Sea can be maintained. The Marsdiep inlet and also the Vlie inlet (see figure 6), are such channels which are both connected with the Wadden Sea, which is the flooded basin. Another kind of tidal inlet is the river tidal inlet. For example the Columbia, Eems and Amazon rivers are river tidal inlets. In river tidal inlets fresh (muddy) water coming from the river has significant effects on the water motions in these inlets. In general there is little fresh water inflow from rivers in barrier tidal inlets which, as a result, cause the tidal motions to be the most dominant processes in barrier tidal inlets. In the Marsdiep inlet the semi diurnal astronomical tidal wave of  $M_2$  frequency is the most dominant factor determining the water velocities [4]. The tide in the Wadden Sea is co oscillating with the tide in the North Sea which co oscillates with the tide in the Atlantic ocean. Because the English channel narrows such that the incoming tidal waves, behaving as Kelvin waves, are almost completely reflected, the tide enters the North Sea via the English east coast. The tidal waves coming from the north propagates in anticlockwise direction along the English, Belgium, Dutch, German and Danish coasts as in figure (8). Because the incoming tidal wave moves from south to north along the Dutch coasts, the Marsdiep inlet will be the first to be reached from all the barrier inlets of the Wadden Sea. As a consequence there is a phase difference between the Marsdiep and other tidal inlets (for example the Vlie inlet). The phase difference results in a Sea surface height (SSH) difference and therefore a pressure gradient between the inlets. The tidal inlets are sometimes connected (especially during high tides) resulting in small net flows between basins due to the pressure gradients [31, 3]. Due to decreasing depth from the North Sea into the Wadden Sea, the incoming tidal wave loses energy due to the increasing bottom friction as it moves into the Wadden Sea basin. In the Wadden Sea the wave is reflected. As a result the tidal wave in the Wadden Sea and Marsdiep can be treated as a mixture between a standing wave and progressive wave [28]. This character of the tidal wave and the linear combination of different dominant tidal constituents causes the sea level rise to be quicker than the sea level fall. This causes stronger flood currents than ebb currents in the western Wadden Sea. The duration of the ebb period is therefore longer.

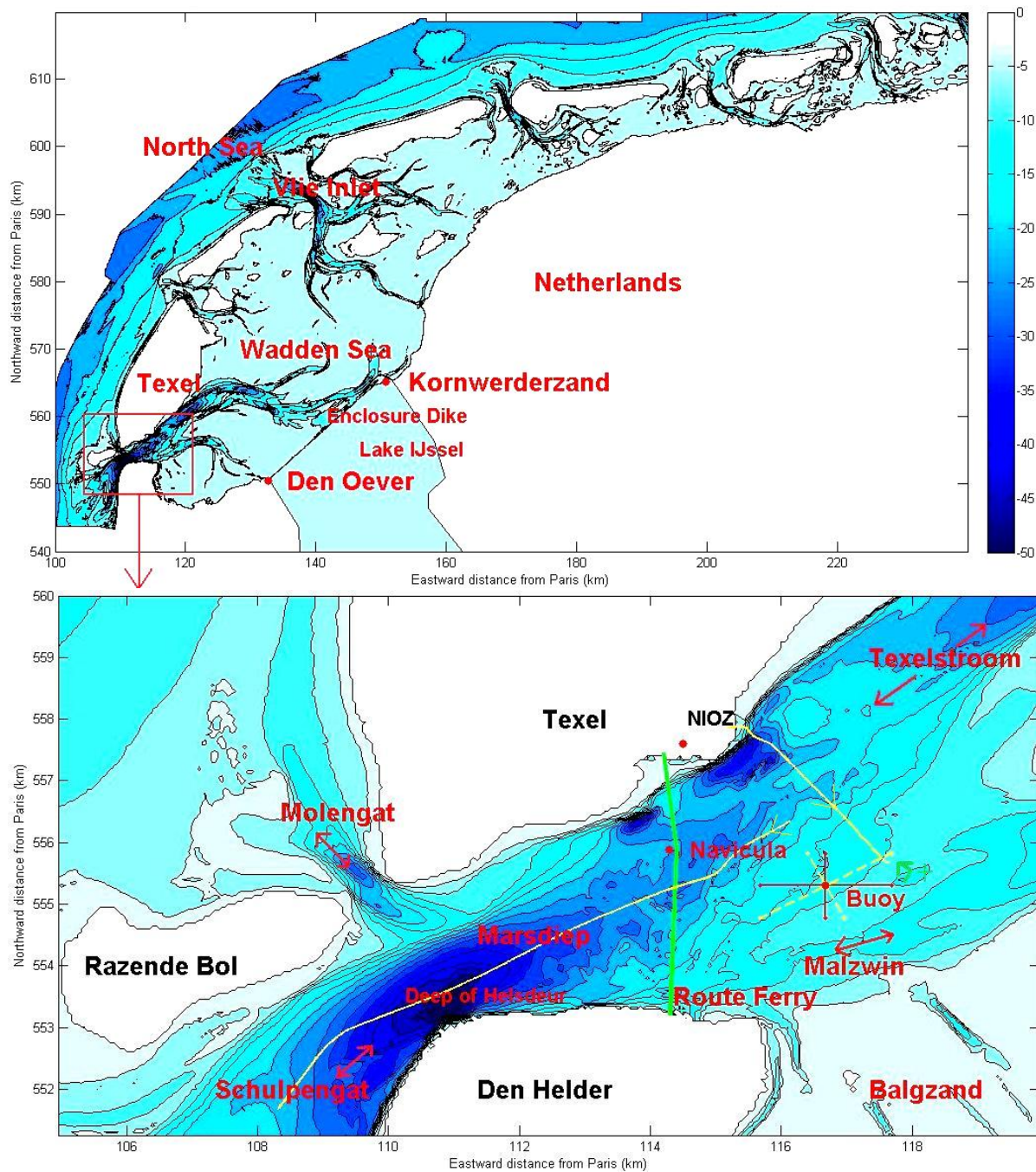


Figure 6: A representation of the study area. In the upper panel a large view of the Netherlands with the location of the North Sea and Wadden Sea is shown. In blue the bathymetry of the Wadden Sea and partly of the North Sea is indicated. The latest depth measurements used are obtained in 2002. White denotes location with no data. Lake IJssel and its color is placed in manually. The sluices of Lake IJssel are Kornwerderzand and Den Oever, which are connection via the Enclosure Dike. In the upper left side the white area is still the North Sea. The rest of the White areas denote coast lines and sand plates. The red square denotes the area that is shown in more detail in the lower panel. Important features as the directions of the main currents (Malzwin, Texelstroom, Schulpengat en Molengat) are indicated with red arrows. Measurements obtained with the buoy and R.V Navicula of the NIOZ and the location of the NIOZ itself, are indicated with a red dot. At the location of the buoy the direction of the along and cross stream currents (dashed yellow lines) with respect to the east and north axis (red lines) is shown. The current is rotated  $27.7^\circ$  anti clockwise, as will be shown in section 3. The route of the TESO ferry Dokter Wagemaker is indicated with a green line. In yellow the routes are shown that are used to obtain the along stream and cross stream section shown in figure (7).

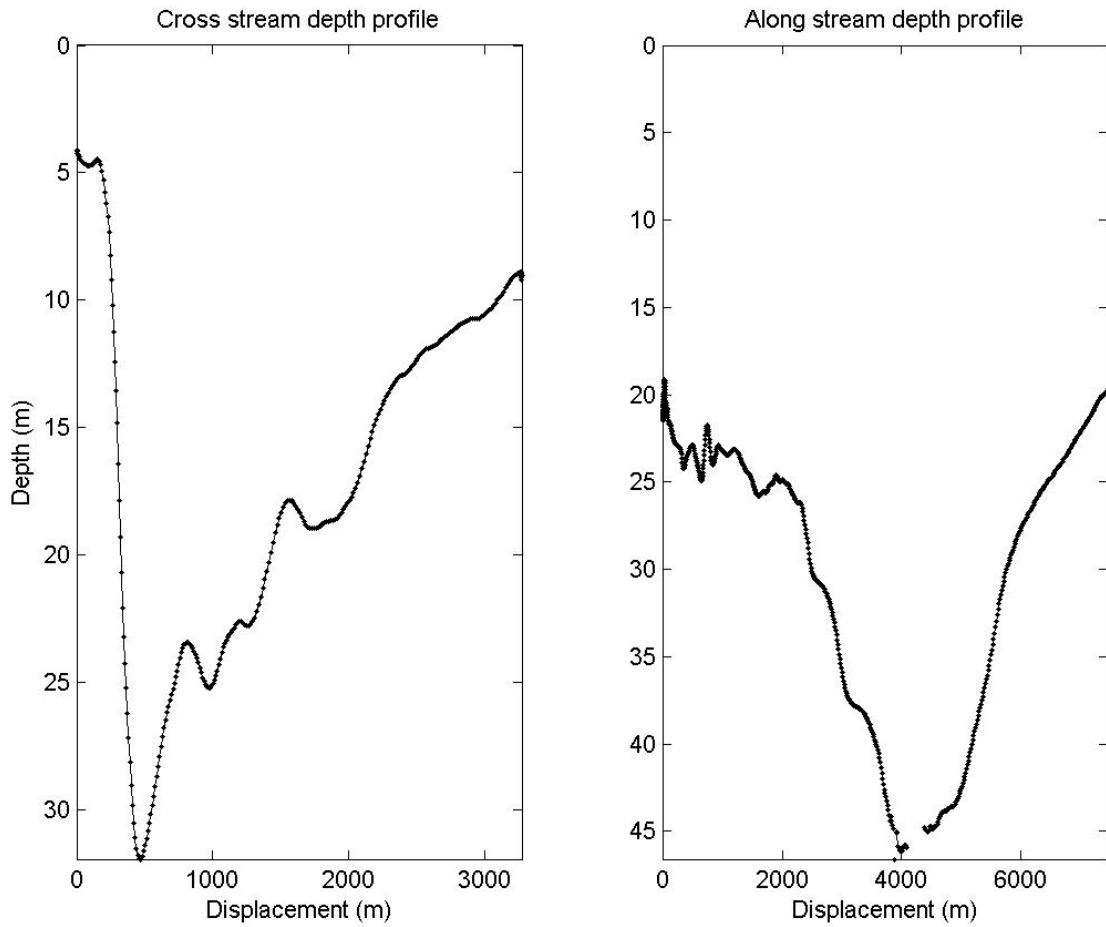


Figure 7: Along and cross stream depth profiles of Marsdiep obtained on 28-04-10, close to the location where the deployment was located. In figure (6) the transect measured to obtain the depth profiles are indicated with yellow lines. The cross stream direction was measured starting in the north and going southward. The alongstream transect started east and ended west.

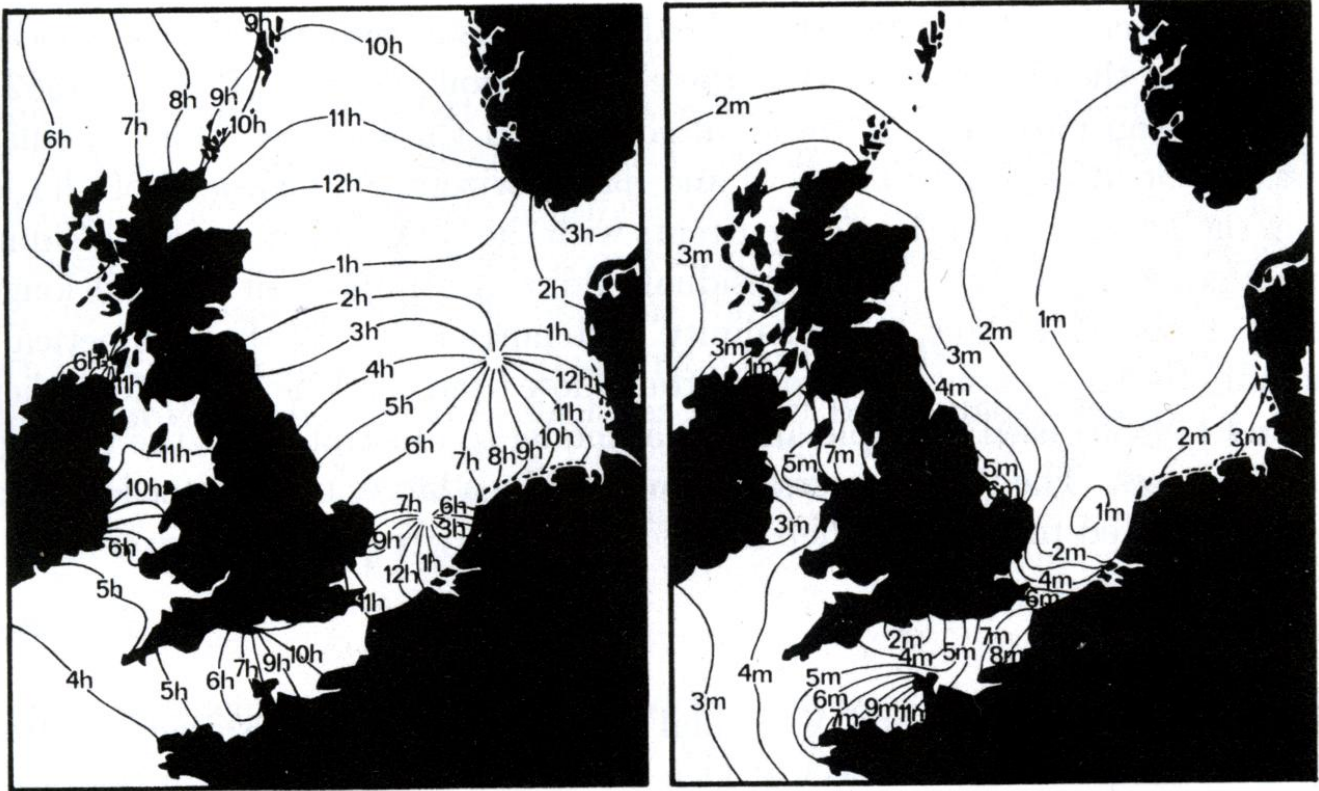


Figure 8: The left panel shows contours of equal times of high water and the right panel shows the tidal range during spring tide in the North Sea. This is a picture is adapted from [2] and clearly shows a tidal wave entering the North Sea from the Atlantic Ocean in the North and then rotates around two amphidromic points.

### 1.3.2 The Marsdiep as an estuary

An estuary can be defined as a semi enclosed body of water having a free connection with the open sea and within which sea water is measurably diluted with fresh water derived from land drainage [22]. As a result of the horizontal density gradient a baroclinic flow will occur. Using figure (9) one can get an impression how a baroclinic flow can exist. Starting with a two dimensional basin in which there are two reservoirs of water with equal depth and surface height. The right reservoir is filled with dense ( $\rho_1$ , Salt) water and the left reservoir is filled with less dense ( $\rho_2$ , Fresh) water, so that  $\rho_1 > \rho_2$ . Due to a barrier no interaction is initially possible between both reservoirs. Using the hydrostatic balance, the pressure over a unit square at a certain depth ( $p(z)$ ) can be calculated (assuming a constant density) resulting in  $p(z) = -\rho gz$ . The pressure difference between both reservoirs at a certain depth ( $\delta p(z)$ ) can then be expressed as:

$$\delta p(z) = \delta \rho g z \quad (1)$$

Where  $\delta \rho = |\rho_1 - \rho_2|$ , so that it can be concluded that the density gradient between two reservoirs produces pressure gradients at a certain depth that increases with depth. When the barrier is removed the water will start moving from the high pressure to the low pressure area meaning a water flow from the dense (Salt) water towards the less dense (fresh) water. As a result the fresh water surface level will increase and the salt water surface height will decrease. The difference in surface height also creates a pressure difference (between water and air at the same height) causing the fresh water to flow over the salt water. If this system can move undisturbed this will end up in a situation in which the fresh water is on top of the salt water. It can be concluded that the water circulates in such a manner that the vertically well mixed water reservoirs, having vertical isopycnals, have changed to a situation that the isopycnals are horizontal and the situation is balanced. From this it can be concluded that the situation with vertical isopycnals is an unstable situation. When this kind of stratification is found in nature due to freshwater discharge by, for example, a river, the resulting water movements is called estuarine circulation.

The question is if estuarine circulation can also be expected in the Marsdiep. First the Marsdiep can be seen as a body of water and the diluting freshwater originates from discharge from the sluices at Den Oever and Kornwerderzand that are located at the landward end of the Malzwin and Texelstroom tidal channels. This leads to density differences between the fresher water at the landward side of the Marsdiep close to the sluices and the more saline water at the seaside of the Marsdiep, close to the North Sea. These are the characteristics of an estuary, but due to strong tidal currents and wind the different water masses are in general well mixed [38, 39, 40, 5] reducing the stratification and therefore estuarine circulation. Still the tide has phases of weak currents and the freshwater discharge from Lake IJssel can be large leading to situations in which stratification and therefore estuarine circulation can occur in the Marsdiep [3, 5]. The motions due to density gradients are also called baroclinic motions and have yet only been found in cross channel direction [5] and due to the dominance of the barotropic tidal currents, not in along channel direction. As said before, density gradients are available in along channel direction so that baroclinic motion in along channel direction must be present too and may possibly lead to a situation in which the isopycnals are bend as in the middle panel of figure (9). This is a situation, in combination with other circumstances (section 1.2), in which IS may occur.



### 1.3.3 Expected (secondary) effects on the currents in the Marsdiep

From the above it can be concluded that currents in the Marsdiep are, in first order, governed by the tides. Several other effects may interact with the tide causing second order variations or cause a second order (or secondary) currents on its own. Several of the know secondary currents and/or effects, obtained from previous research, are discussed in this section. Even though these secondary currents are not as dominant as tidal currents in the Marsdiep, they are certainly significant in the measurements obtained for this thesis.

In a first order approximation the tide induced currents are uniform over depth and across the Marsdiep, but the tidal currents are under influence of friction from the bottom and the coast. Friction in general causes a decrease of currents and mixing of the water. Bottom friction causes a decrease of the currents towards the bottom and mixing in the vertical. Depending on the depth the influence of bottom friction can even be 'felt' by the currents at the surface. The coast (or a side wall of a channel trough which the water flows) has effects on the current in the horizontal and in the vertical, decreasing currents close to the coast compared with currents further from the coast and causes mixing in the horizontal and vertical [40]. The modification of the tidal current by the bottom and coastal friction can be interpreted as a secondary effect.

Besides friction due to the bottom and the coast there is also friction of the water with the atmosphere. As long as there is relative movement of the water compared to the atmosphere, than there will be friction. Wind often increases the relative velocity difference between the water and the atmosphere and therefore increasing the friction effects. Wind causes mixing and may also transport water and thereby influences the currents in the Marsdiep in several ways. The effect of the wind depends on its strength, duration and direction. Wind causes drag at the surface, leading to a (direct) wind driven current which decreases with depth. If the displaced water, due to the wind driven current, encounters a rigid boundary (such as a coast), than the wind driven current will lead to a set-up (or set-down) of the sea surface height, causing a pressure gradient and therefore (indirectly) a balancing wind driven current which is, in first order approximation, uniform over the depth (but of course influenced by bottom friction). Via channels in the Wadden Sea the Marsdiep inlet is connected with the Vlie inlet. Due to the (in)direct wind effect a net flow towards or from another channel can cause a net flow in or out of the Marsdiep inlet. In particular southwesterly wind causes transport from the Marsdiep to the Vlie basin and easterly wind causes transports in opposite direction [38, 31, 3]. It can be concluded that wind causes modification of the tidal current which can be seen as a secondary effect, but is also able to directly induce a secondary current.

Another secondary current is caused by curvature of the Marsdiep basin. The water moving through a curve will be under influence of a centrifugal force. This causes a pile up of water on the outside of the curve. A pile up causes an inward pressure gradient which results in a cross stream current balancing the curvature effect [5].

As noted in section (1.3.2) the sluices of lake IJssel discharge fresh water into the Wadden Sea at Den Oever and Kornwerderzand. This results in two secondary currents. The first is a net current from the Wadden Sea towards the North Sea as a direct consequence of the discharge. The second effect is due to the induced salinity (and often a temperature) difference between the North Sea and the Wadden Sea. These differences result in along stream, cross stream and vertical density gradients in the Marsdiep. As explained in section (1.3.2) the density gradients will induce secondary baroclinic currents that will be of importance during some phases of the tide.

Because the tidal currents are so strong in the Marsdiep, the Coriolis force has a significant deflecting effect on the currents. As a result the Coriolis effect causes the along channel currents

to veer in such a way that a secondary cross channel current exist [5]. As illustrated in figure (10), the secondary cross channel current resulting from the Coriolis force are expected to induce cross channel circulation cells [15, 34].

It can be concluded that the currents in the Marsdiep are in first order governed by the tide and in second order by wind, discharge, curvature and baroclinic effects. All currents are under influence of friction from the bottom, coast and atmosphere and are deflected by the Coriolis force. It depends on temporal and spatial distribution of these processes which currents will be significantly visible in the measured velocity profiles. Based on previous research it is expected that in general all effects together contribute to a net outflow trough the Marsdiep [31, 3]. In this thesis a least squares harmonic analysis will be used to find structures in the velocity measurements that are coherent with tidal frequencies. The incoherent part contains current structures that are not influenced by the tide or that are partly tidally driven, but not on a regular base. An analytical barotropic model is developed that gives the opportunity to estimate the barotropic current, which is defined as the tidal current that is affected by Coriolis force and bottom friction. The model results in an opportunity to explain processes found in the coherent signal and to reproduce and predict a part of the tidally driven current.

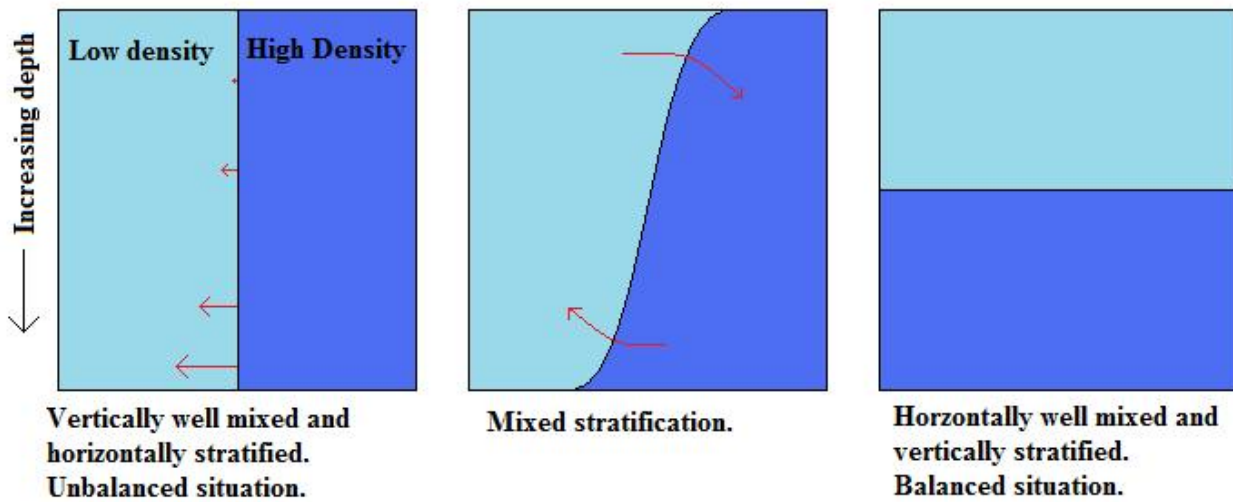


Figure 9: In this figure the currents due to density differences are shown (red arrows). The system changes from an unbalanced situation to a balanced situation in which there are no more density induced currents.

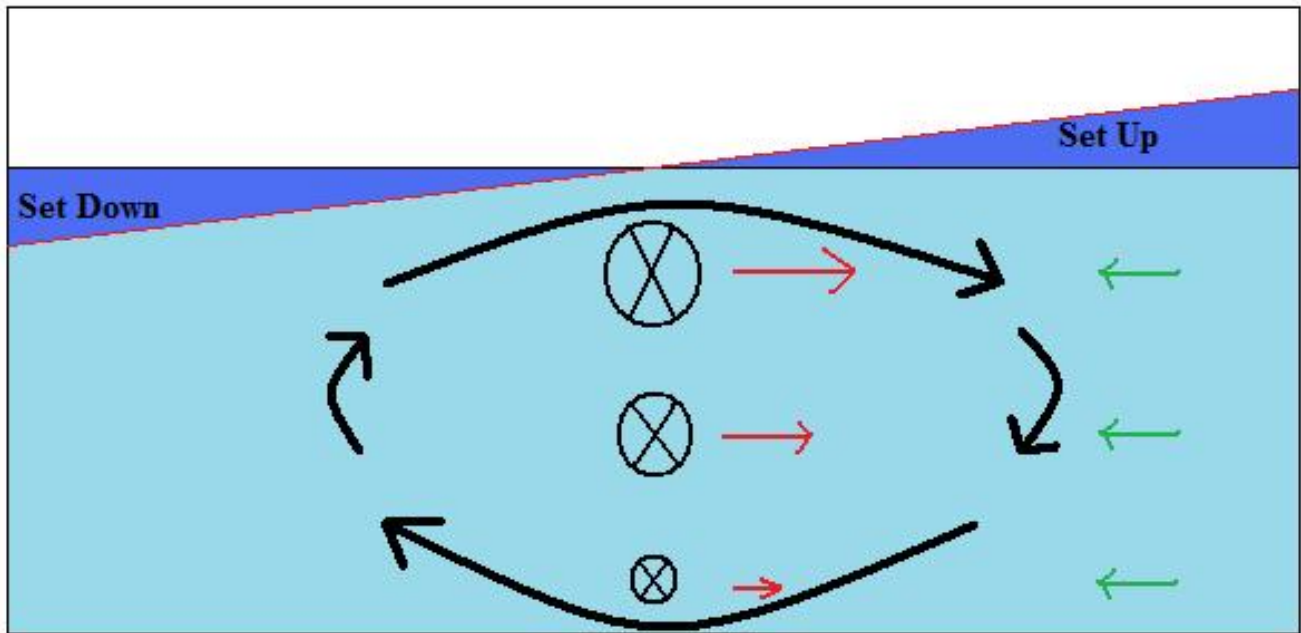


Figure 10: A very simplistic sketch that represent the basic idea behind cross stream circulation cells due to Coriolis deflection. If there is an along stream current on the Northern hemisphere directed into the page, than this current is deflected to the right due to the Coriolis force. This can be represented as a cross stream velocity component (red arrows). As a result water is transported to the right. When this happens in a finite width basin a set up occurs against the right boundary (or coast). The set up causes a pressure gradient that leads to a cross stream current in the opposite direction of the current due the Coriolis deflection (green arrows). The velocity due to set up is uniform over depth. The velocity due to Coriolis force decreases towards the bottom due to an decrease in along stream velocity towards the bottom. As a result on obtains a cross stream circulation cell (black arrows) with velocities at the surface in the direction of the Coriolis deflection and velocities at the bottom in the opposite direction.)

## 2 The Deployment

### 2.1 Requirements and circumstances

When the project was started it was tried to achieve relatively high frequency (about  $1Hz$ ) and long term (3 months) measurements with a down looking ADCP. This high sampling rate increases the chance of accurate capture of passing IS. An online connection with the ADCP was wished for so that there was a possibility to change the ADCP configurations and make the changes visible on a computer screen located at the NIOZ institute. As explained in section (1.3) the measurements are done under rough sea conditions. This combination of requirements and circumstances made this type of deployment highly experimental for the NIOZ institute. Therefore the design of the deployment was a significant part of the project.

### 2.2 Design of the deployment

The measurements are collected with a  $1200kHz$  RDI Workhorse Rio Grande ADCP that was mounted in a syntactic elliptical  $499kg$  buoy with an initial buoyancy of  $528kg$  (figure 11). On top of this buoy the energy supply for the ADCP was mounted together with a light signal, a Xeos Iridium Satellite Beacon with GPS location and a pole with a data transmitter and receiver couple (figure 12). The energy for the instruments was supplied by an EFOY Pro 600 Series Smart Fuel Cell (SFC). The SFC was fueled with  $10L$  methanol which can deliver  $9.1kWh$  of energy. The SFC charged a ( $12V$ ) car battery with a capacity of  $40Ah$  ( $=0.48kWh$ ). When the voltage of the battery dropped beneath  $12.3V$  the fuel cell automatically turned on to charge the battery. The battery, fuel cell and methanol were all inserted in a water proof aluminum box that was mounted on top of the buoy (figure 13 and 14). The fuel cell required an outlet for gasses and heat and an inlet for cool air, therefore the aluminum box on top of the buoy had 3 open connections with the atmosphere that were installed in such a way that no splashing sea water or rain could get in. The light signal, carried by the buoy for protection, was a clear white colored IML 200 PU LED of  $1.5W$  that only worked from dusk till dawn to save energy. An A-RF35 Long Range multi-channel radio (LRr) modem at  $869MHz$ ,  $0.01A$  at  $12V$  was used for the online communication with the ADCP. Two pairs were used because the ADCP could not sent and receive signals trough one pair at the same time. A pair of transmitter receiver must have visual contact to be able to exchange data. Therefore a  $2.5m$  pole was mounted on top of the Buoy. This way the transmitters and receivers on the Buoy and on the roof of the NIOZ institute had a clear sight. The transmitter and receiver on top of the mast had to be separated for at least  $1m$  not to get interference of the signals. Therefore the pole had a T shape. The distance covered between the buoy and the roof was  $2.3km$  of the maximal  $6km$  allowed by the radio.

Several cables needed to connect instruments from inside with instruments outside the aluminum box. These cables used a water proof wire outlet, which is a well known technique on ships (figure 15). The whole buoy with all the equipment described above was attached, with a chain and a cable, to two  $1500kg$  weights on the sea bottom. The buoy does describe a small ellipse due to the tidally changing direction of the currents in combination with a little margin in the length of the cable between the buoy and the first weight. This movement might be of influence in the depth signal because it crosses different locations. It is assumed that the influence of the movement on the depth signal will be negligible compared to depth differences due to the tidal rise and fall of the sea surface found back in the depth signal.

The LRr, the light and the ADCP need an amount of power. There is a limited amount of

power available and therefore the configuration of the ADCP has also limited duration. To be able to determine the best configuration we need to know how much power is available for the ADCP. The energy consumption is expressed in  $kWh$  which is a value in joules, this is done using the following formula's:

$$E = Pt \quad (2)$$

$$P = UI \quad (3)$$

Where,  $E$  is the energy in Joules,  $P$  is the power in Watt,  $t$  is the time in seconds,  $U$  is the electrical potential difference in Volt ( $V$ ) and  $I$  is the currents in Coulombs per second ( $A$ ). Using these formula's the calculated energy supply and consumption is given in table (1). This leads to  $7.44kWh$  available for the ADCP. The energy usage of the ADCP is a function of deployment duration, depth cell size, number of depth cells, amount of (sub)pings to detect the water velocity, amount of pings to detect the bottom, deployments mode and many more. The configuration is optimized for the circumstances and resulted in a configuration in which every  $3s$  a measurements was made with a single ping std of  $2.32\text{ cms}^{-1}$  and 40 vertical bins with a resolution of  $0.5m$ . This design with the configurations as above, was deployed on 25-03-2009. On 26-03-2009 there was a failure and the buoy was retrieved. The problem was clear, the water proof box was not water-proof and therefore the battery and the SFC were destroyed. Through the heat outlets water had poured in. There are several possible explanations that might have caused the box to flood. The most easy explanation is that the cable between the buoy and the weights was too short. The maximal possible difference between the inlets and the bottom was  $21.15m$ . Depths of approximately equal magnitude have been measured. Analyzing available data (duration was approximately  $12h$ ) showed extreme pitch and roll events that could have caused the flooding of the aluminum box. The extreme pitch and roll events can be explained by analyzing the force balance of the buoy during the deployment (figure 16).

First the most important forces acting on the buoy must be described, which are the gravity force ( $F_g$ ), the buoyancy force ( $F_b$ ), the force due to the currents that are acting on the buoy ( $F_c$ ) and the force due to cables that are attached to the buoy ( $F_p$ ). In figure (16), which is not on scale, three situations drawn. The first situation assumes that the buoy is in water without currents and with a flat sea surface without wind waves causing only the gravity ( $F_g$ ) and buoyancy ( $F_b$ ) forces to act on the buoy. Depending on the density of the water, the material and weight of the buoy, a balance will be found which determines how deep the buoy will be in the water. This buoy sinks about half its height into the water and then moves up and down with the sea surface height variations due to the tide. This is a stable situation. In the second situation a current, coming from the right to the left, is superposed. At that moment the buoy will float in the direction of the current until at a certain moment the cable has no more length and starts to pull the buoy into the direction of the cable (elasticity). The elasticity can be decomposed in forces directed parallel or perpendicular to the gravity force. The component directed parallel to gravity is balanced by Buoyancy forces. The component perpendicular to gravity is not balanced and therefore exerts a torque on the buoy causing it to rotate in such a way that the up current side wants to move out of the water and the down current side wants to move into the water. Due to this rotation the gravitational forces, buoyancy forces and the force created by the current acting on the buoy, will change. This all leads to a change in the elasticity of the cable because, when the buoy is rotated, the up current side will be lifted into the air and the down current side is pulled into the water. A larger area is now in the water and under influence of the current. This is shown in the third situation. Though this force is spread over the whole part of the buoy that is under water, it is

Device	t (days)	E (kWh)
trans./reciev	90	-0.52
Light(at night)	0.5x90	-1.62
Battery	NA	0.48
SFC	NA	9.1
Total	NA	7.44

Table 1: Energy calculations for the deployment

represented as  $F_c$  at the end of the buoy. This is done to illustrate that this force also creates momentum and therefore it leads to rotation in the opposite direction than the rotation due to the cable. The force due to the current is a restoring force, because it tries to rotate the buoy back into the position as described in the second situation. The gravity force ( $F_g$ ) is also represented by one arrow at the end of the buoy but is effective all over the buoy and in the same direction. The gravity forces on the up current side are not balanced anymore by the buoyancy forces and will therefore act as a restoring force. The down current side that is pulled into the water is still under influence of gravity but the buoyancy forces have increased because that part of the buoy has more volume (deeper) inside the water leading to an increase in upward forces that acts as a restoring force. The length of the cable determines the angle in which it pulls the buoy. The longer the cable is, the larger the pitch can be because in the ideal situation the pulling direction of the cable is directed straight to the centre of gravity and therefore a longer cable would create a larger pitch. The strength of the current determines the pulling strength of the cable. The balance between all the forces described above result in a certain tilted position of the buoy in which it is in balance. This changes during the tide due to changing current strength. To be able to really know what happens with the buoy, the effect of surface waves must be taken into account. Unfortunately the effect of surface waves are hard to predict, but for certain, increases instability and therefore the possibility of flooding our fuel tank.

From the above it can be concluded that, with some effort, it might be possible to calculate the tilt as in situation 3 of figure (16) but the effect of the surface waves is very hard to predict. In any case, surface waves might be of great importance for outbalancing the buoy to a position where water can pour into the aluminum box through gaps that were thought to be water proof. This would have been the case in a more stable situation without surface waves. The combination of short cable, high pitch and roll events due to the force balances explained above and the surface waves lead to the failure.

## 2.3 The second deployment

The second deployment, shown in figure (20), was different from the first one. The most important difference was the length of the cable which was lengthened to  $30m$  so the total length between the bottom and the top of the aluminum buoy was  $39.15m$ . The location of attachment of the cable could not be changed on such a short notice. A radar reflector, which is a  $1m$  high pole, was attached on top of the buoy. There was no time and money to order and wait for a new SFC, therefore Lithium Tekcell type D batteries were used, which deliver  $3,6V$  and have a capacity of  $19Ah$ , see figure (18). The batteries are available in pairs which are connected in series. When batteries are connected in series the capacity stays equal but the voltage can be summed up. Two pairs in series (4 batteries) give  $14,4V$  and  $19Ah$ . The length of four batteries is  $230mm$  and they have a diameter of  $34mm$ . The time of the deployment is now shortened because the license still

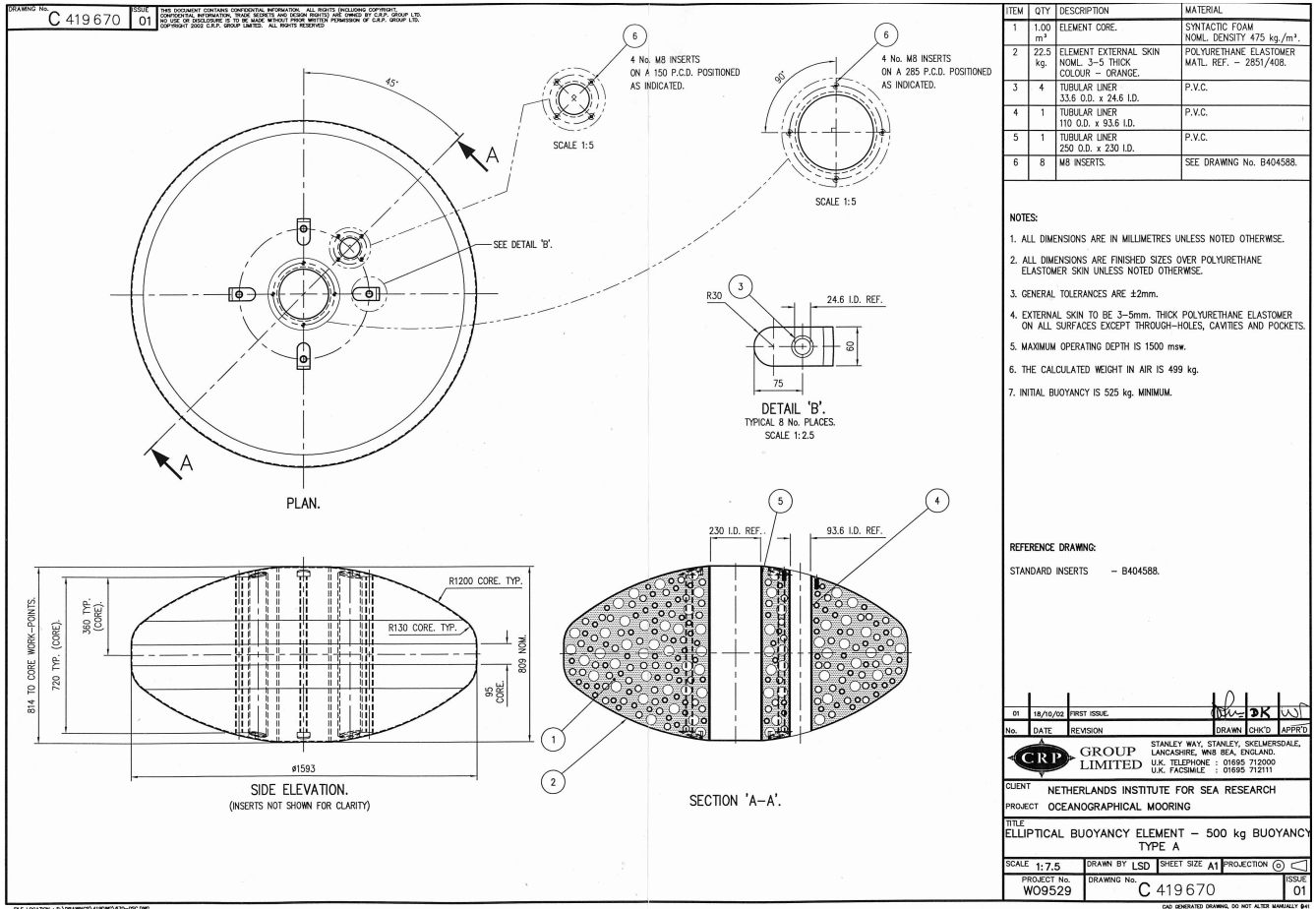


Figure 11: The technical representation of the buoy.



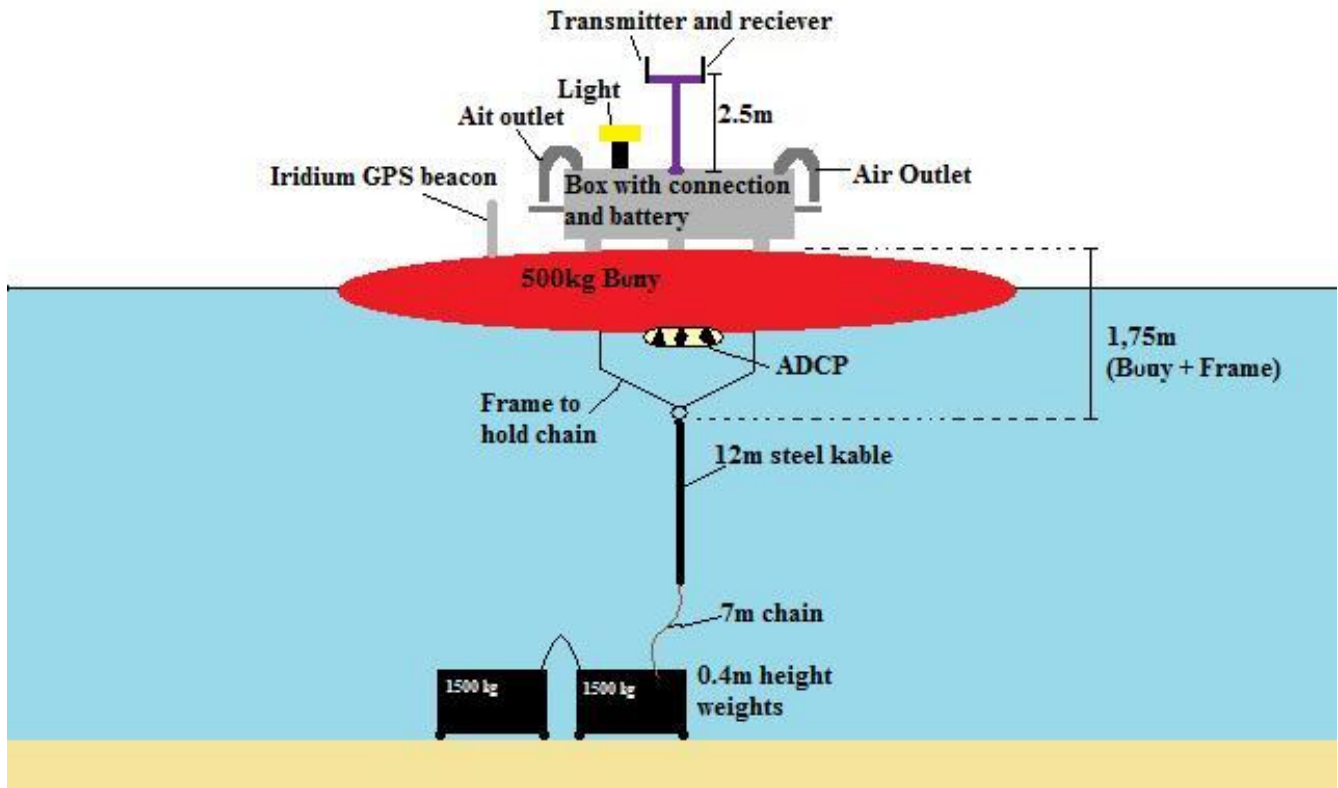


Figure 12: The design of the deployment as it was in the water.

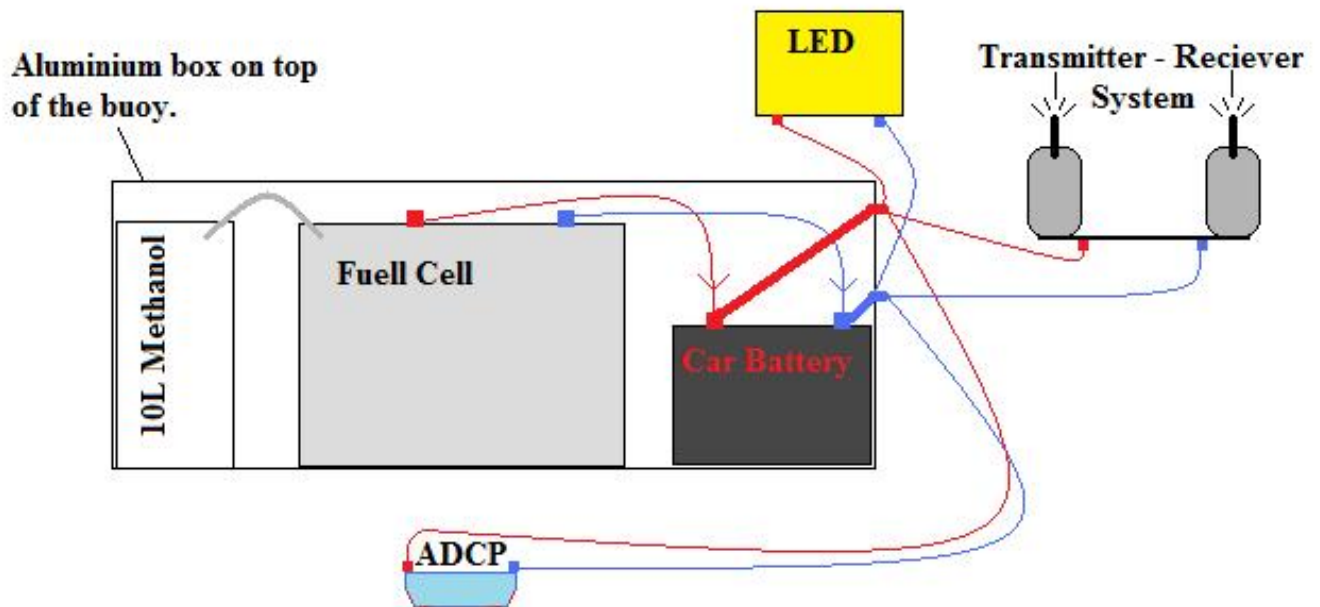


Figure 13: A representation of the connections between energy suppliers and energy absorbers.

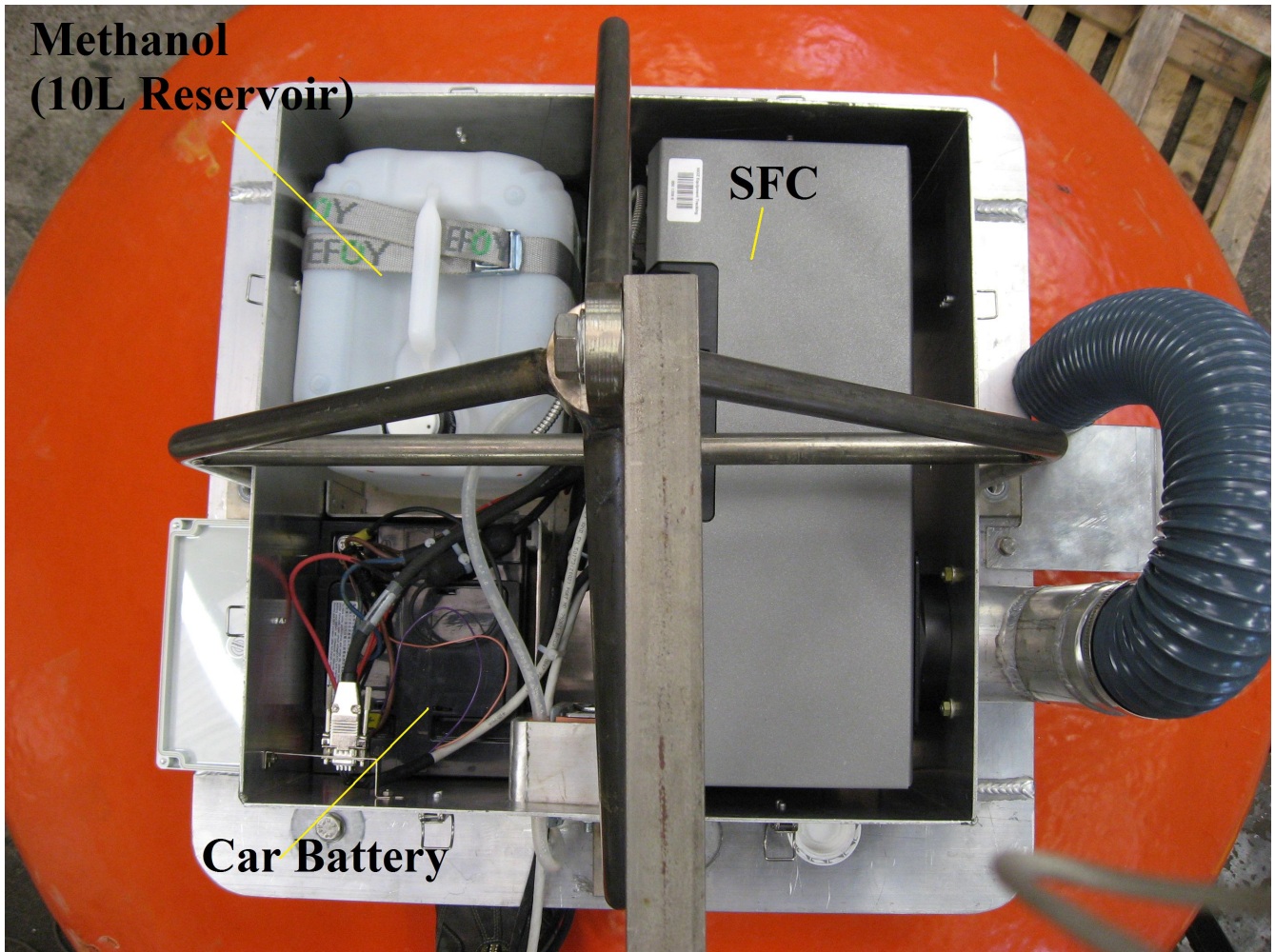


Figure 14: A picture showing the inside of the aluminum box that is located at the top of the buoy. The three components used for the energy supply are clearly visible.



Figure 15: The water proof wire outlet.

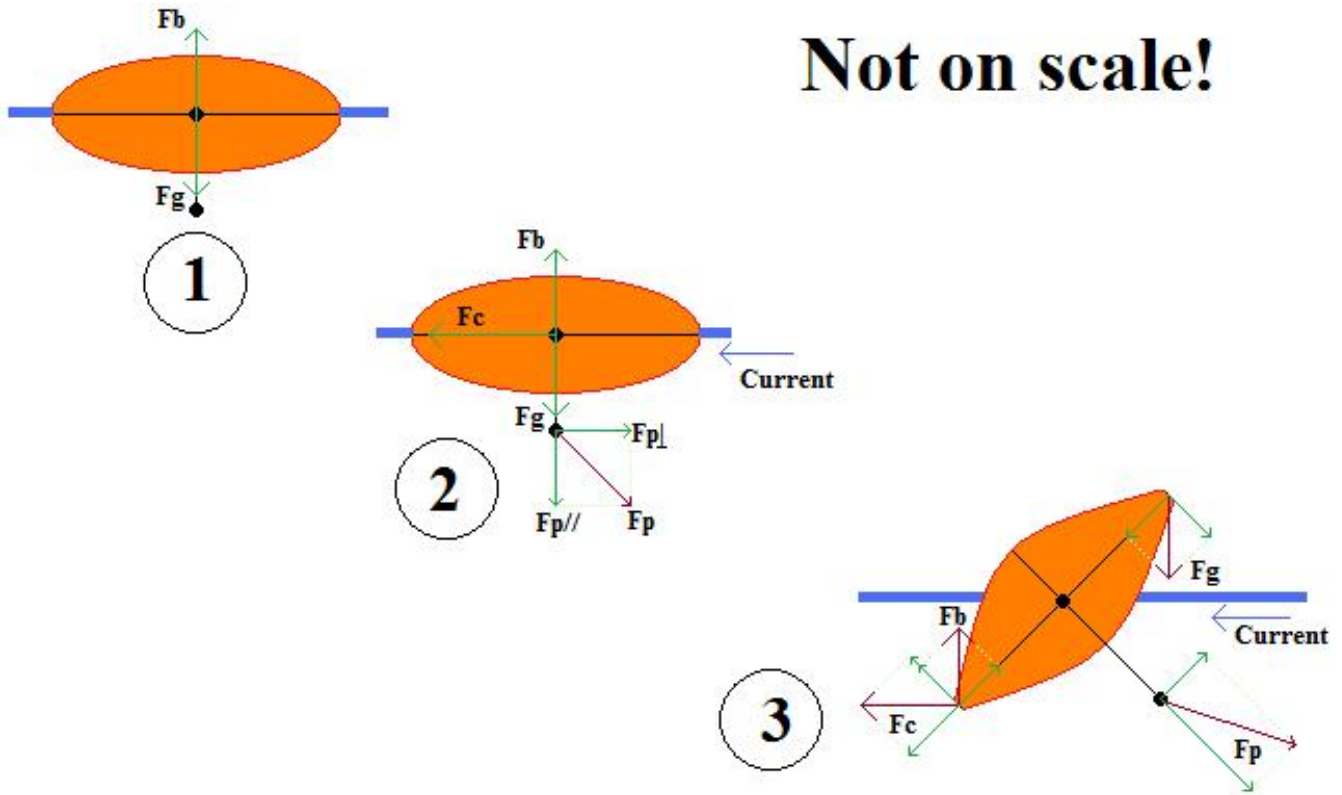


Figure 16: A sketch of the forces acting on the buoy and the resulting balance. Note that this is a qualitative sketch to illustrate which forces are acting on the buoy so some forces act on the entire buoy while they are represented at one position and the forces are not drawn on scale relative to each other.

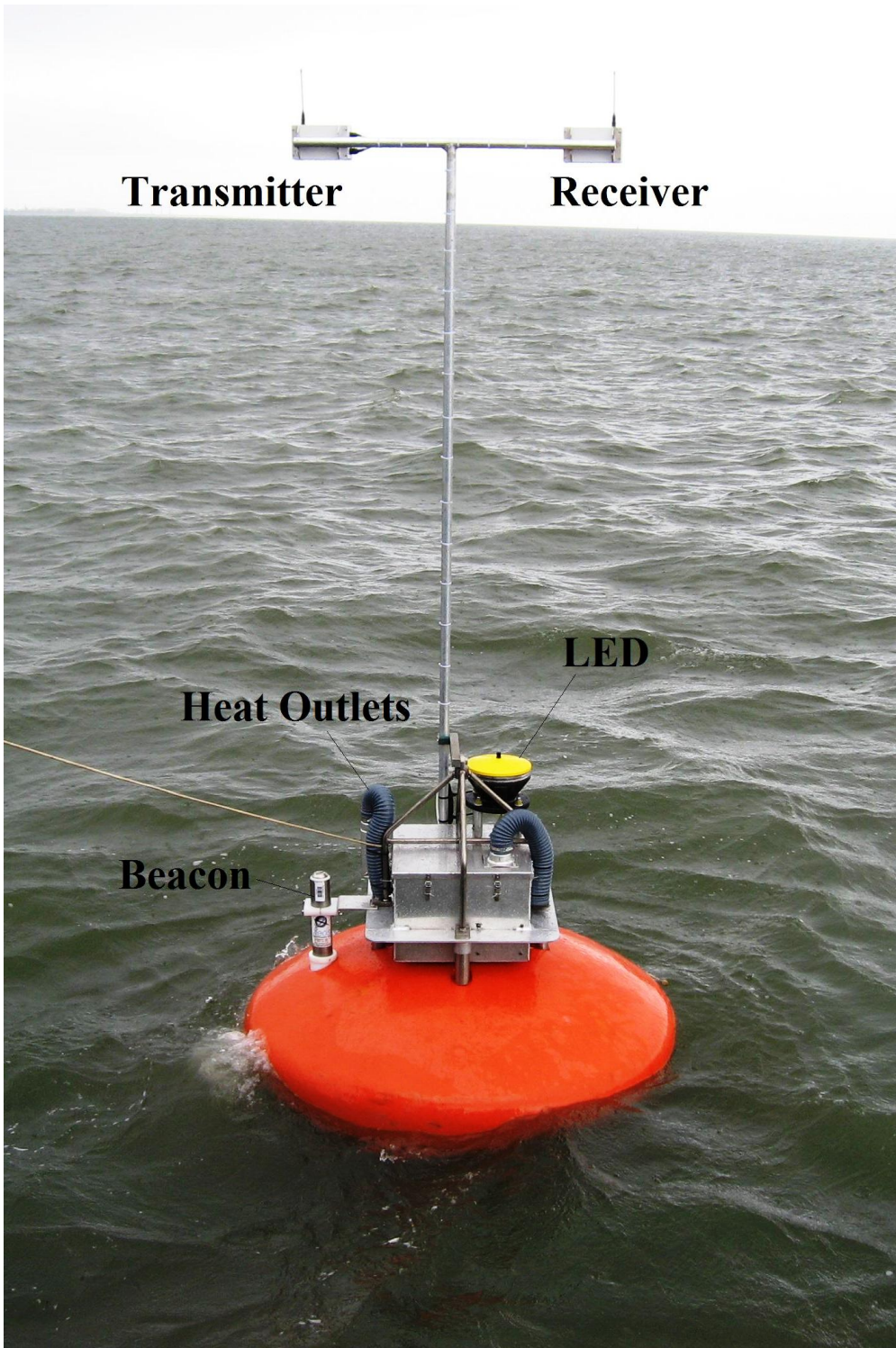


Figure 17: The deployment as it was in the water. *Picture by Ivo Witte.*

Device	E (kWh)
trans./reciev	-0.41
Light(at night)	-1.26
ADCP	4.2
Total	5.87

Table 2: Energy calculations for the second deployment.

expired on the same date and the new deployment was postponed for 2 weeks due to the problems. Assuming the same ADCP configurations and a duration of 70 days, new energy calculations (given in table 2) are needed to define the amount of batteries necessary for the deployment. This results in an energy usage of  $5.87kWh$  which (by dividing by  $12V$ ) can be recalculated to a needed capacity of  $490Ah$ . To be sure to have enough energy available it was decided to use 30 sets of 4 batteries and separate the battery pack for the light from the battery pack of the ADCP and LRR. The batteries are stored in a closed plastic box of  $385mm$  length,  $285mm$  width and  $215mm$  height (see figure 19) which was inserted in the aluminum box that was also used for the SFC in the first deployment. Knowing that the batteries will explode if they have contact with water and knowing that the chain was still connected at the same location, so extreme pitch and roll events might still be possible, the aluminum box was made fully water-proof by completely closing it (no more outlets for air). The only outlet is the water proof wire outlet as shown in figure (15). The new design was deployed on 09-04-2009 and successfully collected and transmitted data in the next 20 days until 29-04-09. On 29-04-09 changes were made to the configuration of the ADCP. While doing so the connection with the ADCP failed. The reason was a missing softbreak2hardbreak converter between the input of the LRR and the ADCP. The need for this apparatus was not known at the start of the experiment. A converter was acquired. A few days later, when the converter was going to be installed on the buoy, it was discovered that the pole with the LRR was broken off and had disappeared. The pole broke down at its attachment point due to the movements of the buoy due to the surface waves (fatigue). Due to lack of time and money to solve this problem, the experiment was stopped and the search for IS is continued using only these 19.8 days of available data instead of, as intended, a longer period of measurements. When the buoy was retrieved it turned out that the second design was not water proof and a little water was found inside the aluminum box. Luckily it had no influence on the data collection or quality, nor on the batteries. The experimental failures gave useful insights in the used techniques that can be applied when constructing future deployments of the same kind. From the data collection point of view it was a pity that no more data were collected.

## 2.4 Recommendations for future deployments

Considering the data failures, certain aspects of the design should be changed for future deployments of the same kind. An important aspect to reconsider is the attachment location of the cables. In the design used for the deployments described above, the cable was attached to a ring in the middle of the buoy. A different attachment location causes a different force balance leading to different behavior of the motions of the buoy. One new method that might be of interest is illustrated in figure (21). The cables are attached to the buoy's side. Using the same forces ( $F_g$ ,  $F_b$ ,  $F_c$  and  $F_p$ ) and similar explanation as for figure (16), the first situation of figure (21) is again a balance between gravity and buoyancy forces. In the second situation the current is superposed and again the buoy will float in the direction of the current until the cable is out of length. The



Figure 18: The Tekcell batteries used for the second deployment.



Figure 19: In this picture the Tekcell batteries are shown inside a plastic box with water proof outlets. This plastic box was then closed and inserted in the aluminium box on top of the buoy.



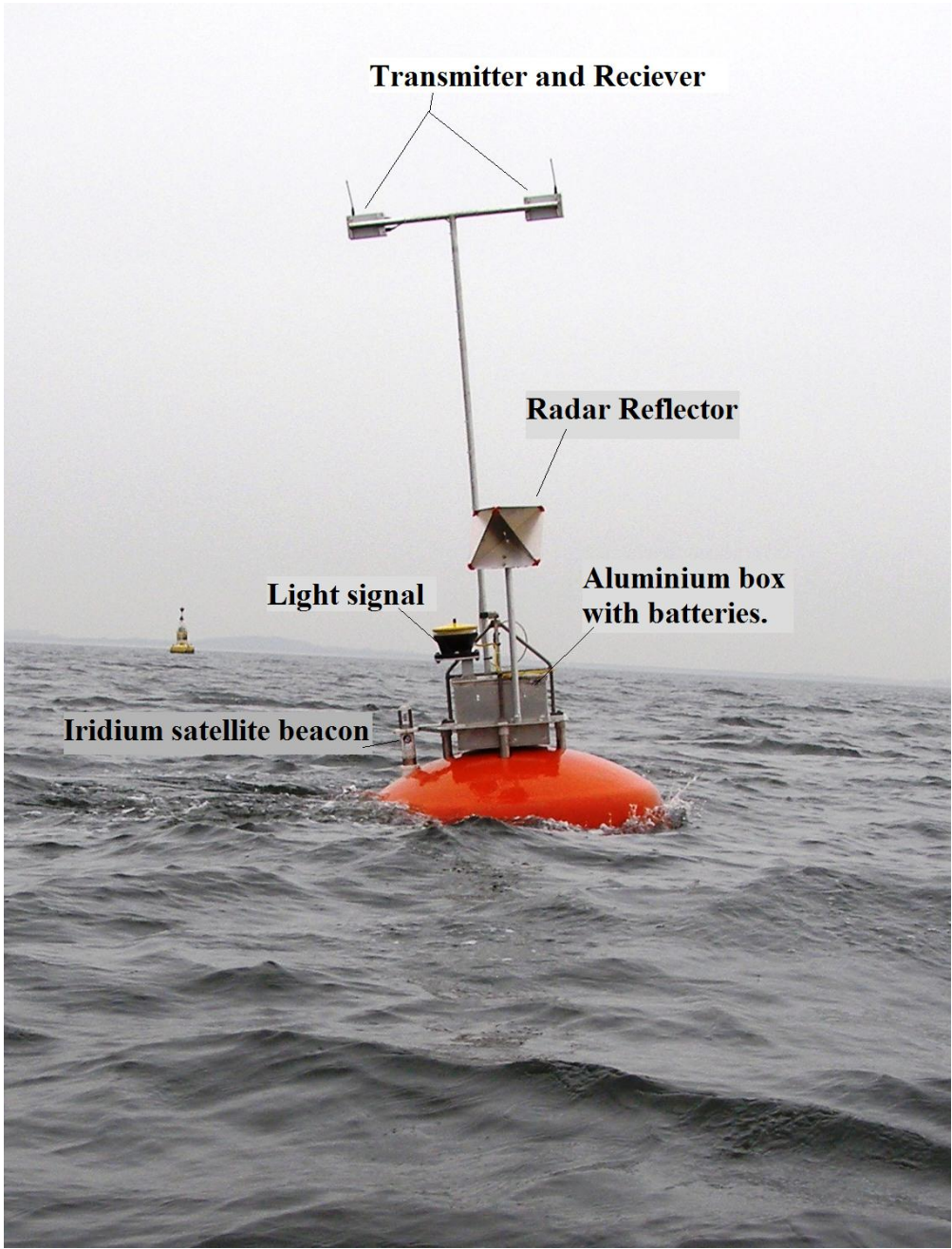


Figure 20: The second deployment as it was in the water.

cable will then start to pull the buoy in the direction of the cable. This direction can be decomposed into two effects of which one is trying to pull down the buoy on the upstream side. Due to the arm with respect of the centre of gravity, a torque is obtained which results in a rotation into the water of the upstream side. As a result the downstream side will be forced upwards which is sketched in situation 3 of figure (21). The forces due to the current, gravity and buoyancy are not located at one point but are (not equally) spread over the buoy. To illustrate the effect of these forces they are represented in one point. From this it is clear that the gravity and buoyancy forces will again act as restoring forces. In this design the force due to the current results in a larger tilt of the buoy. This is a disadvantage of this design. This disadvantage is counteracted by the advantage that the down pulling forces of the cable decrease when the length of the cable is increased. The final situation will be a balance between all forces shown in situation 3. The effect of surface waves is not taken into account in obtaining this balance. As concluded before, the effect of surface waves is unclear but might be severe and will bring the buoy out of balance and maybe cause the buoy to flip over.

It may be concluded that the surface waves have unpredictable effects on the design. To be able to conclude which design is most stable, taking into account strong currents and surface waves, both designs should be tested while equipped with pitch and roll equipment. There is also a third design that is worth testing. This is a combination of two buoys using both methods of attachment. The first buoy, not carrying the equipment for measurements, is attached as in the deployment used in this project. This buoy will then be connected with a second buoy carrying the equipment. This connection is ridged and from the side of buoy one to the side of buoy two, comparable with figure (21). As a result it is expected that the first buoy will be acting as a buffer for all the movement. This buoy tries to make the same movements as the deployment of this project but due to a change in the location of the centre of gravity and the added weight of the second buoy, this motion is expected to be damped. The first buoy can never pull down the second buoy as much as a cable can as in figure (21). Therefore it is expected that pitch and roll movements due to the current and cable are negligible. The larger total weight will also dampen the movements due to surface waves, also decreasing the pitch and roll and vertical movements. The only way to be sure this is a good design is by testing.

Besides testing and realizing the different methods to attach the buoy to the weights some small other improvements can be made. For example the use of a stronger pole for the LRR is advisable and it should be attached higher so the forces on the point where the pole is attached will be smaller. Installing a softbreak2hardbreak converter is necessary when online communication is required. Coating against bio fouling (with milking grease) for deployments that are in the water for more than a week (the bio fouling is enormous in the Marsdiep). Another improvement would be the use of an antenna that communicates via satellite instead of by visual contact. This increases the distance that can be covered and makes it independent of all kind of disturbing factors like passing boats.

**Not on scale!**

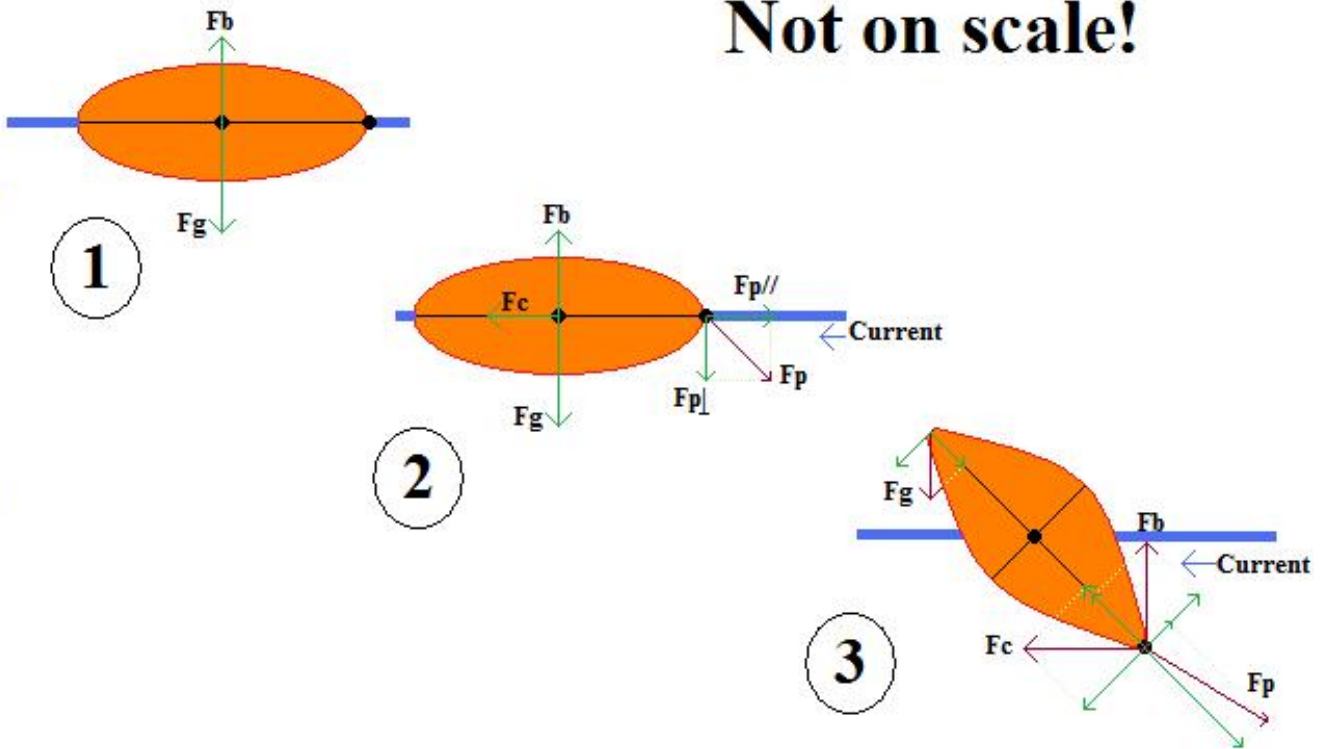


Figure 21: A sketch of the forces acting on the buoy when an alternative attachment location is used. Note that this is a qualitative sketch to illustrate which forces are acting on the buoy so some forces act on the entire buoy while they are represented at one position and the forces are not drawn on scale relative to each other.

## 3 Data Collection and Processing

### 3.1 General collection and processing

In this section the data collection and processing methods are discussed. The data is gathered using a downward looking ADCP that is mounted in a buoy and lies about  $0.5m$  under the surface. The ADCP has a blanking distance of  $1m$  resulting in a coverage from  $1.5m$  beneath the sea surface to the bottom with a vertical resolution (binsize) of  $0.5m$  and a sampling period of  $3s$ . The most important data retrieved are the pitch, roll, heading, time, temperature, depth and east, north and vertical water velocity, acoustic backscatter intensity, error velocity, velocity magnitude (horizontal) and direction (horizontal). To obtain water velocities the ADCP uses 9 individual measurements, equally spaced in time over  $3s$  and averaged to one value, resulting into a value for the water velocity with a standard deviation of  $2.32cms^{-1}$  representing the whole  $3s$ . The measurements are then sent online to a computer at the NIOZ institute where the results are stored. Due to extreme pitch and roll events, software errors, ships passing between the LRr or other unexplained events, connection failures occurred, resulting in data gaps in the order of 1 to 20 measurements ( $6s - 60s$ ). For all retrieved variables these gaps are linearly interpolated to restore a  $3s$  sampling interval. In total there were 414830 measurements. When the interpolated gaps are included there are 546165 measurements including 24% interpolated data. Due to unexplained software or system failure, data gaps in the order of several hours appeared. These gaps are too large to be restored with interpolation and are considered lost. In the time span between the first measurement and the last measurement, 546165 of the maximal 573050 possible measurements are gathered (95.3%, including interpolated gaps). To these obtained data some rejection criteria are applied.

### 3.2 Specific processing: The depth measurements

The ADCP retrieves depth measurements. The depth measurements are used to determine the location of the bottom and insert the bottom profile into the velocity measurements. As will be explained later in section (3.4), the depth measurements are also used to determine the quality of velocity data, therefore the depth measurements are important. The software program, delivered as ADCP equipment, used to load and process the raw measurements to obtain readable files, was not prepared for extreme pitch and roll events. Though it did correct the velocity measurements for pitch and roll events, it did not correct the depth measurements for pitch and roll events. When the ADCP is tilted, the sound pulse of some beams will follow a longer or shorter route through the water and therefore measure an incorrect depth. This can simply be corrected by multiplying the measured depth with  $\cos(\alpha)$  where  $\alpha$  is the tilt angle. For the sound pulses from beam 1 and 2 the tilt is defined as the roll. For beam 3 and 4 the tilt is defined as the pitch (see figure 22). Therefore the depths obtained from beam 1 and 2 are multiplied with the cosine of the roll and the depth obtained from beams 3 and 4 are multiplied with the cosine of the pitch. The four resulting beams are then separately treated to obtain realistic values for the depth. The resulting processing takes the following steps:

- Step 1: Remove all measurements that differ more than 2 standard deviations from the average.
- Step 2: Interpolate the resulting gaps.
- Step 3: Remove all successive measurements with a difference larger than  $0.5m$ .

- Step 4: Interpolate the resulting gaps.
- Step 5: Apply a 21 point (average over 63s) running mean filter.

The measured depth is from the transducer’s head to the bottom. So the resulting depth measurements are then averaged and the depth of the transducers head (0.5m) is added to obtain the water depth. Once the depth is determined one can proceed processing the velocity measurements.

### 3.3 Specific processing: The acoustic backscatter intensity measurements

The acoustic backscatter intensity measurements retrieved by the ADCP are given in counts. A count is an internal measure for the intensity of the reflected acoustic pulse. This value can be rescaled to a number in decibels. Besides this rescaling the acoustic backscatter intensity data also has to be corrected for attenuation and geometrical spreading, before it can be interpreted as a realistic physical signal. This can be done using a method developed by [7]. The following formula is therefore applied to the measured acoustic backscatter intensity of the ADCP:

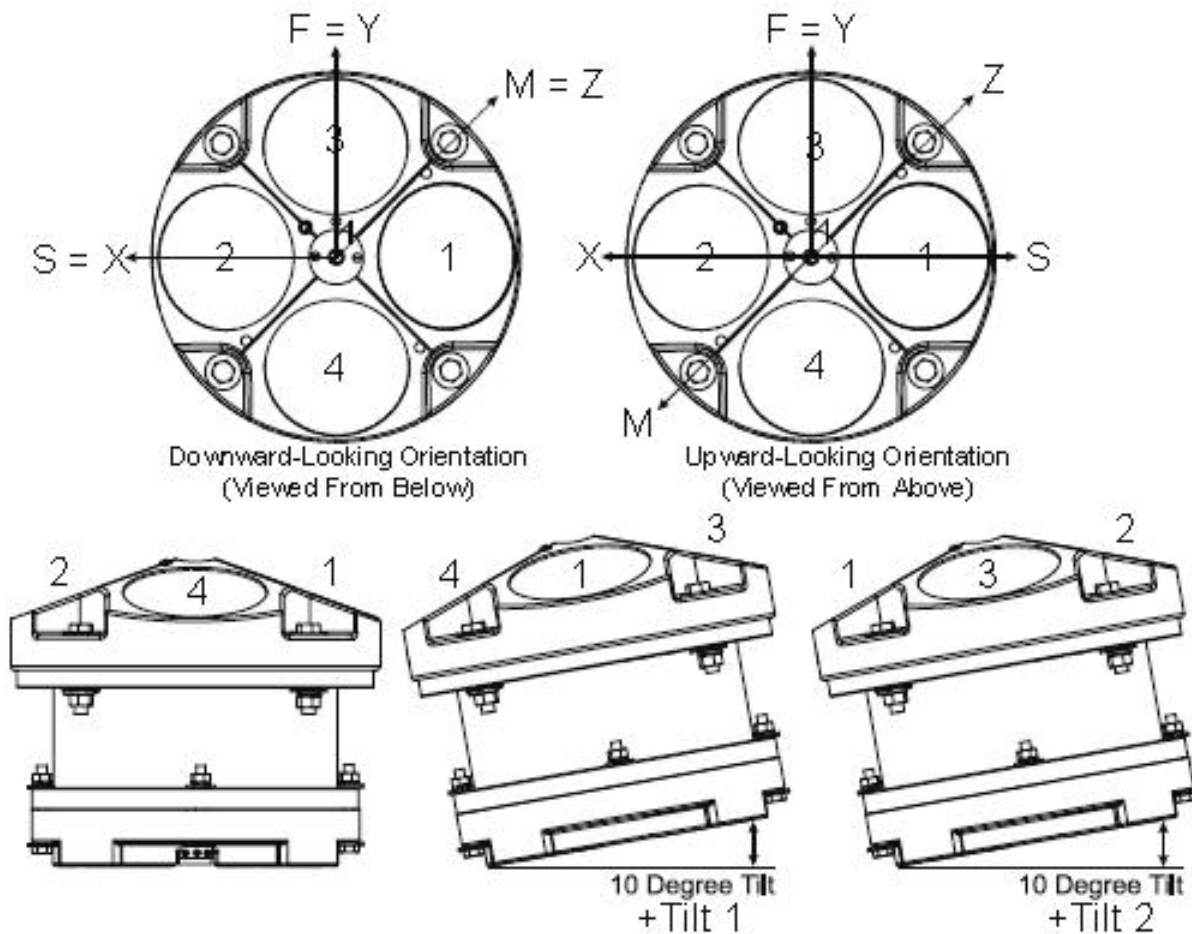
$$I = k(I_c - N_t) + 20^{10} \log(r) + 40\alpha r^{10} \log(e) \quad (4)$$

Where  $I_c$  is the acoustic backscatter intensity measured in counts,  $k$  is constant to convert counts to decibels,  $N_t = 20$  is a certain threshold value given by [7],  $r = \frac{z}{\cos(\phi)}$ ,  $z$  is the distance from the ADCP transducer head and  $\phi = 20$  is the angle the ADCP beams make with the vertical. This is done for each of the four beams retrieved with the ADCP. Then all four beams are averaged to obtain the final measurements for the intensities in decibels.

### 3.4 Specific processing: The velocity measurements

The eastward ( $u$ ), northward ( $v$ ) and vertical ( $w$ ) velocity data is collected with the ADCP. The ADCP is under influence of the movement of the buoy, such as pitch and roll and vertical or horizontal displacements. The measured water speeds are corrected for all of these movements. The corrections are only reliable when the beam of the ADCP is able to reach the bottom (to know speed relative to the bottom, path length of the sound pulse, etc). As a consequence the velocity profile is only reliable when all 4 beams are able to detect the bottom. This leads to the first criterion for velocity measurements, this and more criteria are listed:

- If one or more of the four ADCP beams is not able to detect the bottom, then the velocity measurements of the corresponding columns of the  $u, v$  and  $w$  velocities are not reliable and will be completely rejected.
- The maximum magnitude of the velocity in a bin at the measurement site, is not expected to exceed  $2ms^{-1}$ . Therefore magnitudes ( $=\sqrt{u^2 + v^2}$ ) larger than  $2ms^{-1}$  are not physically realistic and will be rejected in both the  $u$  and  $v$  measurements.
- If the absolute value for the vertical velocity exceeds  $0.4ms^{-1}$ , then the data is rejected because these are not physically realistic values.
- The error velocity is one of the parameters obtained by the ADCP. It is a measure for the accuracy of the velocity measurements. It is scaled in such a way that it can be treated as



### ADCP Coordinate Transformation

Sign of Angle for a Unit Facing	Up	Down
Tilt 1 (Pitch) Beam 3 higher than Beam 4	+	+
Tilt 2 (Roll) Beam 2 higher than Beam 1	+	-

Figure 22: A sketch indicating the difference between pitch and roll of the ADCP. *The picture is a copy taken from Workhorse Rio Grande Technical Manual of November 2007*

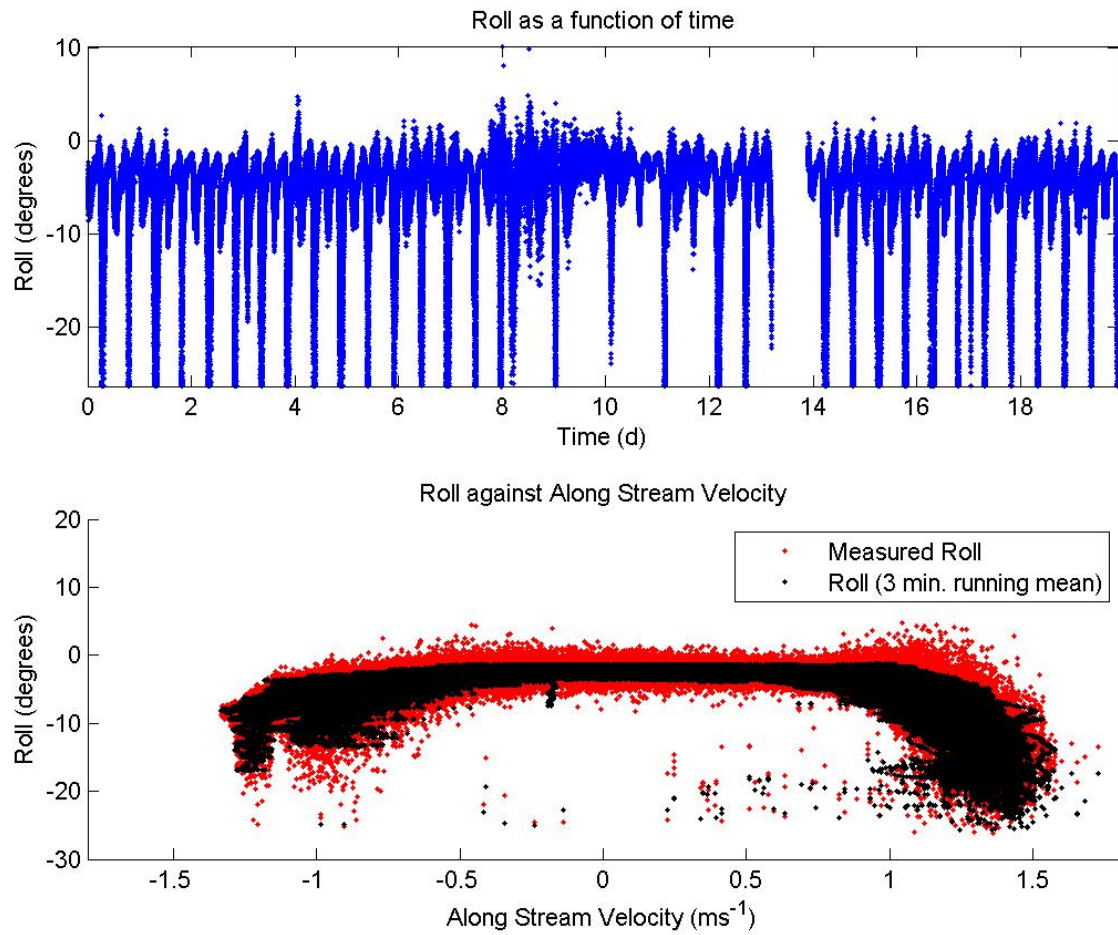


Figure 23: The upper panel shows the measured roll during the whole time series. The lower panel shows the measured roll (red) and measured roll filtered with a 3 minute running mean (black), as a function of the along stream velocity as it was measured in the first bin.

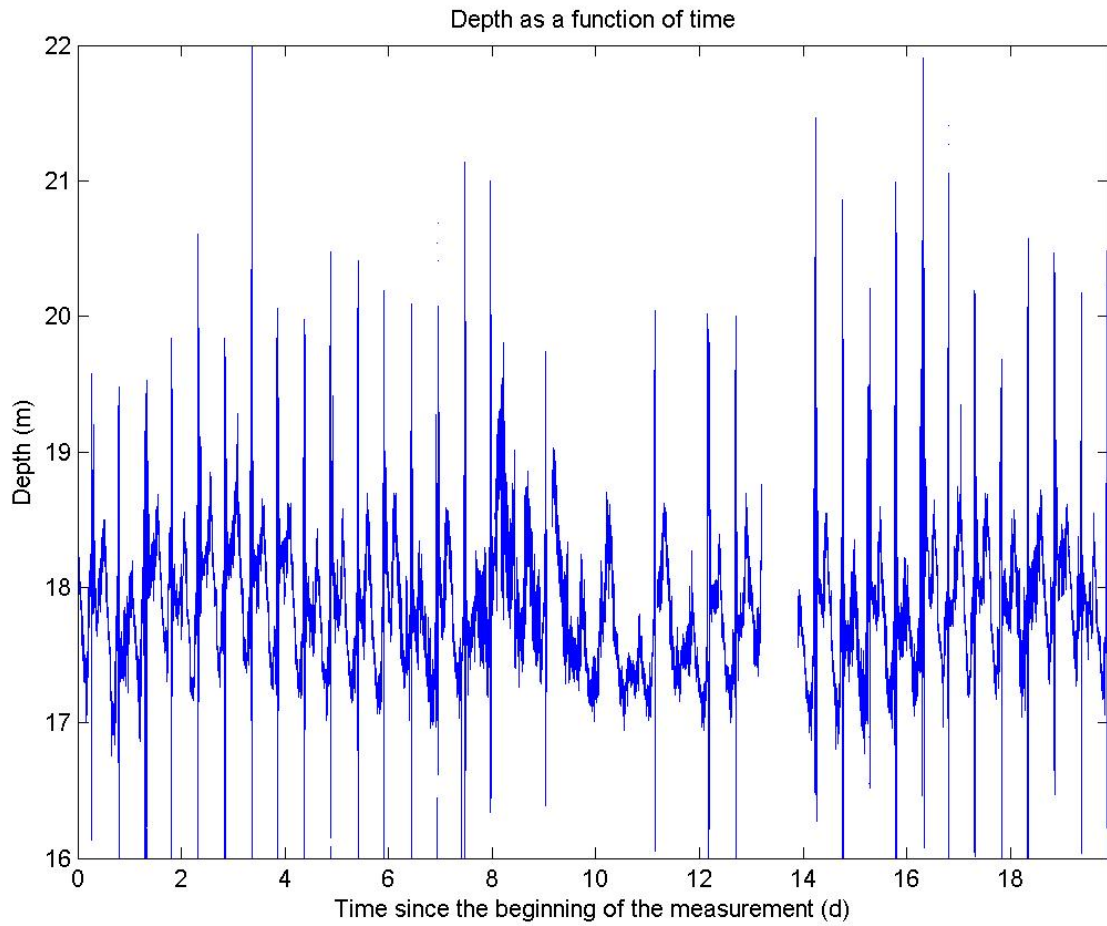


Figure 24: The measured depth during the whole time series. The spikes are due to errors in the measurements caused by extreme pitch and roll events.



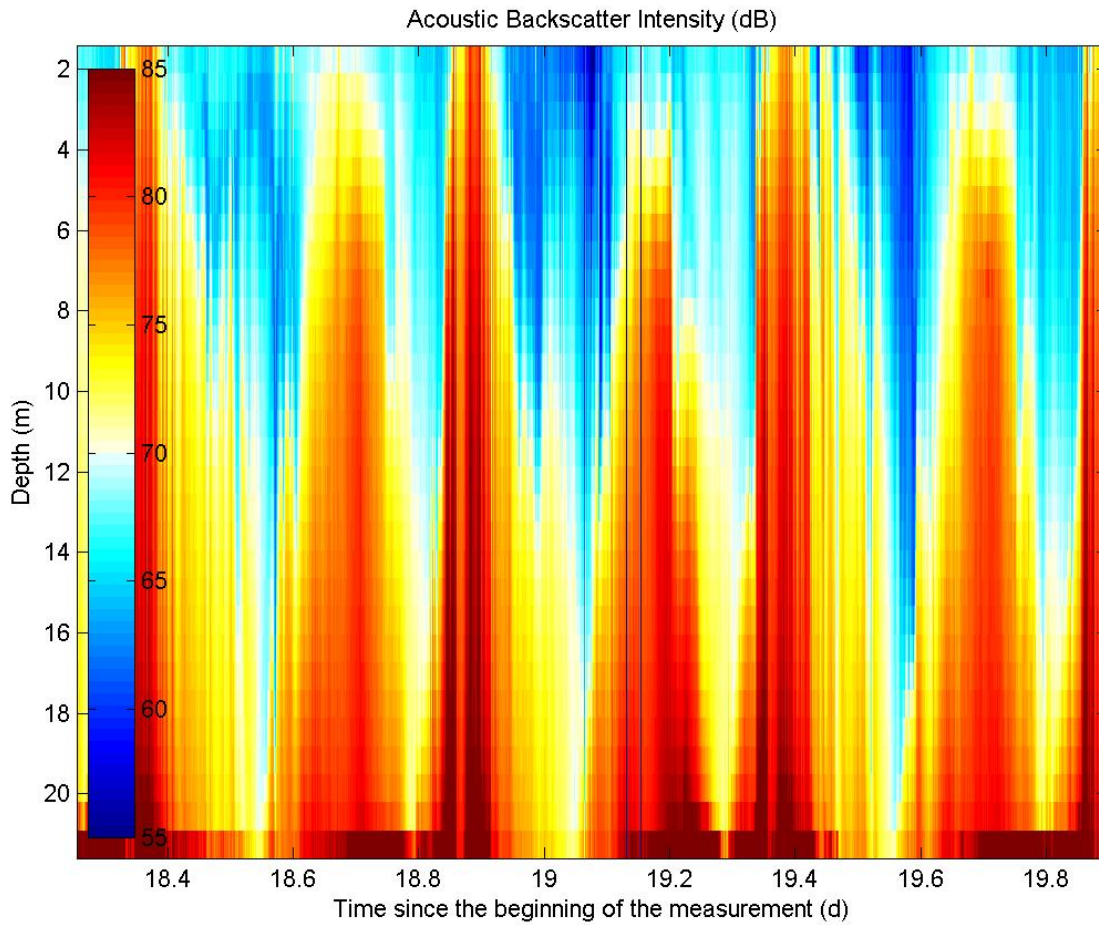


Figure 25: The Acoustic Backscatter Intensity measured by the ADCP, corrected for attenuation and geometrical spreading and converted to decibels. Higher values indicate more suspended matter in the water.

a measure for the standard deviation for the horizontal measurements. If the error velocity has a value higher than  $0.2ms^{-1}$  the data of this bin, for  $u,v$  and  $w$ , will be rejected.

- The device that measures the pitch and roll is not accurate above  $20^\circ$ . It is therefore advised (and applied) to reject data measured with a pitch or roll higher than  $17.5^\circ$ .
- The obtained depth measured by the ADCP is accurate within the order of centimeters, while the bin resolution is 0.5m. Using the depth of the water column and the depth range of each bin, it can be determined in which bin the bottom is located. This bin and all bins located deeper are set as the bottom in the matrix that represent the velocity measurements. For various reasons the ADCP is not always able to obtain accurate velocity data close to the bottom. Therefore the first bin above the bottom is also removed from the data set.
- Velocity measurements that are larger than 3std of the local average (which is the average of 30s before and 30s after the measurements) are not useful physical results and will be rejected. These variations are too fast compared to velocity differences due to tidal waves or internal waves expected in the Marsdiep area and can therefore be treated as spikes.
- The sea surface height variation due to the tide are projected in the measurements as a moving bottom. Meaning that some bins may sometime be defined as bottom and sometimes be defined as a measurement during different phases of the tidal cycle. Close to the bottom some depths therefore contain less velocity data. It is known that the presence of the bottom often produces more spikes and biases in ADCP measurements than further above the bottom, also causing a reduction of useful data at the bottom. Both effects described above may, from a certain depth on, cause more than 50% of the velocity measurements of one time series to be rejected. Taking into account the goal of the research (finding IS which are expected to be present in the middle of the water column) the depth at which 50% or more is rejected is used as the 'bottom'. All measurements beneath this depth are removed. As a side effect this also has the advantage that the size of the data files reduce. This results in rejection of all measurements that are located beneath the 31<sup>st</sup> bin (depth of 16.75m). Though this range is determined using the eastward velocity, it is also applied to the northward and vertical velocity.

Once all criteria above are applied the last steps are taken. The resulting  $u, v$ , and  $w$  data will be filtered by a 21 point running mean (average over 63s) to remove any other resulting spikes and reduce the influence of surface (wind) waves. As a result of the above criteria the eastward, northward and vertical velocity matrixes have the dimension 31x546165 [Depth x # of Measurements]. Of all these measurements, within this matrix, 91.2% of the horizontal velocity data is left and 87.5% of the vertical velocity data is left. This data is used for further research.

### 3.4.1 Determining the along stream direction

Changing the north ( $v$ ) and east ( $u$ ) velocities to along stream ( $\check{u}$ ) and cross stream ( $\check{v}$ ) velocities is a more physical approach because the processes studied in this research are mainly found in the along stream direction. Velocity directed to the north (south) is positive (negative). Velocity directed to the east (west) is positive (negative). Up ward (down ward) velocity is positive (negative). As a result of this transformation a new coordinate system must be defined where the axis are orientated in the along stream ( $\check{x}$ ) and cross stream ( $\check{y}$ ) direction. To transform  $(u, v)$  to  $(\check{u}, \check{v})$  the angle  $\alpha$ , which is the angle between  $x$  and  $\check{x}$ , is needed. A widely used method to find  $\alpha$  is to

take a map and see in which direction the channel, through which the water moves, is orientated. Unfortunately this is not possible for the Marsdiep because its channel, at the position where the buoy is deployed, is not well defined. A second possibility is to use the  $(u, v)$  velocities to find the direction of the maximum current, using equation (5). The direction of the channel is clearest when the velocities are high and the barotropic flow is dominant. Therefore only the measurements are selected of which the magnitude  $(\sqrt{u^2 + v^2})$  is larger than  $1ms^{-1}$ .

$$\theta = \frac{1}{N_{large}} \sum_{i=1}^{N_{large}} \arctan \left( \frac{|v_{large,i}|}{|u_{large,i}|} \right) \quad (5)$$

Where  $u_{large}$  and  $v_{large}$  are the measurements where the magnitude is larger than  $1ms^{-1}$  and  $N_{large}$  is the amount of measurements of which the magnitude is larger than  $1ms^{-1}$ . This method resulted in an angle ( $\alpha$ ) of  $27.4^\circ$ . This angle can now be used to rotate the northward ( $u$ ) and eastward ( $v$ ) velocities to along stream ( $\check{u}$ ) and cross stream ( $\check{v}$ ) velocities by applying the following transformation:

$$\check{u} = u \cos(\alpha) + v \sin(\alpha) \quad (6)$$

$$\check{v} = -u \sin(\alpha) + v \cos(\alpha) \quad (7)$$

As a result a positive (negative) along stream velocity is directed into (out of) the Wadden Sea. A current directed into (out of) the Wadden Sea is associated with a flood current (ebb current). A positive (negative) cross stream velocity is, more or less, directed towards Texel (Den Helder).

### 3.5 Discussing the obtained data

To start with figure (23) which gives the roll of the buoy as a function of time (upper panel) and as function of the along stream velocity (lower panel). From the upper panel it is clear that, with a certain periodicity (nearly every tidal cycle), the roll can be up to 25 degrees. Higher rolls very likely occurred but the device measuring the roll is not accurate above  $25^\circ$ . In the second panel the roll is combined with the along stream velocity and the periodicity of the extreme pitch and roll events can be explained. The red dots are the measured rolls when a certain velocity was measured. The black dots are the same but here a 183s running mean was applied to the roll measurements. From the black dots it can be concluded that an increase in speeds causes an increase in roll. This is in agreement with the prediction made using the force balance of figure (16). The positive (flood) speeds result in higher pitch and roll events because the flood speeds are in general higher than the ebb speeds causing asymmetry in the figure. Another remarkable feature is the roll offset, of about  $-1.5^\circ$  degrees, even when the water velocity is about 0. This can be explained by the unevenly distributed weight of the equipment on top of the buoy which will cause the deployment to be out of balance, at all times. The results for the pitch has the same shapes, characteristics and approximately the same magnitude and are therefore not shown. Because the buoy has a circular shape, there is not a very physical difference between pitch and roll.

The influence of the extreme pitch and roll events are visible in the depth measurements which are shown in figure (24). Even though the depth was corrected for the pitch and roll, the effect is visible due to an increase in spikes. This can be related to the device that measures the pitch and roll and does not work accurate during high pitch and roll events causing the ADCP to miss

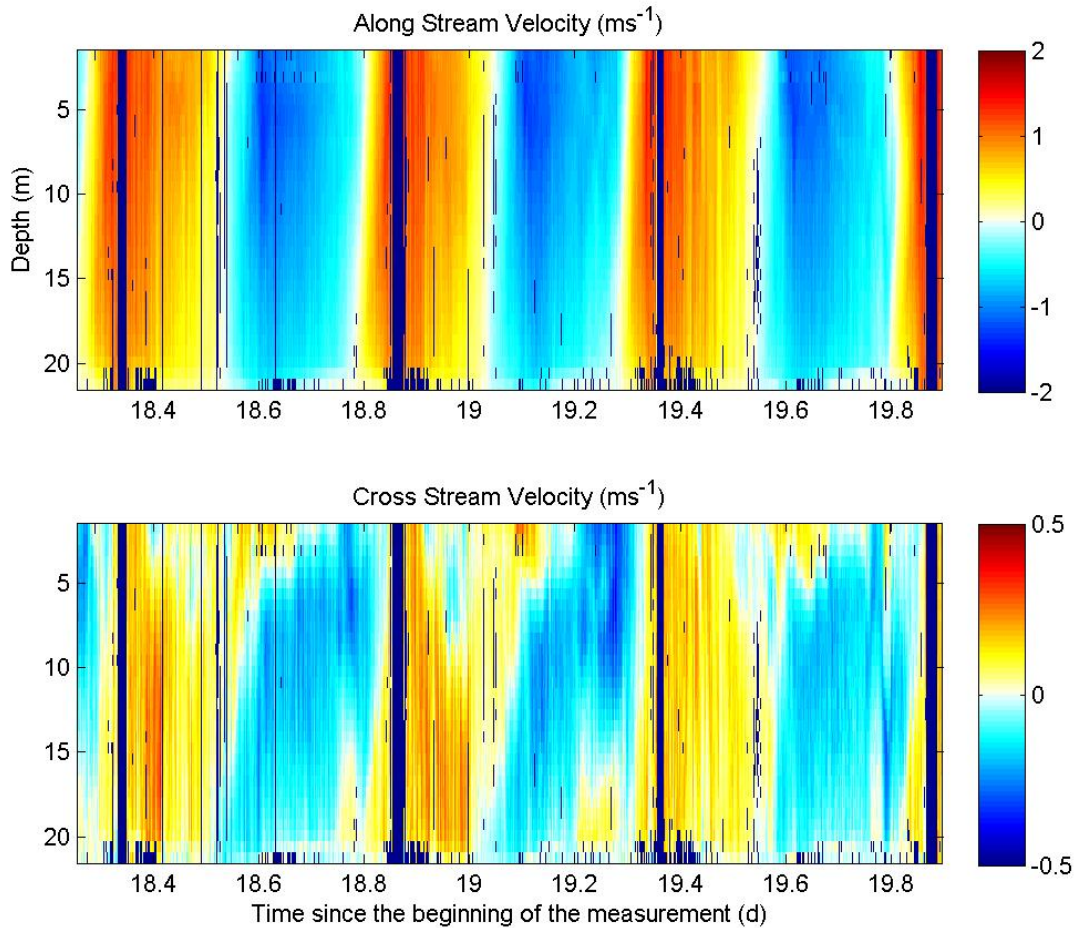


Figure 26: The upper panel is a part of the measured along stream velocity. Red (blue) indicates positive (negative) values associated with flood (ebb) currents directed into the Wadden Sea (North Sea). The lower panel is a part of the measured cross stream velocity. Red (blue) indicates positive (negative) values associated with currents directed more or less towards Texel (Den Helder). Both panels contain very dark blue values that indicate rejected data.

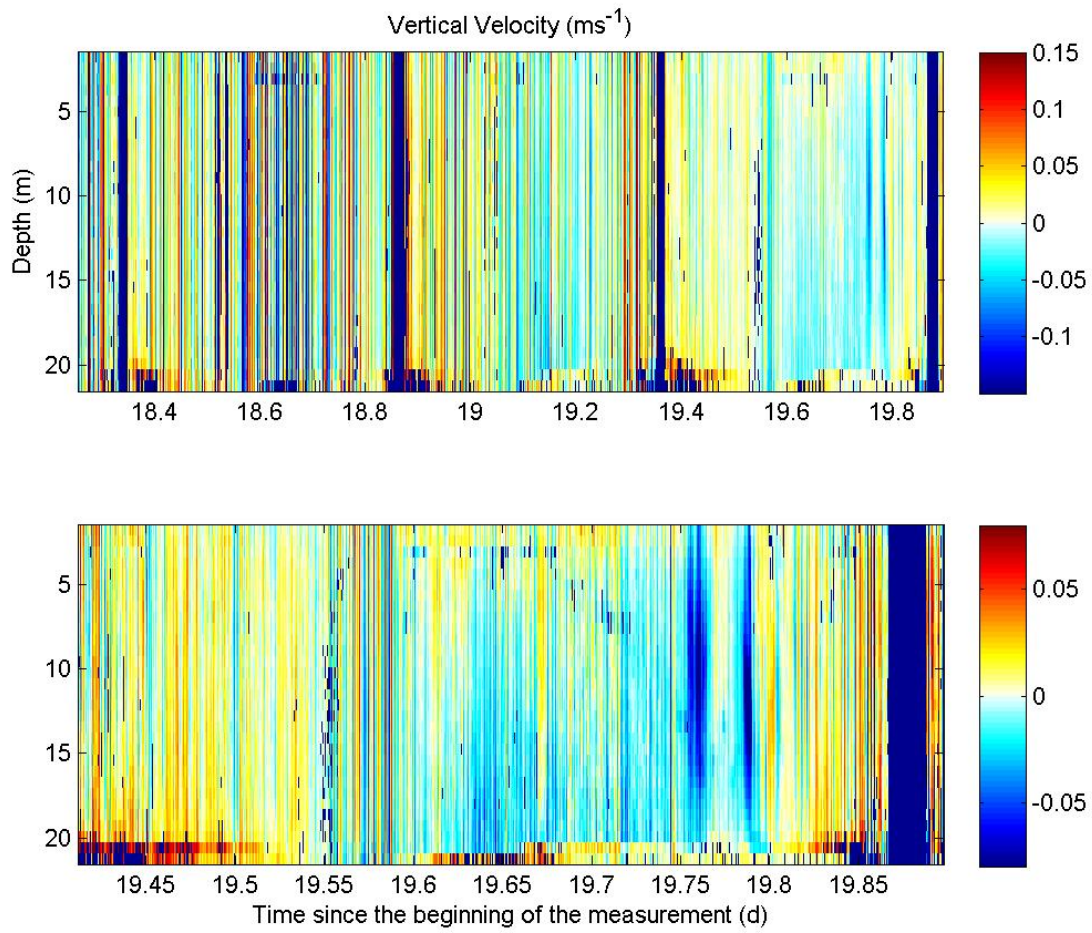


Figure 27: Both panels show a part of the measured vertical velocity. The lower panel shows a section of the upper panel. Positive red (negative blue) values indicate currents directed towards the surface (bottom).

some depth measurements during these events. Therefore not finding the depth is an indication of extreme pitch and roll events and fast movements leading to data rejection of velocity measurements by criteria given in section 3.4. Most extreme pitch and roll events and therefore spikes in the depth measurements, are found during (strong) flood currents. The influence of the tidal cycle is also visible in the depth signal.

In figure (25) the acoustic backscatter intensity measured during a part of the measured period, is shown. Blue (red) values are related with relatively low (high) acoustic backscatter intensities. The higher the measured acoustic backscatter intensity is, the more particles (sand, algae) are floating in the water. When relating this with figure (26) one can conclude that during the flood phase, higher acoustic backscatter intensity values are measured. High velocities are also measured closer to the surface during flood than during ebb. This is caused by higher velocities during flood currents than during ebb currents. Higher velocities are related with stronger effect of bottom friction causing vertical eddies that stir up more matter from the bottom and cause better mixing throughout the water column. When velocities decrease, also the acoustic backscatter intensity decreases.

In the upper and lower panel of figure (26), respectively the along and cross stream velocities are shown with the rejection criterion applied. The very dark blue spots are rejected measurements. Sometimes the chain is visible in the second or third bin as a line of rejected data. The profile that is shown lasts approximately 2 days while the whole measurements took 19.8 days. The remaining velocity profile is comparable. Do note the difference in scale between along stream and cross stream velocities. The positive along stream velocity is directed into the Wadden Sea which can be interpreted as flood currents. The blue colors indicate velocities directed out of the Wadden Sea and therefore ebb currents. In general the along stream flood currents are a little stronger than the ebb currents. A clear decrease of speed towards the bottom can be seen (darker colors close to the surface compared to the bottom). The rejected velocity profiles, due to extreme pitch and roll events, are clearly visible in both the along stream and cross velocities. The tidal cycle is visible in both panels but the vertical and time depending structures differ a lot from one another. For the along stream currents the tidal currents are dominant and will determine the main structure of the measured profiles. For the cross stream currents the velocity is partly determined by the tide and partly by secondary currents such as baroclinic currents, curvature, Coriolis force and wind induced currents as explained in the introduction (section 1.3). The magnitudes of the different secondary currents are for example influenced by the amount of stratification. In stratified conditions it may be expected that currents due to the wind are not large (otherwise it would have been mixed conditions due to wind stresses) so that the resulting currents will mainly be explained using the Coriolis force, the baroclinic currents and the curvature. During well mixed conditions the structure of the currents will mainly be determined by curvature, Coriolis force and when present, wind [5]. In the measurement period shown in figure (26) it seems that during slack tide circulation cells occur (water moving in opposite direction at different depths). These are interesting processes to take into account when the search for IS begins further in this report.

The vertical velocity, shown in figure (27) is automatically corrected for the vertical motion of the buoy using the vertical velocity of the buoy with respect to the bottom. The correction is only valid when the vertical motions are not too large, so steep and large surface waves will cause errors in the measured vertical velocity. The vertical velocity has different rejection limits as the horizontal velocities and therefore the rejected data differs a lot from that of the horizontal measurements. No clear tidal signal is visible in the vertical velocity profile, indicating that tidal forcing is not the dominant factor that determines the vertical velocity. This is easily explained when comparing the expected vertical velocity due to the SSH variation due to the tide (order

of  $10^{-3}ms^{-1}$  or smaller) with the measured vertical velocity (order  $10^{-2}ms^{-1}$  or higher). The vertical velocity will probably be determined by surface waves, interaction between currents and topography and turbulence. Even though the vertical velocity seems to contain a lot of randomness it might be useful to find long time and strong events of vertical motion that differ from the general signal. These events may indicate the possible existence of IS, like the light blue parts at 19.77 days.

In figure (28) the temperature measured by the ADCP is given. The measurements are done close to the surface and can therefore be interpreted as the sea surface temperature (SST). In the upper panel the long term variation is given and in the lower panel a shorter period is shown. The upper panel shows a clear tidal signal and warming trend. The warming trend can be explained by the deployment duration. It was spring time and therefore the SST increased in time. The tidal variation can be explained when taking into account the difference between the North Sea basin and the Wadden Sea basin. The Wadden Sea contains a lot less water than the North Sea and is very shallow (containing tidal flats). As the heat capacity of sun exposed soil is much less than that of water, heating and cooling due to the interaction with the atmosphere and sun has much more effect on the SST than in the North Sea. Especially in the shallow water parts the bottom of the sea can be reached by solar insolation, causing it to warm up and heat the water from beneath. At the same time, if the air temperature is warmer than the SST, one may expect an increase of the SST when the water is in the Wadden Sea. A decrease of the SST may be expected when the air temperature is colder than the SST. During the time of year in which the measurements are made, the atmospheric temperatures are warmer than the SST and therefore the water will be warmed from both sides (surface and bottom) causing a significant difference in SST between the North Sea and Wadden Sea. When the buoy measures the water that flows through the Marsdiep, it depends on the origin of the water (Wadden Sea or North Sea) which temperature is measured. The origin of the water depends on the tidal currents and therefore causes a clear tidal signal in the temperature data. Another influence that changes the Wadden Sea temperature is the water from Lake IJssel that is released into the Wadden Sea. The SST of this lake is also greatly depending on atmospheric temperature and increases the effect of increasing or decreasing SST. The lower panel shows clear temperature jumps. These are jumps that can be related to (ebb) currents pushing a water mass heated in the Wadden Sea toward the North Sea. These water masses do not always mix well with the colder North Sea water and, when moved towards the North Sea, sudden temperature jumps due to the clear border between the water masses are visible. These jumps also indicate large differences in North Sea and Wadden Sea water and are therefore interesting when using the data to search for IS.

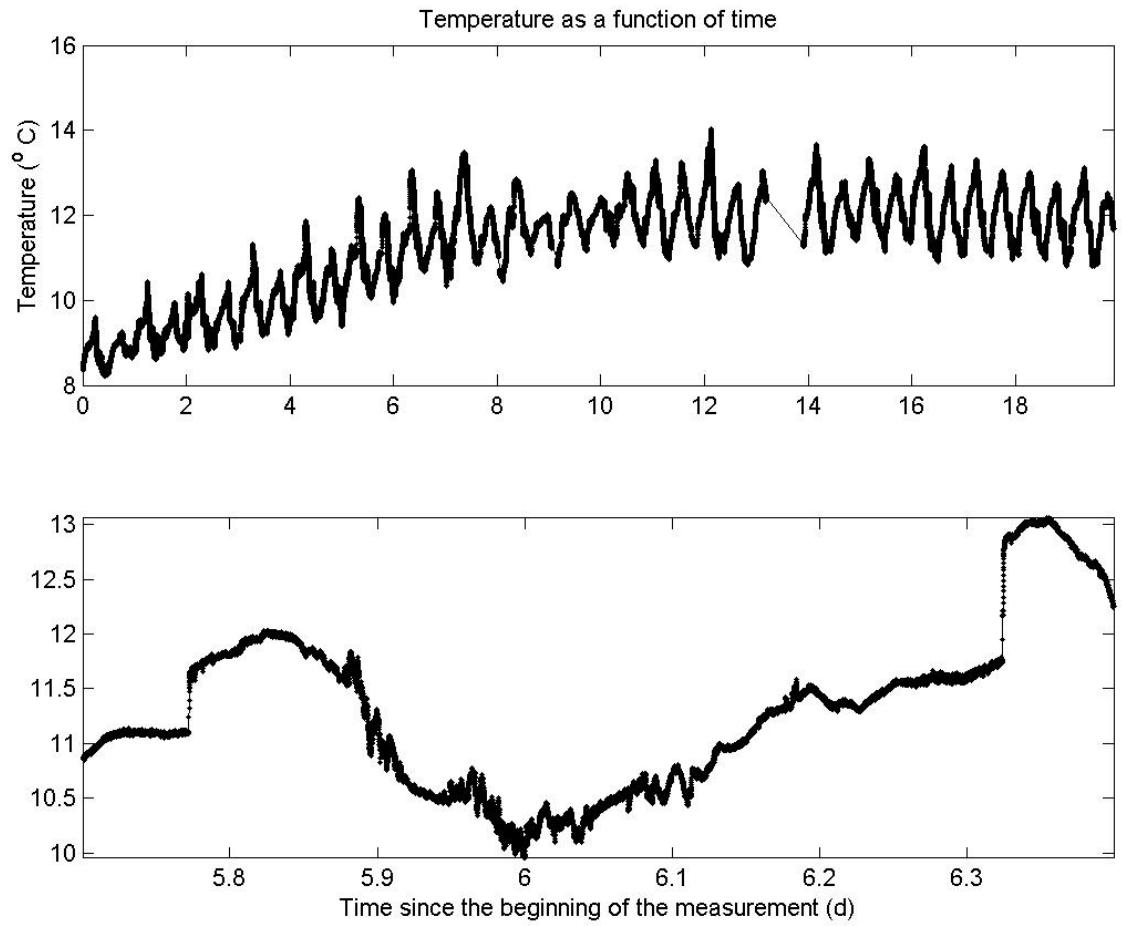


Figure 28: The upper panel shows the measured temperature during the whole period. The lower panel shows the measured temperature of a part of the measurements.



## 4 The Velocity Triangle

After having made the measurements, applied the rejection criteria and transformed the data set, a good data set is left. This data set gives knowledge about the water velocities at one location, over the whole water column, for 20 days. The 'velocity triangle' refers to ways in which velocity data can be written into three different sets of physical parameters (figure 29) which will give insight in the processes that determine the characteristics of the measured water currents. The first set of parameters decomposes the measurements in amplitude and phase of different tidal components that are present in the Marsdiep area and therefore also in the data set. This is done for the along stream and cross stream direction using a Least Squares Harmonic Analysis (LSHA), which is explained in detail in section (4.1). Using the resulting amplitudes and phases one can find the dominant tidal components in this area. When the LSHA is applied to each depth level, the vertical structure of the tidal components can be studied. The LSHA can be used as a good approximation for the barotropic current in this area or to interpolate missing data or extrapolate to historical or future events.

The second set of physical parameters are the rotary (clockwise ( $C$ ) and anti-clockwise ( $AC$ )) amplitudes and phases, which are explained in detail in section (4.2). These are velocity amplitudes and phases of the different tidal components in the measured data obtained by splitting the data set into a current rotating clockwise (against the earth's rotational direction) and anti-clockwise (in the direction of the earth rotation). This is convenient when studying the structure of the Ekman layer. The Ekman Layer is composed of a  $C$ & $AC$  rotating constituent which can be obtained when studying the vertical structure of the two components. Knowing the structure of the Ekman layer gains physical insight in the frictional processes to which the currents are subjected.

The third set of physical parameters are the ellipse parameters (explained in detail in section (4.3)) of the different tidal components found within the measured data. Over one tidal period the horizontal tidal current vector describes an ellipse. By finding its ellipse parameters, which are the amplitudes ( $U_{Ma}$  and  $U_{Mi}$ ) of the Semi-Major axis ( $SEMA$ ) and Semi-Minor axis ( $SEMI$ ), Eccentricity ( $ECC$  or  $e$ ), Phase ( $PHA$  or  $\psi_P$ ) and Inclination ( $INC$  or  $\psi_I$ ), one is able to get physical insight of the structure of the tide. By examining the dependence of the inclination and the other ellipse parameters on the distance from the bottom one can obtain insight in the effect of bottom friction on the tidal current.

All the three data sets above are linked with each other. Using one of the three sets of parameters it is possible to calculate all the other parameters. For the measurements obtained in this study it is most convenient to obtain the amplitudes and phases of the different tidal components using the LSHA and use those to calculate the other sets of parameters. In the remaining of this section it is explained how the three different set of parameters are obtained and the results are discussed.

### 4.1 The Harmonic analysis

A Least Squares Harmonic Analysis [8, 3] is a method used to explain as much as possible of the measured variance in the measurements using least squares techniques in combination with known astronomic tidal frequencies that should be present within the data set. To each astronomic frequency a phase and amplitude is fitted to obtain the best possible harmonic fit for the measured variance. The resulting amplitudes and phases of the LSHA serve several purposes. They will be used to calculate all parameters of the velocity triangle. To understand the other purpose one must recall the main goal of the research which is to find IS in the Marsdiep. The results of the LSHA

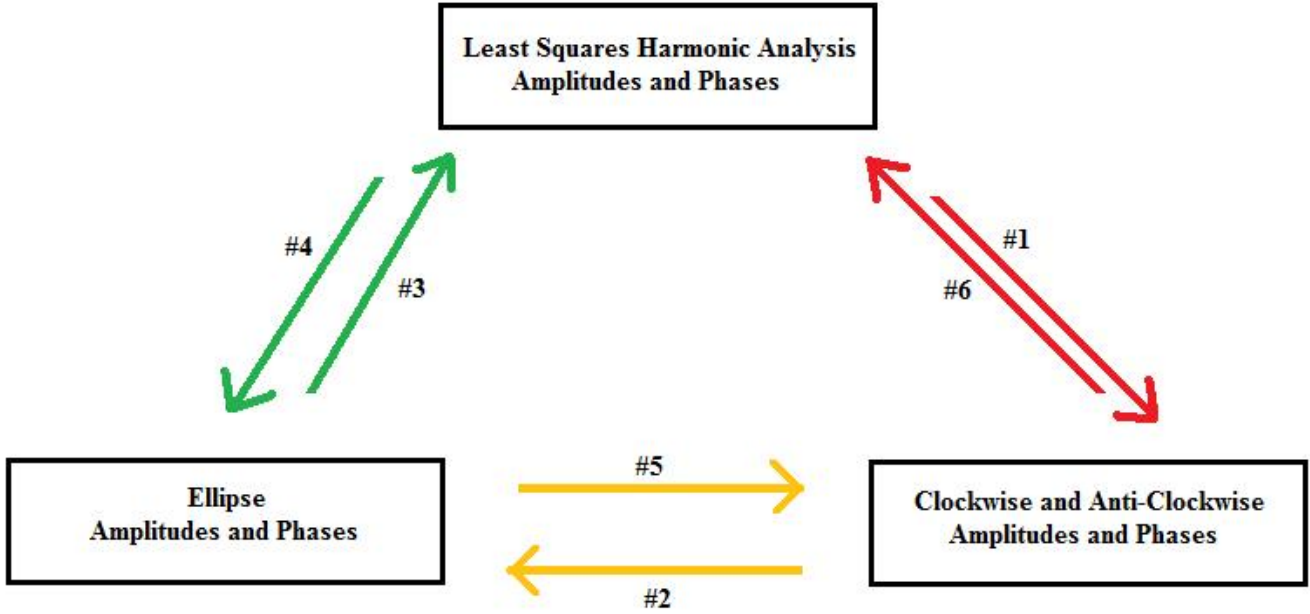


Figure 29: A sketch showing the different steps in the velocity triangle. In the text, the calculations belonging to a certain step, are derived.

can be used to reconstruct the water motion during the time span in which the measurements are obtained. The resulting LSHA approximation of the measurements is the coherent part of the measurements. All processes in the data set that are coherent with tidal frequencies used as input for the LSHA, will influence the resulting amplitude and phase for this particular frequency. The IS are not expected to be present on a regular bases but only if the circumstances are right during some phases of the tide. As a result it is expected that the IS are not found in the coherent part of the signal and should therefore be pronounced in the incoherent motion within the measured velocity data. To obtain only the incoherent motion, the coherent motion which is forced by the tide, must be subtracted from the measurements. The LSHA amplitudes and phases serve as input for an analytical barotropic model, containing bottom friction with slip conditions and Coriolis force effects and is derived in section 5. The model uses the tidal amplitudes and phases of the LSHA at the surface to calculate the expected values for the rest of the water column. This leaves the barotropic motion over the whole water column which can be used to explain and understand the coherent signal obtained with the LSHA. The focus in this section will be on deriving and understanding the LSHA.

#### 4.1.1 Derivations

The LSHA amplitudes and phases will be derived in such a way that the difference between the measurements and the resulting fit, using these amplitudes and phases, will be minimal. Now define a measured time series of a current as  $\tilde{u}_i$  and the average of this time series as  $\bar{u}$ . The fit will be composed out of two components. If one makes a fit on the data the clue is to be able to reproduce the data, from which the average is subtracted, as accurately as possible and then add the average to it. The average can be exactly calculated and is therefore not a challenge to reproduce. The data from which the average is subtracted,  $u_i$ , is harder to reproduce. The LSHA will therefore be derived to make a best fit for this part of the data which is represented by  $\hat{u}$ . This leads to the following equation:

$$\tilde{u}_i = u_i + \bar{u} = \hat{u}_i + \bar{u} + u_i^r \quad (8)$$

Here the measurements ( $\tilde{u}_i$ ) are reproduced when summing up the LSHA best fit ( $\hat{u}_i$ ), the mean of the measurements ( $\bar{u}$ ) and the residual ( $u_i^r$ ), which is the difference between the measurements and the LSHA fit. The better the LSHA fit, the smaller the residual current will be. The best fit ( $\hat{u}_i$ ) of the mean subtracted measurements ( $u_i$ ) is obtained using a summation of harmonic components with known astronomical tidal frequencies. For the derivation it is convenient to start with one tidal frequency, leading to the following expression for the fit function:

$$\hat{u}_i = A_0 + a \cos(\omega t_i) + b \sin(\omega t_i) \quad (9)$$

Where  $\hat{u}_i$  is the best harmonic fit,  $A_0$  is the tidal average,  $a$  and  $b$  are the tidal components,  $\omega$  the tidal frequency and  $t_i$  is the time at measurement  $i$  and  $i \in (1, I)$ , where  $I$  is the maximal amount of measurements. Note that  $A_0$  is not the average value of the current of the measured time series, because the average has already been subtracted,  $A_0$  is a value representing effects due to incomplete periodic cycles of some components due to the sudden start and end of the time series. If the time series would have had a length in which the frequency  $\omega$  would fit an exact amount of times, than  $A_0$  should be zero as explained in more detail in table (3). The difference between  $u_i$  and  $\hat{u}_i$  should be as small as possible leading to a small as possible residual current  $u_i^r$ . Therefore the difference is calculated and squared. It is now possible to find the difference between the fit and the measurements as a function of the fit parameters  $a$ ,  $b$  and  $A_0$ . This results in the following expression:

$$r^2 = SSE = \sum_{i=1}^I u_i^2 = \sum_{i=1}^I [u_i - \hat{u}_i]^2 = \sum_{i=1}^I [u_i - A_0 - a \cos(\omega t_i) - b \sin(\omega t_i)]^2 \quad (10)$$

The function  $r^2$  is the sum of squared errors (SSE) or total variance that is not explained by the best fit  $\hat{u}_i$ . The minimum in the function  $r^2$  represents a fit with the best estimate of the fit parameters  $a$ ,  $b$  and  $A_0$ . The minimum can be found by taking the derivative with respect to the parameters that are to be fitted, leading to the following set of equations:

$$\frac{\partial r^2}{\partial a} = -2 \sum_{i=1}^I [u_i - \hat{u}_i(A_0, a, b)] \frac{\partial \hat{u}_i(A_0, a, b)}{\partial a} = 0 \quad (11)$$

$$\frac{\partial r^2}{\partial b} = -2 \sum_{i=1}^I [u_i - \hat{u}_i(A_0, a, b)] \frac{\partial \hat{u}_i(A_0, a, b)}{\partial b} = 0 \quad (12)$$

$$\frac{\partial r^2}{\partial A_0} = -2 \sum_{i=1}^I [u_i - \hat{u}_i(A_0, a, b)] \frac{\partial \hat{u}_i(A_0, a, b)}{\partial A_0} = 0 \quad (13)$$

By inserting equation (9) into equations (11), (12) and (13), the following set of equations is obtained:

$$\sum_{i=1}^I [-u_i \cos(\omega t_i) + A_0 \cos(\omega t_i) + a \cos^2(\omega t_i) + b \sin(\omega t_i) \cos(\omega t_i)] = 0 \quad (14)$$

$$\sum_{i=1}^I [-u_i \sin(\omega t_i) + A_0 \sin(\omega t_i) + a \cos(\omega t_i) \sin(\omega t_i) + b \sin^2(\omega t_i)] = 0 \quad (15)$$

$$\sum_{i=1}^I [u_i - A_0 - a \cos(\omega t_i) - b \sin(\omega t_i)] = 0 \quad (16)$$

This set of equation can be rewritten to:

$$\sum_{i=1}^I A_0 \cos(\omega t_i) + a \sum_{i=1}^I \cos^2(\omega t_i) + b \sum_{i=1}^I \sin(\omega t_i) \cos(\omega t_i) = \sum_{i=1}^I u_i \cos(\omega t_i) \quad (17)$$

$$\sum_{i=1}^I A_0 \sin(\omega t_i) + a \sum_{i=1}^I \cos(\omega t_i) \sin(\omega t_i) + b \sum_{i=1}^I \sin^2(\omega t_i) = \sum_{i=1}^I u_i \sin(\omega t_i) \quad (18)$$

$$A_0 + a \sum_{i=1}^I \cos(\omega t_i) + b \sum_{i=1}^I \sin(\omega t_i) = \sum_{i=1}^I u_i \quad (19)$$

To solve the last set of equations it is convenient to rewrite this set into matrix form:

$$\begin{pmatrix} \sum_{i=1}^I \cos(\omega t_i) & \sum_{i=1}^I \cos^2(\omega t_i) & \sum_{i=1}^I \cos(\omega t_i) \sin(\omega t_i) \\ \sum_{i=1}^I \sin(\omega t_i) & \sum_{i=1}^I \sin(\omega t_i) \cos(\omega t_i) & \sum_{i=1}^I \sin^2(\omega t_i) \\ 1 & \sum_{i=1}^I \cos(\omega t_i) & \sum_{i=1}^I \sin(\omega t_i) \end{pmatrix} \begin{pmatrix} A_0 \\ a \\ b \end{pmatrix} = \begin{pmatrix} \sum_{i=1}^I u_i \cos(\omega t_i) \\ \sum_{i=1}^I u_i \sin(\omega t_i) \\ \sum_{i=1}^I u_i \end{pmatrix} \quad (20)$$

The matrix can be rewritten as:

$$Ax = B \quad (21)$$

Where:

$$A = \begin{pmatrix} \sum_{i=1}^I \cos(\omega t_i) & \sum_{i=1}^I \cos^2(\omega t_i) & \sum_{i=1}^I \cos(\omega t_i) \sin(\omega t_i) \\ \sum_{i=1}^I \sin(\omega t_i) & \sum_{i=1}^I \sin(\omega t_i) \cos(\omega t_i) & \sum_{i=1}^I \sin^2(\omega t_i) \\ 1 & \sum_{i=1}^I \cos(\omega t_i) & \sum_{i=1}^I \sin(\omega t_i) \end{pmatrix} \quad (22)$$

$$x = \begin{pmatrix} A_0 \\ a \\ b \end{pmatrix} \quad (23)$$

$$B = \begin{pmatrix} \sum_{i=1}^I u_i \cos(\omega t_i) \\ \sum_{i=1}^I u_i \sin(\omega t_i) \\ \sum_{i=1}^I u_i \end{pmatrix} \quad (24)$$

Leading to the following expression for the unknown best fit parameters represented by  $x$ :

$$x = A^{-1}B \quad (25)$$

The derivation leading to equation (25) uses only one tidal frequency. For a better fit more tidal frequencies should be used, leading to the following expression for the fit function  $\hat{u}_{ij}$ :

$$\hat{u}_{ij} = A_0 + \sum_{j=1}^N [f(t_i, a_j, b_j)] = A_0 + \sum_{j=1}^N [a_j \cos(\omega_j t_i) + b_j \sin(\omega_j t_i)] \quad (26)$$

Where  $N$  is the amount of tidal frequencies that are used to make a best fit,  $a_j$  and  $b_j$  are the tidal amplitudes of the different tidal frequencies. This results in a slightly different expression for the difference between the best fit and the data given by  $r^2$ :

$$r^2 = \sum_{i=1}^I \left[ u_i - \sum_{j=1}^N \hat{u}_{ij} \right]^2 = \sum_{i=1}^I \left[ u_i - A_0 - \sum_{j=1}^N [a_j \cos(\omega_j t_i) + b_j \sin(\omega_j t_i)] \right]^2 \quad (27)$$

As a result the set of equation to be solved has increased, but the method has not changed. This results in the following set of equations:

$$\frac{\partial r^2}{\partial a_j} = 0 \quad (28)$$

$$\frac{\partial r^2}{\partial b_j} = 0 \quad (29)$$

$$\frac{\partial r^2}{\partial A_0} = 0 \quad (30)$$

The set of equations given by (28), (29) and (30) will again be rewritten into matrices  $A$ ,  $x$  and  $B$ . Using  $M = 2N + 1$ , the size of matrices  $A$ ,  $x$  and  $B$  will be  $[M \times M]$ ,  $[M \times 1]$  and  $[M \times 1]$ . The resulting fit can be rewritten in a more convenient form using the following identities:

$$a_j \cos(\alpha_j) + b_j \sin(\alpha_j) = U_j \cos(\alpha_j - \phi_j) = U_j \cos(\alpha_j) \cos(\phi_j) + U_j \sin(\alpha_j) \sin(\phi_j) \quad (31)$$

Where  $\alpha_j = \omega_j t_i$  and  $U_j$  and  $\phi_j$  can be determined from:

$$a_j = U_j \cos(\phi_j) \quad (32)$$

$$b_j = U_j \sin(\phi_j) \quad (33)$$

from which follows that:

$$\frac{a_j}{b_j} = \frac{\cos(\phi_j)}{\sin(\phi_j)} = \frac{1}{\tan(\phi_j)} \rightarrow \phi_j = \arctan\left(\frac{b_j}{a_j}\right) \quad (34)$$

$$\sqrt{a_j^2 + b_j^2} = \sqrt{U_j^2 \cos^2(\phi_j) + U_j^2 \sin^2(\phi_j)} = \sqrt{U_j^2} = U_j. \quad (35)$$

Here  $U_j$  is the amplitude of the current of a tidal component with frequency  $\omega_j$  and phase  $\phi_j$  leading to:

$$\hat{u}_i = A_0 + \sum_{j=1}^N [U_j \cos(\omega_j t_i - \phi_j)] \quad (36)$$

Equation (36) represents the best fit for  $u_i$ . Inserting this back into equation (8) results in:

$$\tilde{u}_i = \bar{u} + A_0 + \sum_{j=1}^N [U_j \cos(\omega_j t_i - \phi_j)] + u_i \quad (37)$$

Velocity profile	$\bar{u}(ms^{-1})$	$A_0(ms^{-1})$	$U_n = \bar{u} + A_0$
$u_1 = \cos(\omega t)$	0	0	0
$u_2 = 1 + \cos(\omega t)$	1	0	1
$u_3 = \cos(\omega \tau)$	0.0303	-0.0303	0
$u_4 = 1 + \cos(\omega \tau)$	1.0303	-0.0303	1
$u_5^* = 1 + \cos(\omega \tau)$	X	1	1

Table 3: Here  $A_0$ ,  $\bar{u}$  and  $U_n$  are respectively the tidal average, mean of the time series and net 'physical' current. The functions  $u_1 - u_5^*$  represent different possible time series of measured velocities. On  $u_1 - u_4$  the LSHA is performed after ( $\bar{u}$ ) is subtracted. On  $u_5^*$  the LSHA is performed without first subtracting ( $\bar{u}$ ). Here  $\omega$  has the values of the tidal  $M_2$  frequency,  $t = [0, 5T_{M_2}]$  in steps of  $1s$ , is a time span of exactly 5 times the  $M_2$  frequency and  $\tau = [0, 5.25T_{M_2}]$  in steps of  $1s$ , is a time span of exactly 2.25 times the  $M_2$  frequency and is not an integer amount of cycles. If one first subtracts  $\bar{u}$  from the measurements to reduce round off errors, as suggested in [8], than one must be careful before interpreting  $\bar{u}$ . In that case  $A_0$  will be a net value representing an unphysical 'net' current due to an 'not integer' amount of tidal periods within the measured time series. This value is also included in  $\bar{u}$ . To correct for this bias and obtain the physical net current, one must sum the results for  $\bar{u}$  and  $A_0$ . If one does not first subtract the average from the measurements (and increase the chance for round off errors) than the calculation of  $\bar{u}$  is not necessary and one directly obtained the physical net current in the form of  $A_0$ .

#### 4.1.2 Restrictions

The tidal frequencies ( $\omega_j$ ) used for the LSHA are bounded to three criteria. First, the period of the smallest (fundamental) frequency ( $T_f$ ) that can be resolved is smaller than or equal to the duration of the time series ( $T$ ):

$$T_f \leq T = N\Delta t = 19.8days \quad (38)$$

Second, the period ( $T_N$ ) of the largest (Nyquist) frequency that can be observed is equal to twice the sampling interval:

$$T_N = 2\Delta t = 6s \quad (39)$$

Because the Nyquist frequency is in the order of the frequency of surface waves, which contains energy, it might be possible that a significant amount of energy is found at frequencies higher than that of the Nyquist frequency. This may lead to leakage of energy from the high frequent motion to lower frequent motion. Because of the enormous difference between the highest tidal frequencies and the Nyquist frequencies this effects is in generally ignored for the results of the LSHA. The third criterion is given by the Rayleigh criterion which states that two adjacent frequencies can only be resolved if the reciprocal of the frequency difference is smaller than or equal to the duration of the time series:

$$\frac{1}{\Delta f} \leq T \quad (40)$$

Where  $\Delta f$  is the difference between two adjacent frequencies used for the LSHA. The criteria above are used to select the frequencies that are used as input for the LSHA. Previous measurements already determined the amplitude and phase of 144 tidal frequencies in the Marsdiep. From these

results the 25 most dominant frequencies and the most dominant low frequencies are used [3]. If the duration of the time series is long enough all frequencies can be taken into account because the difference between two frequencies may be very small. Therefore the rejection criteria due to the Rayleigh criterion must be applied carefully or it may reject frequencies of which it is known that they are dominant and must be used as input for the LSHA. Using the list of the most dominant frequencies, first the fundamental and Nyquist criterion are applied. Then the Rayleigh criterion is used starting with the most dominant frequency and from there on finding all frequencies that are within the Rayleigh criterion. From the left over frequencies the most dominant one (in terms of amplitude) is selected and so on. After applying all criteria, 14 tidal components are obtained for the LSHA. The resulting names, frequencies, amplitudes and phases are given in table (4) and (5), which will be discussed in section 4.1.5.

It must be noted that from previous measurements in the Marsdiep [3] it follows that  $N_2$  and  $L_2$  are the 3<sup>rd</sup> and 4<sup>th</sup> important components. Because they have almost the same frequency as the  $M_2$  and  $S_2$  frequency and the time series is not long enough, they are not included in the list of tidal frequencies in table (4) and (5) due to the Rayleigh criterion. It is possible that parts of their energy is incorporated in the  $M_2$  and  $S_2$  tidal components.

### 4.1.3 The explained variance

As all the components of the velocity triangle are calculated using the results of the LSHA it is best to first analyze the quality of the LSHA. Recall that the LSHA was performed by finding the minimum of the  $SSE$  (equation 10). The  $SSE$  is the total variance that is not explained by the fit. Equation (10) can be rewritten in a way that results in a number giving the goodness of the fit. Starting with:

$$SSE = \sum_{i=1}^I [(\tilde{u}_i - \bar{u}) - (U_i - \bar{u})]^2 = \sum_{i=1}^I [u_i - \hat{u}_i]^2 = \sum_{i=1}^I u_i^2 + \sum_{i=1}^I \hat{u}_i^2 - 2 \sum_{i=1}^I u_i \hat{u}_i \quad (41)$$

Here  $N$  is the amount of measurements and  $U_i = \hat{u}_i + \bar{u}$  is the complete model. The resulting expression for  $SSE$  can be rewritten as:

$$SSE = SST + SSF + Residue \quad (42)$$

Where  $SST$  is the Total Sum of Squares or the total variance within the measured data set and is given by:

$$SST = \sum_{i=1}^I u_i^2 \quad (43)$$

The value for  $SSF$  is the Fitted Sum of Squares or explained variance by the model and is given by:

$$SSF = \sum_{i=1}^I \hat{u}_i^2 \quad (44)$$

The *Residue* is given by:

$$Residue = -2 \sum_{i=1}^I (\hat{u}_i u_i)$$

$$\begin{aligned}
Residue &= -2 \sum_{i=1}^I (\hat{u}_i u_i) - 2 \sum_{i=1}^I \hat{u}_i^2 + 2 \sum_{i=1}^I \hat{u}_i^2 \\
Residue &= -2 \sum_{i=1}^I \hat{u}_i^2 + 2 \sum_{i=1}^I \hat{u}_i (u_i - \hat{u}_i) \\
Residue &= -2SSF + \epsilon
\end{aligned}$$

Recall that  $u_i$  is defined in equation (8) and is the unexplained difference between the measurements and the fit. Now  $\epsilon$  can be written as:

$$\epsilon = 2 \sum_{i=1}^I \hat{u}_i u_i \quad (45)$$

so that the new expression for the  $SSE$  is given by:

$$SSE = SST - SSF + \epsilon \quad (46)$$

The derivation to obtain  $SSE$  is done in such a way that the right hand side of equation (46) should be small. In that case one can state that if  $\epsilon$  is small, than the explained variance by the measurements and the fit are approximately equal and therefore one has a good fit. In a vector approach this indicates that  $\hat{u}_i \cdot u_i = 0$ . From numerical calculations it follows that for the LSHA  $\frac{\epsilon}{SSE}$  is in the order of  $10^{-13}$  which is much smaller than 1 so that  $\epsilon$  can indeed be neglected resulting in:

$$SSE = SST - SSF \quad (47)$$

Now the total unexplained variance  $SSE$  is expressed as the difference between the total variance ( $SST$ ) and the explained variance by the fit ( $SSF$ ). The ratio of the explained variance by the fit with respect to the total variance is a measure for the goodness of the fit. For a certain depth ( $z$ ) this is given by:

$$\sigma_z^2 = 100 * \left( \frac{SSF}{SST} \right) = 100 * \left( \frac{\sum_{i=1}^I \hat{u}_i^2}{\sum_{i=1}^I u_i^2} \right) \quad (48)$$

To understand the result it is convenient to use examples. For example, assume the perfect fit, so that  $\hat{u}_i = u_i$ . This results in a value of 100. Which may be interpreted as a fit that explains 100% of the data set. Now assume that nothing of the variance is explained by the fit because  $\hat{u}_i = 0$ . In that case 0% of the data is explained. For each depth the LSHA is performed and a value for  $\sigma_z^2$  is known (figure 30). Using the percentages of explained variances for each depth, the total explained variance ( $\sigma_t^2$ ) for the whole measured velocity profile can be calculated using:

$$\sigma_t^2 = \frac{1}{K} \sum_{z=1}^K \sigma_z^2 \quad (49)$$

Where  $K$  is the amount of measurements in the vertical. This results in an explained variance for the along stream velocity of 95.6% and an explained variance for the cross stream current of 71.0%. Now consider figure 30 which shows the explained variance per depth. The first panel and second panel show respectively the explained variance for the along stream and cross stream velocity. Both are clearly under influence of bottom friction. The bottom friction leads to an increase in incoherent processes, causing the tides to become relatively less dominant, so that the tides explain less of



Constituent	T (days)	Along stream		
		A (ms <sup>-1</sup> )	% of $M_2$	Phase (degrees)
$A_0$	0.086	0.08	7.5	
$M_2$	0.518	1.06	100.0	-96
$S_2$	0.500	0.33	30.7	-104
$2MS_2$	0.536	0.24	22.5	66
$2MS_6$	0.171	0.13	12.6	-50
$M_6$	0.173	0.09	8.9	-12
$2SM_2$	0.484	0.09	8.9	-20
$O_1$	1.076	0.08	7.8	-104
$K_1$	0.997	0.06	6.1	-88
$M_4$	0.259	0.05	4.7	164
$3MS_2$	0.557	0.04	4.1	-82
$M_f$	13.661	0.03	3.1	-18
$2MK_3$	0.349	0.03	2.6	167
$MS_4$	0.254	0.03	2.5	75
$3MS_8$	0.128	0.02	1.8	-156

Table 4: The tidal average, amplitudes and phases of the along stream tidal components at 1.75m depth (1<sup>th</sup> bin)

the signal. At the surface similar effects play a role in the cross stream direction. Probably several incoherent secondary currents, as given in the introduction, become more important towards the surface decreasing the influence of the tide. A proof that the LSHA works fine is given in figure (31), which shows the evolution of the explained variance and amplitudes of several tidal frequencies. The explained variance should, as shown, always increase or stay equal because it should define the amplitude of a frequency zero if it does not increase the explained variance. The amplitudes are scaled with their maximum and converge to a saturation amplitude if more frequencies are used.

It must be noted that the mathematical method behind the LSHA uses the first order derivative to find the minimum in  $r^2$  (equation 10). When the derivative is zero a minimum or maximum is found. In the LSHA there are  $M$  parameters to minimize. Therefore the minimum found in this  $M$  dimensional space does not have to be the absolute minimum, because a multidimensional space can have many minima. In theory, this means that there might be an even better approximation (with different amplitudes and phases) of our data set using the same frequencies. A full proof mathematical method to find an absolute minimum in a multidimensional space is not yet fully developed and beyond the scope of this master thesis. The results are therefore interpreted as they are.

#### 4.1.4 Overtides and compound tides

In the Marsdiep the currents due to the incoming tidal wave has several nonlinear aspects which can be explained by taking into account the one dimensional momentum and continuity equations given by:

$$\frac{\partial u}{\partial t} + u \frac{\partial u}{\partial x} = -g \frac{\partial \zeta}{\partial x} - c \frac{1}{H + \zeta} u |u| \quad (50)$$

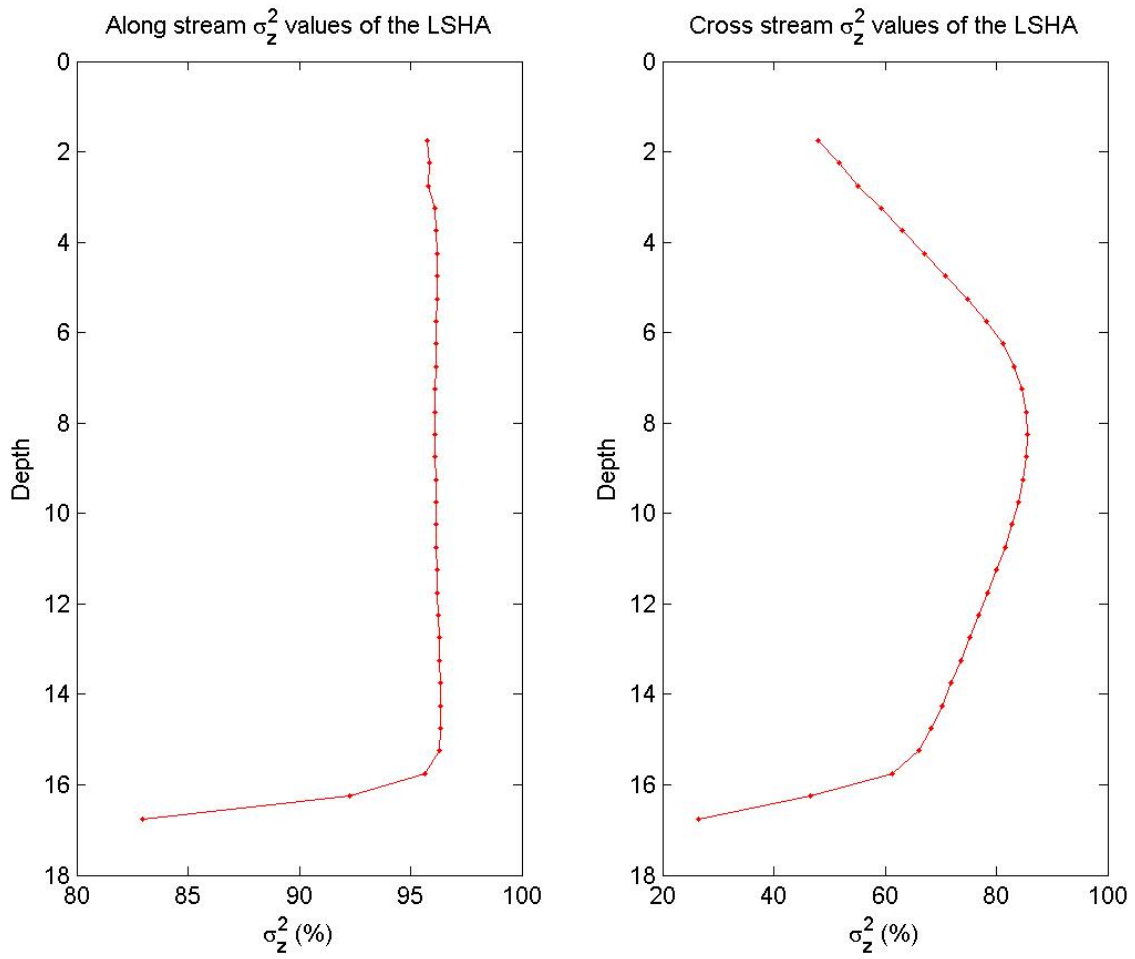


Figure 30: Explained variance ( $\sigma_z^2$ ) by the LSHA using 14 tidal frequencies for each depth. The left panel shows the results for the along stream direction. The right panel shows the results for the cross stream direction. A high value indicates that a large part of the signal is explained using the 14 tidal constituents.

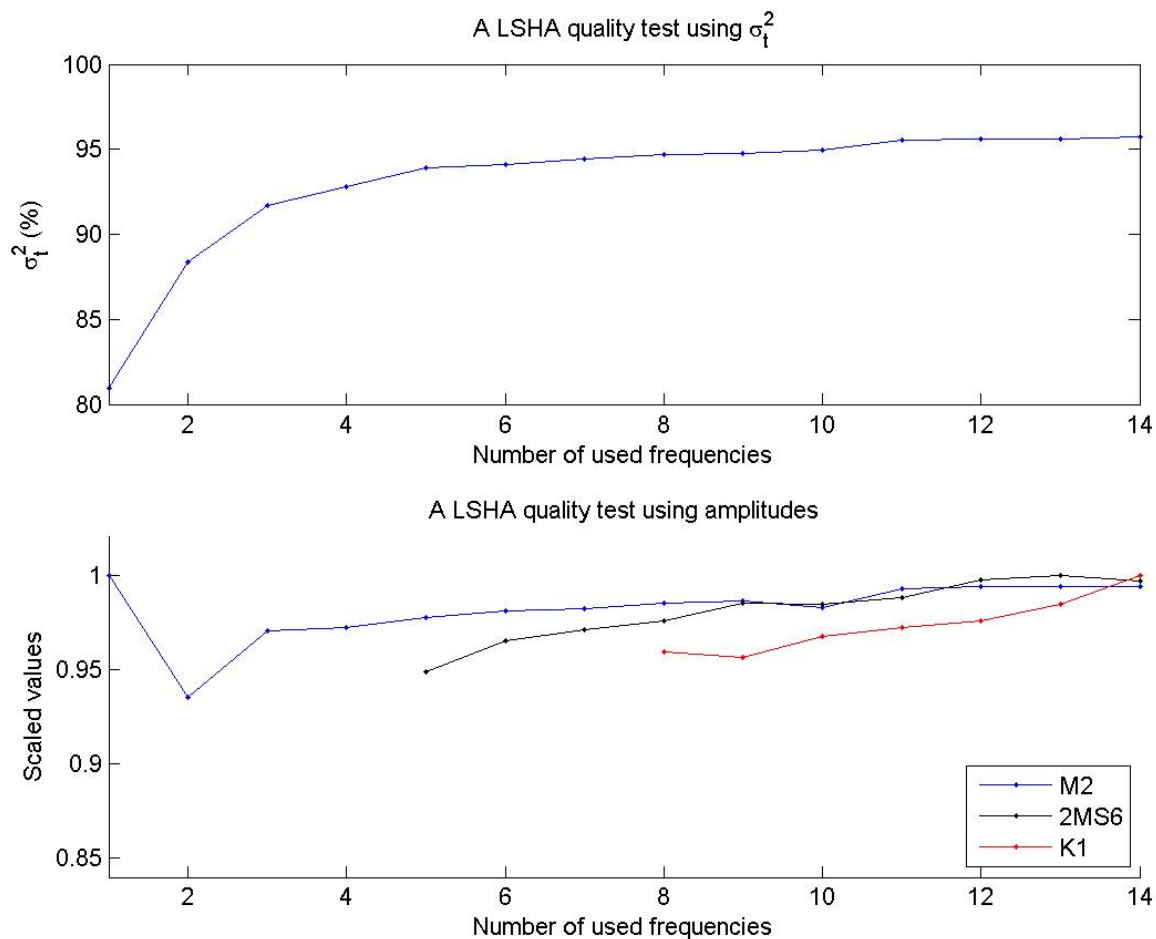


Figure 31: The upper panel shows the explained variance as a function of the amount of used frequencies. It shows that the quality always increases when a frequency is added. This is as expected from the LSHA, so that it may be concluded that the mathematical derivation and computer script performing of the LSHA work fine. In the lower panel the behavior of three amplitudes as a function of the amount of used frequencies is shown. It shows that they converge to their final value. Note that they are scaled with the largest amplitude in the signal, which was the first amplitude obtained for the  $M_2$  frequency.

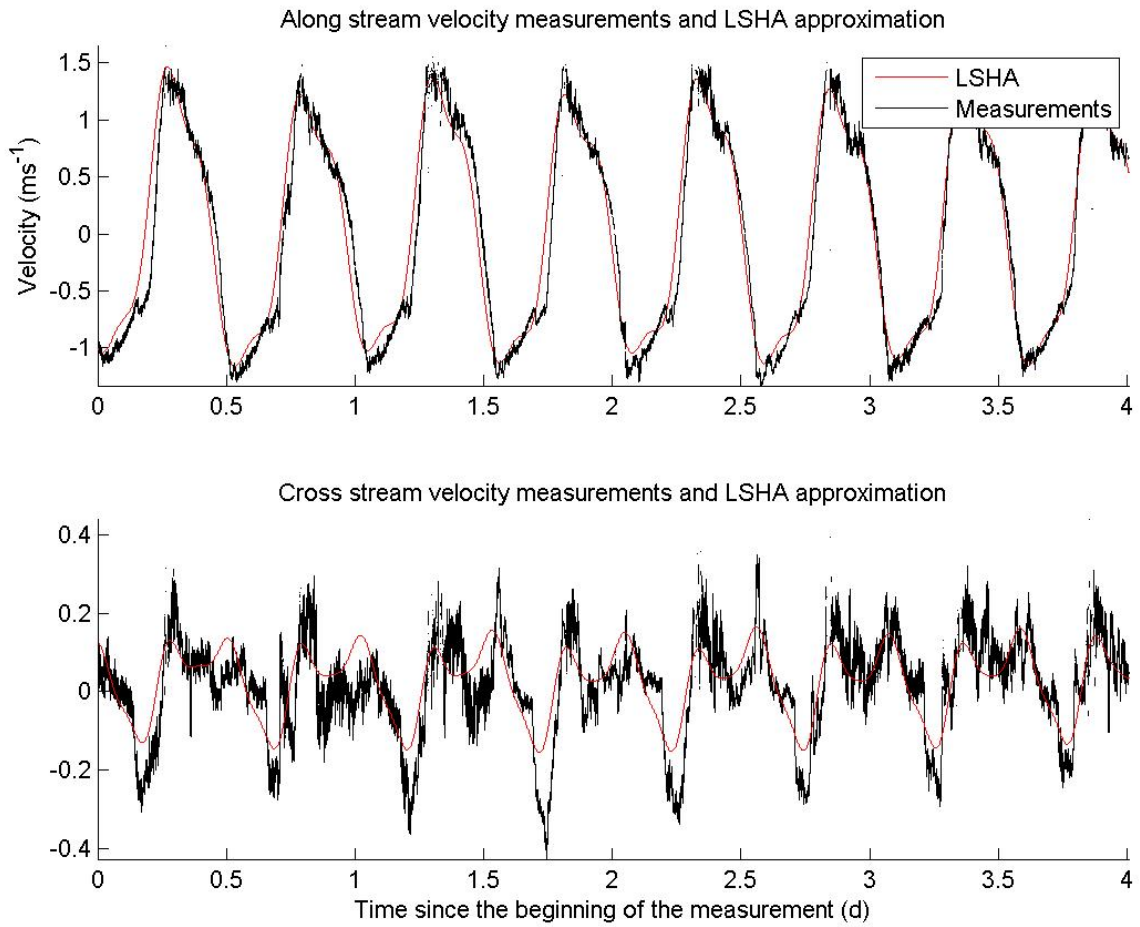


Figure 32: The upper panel shows the LSHA analysis (red) and measurements (black) for the along stream and the lower panels shows the same for the cross stream velocities, both at 1.75m depth (1<sup>th</sup> bin). It confirms that the along stream LSHA is much better than the cross stream LSHA and that the cross stream extreme's are not captured by the LSHA.

Constituent	T (days)	Cross stream		
		A ( $ms^{-1}$ )	% of $M_2$	Phase (degrees)
$A_0$	0.086	0.009	12.1	
$M_2$	0.518	0.073	100.0	-3
$M_4$	0.259	0.048	65.3	142
$MS_4$	0.254	0.035	48.3	116
$M_f$	13.661	0.026	36.0	-30
$S_2$	0.500	0.023	32.1	-96
$3MS_8$	0.128	0.012	27.3	-158
$2SM_2$	0.484	0.017	23.3	-2
$M_6$	0.173	0.012	16.5	53
$3MS_2$	0.557	0.011	15.1	-178
$2MS_6$	0.171	0.008	10.8	28
$O_1$	1.076	0.007	9.5	-92
$2MK_3$	0.349	0.004	5.7	-51
$K_1$	0.997	0.004	5.3	-138
$2MS_2$	0.536	0.002	2.0	-19

Table 5: The tidal average, amplitudes and phases of the cross stream tidal components at 1.75m depth (1<sup>th</sup> bin)

$$\frac{\partial \zeta}{\partial t} + \frac{1}{b} \frac{\partial}{\partial x} [bHu + b\zeta u] = 0 \quad (51)$$

Where  $\zeta$  is the surface elevation above mean sea level,  $u$  is the cross-sectional average velocity,  $b$  is the width of the basin,  $H$  is the cross-sectional averaged depth below mean sea level,  $t$  is the time and  $x$  is the along stream coordinate,  $g$  is the vertical component of the gravity acceleration and  $c$  is the friction coefficient (which is in the order of 0.0025). From these equations three nonlinear terms can be found that cause four different nonlinear effects that will lead to overtides and compound tides to evolve [25]. The first is the nonlinear continuity term ( $\frac{\partial \zeta u}{\partial x}$ ), the second is the inertial term ( $u \frac{\partial u}{\partial x}$ ) and the last is the bottom friction term ( $\frac{u|u|}{H+\zeta}$ ). After a scaling analysis the bottom friction term can be split into two terms [25]. This results in the third term which is the so called quadratic bottom friction term ( $\propto u |u|$ ) causing the tidal frequencies to interact with themselves and the fourth term which gives the effect of elevation on the frictional momentum loss per unit volume of fluid ( $\propto \zeta u |u|$ ), a cubic nonlinearity. In the Marsdiep overtides and compound tides are of significant importance determining the velocity currents [3]. The most important overtides in both the along stream and cross stream direction are the  $M_6$  and  $M_4$  frequencies. The  $M_6$  is caused by the quadratic bottom friction term causing interaction of the tide with itself. The surface elevation terms of the bottom friction, the inertial term, the continuity term and possibly the combination of a net current with the quadratic bottom friction term can produce currents with the  $M_4$  frequency. It is hard to say which term is dominant in which direction (along stream or cross stream). It is clear that in the cross stream direction the  $M_4$  frequency is of great importance. This might indicate that for example the combination of the net current and quadratic friction causes a larger  $M_4$  because the net (shown in figure 42 and discussed in section 4.4) current is relatively important in the cross stream current compared to the along stream current. This is speculative. Using the significant importance of the  $M_6$  and  $M_4$  frequencies it is safe to say that

bottom friction effects are important in both the along and cross stream direction. The most important compound tides in the along stream direction of the Marsdiep area are the  $2MS_2$  and  $2MS_6$  frequencies which are caused by interaction between  $M_2$  and  $S_2$  frequencies due to the quadratic bottom friction term. In the cross stream direction the  $MS_4$  and  $3MS_8$  frequencies are the most important overtides. It is likely that the  $MS_4$  frequency amplitude is caused by the same effects causing the  $M_4$  frequency only this time the interaction is not between  $M_2$  and itself but between  $M_2$  and  $S_2$ . The reason for  $3MS_8$  to exist is comparable with that of  $2MS_2$  and  $2MS_6$  in the along stream direction but then due to interaction of higher harmonic of the  $M_2$  frequency with  $S_2$  frequency. From the great amount of relative important overtides and compounds tides in the cross stream direction it may be concluded that the cross stream current is much more influenced by nonlinear effects than the along stream current, but in both directions nonlinear effects are of significant importance. Thus the Marsdiep can be treated as shallow water (because of the importance of the nonlinear continuity term) with significant influence of the bottom friction.

#### 4.1.5 Discussing the LSHA results using Fourier analysis

The currents measured by the ADCP are due to tides, wind, IS, surface waves, etc. All these act in a different frequency spectrum. For example the spring neap tidal cycle has a period of approximately  $10^6s$  while surface waves have period of approximately  $10^1s$ . Using a Fourier Transform (FT) gives the opportunity to determine which frequency domains have the largest influence on the measured currents. Therefore it is useful to compare the FT of the measurements and the FT of the residual measurements (of which the LSHA fit is subtracted). First a FT capable to deal with discrete measurements must be found. As a starting point the general form for a FT is used:

$$U(\omega) = \int_{-\infty}^{\infty} u(t) \exp(-i\omega t) dt \quad (52)$$

Here  $U(\omega)$  is the FT of the time series of a measured current given by  $u(t)$ ,  $t$  is the time ( $s$ ) and  $\omega$  in the frequency ( $rads^{-1}$ ). The measurements are not continuous and therefore an alternative for the continuous FT is used, the Discrete Time Fourier Transform (DTFT):

$$U(\omega) = \frac{2}{I} \sum_{i=1}^I u_i \exp(-i\omega t_i) = \frac{2}{I} \sum_{i=1}^I u_j [\cos(\omega t_i) - i \sin(\omega t_i)] \quad (53)$$

where  $I$  is the amount of measurements,  $u_i$  is the value of the current at  $t = t_i$ . Note that a single  $i$ , not bound to a letter, is the imaginary  $i$ . Only the positive half of the frequency spectrum is analyzed, resulting in a multiplication factor of 2 to obtain the correct amplitudes corresponding to the frequencies. The frequency spectrum increases gradually from the fundamental frequency, through multiples, to the Nyquist frequency (as discussed in section (4.1.2)). To reduce aliasing within the DTFT a Hanning window is used to multiply the data with. The Hanning window is given by:

$$w = \frac{1}{2} \left( 1 - \cos \left( \frac{2\pi t_i}{t_I} \right) \right) \quad (54)$$

Integrated over time, the multiplication with the Hanning window reduces the velocity measurements with a factor half. As a result the obtained amplitudes that one would obtain from the DTFT are also reduced with a factor half. The DTFT measurements are therefore multiplied with

a factor two to compensate for this loss. The resulting DTFT including the Hanning window, adjusted to range of the summation and scaled with a factor 2 will then be:

$$U(\omega) = \frac{2}{I} \sum_{i=1}^I u_i \left[ 1 - \cos \left( \frac{2\pi(i-1)}{I-1} \right) \right] [\cos(\omega t_i) - i \sin(\omega t_i)] \quad (55)$$

The Fourier transformed  $U(\omega)$  is complex which results in a phase and amplitude for each frequency:

$$A(\omega) = \sqrt{\Re(U(\omega))^2 + \Im(U(\omega))^2} \quad (56)$$

$$\phi(\omega) = \arctan\left(\frac{\Im(U(\omega))}{\Re(U(\omega))}\right) \quad (57)$$

Due to computer memory limitations it was chosen to apply the DTFT to a gridded data set. The gridded data set contains a 1 minute time resolution by averaging 20 measurements and representing it at one point. The resulting resolution is, by far, high enough to find separate tidal components. The LSHA is applied to the gridded data set resulting in phases, amplitudes and  $\sigma_{tot}^2$  values that are practically the same as for the ungridded data set. The results of the DTFT for the along stream and cross stream currents at 3.25m depth (4<sup>th</sup> bin), are shown in figure (33) and (34). It is convenient to discuss the results of the DTFT together with the results of the LSHA shown in table (4) and (5).

In figure (33) the resulting amplitudes of the DTFT of the along stream velocity is shown for the gridded data set and for the residual. Within this plot the frequency of some important tidal components are shown in blue. Note that the scale is limited to  $0.1ms^{-1}$ . Taking into account that semi-diurnal  $M_2$  amplitude has a value of approximately  $1ms^{-1}$ , makes clear that this is by far the most dominant component. Second most dominant component is the semi-diurnal  $S_2$  frequency, as shown in the result of the LSHA analysis in table (4). The peak due to diurnal tidal components such as  $O_1$  and  $K_1$  are also clearly visible. Using the diurnal and semi diurnal tidal components, the ratio  $Ratio = \frac{O_1+K_1}{M_2+S_2}$  is often used to determine if the currents are dominated by semi-diurnal ( $Ratio < 0.25$ ), mixed ( $> 0.25Ratio < 1.25$ ) or diurnal ( $Ratio > 1.25$ ) tides. For the along stream components this ratio is 0.11 which is comparable with earlier results from measurements in the Marsdiep [3] and clearly indicates that the motion is dominated by semi diurnal tidal frequencies. The DTFT of the residual data set shows that both the diurnal and semi diurnal frequencies are removed satisfactory.

From the difference between the DTFT of the along stream currents and of the residual current some aspects are of importance. There is quite some energy in low frequencies that have periods in the order of the duration of the time series. This energy is probably caused by net currents and meteorological factors. Concluding from the decrease of this energy shown in the DTFT some of these effects must be captured by the  $M_f$  or other frequencies because the amount of energy in the low frequencies decreases after applying the LSHA. Another remarkable aspect is the large amount of higher harmonics (even higher than  $M_{12}$ ). These seem to be artifacts of the large  $M_2$  components because they disappear in the residual plot, while these higher harmonics are not frequencies used as input for the LSHA. In the upper panel of figure (35) remarkable behavior of the along stream  $M_4$  and  $M_6$  frequencies is seen. The obtained amplitude of the  $M_4$  frequency in the along stream direction is not as high as could be expected of the results of the DTFT performed on the measurements. After subtracting the LSHA fit the amplitude of the DTFT performed on the residual in fact shows an increase in amplitude at a frequency just a little higher than the  $M_4$

frequency. It is not yet clear what the reason for this abnormal behavior might be. From figure (35) it is also clear that the amplitude of the  $M_6$  frequency should be higher than that of the  $M_4$  frequency. Do note that due to the resolution of the frequency steps which are constructed to perform the DTFT with, the exact  $M_6$  frequency is not used. As a result a band centered around the  $M_6$  of higher amplitudes is obtained. This nonetheless indicated the importance of the  $M_6$  frequency

The cross stream result, shown in figure (34) and table (5), will be discussed. The most dominant frequency is still  $M_2$  but the rest has become relatively more important compared to the along stream results. The ratio  $\frac{O_1+K_1}{M_2+S_2} = 0.09 < 0.25$  still indicates semi-diurnal tides dominate but in this case the overtide and compound tide with a frequency about twice that of the semi diurnal components ( $M_4, MS_4$ ) are not included and seem to have a large influence  $\frac{M_4+MS_4}{M_2+S_2} = 0.86$ . In the lower panel of figure (35) the relative importance of the  $M_4$  frequency compared to the  $M_6$  frequency is clear. It also clearly shows that the  $M_4$  frequency is important in the along stream direction and captured well by the LSHA. This indicates a lot of nonlinearity in the cross stream currents. Currents and therefore tidal currents are much smaller in the cross stream direction and lots of other processes are more dominant than the tides. Especially at the surface and the bottom. Again a lot of energy is found in the very low frequencies, but most of it is removed by the LSHA and was probably included in the  $M_f$  frequency.

When considering both the along stream and cross stream DTFT and that of their residuals it may be concluded that the LSHA works well and removes the coherent part of the signal. The residual or incoherent part of the signal is expected to include the baroclinic currents and other processes not captured by the LSHA. A comparison between the predicted and measured along stream and cross stream velocity at 3.25m depth (4<sup>th</sup> bin), are shown in figure (32). This clearly shows that the along stream currents are well predicted and that for the cross stream currents the tides predict only the general behavior and other secondary processes must be more dominant, especially during the change from ebb to flood currents.

## 4.2 The clockwise and anti-clockwise phases and amplitudes

Using the LSHA, amplitudes and phases for the along stream ( $U, \phi_u$ ) and cross stream ( $V, \phi_v$ ) current are obtained. For each separate tidal frequency the resulting along stream ( $\check{u}$ ) and cross stream ( $\check{v}$ ) current can be described as follows:

$$\check{u} = U \cos(\omega t - \phi_u) \quad (58)$$

$$\check{v} = V \cos(\omega t - \phi_v) \quad (59)$$

Using  $\check{u}$  and  $\check{v}$  a complex tidal current  $w$  is constructed:

$$w = \check{u} + i\check{v} \quad (60)$$

Projecting this in a complex plane over a time span of one period ( $T = \frac{2\pi}{\omega}$ ) a tidal current ellipse is obtained which can be decomposed in a *C&AC* rotating circle (as shown in figure 36) [30, 20]. By decomposing the complex velocity  $w$  the *C&AC* rotating velocities can be found:

$$w = U \cos(\omega t - \phi_u) + iV \cos(\omega t - \phi_v) \quad (61)$$



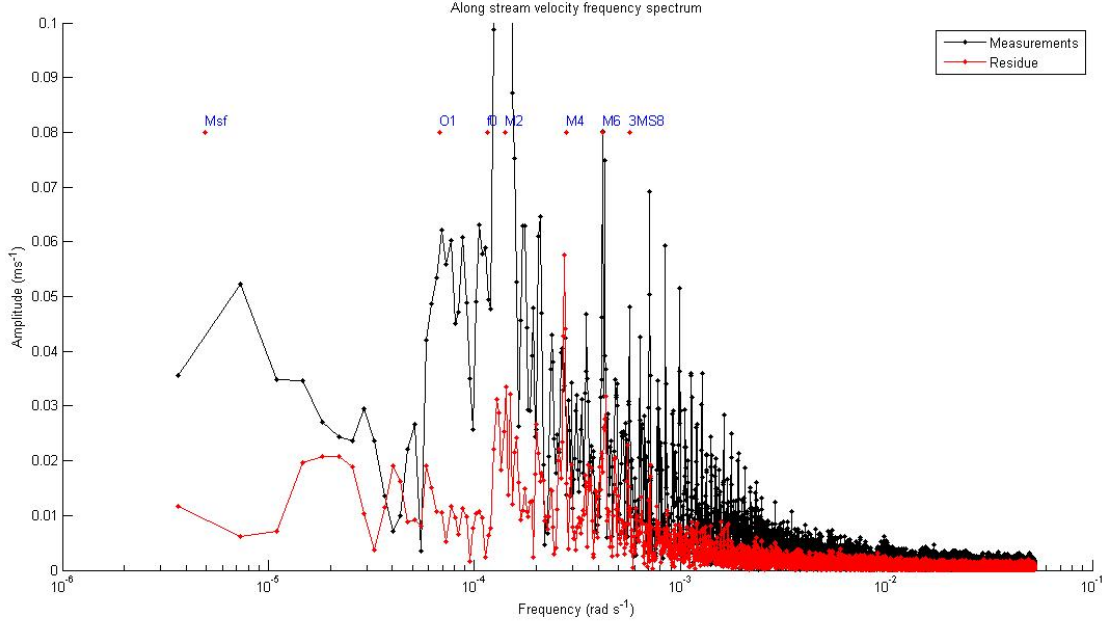


Figure 33: Here the DTFT of the gridded along stream velocity (black) and of the residue after subtracting the LSHA (red) are shown. The positions in the frequency spectrum of several important tidal frequencies and the inertial frequency, are indicated with a name and red dot. Note that the horizontal axis is logarithmic and that the largest amplitude (of the  $m_2$  frequency, exceed the range of the vertical axis.

$$w = \frac{1}{2}U \left( e^{i\omega t} e^{-i\phi_u} + e^{-i\omega t} e^{i\phi_u} \right) + \frac{1}{2}iV \left( e^{i\omega t} e^{-i\phi_v} + e^{-i\omega t} e^{i\phi_v} \right) \quad (62)$$

$$w = \frac{1}{2} \left( U e^{-i\phi_u} + iV e^{-i\phi_v} \right) e^{i\omega t} + \frac{1}{2} \left( U e^{i\phi_u} + iV e^{i\phi_v} \right) e^{-i\omega t} \quad (63)$$

This expression can be rewritten as:

$$w = U_{ac} e^{i\theta_{ac}} e^{i\omega t} + U_c e^{i\theta_c} e^{-i\omega t} \quad (64)$$

Where:

$$U_{ac} e^{i\theta_{ac}} = \frac{1}{2} \left( U e^{-i\phi_u} + iV e^{-i\phi_v} \right) \quad (65)$$

$$U_c e^{i\theta_c} = \frac{1}{2} \left( U e^{i\phi_u} + iV e^{i\phi_v} \right) \quad (66)$$

Where  $U_{ac}$ ,  $U_c$ ,  $\theta_{ac}$  and  $\theta_c$  are the radii and phases of the  $AC$  rotating circular current  $e^{i\omega t}$  and  $C$  rotating circular current  $e^{-i\omega t}$ . These terms must be expressed in the known variables  $V$ ,  $U$ ,  $\phi_v$  and  $\phi_u$ . Therefore (65) and (66) must be rewritten:

$$2U_{ac} \cos(\theta_{ac}) + 2iU_{ac} \sin(\theta_{ac}) = U \cos(\phi_u) - iU \sin(\phi_u) + iV \cos(\phi_v) + V \sin(\phi_v) \quad (67)$$

$$2U_c \cos(\theta_c) + 2iU_c \sin(\theta_c) = U \cos(\phi_u) + iU \sin(\phi_u) + iV \cos(\phi_v) - V \sin(\phi_v) \quad (68)$$

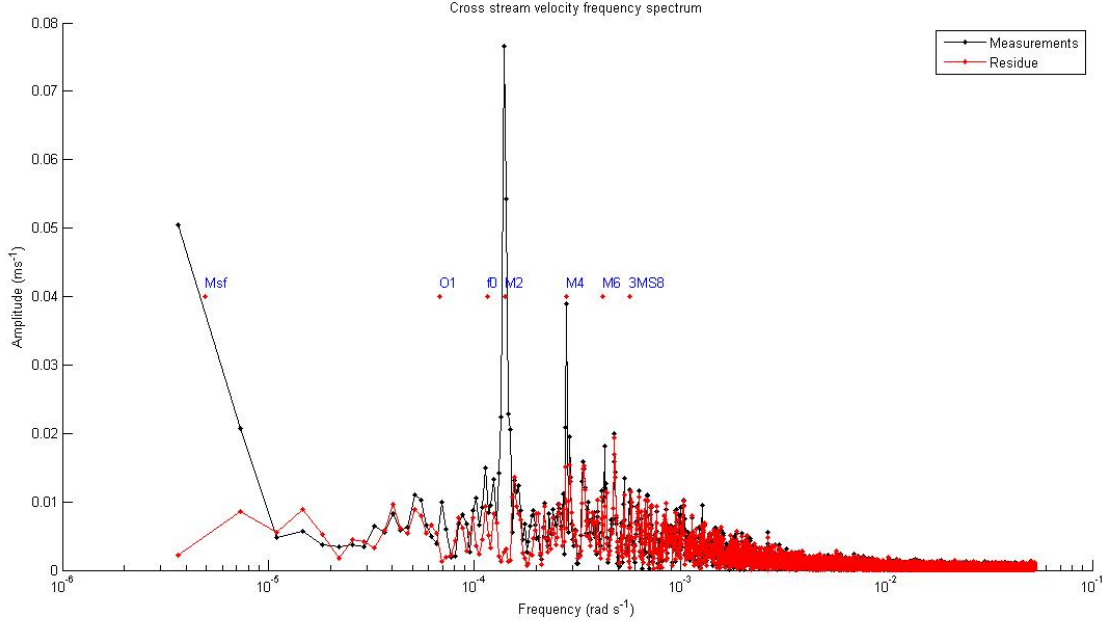


Figure 34: Here the DTFT of the gridded cross stream velocity (black) and of the residue after subtracting the LSHA (red) are shown. The positions in the frequency spectrum of several important tidal frequencies and the inertial frequency, are indicated with a name and red dot. Note that the horizontal axis is logarithmic and that the largest amplitude (of the  $M_2$  frequency, exceed the range of the vertical axis.

Separating the real and imaginary parts:

$$2U_{ac} \cos(\theta_{ac}) = U \cos(\phi_u) + V \sin(\phi_v) \quad (69)$$

$$2U_{ac} \sin(\theta_{ac}) = -U \sin(\phi_u) + V \cos(\phi_v) \quad (70)$$

$$2U_c \cos(\theta_c) = U \cos(\phi_u) - V \sin(\phi_v) \quad (71)$$

$$2U_c \sin(\theta_c) = U \sin(\phi_u) + V \cos(\phi_v) \quad (72)$$

With these equations the expressions for the  $C\&AC$  phases ( $\theta_{ac}, \theta_c$ ) and amplitudes ( $U_{ac}, U_c$ ) can be found. Divide (70,69) and (72,71) to find the phases:

$$\theta_{ac} = -\arctan\left(\frac{U \sin(\phi_u) - V \cos(\phi_v)}{U \cos(\phi_u) + V \sin(\phi_v)}\right) \quad (73)$$

$$\theta_c = \arctan\left(\frac{U \sin(\phi_u) + V \cos(\phi_v)}{U \cos(\phi_u) - V \sin(\phi_v)}\right) \quad (74)$$

By taking the squares of equations (70,69) and (72,71) and adding them up, a nice expression for the amplitudes is obtained:

$$U_{ac} = \frac{1}{2} \sqrt{U^2 + V^2 + 2UV \sin(\phi_v - \phi_u)} \quad (75)$$

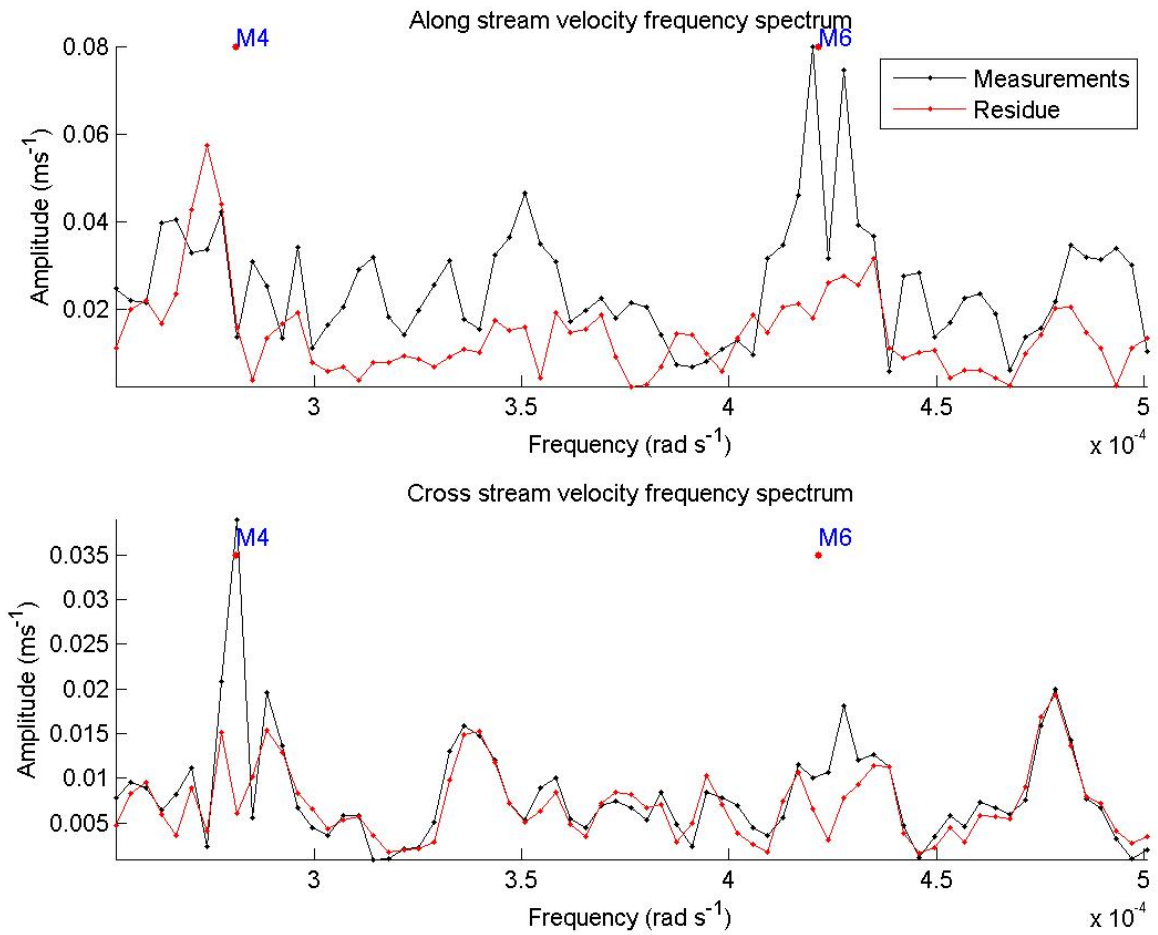


Figure 35: The upper panel shows the same as figure (33) for the along stream velocity signal, but than focused on a small part of the frequency spectrum around the  $M_4$  and  $M_6$  frequencies. The lower panel is the same but than for the cross stream velocity.

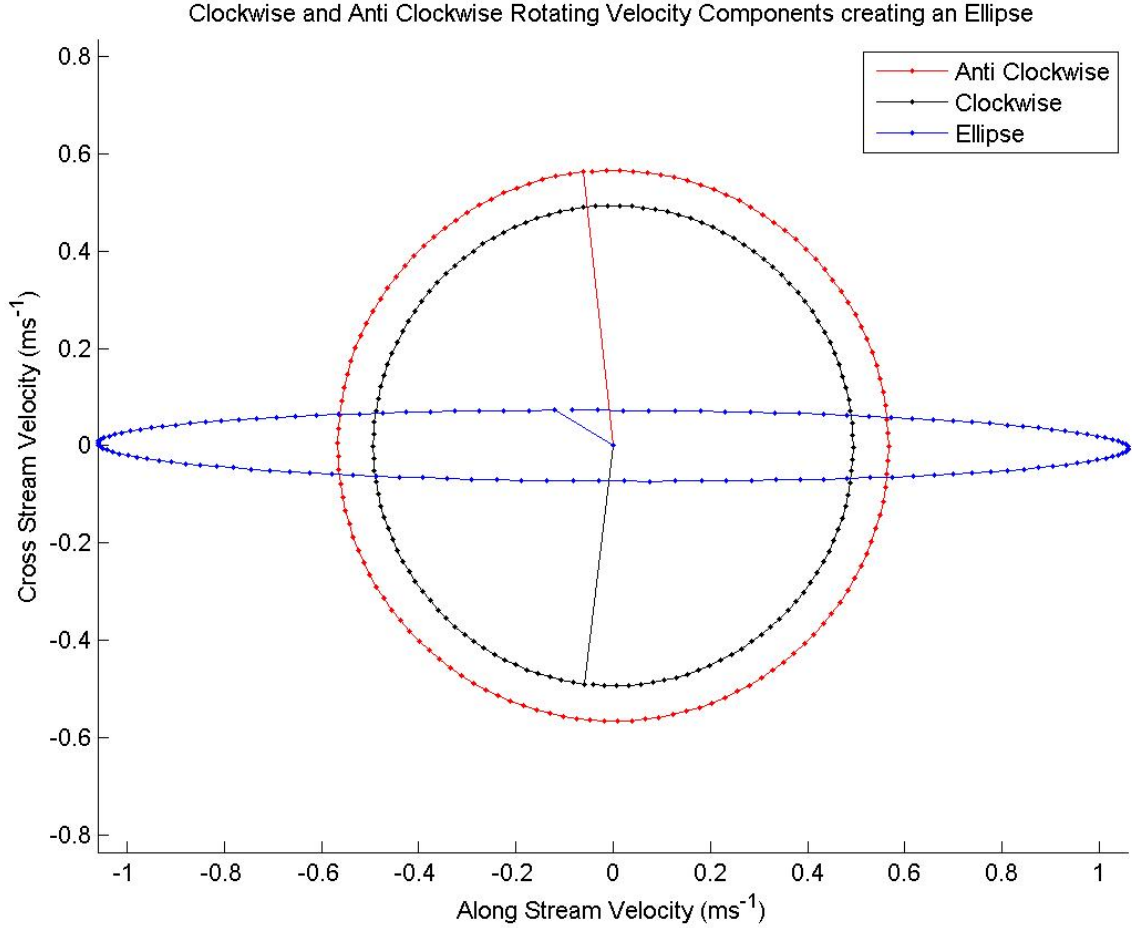


Figure 36: In blue the tidal ellipse is shown that is obtained when adding up a clockwise (black) and anti clockwise (red) rotating current. The lines indicate the location of the starting points.

$$U_c = \frac{1}{2} \sqrt{U^2 + V^2 - 2UV \sin(\phi_v - \phi_u)} \quad (76)$$

Equations (76),(75),(74) and (73) are the amplitudes and phases of the *C&AC* rotating velocity components of the measured velocity calculated using the LSHA amplitudes and phases. As a result this is step #1 of figure (29).

### 4.3 The ellipse parameters

Using the *C&AC* phases and amplitudes the measured current can be described using ellipse parameters [30, 1, 20, 13, 3]. The *SEMA* (with amplitude  $U_{Ma}$ ) is the larger axis of the ellipse in the direction of the along stream current. The *SEMI* (with amplitude  $U_{Mi}$ ) is the small axis of the ellipse and is directed in the cross stream direction. The *PHA* ( $\psi_P$ ) is the angle at which the current is maximum and depends on the moment at which the measurement is started. The *INC* ( $\psi_I$ ) gives the direction (or angle) of the *SEMA* relative to the direction of  $U$ . Note that the *INC* angle changes if one uses the along/cross stream amplitudes or the east/north amplitudes as input. To calculate the ellipse parameters from the *C&AC* amplitudes and phases a method

by is used in which it is assumed that the angles involved in the calculations are mapped in the range  $[-\pi, \pi]$  [37]. When the two radial vectors of the *C&AC* rotating circles are aligned into the same direction then the tidal current will reach a maximum speed. From equation (64) it can be derived that this will be the case when:

$$\theta_{ac} + \omega t = \theta_c - \omega t + 2\pi k \quad (77)$$

Where  $k$  is an integer ( $k = 0, \pm 1, \pm 2, etc$ ). This leads to:

$$\psi_P = \omega t_{max} = \frac{1}{2}(\theta_c - \theta_{ac}) + \pi k \quad (78)$$

Where  $t_{max}$  is the moment at which equation (77) is satisfied and  $\omega t_{max}$  or  $\psi_P$  is the phase angle at which equation (77) is satisfied. Note that in one tidal period the vectors align twice ( $k = 0, k = 1$ ). Both direction can be used as the directions of the semi major axis. In this case the northern axis convention is used ( $\psi_P$  lies between  $[0, \pi]$ ). Insert  $\psi_P$  into equation (64) to obtain:

$$w_{max} = U_{ac}e^{i(\frac{1}{2}(\theta_c + \theta_{ac}) + \pi k)} + U_c e^{i(\frac{1}{2}(\theta_c + \theta_{ac}) - \pi k)} \quad (79)$$

$$w_{max} = U_{ac}e^{i(\frac{1}{2}(\theta_c + \theta_{ac}) + \pi k)} + U_c e^{i(\frac{1}{2}(\theta_c + \theta_{ac}) - \pi k + 2\pi k)} \quad (80)$$

$$w_{max} = (U_{ac} + U_c) e^{i(\frac{1}{2}(\theta_c + \theta_{ac}) + \pi k)} \quad (81)$$

Using these equations one can derive the *SEMA* amplitude ( $U_{Ma}$ ):

$$U_{Ma} = |w_{max}| = U_{ac} + U_c \quad (82)$$

And the direction of this current is given by the *INC* angle ( $\psi_I$ ), which is:

$$\psi_I = \text{arg}(w_{max}) = \frac{1}{2}(\theta_c + \theta_{ac}) + \pi k \quad (83)$$

Using equation (83) it depends on whether  $k = 0$  or  $k = 1$  gives the first alignment. This depends on the relation between  $\theta_c$  and  $\theta_{ac}$ . If  $\theta_c > \theta_{ac}$  than the first alignment is  $k = 0$ . If  $\theta_c < \theta_{ac}$  than the first alignment is  $k = 1$ . To find  $U_{Mi}$  the same kind of trick is used, as used for the  $U_{Ma}$ , but the starting value is now different. That is because the two vectors must be aligned in opposite direction to construct the *SEMI* amplitude. This is the case when:

$$\omega t_{min} = \frac{1}{2}(\theta_c - \theta_{ac}) + \pi(k + \frac{1}{2}) \quad (84)$$

$$w_{min} = U_{ac}e^{i(\frac{1}{2}(\theta_c + \theta_{ac}) + \pi(k + \frac{1}{2}))} + U_c e^{i(\frac{1}{2}(\theta_c + \theta_{ac}) - \pi(k + \frac{1}{2}))} \quad (85)$$

$$w_{min} = (U_{ac} + U_c e^{-i\pi}) e^{i(\frac{1}{2}(\theta_c + \theta_{ac}) + \frac{\pi}{2})} \quad (86)$$

$$w_{min} = (U_{ac} - U_c) e^{i(\frac{1}{2}(\theta_c + \theta_{ac}) + \frac{\pi}{2})} \quad (87)$$

Resulting in the following expression for the *SEMI* amplitude ( $U_{Mi}$ ):

$$U_{Mi} = |w_{min}| = U_{ac} - U_c \quad (88)$$

With the  $U_{Ma}$  and  $U_{Mi}$  the *ECC* ( $e$ ) of the ellipse can be determined:

$$e = \frac{U_{Mi}}{U_{Ma}} = \frac{U_{ac} - U_c}{U_{ac} + U_c} \quad (89)$$

The rotation direction depends on the component with the largest radius. When ( $U_c < U_{ac}$ )  $U_c > U_{ac}$  than the ellipse rotates (anti-) clockwise. In the above the *C&AC* amplitudes are used to calculate the ellipse parameters. This is the same as step #2 of figure (29). From all the equation for the (82),(88),(83) and (78) a relationship between *C&AC* parameters and the ellipse parameters can be derived:

$$U_{ac} = \frac{U_{Ma} + U_{Mi}}{2} \quad (90)$$

$$U_c = \frac{U_{Ma} - U_{Mi}}{2} \quad (91)$$

$$\theta_{ac} = \psi_I - \psi_P \quad (92)$$

$$\theta_c = \psi_I + \psi_P \quad (93)$$

Equations (90),(91),(92) and (93) are necessary to calculate step #5 of figure (29). In the above the LSHA amplitudes and phases are used to calculate the ellipse parameters and rotary currents. For data analysis of the measurements this is all that is needed. Still in the introduction of this section it was claimed that when one knows only one of the 3 sets of physical parameters, all can be computed. The calculation needed for this are given in the appendix.

## 4.4 Discussing the results of the velocity triangle

As a result of the velocity triangle there are 3 sets of 2 amplitudes and 2 phases obtained for each tidal frequency, together with the inclination and eccentricity. Also there are the mean velocity and tidal average. In this section the physical characteristics of the measured vertical structure of all the parameters are explained for the  $M_2$  tidal frequency. The amplitudes of the different physical parameters are shown in figure (37), the phases are shown in figure (38), the inclination is shown in figure (41) and the mean velocity and tidal average are shown in figure (42). The vertical structure of the observed velocity profiles will now be explained taking into account physical and non physical influences.

### 4.4.1 Velocity triangle parameters and bottom friction

Bottom friction decreases the magnitude of the currents toward the bottom. The decrease of the current with depth results in shear of the horizontal velocity in the vertical and therefore vertical circulation cells (eddies) causing turbulence and mixing in the vertical. The stronger the bottom friction (depending on current speed and structure of the bottom) the larger these effects and the higher the shear effects will penetrate into the water column. Due to turbulence more variance is caused by turbulent incoherent motion which cannot be explained by tide alone. As a result the explained variance due to tides decreases. To be able to judge what the effect of bottom friction is on the vertical structure of a measured tidal velocity amplitude or phase, one must take into account the parameters one is discussing. For each set of parameters the effect is pronounced in a

different way. Starting with the rotary currents the expected Ekman layer depth, an indication of the penetration depth over which bottom friction is significant, can be calculated using:

$$\delta_{\pm} = \sqrt{\frac{2\nu}{|f \pm \omega|}}, \quad (94)$$

where  $\delta_+$  is the typical Ekman value for the *AC* rotating current and  $\delta_-$  for the *C* rotating current and  $\nu$  is the turbulent eddy viscosity parameter which is a measure of the influence of the interior friction between adjacent water layers [35]. The viscosity is value is not yet available (nor necessarily constant throughout the water depth) for the Marsdiep, so the absolute values for the Ekman layer due to the  $M_2$  tidal frequency cannot be calculated. Therefore the ratio between the turbulent layers is of interest and is given by  $\frac{\delta_-}{\delta_+} = \sqrt{\frac{|f+\omega|}{|f-\omega|}} = 3.3$ . This would indicate that in the *C* rotating component the effect of bottom friction penetrates 3.3 times as deep as for the *AC* rotating component. As soon as the effect of bottom friction is negligible the 'free stream velocity' is reached (no differences in velocity at different depths, means no shear and therefore no stress forces). This means that the *AC* rotating current should reach its free stream velocity earlier than the *C* rotating current. From the measurements it is not very clear if the free stream velocity is reached at all, in the shallower Marsdiep. The only indication of the difference in Ekman depths is given by the amplitudes of the *C* current, which are smaller than that of the *AC* current indicating an increased effect of friction. In general it can be concluded that the majority of the water column is under influence of the bottom friction. Another argument for this conclusion is given when interpreting the results published by [20] as shown in figure (39). Here an analytical model was used to predict *C&AC* phases and amplitudes in the 40m deep North Sea. This model was fitted to measurements. The North Sea is deeper, currents are smaller and therefore frictional effects do not reach the top of the water column. As a result the different Ekman depths are clearly visible. This is not the case for the measurements presented in this thesis. A possible explanation is that the Ekman depths are bigger than the water depth. This conclusion also applies to the *SEMA* and along stream amplitudes. The difference between the *SEMA* and along stream amplitudes are minimal because the *SEMA* amplitude is deduced from the LSHA amplitudes which were already converted to along stream and cross stream direction. These should be in the same direction as the *SEMA* and *SEMI* and therefore the differences are minor. Both the *SEMA* and along stream amplitudes show a gradual increase from the bottom towards the surface due to the bottom friction. For the cross stream and *SEMI* velocities the velocities are smaller. Taking this into account, together with the resemblance between the explained variance due to the tidal frequencies (figure 30) and the vertical structure of the cross stream amplitudes, it is fair to say that the tidal forces and resulting bottom friction are not necessarily the dominant forces determining the cross stream and *SEMI* amplitudes. The more important processes are for example baroclinic motions, Coriolis effects and especially geometry of the basin. Using the barotropic model derived in section(5) better insight in these processes are given in section (5.7).

Bottom friction also has an effect on the phases of physical parameters. Starting with the *C&AC* phases, when a current rotates clockwise than the phase will become more negative (from  $0^\circ$  to  $-360^\circ$ ) while for an *AC* rotating current the phases increases from  $0^\circ$  to  $360^\circ$ . This means that a more negative phase of a *C* rotating current indicates a current that is already further in its cycle. For an *AC* rotating current a more positive phase leads to a current already further in its cycle. From figure (38) it follows that towards the bottom, the *AC* phase increases which means that at the bottom a certain phase of the tidal cycle is reached earlier than at the surface. The phase of the *C* rotating current, starting halfway the column, becomes more negative towards the

bottom, again stating that a certain phase of the tidal cycle is reached earlier near the bottom than at the surface. Bottom friction causes a momentum exchange between bottom and water. This exchange acts as a sink of momentum into the bottom. As a result the velocity of the water layer above the bottom decreases, in turn decreasing the velocity of the layer above that, etc. The effect of the decrease of the current diffuses from the bottom upward. In first order it may be assumed that the forcing mechanism of the tide is dominant and therefore instantaneous at all depths, but from the measurements it can be concluded that the second order, bottom frictional effect is significant in the Marsdiep over the whole water column. This indicates the importance of the bottom friction in this area. The different phase structure close to the surface will be discussed later. The  $AC$  phase difference between the top and the bottom is about  $15^\circ$  corresponding with approximately  $(\frac{15}{360}T_{M_2} =)$  31 minutes. For the  $C$  phase difference the effects seem similar when taking the difference between the middle of the column (from which the decrease starts) and the bottom.

From figure (37) it is shown that (except for the last 4 bins) the  $AC$  amplitude is larger than the  $C$  amplitude leading to an  $AC$  rotating tidal ellipse. From figure (38) it is distracted that the phase decreases towards the bottom (more negative values). When a negative phase value is inserted into equations (58) and (59), than a more negative value results in adding a larger value. This results in a greater phase advance for  $AC$  rotating currents. Therefore a decrease of the phase towards the bottom, indicates that a certain state of the tidal cycle is reached earlier at the bottom and then propagates upward. This effect is indeed visible in the along stream and cross stream velocity. Another remarkable feature is the extreme decrease in phase of more than  $100^\circ$  of the cross stream current. The phase differences for the along stream and cross stream currents cause a delay of respectively 33 minutes and (a remarkable) 4 hours. For the along stream current this is in agreement with the  $C$  &  $AC$  phases and bottom friction may be pointed as its reason. The cross stream phase difference is extremely large and therefore, in line with the corresponding amplitudes in these directions, the large differences cannot be attributed to bottom friction (alone).

The  $PHA$  indicates the phase of the tidal ellipse at the moment that the maximum current is reached. The ellipse rotates  $AC$  in the main part of the water column, the cycle starts at  $t = 0$  and  $PHA$  is given between  $[-\pi, \pi]$ . This leads to the following conclusion: the higher (or the less negative) the  $PHA$ , the longer it takes to reach the maximum current. Applying this to the measured  $PHA$  one can conclude that, again there is a phase propagation upwards, meaning that the maximum current is reached earlier (about 25 minutes) close to the bottom than at the surface.

The  $INC$  (and thus  $SEMA$  direction) of the ellipse is very small in the beginning. The reason is that the  $INC$  is determined with respect to the along stream velocity, at the surface, which was already rotated  $27.4^\circ$  degrees with respect to the east. The  $INC$  then rotates  $10^\circ$  in  $AC$  direction towards the bottom, which is comparable with other measurements in the Marsdiep [3]. To explain the vertical structure of the  $INC$  one probably needs to know the processes, that also influence the cross stream phases and amplitudes. It seems that these cross stream processes are more pronounced in the  $INC$  than in the  $PHA$ .

#### 4.4.2 Velocity triangle parameters and effects near the surface; The wind induced effects and attachment chain interference.

Besides the possibility that bottom friction penetrates all the way to the surface, there are two other influences that determine the current at the surface. These are the effects due to the wind and due to interference of the chain that is attached between the buoy and the weight at the bottom. The chain sometimes obstructs the sound pulse of one of the ADCP beams. The chain



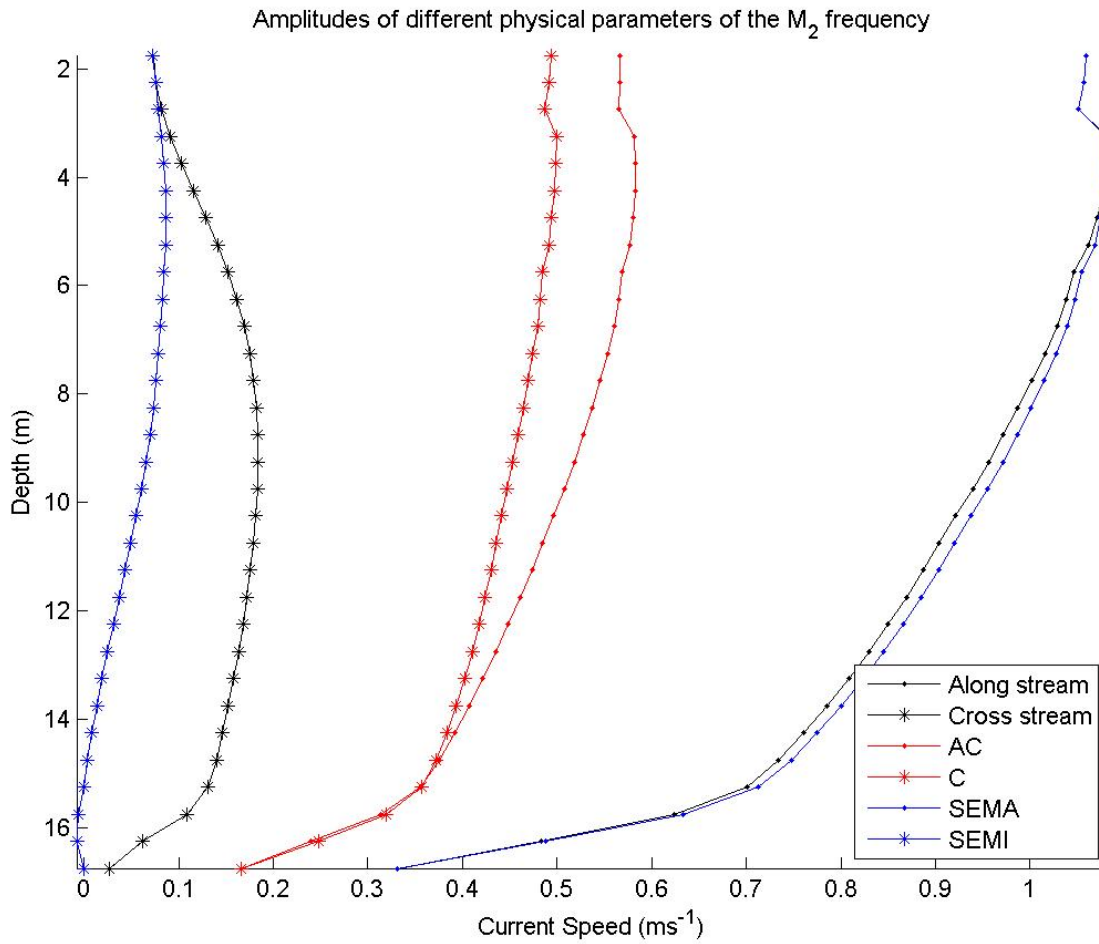


Figure 37: The amplitudes of the  $M_2$  tidal frequency of the physical parameters of the velocity triangle. These are derived from the LSHA that was performed on the measurements.

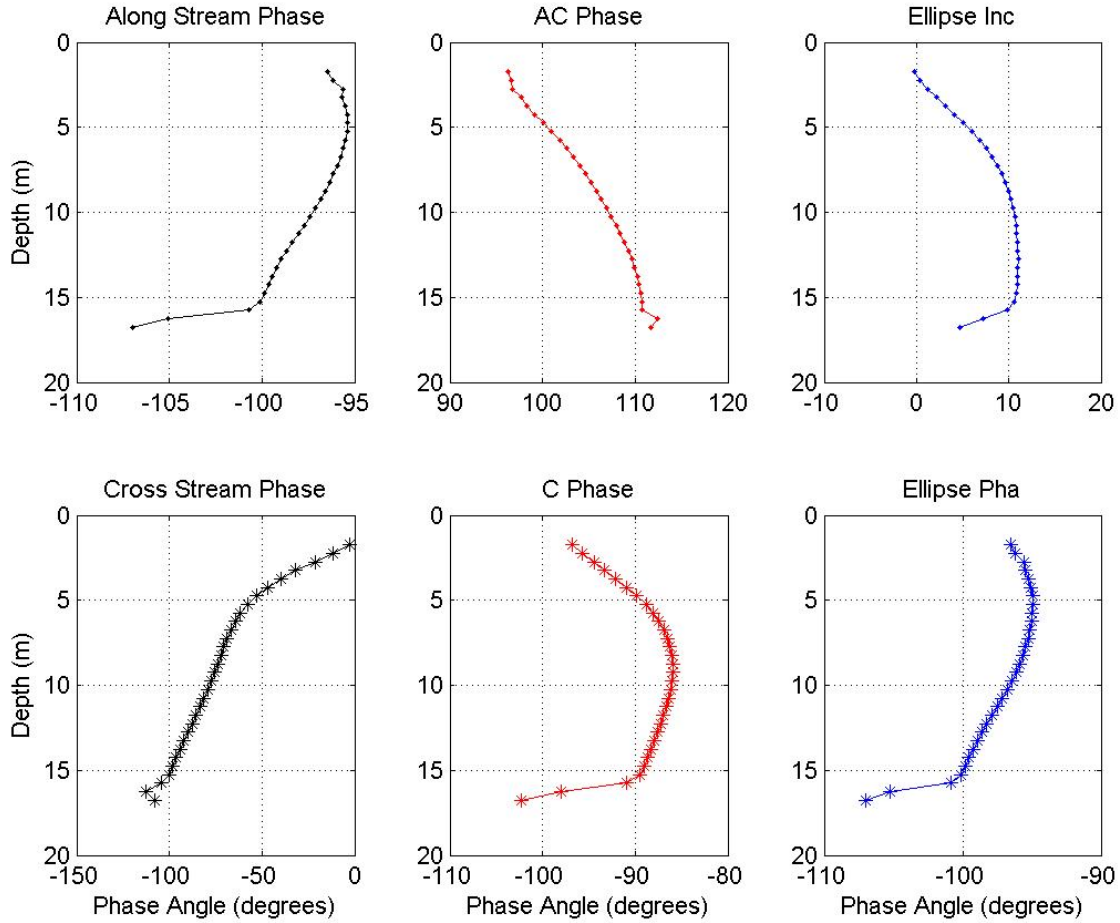


Figure 38: The phases of the  $M_2$  tidal frequency of the physical parameters of the velocity triangle. These are derived from the LSHA that was performed on the measurements.

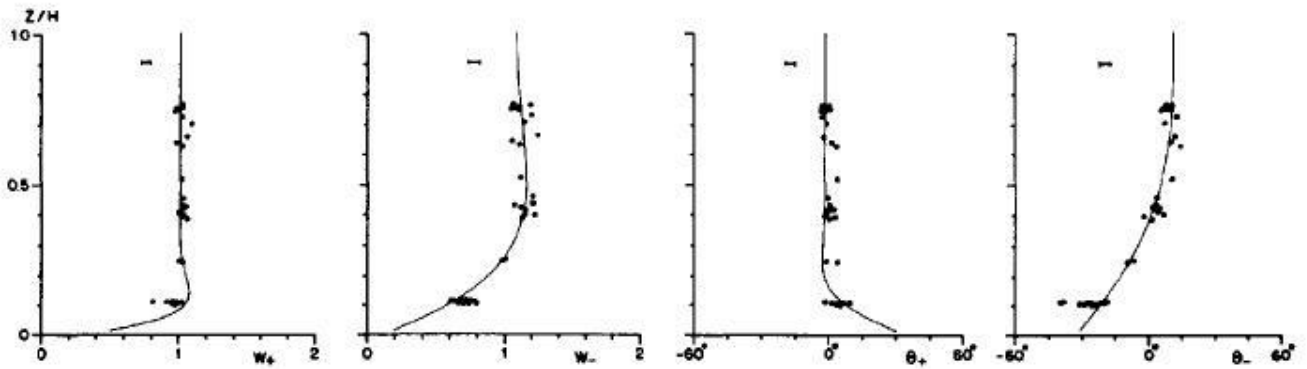


Figure 5. Observations (denoted by dots) of amplitudes  $W_{\pm}$  and phase angles  $\theta_{\pm}$  of the  $M_2$  frequency rotary current components as a function of normalized depth. Solid curves are best fit theoretical curves. Error bars are indicated at the top.

Figure 39: Modeled  $C$  &  $AC$  amplitudes and phases of the measurements done by [20] in the North Sea. This picture is copied from [20].

will move less fast than the water and therefore the ADCP calculates a lower velocity. The chain is mostly found in the third bin from the surface (see figure 26). Many of the chain detection are removed by the steps taken to increase the data quality described in section (3.4), unfortunately not all could be removed. This results in odd values, especially in the third and second bin and a little in the first bin. Taking this into account it is expected that the profile should not decrease with such large irregular steps but should gradually decrease from the value in the fourth bin towards, approximately, the value in the first bin. This means that there is still a small decrease of the current towards the surface. This can probably be explained using the effects of wind.

Wind has several effects that influence horizontal currents. These are frictional effects, inducing shear currents, wind set up causing net currents and wind waves causing high frequency oscillatory currents and Stokes transport. The wind has a broad frequency spectrum, making it possible that for every tidal frequency there is also a wind component. As a result some part of the wind may end up in the coherent signal obtained with the LSHA. The sea surface experiences this as friction with the atmosphere that will be quadratic proportional to the velocity difference between the sea surface and the atmosphere. This can induce an increased and decreases current depending on the sign of the velocity difference. The effect of friction again diffuses into the vertical causing vertical shear of the horizontal current that leads to (vertical) mixing and turbulence. This can be described by the same equation as for the bottom friction (equation 94). The difference will be that the friction coefficient will be smaller than for bottom friction leading to less shear and a lower penetration depth. During the measurements also wind data were collected on the roof of the NIOZ institute. This wind data is representative for the location of the Buoy. The data is collected every second and reduced to 5 minute averages and is represented in figure (40). The average wind during the deployment were about  $4.0 \text{ m s}^{-1}$  (3Bft) but often higher with peaks up to  $12.7 \text{ m s}^{-1}$  (6Bft), causing the wind induced shear at the surface a realistic explanation for the decrease of the velocity at the surface.

If wind is blowing for a longer time from one direction and the wind driven shear current reached a ridged boundary (such as a coast) a wind induced water set up may occur. This leads to a gradient in the SSH and therefore to a pressure gradient. A pressure gradient leads to a current that is uniform with depth. Therefore the wind set up causes a current in the opposite direction of the wind direction. This current might be visible as a net current over the whole time series over the whole depth. The last effect of the wind is the formation of surface waves. Though the currents induced by the surface waves may affect a large part of the water column, they are oscillatory with a frequency much higher than that of the tides. Therefore it is assumed that the surface waves will not have significant effect on the amplitudes and phases of the tidal frequencies. To affect the tidal amplitudes and phases one has to account for the long term effect of surface waves, like Stokes drift. If Stokes drift is at all significant it would lead to a larger magnitude of the net current and therefore possibly reducing the significance of the contributions of the tidal frequencies. In the along stream direction the decrease of amplitude towards the surface is only small and the reduction of the explained variance (or significance) due to the tidal currents is minor. In the cross stream direction the explained variance due to tidal currents does decrease significantly indicating that the effects of wind and mean current may be more significant.

As a result of chain interference and wind effects the decrease in amplitude, of the  $M_2$  frequency induced current near the surface can be explained. The frictional effect of the wind causes the currents to reach a certain phase of the tidal cycle earlier at the surface with respect to a deeper part of the column. It works in the same way as bottom friction but than from the surface downwards. This effects is clearly visible in the along stream phase, the ellipse phase and the  $C$  phase. In the  $AC$  phase the effect might be visible reducing the vertical phase gradient in the upper part.

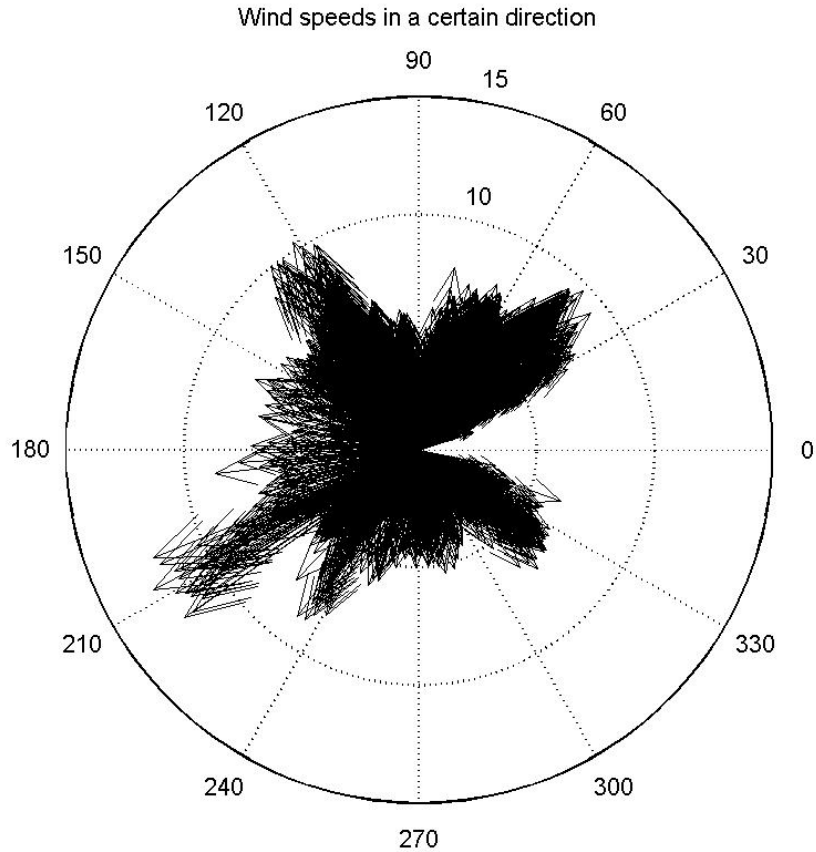


Figure 40: The measured wind direction and corresponding velocities at the roof of the NIOZ institute in the period that the buoy was deployed. In this figure  $0^\circ = \text{East}$ ,  $90^\circ = \text{North}$ ,  $180^\circ = \text{West}$  and  $270^\circ = \text{South}$ . The length of an arrow is a measure for the velocity. The dashed circles are respectively the  $5\text{ms}^{-1}$ ,  $10\text{ms}^{-1}$  and  $15\text{ms}^{-1}$  contour.

For the cross stream phase and the *INC* the effect is not clear and as explained before, different processes must be of greater importance.

#### 4.4.3 Eccentricity, mean currents and concluding notes.

The eccentricity is shown in figure (41) and is positive if the *AC* amplitude is larger than the *C* amplitude and vice versa (Equation 89). A larger *AC* amplitude (positive eccentricity) indicates an *AC* rotating ellipse. A larger *C* amplitude (negative eccentricity) indicates a *C* rotating ellipse. In almost the whole water column the current is rotating *AC*. Below  $15.25\text{m}$  depth ( $28^{\text{th}}$  bin) the eccentricity is negative, meaning the tidal ellipse rotates *C*. From the eccentricity and the explained variance by tidal frequencies in the cross stream direction it can be concluded that in the middle of the column the tides are more important determining the cross stream or SEMI velocities than close to the surface and bottom where other processes must be of equal or greater importance. Still the eccentricity is small ( $< 0.08$ ) which is in agreement with the much stronger tidal currents measured in the along stream direction.

The best fit for the measured data using the LSHA also obtained a tidal average ( $A_0$ ) and mean current ( $\bar{u}$ ) which are shown in figure (42). The mean current is the average of all the measurements at one depth. The tidal average is a small value that corrects the LSHA approximation for incomplete tidal cycles due to the sudden start and end of the measurements that, integrated over the complete time series, leave a net velocity. Therefore the tidal average is a net flow that is not induced by a physical process. The tidal average is obtained using the data set of which the mean is subtracted. Within the calculation for the average velocity the tidal average is not yet subtracted and therefore included. To obtain the net current induced by physical processes for the along stream and cross stream directions, the sum of  $\bar{u}$  and  $A_0$  has to be calculated (as explained in table 3) and is also shown in figure (42). The net along stream current obtained in this thesis is (remarkably) into the Wadden Sea. This differs from other observations showing that, averaged over the whole cross section of the Marsdiep Inlet, water leaves the Wadden Sea [31, 32, 4, 3]. The Results of [3] already showed that the net along stream current is not uniform over depth and the whole cross stream inlet and can locally be directed towards the Wadden Sea due to for example the effects of curvature, wind, density gradients and Coriolis force. The explanation for the net current directed into the Wadden Sea found in this thesis must therefore be found in these processes inducing secondary currents. These secondary currents are sometimes more pronounced in certain times of the year and therefore the short term measurements obtained in this thesis may not average out these effects relative to measurements obtained over the time span of a year, resulting in a local net current into the Wadden Sea. The net cross stream current shows great variations with depth and a circulation cell (water moving towards the left (Texel) at the surface and towards the right (Den Helder) in the middle. This might perhaps be explained by the fact that the average wind direction was *WNW*. This is more or less in the positive cross stream direction. It might therefore be possible that the positive net water transport at the surface might be induced by the wind while at other positions other mechanisms are stronger.

Using the effect of bottom friction, wind and the chain interference the along stream, *AC* and *SEMA* currents are well explained. In this direction the Marsdiep can therefore be seen as a tidal dominated area which has high currents, bottom friction and possibly significant influence of the wind. In the cross stream, *C* and *SEMI* currents all the effects are also present, but other processes are of equal or greater importance determining the vertical structure of the physical parameters. These processes are considered in more detail in section (5.7). As a result the explained variance by tides, or the coherent part of the measured signal in the along stream direction, is on average 95.6% which is much higher than that of the cross stream velocities which is, on average 71%. The vertical structure of the explained variance varies a bit for the along stream direction but varies a lot in the cross stream direction. The lower the explained variance by tidal frequencies the more important secondary (incoherent) currents, due to for example bottom, wind and coastal friction, baroclinic motion, geometry and curvature, become.

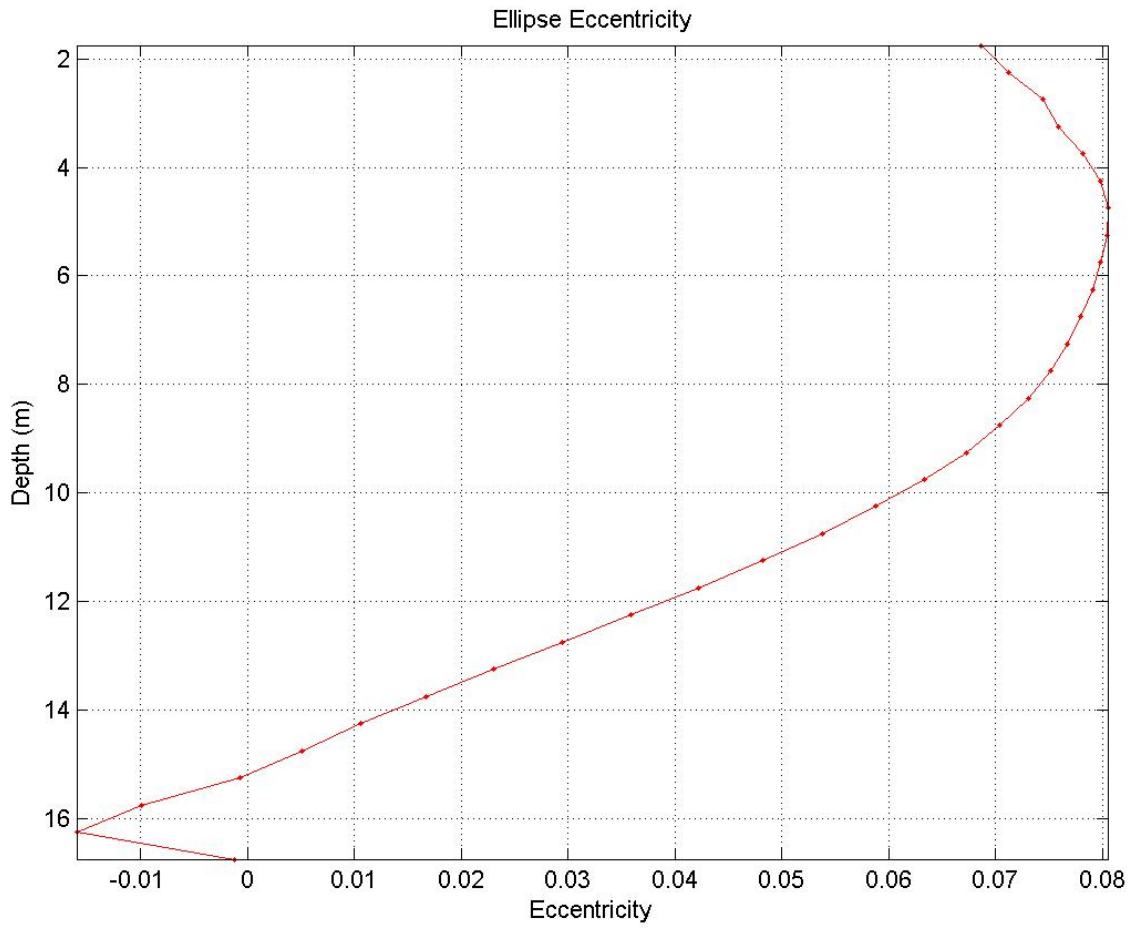


Figure 41: The eccentricity as a function of depth, calculated using the ellipse amplitudes.

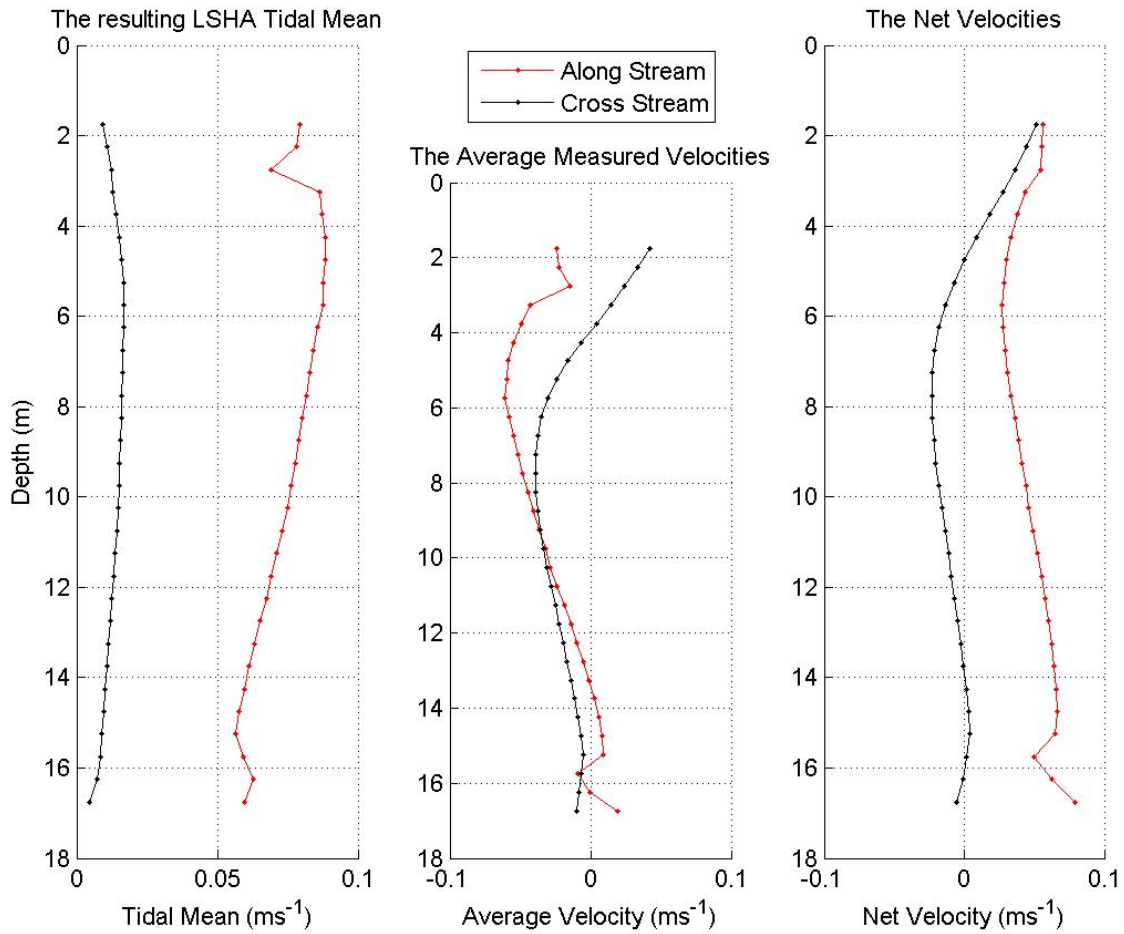


Figure 42: The average velocity of the measurements, the tidal average and the net currents as a function of depth.

## 5 Barotropic Model

The main goal of this thesis is to find events that indicate the existence of ISs in the Marsdiep. To do so, first long term measurements of the vertical structure of the horizontal and vertical velocity are made. By subtracting the coherent signal from the measurements, the incoherent currents are left which are expected to manifest the IS. The coherent current can be obtained using the results of the LSHA because the time series is long enough to be able to apply a LSHA accurately. For shorter time series, which are also available within the Marsdiep area but not yet discussed in this thesis, a LSHA cannot be performed. Still IS can be present within these measurements. To be able to find a coherent current of the shorter time series it is convenient to derive an analytical model which is capable to reproduce the coherent current within the Marsdiep area only knowing the amplitudes and phases of the most important tidal frequencies within this area at a particular depth (for example obtained with a current meter). In this section an barotropic analytical model is derived that will be forced by tides and takes into account the Coriolis and bottom frictional effects. The resulting model therefore represent the barotropic currents in the Marsdiep. Using the measurements from the buoy it is possible to fit the model to a large data series and compare the model with the LSHA results. Comparing the model with the LSHA amplitudes and phases, results in better insight in processes that are found in the coherent structure of the measurements and give insight in the (dis)advantages of the simple analytical model before applying it to other data series. In this section the analytical model is derived, fitted to measurements and discussed using the coherent signal as a reference.

### 5.1 The governing equations

From the results in section 4 it can be concluded that Marsdiep is a shallow sea where the currents are strongly influenced by bottom friction. Therefore shear dominates the whole vertical velocity profile. The governing equations are described by the linearized shallow water equations for a homogeneous fluid on the f-plane extended with a bottom friction term. Vertical shear of the along stream velocity can be expressed as:  $\frac{\partial u}{\partial z}$ . Shear causes friction between water layers and friction causes frictional stresses (or stress). The stresses are therefore related with the magnitude of the shear. A common way to express shear stress between certain water depths is as follows:  $\tau_s = \nu \frac{\partial u}{\partial z}$ . Here  $\nu$  is the eddy viscosity parameter. At different depths different stresses can occur. A difference between stresses at two depth levels causes shear in the stresses, which act as a force on a water package. The forces due to vertical shear of the shear stresses can be expressed as follows:  $F_{ss} = \frac{\partial \tau_s}{\partial z} = \frac{\partial}{\partial z} \left( \nu \frac{\partial u}{\partial z} \right)$ . This can be seen as the turbulent vertical transport of momentum due to turbulent eddies. The easiest method is to treat the vertical turbulent eddy viscosity parameter (from here on viscosity parameter or  $\nu$ ) as a constant as many authors have done [20, 30]. Because it is expected that the mixing length scales increase with the height above the bottom,  $\nu$  is expected to reduce with the height above the bottom [30]. Therefore also some research has been done using a depth depending  $\nu$  [1]. Taking into account the goal of the analytical model, to give a reasonable approximation of the barotropic current, I chose however a constant  $\nu$ . As a result the expression for shear stress in the momentum equation can be written as:  $F_{ss} = \nu \frac{\partial^2 u}{\partial z^2}$ . This way bottom friction causes dissipation of the momentum over the vertical. The larger  $\nu$ , the larger the forces due to bottom friction. Even though the measurements may suggest that there are some effects of the wind, the effects will be less than that of the bottom friction and will not be inserted in the momentum equation. This results in the following set of frictionally modified long wave equations:



$$\frac{\partial u}{\partial t} - fv = \nu \frac{\partial^2 u}{\partial z^2} - g \frac{\partial \zeta}{\partial x} \quad (95)$$

$$\frac{\partial v}{\partial t} + fu = \nu \frac{\partial^2 v}{\partial z^2} - g \frac{\partial \zeta}{\partial y} \quad (96)$$

$$\frac{\partial \zeta}{\partial t} + H \left( \frac{\partial u}{\partial x} + \frac{\partial v}{\partial y} \right) = 0 \quad (97)$$

Where  $u$  and  $v$  are the eastward and northward water velocities ( $ms^{-1}$ ),  $t$  is the time (s),  $f$  is the Coriolis parameter ( $s^{-1}$ ),  $\nu$  is the turbulent eddy viscosity ( $m^2s^{-1}$ ),  $z$  is the depth at which a water parcel is located ( $m$ ),  $g$  is the gravitational acceleration ( $ms^{-2}$ ),  $\zeta$  is the sea surface height ( $m$ ),  $x$  and  $y$  are the eastward and northward directions coordinates ( $m$ ) and  $H$  is the water depth ( $m$ ). Pretending that there are means to estimate the pressure gradient terms due to the tides, the forcing terms of the tidal currents in the Marsdiep,  $-g \frac{\partial \zeta}{\partial x}$  and  $-g \frac{\partial \zeta}{\partial y}$  are assumed to be known. Therefore it is not necessary to use equation (97) to solve this set of equations. With two unknowns and two equations this set of momentum equations can be solved using four boundary conditions. The first two boundary conditions state that  $u$  and  $v$  are influenced by bottom friction. At the bottom ( $z = -H$ ) the flow is influenced by stress that is exerted by the bottom, creating a shear flow. The stress exerted by the bottom is given, using the linearized version of the quadratic stress law:  $\tau_b = C_d |u| u \approx su$ . The stress parameter,  $s$  ( $ms^{-1}$ ), may vary between no stress conditions (slip,  $\frac{\partial u}{\partial z} = 0, s \rightarrow 0$ ) and between maximal stress conditions (stick,  $u(-H) = 0, s \rightarrow \infty$ ). During slip conditions the bottom does not exert any stress on the flow so the flow is left uninfluenced by the bottom boundary. So the higher the velocity at the bottom, the lower  $s$  will be. During stick conditions the flow is zero at the bottom. In an expression for the boundary condition at the bottom this is expressed as:

$$\left( \nu \frac{\partial u(t, -H)}{\partial z}, \nu \frac{\partial v(t, -H)}{\partial z} \right) = s(u(t, -H), v(t, -H)) \quad (98)$$

The third and fourth boundary condition state that there is no shear at the surface ( $z = 0$ ). This can be interpreted as having no wind stresses at the surface. In the Marsdiep this is a rather crude assumption because it is a windy environment. Therefore care must be taken when the barotropic model is subtracted from the measurements; residual currents are not only caused due to density gradient but also due to wind stress at the surface. The boundary conditions read:

$$\nu \frac{\partial u(t, 0)}{\partial z} = \nu \frac{\partial v(t, 0)}{\partial z} = 0 \quad (99)$$

The set of equations given by (95), (96), (98) and (99) can be solved. The result is an expression for the eastward ( $u$ ) and northward ( $v$ ) barotropic currents in the Marsdiep.

## 5.2 Rewriting the governing equations

The water is forced to move due to pressure gradients. Pressure gradients occur due to sea surface level variations. Sea surface level variations are forced by the tide which is forced by the gravitational pull of the sun and moon. If an estimation of the pressure gradient terms due to the tides can be given, than the tidal forcing at a single location in the Marsdiep can be written

as a function of time. Assuming that this is possible, the pressure gradient forcing terms in the momentum equations can be replaced by arbitrary supposedly known functions ( $f(t), g(t)$ ) of time:

$$\frac{\partial u}{\partial t} - fv = \nu \frac{\partial^2 u}{\partial z^2} + f(t) \quad (100)$$

$$\frac{\partial v}{\partial t} + fu = \nu \frac{\partial^2 v}{\partial z^2} + g(t) \quad (101)$$

Rewrite (100) by replacing the minus sign with an  $i^2$  and multiply (101) with  $i$  to obtain:

$$\frac{\partial u}{\partial t} + i^2 fv = \nu \frac{\partial^2 u}{\partial z^2} + f(t) \quad (102)$$

$$i \frac{\partial v}{\partial t} + ifu = i\nu \frac{\partial^2 v}{\partial z^2} + ig(t) \quad (103)$$

Add (102) and (103) to obtain:

$$\frac{\partial(u + iv)}{\partial t} + if(u + iv) = \nu \frac{\partial^2(u + iv)}{\partial z^2} + k(t) \quad (104)$$

With:

$$k(t) = f(t) + ig(t) \quad (105)$$

Replace  $u + iv$  by a new complex variable  $w$ , the complex velocity used to solve the set of equations. This results in:

$$\frac{\partial w}{\partial t} + ifw = \nu \frac{\partial^2 w}{\partial z^2} + k(t) \quad (106)$$

Here  $w(t, z)$  contains the eastward and northward velocities. Influences on  $w(t, z)$  are also influencing  $u(t, z)$  and  $v(t, z)$ . From this equation it is shown that changes in  $w(t, z)$  (given by  $\frac{\partial w}{\partial t}$ ) are due to:

- The Coriolis force (given by  $ifw$ )
- The bottom friction (given by  $\nu \frac{\partial^2 w}{\partial z^2}$ )
- A forcing term due to the tide (given by  $k(t)$ )

To solve this equation two boundary condition are needed. Using (98) and (99) the boundary condition again states that, at the bottom ( $z = -H$ ), there is bottom stress exerted on the flow. The second states that there are no tangential forces at the surface ( $z = 0$ ). Resulting in:

$$\frac{\partial w(t, -H)}{\partial z} = \frac{s}{\nu} w(t, -H) \quad (107)$$

$$\frac{\partial w(t, 0)}{\partial z} = 0 \quad (108)$$

The momentum equation for  $w(t, z)$ , (106), and its boundary conditions (107) and (108) now form a complete set of equations with which an expression for  $w(t, z)$  can be found. The real part of this expression is the eastward water velocity ( $u$ ). The imaginary part of this expression is the

northward water velocity ( $v$ ). The variable  $w(t, z)$  is forced by a time dependent expression, but due to the bottom friction the expression is also dependent on depth. Because the forcing is only time depending it is possible to rewrite  $w(t, z)$  into a part that only depends on time;  $w_1(t)$  and a part that depends on depth and time;  $w_2(t, z)$  resulting in:

$$w = w_1(t) + w_2(t, z) \quad (109)$$

Insert (109) into (106) to obtain:

$$\frac{\partial w_1(t)}{\partial t} + \frac{\partial w_2(t, z)}{\partial t} + ifw_1(t) + ifw_2(t, z) = \nu \frac{\partial^2 w_2(t, z)}{\partial z^2} + k(t) \quad (110)$$

This is the equation that has to be solved. When this equation is solved for  $w_1(t)$  and  $w_2(t, z)$ , they can be added up together to obtain an expression for  $w(t, z)$ .

### 5.3 Solving the governing equation

Equation (110) will be split into two separate equations. One for  $w_1(t)$  and one for  $w_2(t, z)$ . Variable  $w_1(t)$  is defined in such a way that it is only forced by the parts that only depend on time. For  $w_2(t, z)$  the forcing comes from the parts that depend on time and depth. Using the definition for  $w_1(t)$  and  $w_2(t, z)$  the following equations are obtained:

$$\frac{\partial w_1}{\partial t} + ifw_1 = k(t) \quad (111)$$

$$\frac{\partial w_2}{\partial t} + ifw_2 = \nu \frac{\partial^2 w_2}{\partial z^2} \quad (112)$$

#### 5.3.1 Finding an expression for $w_1(t)$

First an expression for  $w_1(t)$  is found by solving:

$$\frac{\partial w_1}{\partial t} + ifw_1 = k(t) \quad (113)$$

It is now assumed that  $w_1(t)$  has a solution of the following form:

$$w_1(t) = \exp(-ift)X(t) \quad (114)$$

Insert this into (113) to obtain an expression from which  $X(t)$  can be determined:

$$\exp(-ift) \frac{\partial X(t)}{\partial t} = k(t) \quad (115)$$

This can be written as:

$$\frac{\partial X(t)}{\partial t} = k(t) \exp(ift) \quad (116)$$

From this  $X(t)$  can be written as:

$$X(t) = \int_{t_0}^t k(\tau) \exp(if\tau) d\tau + X(t_0) \quad (117)$$

The solution for  $X(t)$  can be substituted back into (114) to obtain the final expression for  $w_1(t)$ :

$$w_1(t) = \exp(-ift) \left[ \int_{t_0}^t k(\tau) \exp(ift) d\tau + X(t_0) \right] \quad (118)$$

The currents due to the Coriolis force, without the influence of the forcing  $k(t)$ , are always present. This is the so called inertial oscillation. In (118) the clockwise inertial oscillation is represented by  $\exp(-ift)X(t_0)$ .

### 5.3.2 Finding an expression for $w_2(t, z)$

An expression for  $w_2(t, z)$  can be found by solving:

$$\frac{\partial w_2}{\partial t} + ifw_2 = \nu \frac{\partial^2 w_2}{\partial z^2} \quad (119)$$

This equation can be solved using separation of variables:

$$w_2(t, z) = p(t)q(z) \quad (120)$$

Insert this into (119) to find:

$$q(z) \frac{\partial p(t)}{\partial t} + ifp(t)q(z) = \nu p(t) \frac{\partial^2 q(z)}{\partial z^2} \quad (121)$$

Which can be written as:

$$\frac{1}{p} \frac{\partial p}{\partial t} + if = \frac{\nu}{q} \frac{\partial^2 q}{\partial z^2} = \lambda \quad (122)$$

Here  $\lambda$  is a complex constant that can be arbitrarily chosen and will later be determined. First a solution for  $p(t)$  and  $q(z)$  must be found and used to construct  $w_2(t, z)$ . First find the equation for  $p(t)$ :

$$\frac{1}{p} \frac{\partial p}{\partial t} + if = \lambda \quad (123)$$

The general solution for this equation is:

$$p(t) = c_2 \exp(\lambda t - ift) \quad (124)$$

The next step is to find a solution for the following equation:

$$\frac{\nu}{q} \frac{\partial^2 q}{\partial z^2} = \lambda \quad (125)$$

The general solution to this equation is:

$$q(z) = c_3 \exp\left(\sqrt{\frac{\lambda}{\nu}} z\right) + c_4 \exp\left(-\sqrt{\frac{\lambda}{\nu}} z\right) \quad (126)$$

Combining the expressions for  $p(t)$  and  $q(z)$  results in an expression for  $w_2(t, z)$ :

$$w_2(t, z) = p(t)q(z) \quad (127)$$

$$w_2(t, z) = c_2 \exp(\lambda t - i f t) \left[ c_3 \exp\left(\sqrt{\frac{\lambda}{\nu}} z\right) + c_4 \exp\left(-\sqrt{\frac{\lambda}{\nu}} z\right) \right] \quad (128)$$

Which is equal to:

$$w_2(t, z) = c_5 \exp(\lambda t - i f t + m z) + c_6 \exp(\lambda t - i f t - m z) \quad (129)$$

$$m = \sqrt{\frac{\lambda}{\nu}} \quad (130)$$

### 5.3.3 Constructing $w(t, z)$

By combining the equations obtained for  $w_1(t)$  and  $w_2(t, z)$  an expression for  $w(t, z)$  is obtained:

$$w(t, z) = \exp(-i f t) \left[ \int_{t_0}^t k(\tau) \exp(i f \tau) d\tau + X(t_0) + c_5 \exp(\lambda t + m z) + c_6 \exp(\lambda t - m z) \right] \quad (131)$$

### 5.3.4 Applying the boundary conditions to $w(t, z)$

The boundary condition given by equations (107) and (108) are used to find the unknown constants  $c_5$  and  $c_6$ . Starting with the boundary condition at the surface given by equation (108). This leaves:

$$c_5 m \exp(\lambda t) - c_6 m \exp(\lambda t) = 0 \quad (132)$$

From which it can be concluded that:

$$c_5 = c_6 \quad (133)$$

Insert this into the expression for  $w(t, z)$  to obtain:

$$w(t, z) = \exp(-i f t) \left[ \int_{t_0}^t k(\tau) \exp(i f \tau) d\tau + X(t_0) + 2c_5 \exp(\lambda t) \cosh(m z) \right] \quad (134)$$

What is left is the unknown constant  $c_5$  and complex constant  $\lambda$ . These can both be found using the second boundary condition. To do so, first the forcing term  $k(t)$  needs to be rewritten. The forcing term originates from the summation of the pressure gradients caused by tidal sea surface height variations due to different tidal components with a certain frequency. This can be written as follows:

$$k(\tau) = \sum_{n=1}^N A_n \cos(\omega_n \tau - \phi_n) = \frac{1}{2} \sum_{n=1}^N A_n e^{i(\omega_n \tau - \phi_n)} + A_n e^{i(-\omega_n \tau + \phi_n)} \quad (135)$$

Where  $A_n$  and  $\phi_n$  are the magnitude and phase of the pressure gradient term of the tidal component with frequency  $\omega_n$ . This can be rewritten in a more convenient way:

$$k(\tau) = \sum_{n=-N}^N \hat{k}_n \exp(i \omega_n \tau) \quad (136)$$

Here  $\omega_{-n} = -\omega_n$ ,  $\hat{k}_{-n} = \hat{k}_n^*$  and  $\omega_n$  are the frequencies of all the tidal components used to construct the forcing term with. When  $n = 0$  the forcing does not depend on a certain frequency ( $\omega_0 = 0$ )

and  $k_0$  is obtained. The meaning of  $k_0$  will be explained in section (5.4). Insert the forcing term into the equation for  $w(t, z)$  to obtain:

$$w(t, z) = \exp(-ift) \left[ \int_{t_0}^t \sum_{n=-N}^N \widehat{k}_n \exp(i\omega_n \tau) \exp(iff\tau) d\tau + X(t_0) + c_5 \exp(\lambda t) \cosh(mz) \right] \quad (137)$$

It is convenient to rewrite the integral term:

$$\int_{t_0}^t \sum_{n=-N}^N \widehat{k}_n \exp(i\omega_n \tau) \exp(iff\tau) d\tau \quad (138)$$

To:

$$\sum_{n=-N}^N \int_{t_0}^t \widehat{k}_n \exp((f + \omega_n)i\tau) d\tau \quad (139)$$

$$= \sum_{n=-N}^N \frac{-i\widehat{k}_n}{f + \omega_n} [\exp((f + \omega_n)it) - \exp((f + \omega_n)it_0)] \quad (140)$$

Insert this back into the expression for  $w(t, z)$  to obtain:

$$w(t, z) = \exp(-ift) \left[ \sum_{n=-N}^N \frac{-i\widehat{k}_n}{f + \omega_n} [\exp((f + \omega_n)it) - \exp((f + \omega_n)it_0)] \right] + \exp(-ift) [X(t_0) + 2c_5 \exp(\lambda t) \cosh(mz)] \quad (141)$$

Combine the expression for  $w(t, z)$  with the boundary condition at the bottom, given by equation (107) to obtain:

$$\begin{aligned} \nu m c_5 \exp(\lambda t) \sinh(-mH) &= s \sum_{n=-N}^N \frac{-i\widehat{k}_n}{f + \omega_n} [\exp(f + \omega_n)it) - \exp(f + \omega_n)it_0)] \\ &+ sX(t_0) + 2sc_5 \exp(\lambda t) \cosh(-mH) \end{aligned} \quad (142)$$

It is most convenient if the constant parts of this equation cancel out each other. Therefore the equation is split into two equations. One for the constant part and one for the time dependent part. Choosing the constant part in such a way that it cancel out each other the following equations are obtained:

$$s \sum_{n=-N}^N \frac{-i\widehat{k}_n}{f + \omega_n} \exp((f + \omega_n)it_0) = sX(t_0) \quad (143)$$

$$\sum_{n=-N}^N \frac{-i\widehat{k}_n}{f + \omega_n} \exp((f + \omega_n)it) = 2c_5 \exp(\lambda t) \left[ \frac{\nu m}{s} \sinh(-mH) - \cosh(-mH) \right] \quad (144)$$

Which can be rewritten as:

$$\sum_{n=-N}^N \frac{i\widehat{k}_n}{f + \omega_n} \exp((f + \omega_n)it) = 2c_5 \exp(\lambda t) \left[ \frac{\nu m}{s} \sinh(mH) + \cosh(mH) \right] \quad (145)$$

What is left is to determine  $c_5$  in equation (145). For each wave with a certain frequency and amplitude that originates from the Fourier transform of  $k(t)$  on the left hand side of equation (145), a wave with the same phase and amplitude on the right hand side must be constructed to be able to compare both sides of the equation and find a solution for equation (145). This leads to the following discretisation of the right hand side of equation (145):

$$2c_5 \exp(\lambda t) \left[ \frac{\nu m}{s} \sinh(mH) + \cosh(mH) \right] = \sum_{n=-N}^N D_n \exp(\lambda_n t) \quad (146)$$

Define:

$$D_n = 2c_5 \left[ \frac{\nu m}{s} \sinh(mH) + \cosh(mH) \right] \quad (147)$$

Replace parts of equation (145) with  $D_n$  to obtain:

$$\sum_{n=-N}^N \frac{i\hat{k}_n}{f + \omega_n} \exp((f + \omega_n)it) = \sum_{n=-N}^N D_n \exp(\lambda_n t) \quad (148)$$

This can only be true if:

$$D_n = \frac{i\hat{k}_n}{f + \omega_n} \quad (149)$$

$$\lambda_n = i(f + \omega_n) \quad (150)$$

This results in two expressions for  $D_n$  which are equations (147) and (149) and can be combined to find an expression for  $c_5$ :

$$c_5 = \frac{D_n}{2 \left[ \frac{\nu m_n}{s} \sinh(m_n H) + \cosh(m_n H) \right]} = \frac{i\hat{k}_n}{2(f + \omega_n) \left[ \frac{\nu m_n}{s} \sinh(m_n H) + \cosh(m_n H) \right]} \quad (151)$$

Insert all the above back into expression (141) for  $w(t, z)$  to obtain:

$$w(t, z) = - \sum_{n=-N}^N \frac{i\hat{k}_n}{f + \omega_n} \exp(i\omega_n t) \left[ 1 - \frac{\cosh(m_n z)}{\frac{\nu m_n}{s} \sinh(m_n H) + \cosh(m_n H)} \right] \quad (152)$$

with:

$$m_n = \sqrt{\frac{\lambda_n}{\nu}} = \sqrt{i \frac{f + \omega_n}{\nu}} \quad (153)$$

From equation (152) it can be concluded that inserting slip conditions ( $s \rightarrow 0$ ) causes viscous effects to vanish. Inserting stick conditions: ( $s \rightarrow \infty$ ) causes the viscous effects to be of significant influence.

## 5.4 Determining the forcing term

In section (5.3) a nice expression for  $w(t, z)$  is constructed. Still, in this expression, not all factors are yet known. The factor  $\hat{k}_n$  is not determined. To be able to determine this factor it is necessary to reconsider the forcing term  $k(t)$ . Using equations (102),(103) and (105) the following expression can be constructed:

$$k(t) = f(t) + ig(t) = -g\frac{\partial\zeta}{\partial x} - ig\frac{\partial\zeta}{\partial y} \quad (154)$$

The terms  $-g\frac{\partial\zeta}{\partial x}$  and  $-g\frac{\partial\zeta}{\partial y}$  contain the horizontal pressure gradient caused by the sea surface variations. These are not known. The variations of the water speed in the horizontal directions are known far above the bottom, where frictional influences are small. Therefore the pressure gradient forcing terms are expressed as follows:

$$-g\frac{\partial\zeta}{\partial x} = \frac{\partial u}{\partial t} - fv \quad (155)$$

$$-g\frac{\partial\zeta}{\partial y} = \frac{\partial v}{\partial t} + fu \quad (156)$$

Which are the equations describing the motion of the water forced by sea level variations, without the effect of bottom friction. Therefore it represents the free motion of the water far from the bottom where the friction effects are of minor influence. For  $u$  and  $v$  the predicted values, using astronomical tidal components, are given by:

$$u(t) = \sum_{n=1}^N a_n \cos(\omega_n t - \alpha_n) \quad (157)$$

$$v(t) = \sum_{n=1}^N b_n \cos(\omega_n t - \beta_n) \quad (158)$$

Where  $a_n, b_n, \alpha_n$  and  $\beta_n$  are the amplitudes and phases of the different tidal components in the eastward and northward directions. This is inserted into (155) and (156) to obtain:

$$-g\frac{\partial\zeta}{\partial x} = \sum_{n=1}^N -a_n\omega \sin(\omega_n t - \alpha_n) - fb_n \cos(\omega_n t - \beta_n) \quad (159)$$

$$-g\frac{\partial\zeta}{\partial y} = \sum_{n=1}^N -b_n\omega \sin(\omega_n t - \beta_n) + fa_n \cos(\omega_n t - \alpha_n) \quad (160)$$

Insert this equation into the equation for  $k(t)$  to find:

$$k(t) = \sum_{n=1}^N -a_n\omega \sin(\omega_n t - \alpha_n) - fb_n \cos(\omega_n t - \beta_n) - ib_n\omega \sin(\omega_n t - \beta_n) + ifa_n \cos(\omega_n t - \alpha_n) \quad (161)$$

This can be rewritten in the following form:

$$k(t) = k_1 e^{i\omega_n t} + k_2 e^{-i\omega_n t} \quad (162)$$

The expression for  $k_1$  is found as follows:



$$k_1 = \frac{1}{2} \left[ \omega_n a_n i e^{-i\alpha_n} - f b_n e^{-i\beta_n} - \omega_n b_n e^{-i\beta_n} + i f a_n e^{-i\alpha_n} \right] \quad (163)$$

$$k_1 = i \frac{1}{2} \left[ \omega_n a_n e^{-i\alpha_n} + i f b_n e^{-i\beta_n} + i \omega_n b_n e^{-i\beta_n} + f a_n e^{-i\alpha_n} \right] \quad (164)$$

$$k_1 = i \frac{1}{2} \left[ a_n e^{-i\alpha_n} (f + \omega_n) + i b_n e^{-i\beta_n} (f + \omega_n) \right] = i \frac{1}{2} (a_n e^{-i\alpha_n} + i b_n e^{-i\beta_n}) (f + \omega_n) \quad (165)$$

And the expression for  $k_2$  is found in the same way:

$$k_2 = \frac{1}{2} \left[ -\omega_n a_n i e^{i\alpha_n} - f b_n e^{i\beta_n} + \omega_n b_n e^{i\beta_n} + i f a_n e^{i\alpha_n} \right] \quad (166)$$

$$k_2 = i \frac{1}{2} \left[ -\omega_n a_n e^{i\alpha_n} + i f b_n e^{i\beta_n} - i \omega_n b_n e^{i\beta_n} + f a_n e^{i\alpha_n} \right] \quad (167)$$

$$k_2 = i \frac{1}{2} \left[ a_n e^{i\alpha_n} (f - \omega_n) + i b_n e^{i\beta_n} (f - \omega_n) \right] = i \frac{1}{2} (a_n e^{i\alpha_n} + i b_n e^{i\beta_n}) (f - \omega_n) \quad (168)$$

Insert  $k_1$  and  $k_2$  back into equation (162) to obtain:

$$k(t) = i \frac{1}{2} \sum_{n=1}^N (a_n e^{-i\alpha_n} + i b_n e^{-i\beta_n}) (f + \omega_n) e^{i\omega_n t} + (a_n e^{i\alpha_n} + i b_n e^{i\beta_n}) (f - \omega_n) e^{-i\omega_n t} \quad (169)$$

Before proceeding first define the following input parameters:

$$a_n e^{-i\alpha_n} = A_n \quad (170)$$

$$b_n e^{-i\beta_n} = B_n \quad (171)$$

$$a_n e^{i\alpha_n} = A_n^* = A_{-n} \quad (172)$$

$$b_n e^{i\beta_n} = B_n^* = B_{-n} \quad (173)$$

$$\omega_{-n} = -\omega_n \quad (174)$$

Insert the above into equation (169) to obtain:

$$k(t) = i \frac{1}{2} \sum_{n=1}^N (A_n + i B_n) (f + \omega_n) e^{i\omega_n t} + (A_n^* + i B_n^*) (f - \omega_n) e^{-i\omega_n t} \quad (175)$$

Which is equal to:

$$k(t) = i \frac{1}{2} \sum_{n=1}^N (A_n + i B_n) (f + \omega_n) e^{i\omega_n t} + \sum_{n=-1}^{-N} (A_n + i B_n) (f + \omega_n) e^{i\omega_n t} \quad (176)$$

$$k(t) = i\frac{1}{2} \sum_{n=-N}^N (A_n + iB_n)(f + \omega_n)e^{i\omega_n t} \quad (177)$$

Combine this with equation (136) to find an expression for  $\hat{k}_n$ :

$$\hat{k}_n = \frac{1}{2}i(f + \omega_n)[A_n + iB_n] \quad (178)$$

Inserting this back into (152) to obtain a new equation for  $w(t, z)$ :

$$w(t, z) = \frac{1}{2} \sum_{n=-N}^N [A_n + iB_n] \left[ 1 - \frac{\cosh(m_n z)}{\frac{\nu m_n}{s} \sinh(m_n H) + \cosh(m_n H)} \right] \exp(i\omega_n t) \quad (179)$$

For convenience this can be rewritten as:

$$w(t, z) = \frac{1}{2} \sum_{n=-N}^N [A_n + iB_n] g_n(z) \exp(i\omega_n t) \quad (180)$$

As one can conclude the complex current  $w$  is forced by the pressure gradient due to tidal SSH variations. For each single tidal component this is translated into amplitudes and phases resulting in water velocities. These amplitudes and phases are known from performing LSHA on the data. The LSHA are performed on the along stream and cross stream data. So the result of the barotropic model will also be along stream and cross stream data. For the derivations it does not matter. Therefore the amplitudes and phases obtained from the LSHA on the along stream and cross stream velocities are used as input for the barotropic model. The expression obtained for  $n = 0$  is exceptional and causes a current for the same reasons as  $A_0$  and  $B_0$  in section (4.1) causes a current, therefore  $\omega_0 = 0$  and  $A_0$  and  $B_0$  are as in expression (36). Note that this part of the current is not part of the cosine of equation (135) and isn't multiplied by a factor half.

#### 5.4.1 Scaling with the input amplitude and obtaining the final expression

The input for equation (180) comes from LSHA amplitudes and phases of a certain depth level. The output amplitudes of the model at that particular depth level must be equal to the input amplitudes at that depth. This can easily be done by scaling the depth dependent part of equation (180) with the value of the depth dependent part at the depth at which the amplitudes are found ( $z_0$ ). This results in the following expression for  $w(t, z)$ :

$$w(t, z) = \frac{1}{2} \sum_{n=-N}^N [A_n + iB_n] \frac{g_n(z)}{g_n(z_0)} \exp(i\omega_n t) \quad (181)$$

Where  $z_0$  is the depth at which the input amplitudes are given, resulting in:

$$w(t, z) = \frac{1}{2} \sum_{n=-N}^N [A_n + iB_n] \left[ \frac{\frac{\nu m_n}{s} \sinh(m_n H) + \cosh(m_n H) - \cosh(m_n z)}{\frac{\nu m_n}{s} \sinh(m_n H) + \cosh(m_n H) - \cosh(m_n z_0)} \right] \exp(i\omega_n t) \quad (182)$$

## 5.5 Rewriting the model to obtain the clockwise and anti-clockwise phases and amplitudes

Equation (181) is an expression from which the along stream and cross stream currents can be extracted. As explained in section (4) it is convenient to rewrite the results in terms of *C&AC* rotating velocity components. This can be obtained by rewriting equation (181) to:

$$w(t, z) = W_0 + \frac{1}{2} \sum_{n=1}^N W_n \exp(i\omega_n t) + \frac{1}{2} \sum_{n=-1}^{-N} W_n \exp(i\omega_n t) \quad (183)$$

Where  $W_0$  is given by:

$$W_0 = (A_0 + iB_0) \left[ \frac{\frac{\nu m_0}{s} \sinh(m_0 H) + \cosh(m_0 H) - \cosh(m_0 z)}{\frac{\nu m_0}{s} \sinh(m_0 H) + \cosh(m_0 H) - \cosh(m_0 z_0)} \right] \quad (184)$$

in which  $A_0$  and  $B_0$  are gained from the LSHA and  $m_0 = \sqrt{i \frac{f}{\nu}}$ . Respectively the real and imaginary part of equation (184) gives the along stream and cross stream tidal average with depth. the real and imaginary part of equation (182) gives the along stream velocity  $\check{u}$  and cross stream velocity  $\check{v}$ . Rewriting this in *C&AC* velocities leads to:

$$w(t, z) = W_0 + \sum_{n=1}^N [W_n^{ac} \exp(i\omega_n t) + W_n^c \exp(-i\omega_n t)] \quad (185)$$

Where:

$$W_n^{ac} = \frac{1}{2} [A_n + iB_n] \left[ \frac{\frac{\nu m_n^+}{s} \sinh(m_n^+ H) + \cosh(m_n^+ H) - \cosh(m_n^+ z)}{\frac{\nu m_n^+}{s} \sinh(m_n^+ H) + \cosh(m_n^+ H) - \cosh(m_n^+ z_0)} \right] \quad (186)$$

$$W_n^c = \frac{1}{2} [A_n^* + iB_n^*] \left[ \frac{\frac{\nu m_n^-}{s} \sinh(m_n^- H) + \cosh(m_n^- H) - \cosh(m_n^- z)}{\frac{\nu m_n^-}{s} \sinh(m_n^- H) + \cosh(m_n^- H) - \cosh(m_n^- z_0)} \right] \quad (187)$$

Define:

$$m_n^\pm = \sqrt{i \frac{f \pm \omega_n}{\nu}} \quad (188)$$

This results in a *C* rotating part ( $\exp(-i\omega_n t)$ ) and *AC* rotating part ( $\exp(i\omega_n t)$ ). Each has a complex amplitude  $W_n^{ac}$  and  $W_n^c$ . With these expressions it is possible to find the *C* and *AC* phases and amplitudes. This can be done by rewriting the complex (constant) amplitudes  $W_n^{ac}$  and  $W_n^c$  as follows:

$$W_n^{ac} = U_n^{ac} \exp(i\theta_n^{ac}) \quad (189)$$

$$W_n^c = U_n^c \exp(i\theta_n^c) \quad (190)$$

Which leaves four equations and four unknowns:

$$\Re(W_n^{ac}) = U_n^{ac} \cos(\theta_n^{ac}) \quad (191)$$

$$\Im(W_n^{ac}) = U_n^{ac} \sin(\theta_n^{ac}) \quad (192)$$

$$\Re(W_n^c) = U_n^c \cos(\theta_n^c) \quad (193)$$

$$\Im(W_n^c) = U_n^c \sin(\theta_n^c) \quad (194)$$

From which the following expressions can be deduced:

$$U_n^{ac} = \sqrt{\Re(W_n^{ac})^2 + \Im(W_n^{ac})^2} \quad (195)$$

$$U_n^c = \sqrt{\Re(W_n^c)^2 + \Im(W_n^c)^2} \quad (196)$$

$$\theta_n^{ac} = \arctan\left(\frac{\Im(W_n^{ac})}{\Re(W_n^{ac})}\right) \quad (197)$$

$$\theta_n^c = \arctan\left(\frac{\Im(W_n^c)}{\Re(W_n^c)}\right) \quad (198)$$

## 5.6 Fitting the model with the measurements.

### 5.6.1 Combining the model with the measurements

The calculations above have now led to a model which is capable of predicting the currents caused by the combination of different tidal frequencies. If one knows the horizontal velocity amplitudes and phases of the tidal frequencies at a certain depth, than the whole vertical velocity structure can be calculated taking into account the Coriolis effect and bottom friction. To do so the following input is necessary:

- Time ( $t$ ) in  $s$ .
- Distance ( $z < 0$ ) from the sea surface( $z = 0$ ) in  $m$ .
- Local depth ( $H$ ) in  $m$ .
- The frequencies of the tidal components ( $\omega_n$ ) in  $rads^{-1}$ .
- LSHA Amplitudes of the along stream ( $U$ ) and cross stream ( $V$ ) currents, in  $ms^{-1}$ .
- LSHA Phases of the along stream( $\theta_u$ ) and cross stream ( $\theta_v$ ) currents, in  $rad$ .
- Tidal averages of the along stream( $A_0$ ) and cross stream ( $B_0$ ) currents, in  $ms^{-1}$ .
- The input depth ( $z_0$ ) at which the amplitudes and phases are gained from.
- The fit parameter for the slip ( $s$ ) in  $ms^{-1}$
- The fit parameter for the turbulent eddy viscosity ( $\nu$ ) in  $m^2s^{-1}$ .

One may assume that all input is known expect for the fit parameters  $s$  and  $\nu$ . The resulting values for the fit parameters  $s$  and  $\nu$  depend on the depth ( $z_0$ ) from which the LSHA amplitudes and phases are used. The process of finding the optimal input depth and resulting best fit parameters is described in section 5.6.2. It must first be decided to what the model must be compared and therefore fitted. Using the results of the discussion given in section (4.4) the lowest two bins will be completely rejected. The reason for this can be explained using the parameterization of the bottom friction in the model. The analytical model has a constant turbulent eddy viscosity parameter which will result in a overall friction coefficient. Because it is expected that the mixing length scales increase with the height above the bottom the friction coefficient is expected to reduce with the height above the bottom [30]. An overall friction coefficient would therefore cause an underestimation of the friction effect close to the bottom and an overestimation of the friction effect far from the bottom. To reduce this effects it is chosen to reject the last two bins. This is a quick and rough solution for this problem, but allowed because it does not interfere with the main goal of this thesis; to find IS in the baroclinic signal. The IS are not expected to be most pronounced close to the bottom but in the middle of the column. By rejecting the lowest bins this does not endanger the search for IS. It is expected that as a result the friction coefficient will change in such a way that there is less underestimation near the bottom and less overestimation near the surface. The depth will be determined at  $H = 15.75m$  ( $=29^{th}$  bin). As a result everything beneath this depth is treated as a turbulent layer, which can be interpreted as a nonzero velocity at the 'bottom', leading to a higher slip parameter. It would also be convenient to reject the first three bins close to the surface because of the influence of wind and chain interference, but these data might contain information which is necessary to find the IS and are therefore not rejected and included in the model. As a result the model calculated the velocity profile for a depth of  $1.75m$  to  $15.75m$  beneath the surface.

### 5.6.2 Method to fit $\nu$ and $s$

For a certain  $z_0$  the best fit values can be obtained. Using a least squares technique is not an analytical option because it result in multiplications of the original function with its derivative with nonlinear unsolvable terms as a result. It might be possible using methods developed by for example [29], but for now simpler possibilities are explored first. Another option would be to choose a lot of combinations of  $s$  and  $\nu$  parameters and calculate the difference between the resulting model and measurements and use the combination for which the difference is smallest. Due to the size of the data set and computational power limits this is not possible for the whole data set. It could be done for a part of the data set, but this is not the chosen method either because long term effects are not incorporated in that way. For this particular data set I choose a wide range of combinations for  $s$  and  $\nu$  and computer fit them to the measurements using only the computed  $C\&AC$  phases and amplitudes of the LSHA of the data and of the model. The current vector for both the  $C\&AC$  phases and amplitudes can be decomposed in a real and imaginary part. By subtracting the real and imaginary parts for the  $C\&AC$  current vector calculated using the model from the measured  $C\&AC$  current vector, one obtains the difference. The difference is then squared and by summing the results for the real and imaginary parts, for each depth and different tidal frequency one obtains a measure for the difference between the model and measurements for a certain combination of the  $s$  and  $\nu$  fitting parameters. Taking into account the odd values of the first three bins (which are excluded in this fit), this method results in the following equation:

$$\begin{aligned} \sigma_{z_0}^2 = & \sum_{n=1}^N \sum_{l=1}^{29} \left[ \left[ U_{nl}^c \cos(\phi_{nl}^c) - U_{nl,M}^c \cos(\phi_{nl,M}^c) \right]^2 + \left[ U_{nl}^c \sin(\phi_{nl}^c) - U_{nl,M}^c \sin(\phi_{nl,M}^c) \right]^2 \right] \\ & + \sum_{n=1}^N \sum_{l=1}^{29} \left[ \left[ U_{nl}^{ac} \cos(\phi_{nl}^{ac}) - U_{nl,M}^{ac} \cos(\phi_{nl,M}^{ac}) \right]^2 + \left[ U_{nl}^{ac} \sin(\phi_{nl}^{ac}) - U_{nl,M}^{ac} \sin(\phi_{nl,M}^{ac}) \right]^2 \right] \end{aligned} \quad (199)$$

Here  $N$  is the amount of tidal frequencies obtained using the LSHA, capital  $M$  indicates amplitudes and phases from the model and  $\sigma_{z_0}$  is a value in  $ms^{-1}$  indicating the difference between the measured and predicted values for input depth  $z_0$ . Using equation (199), it is important to choose the right combinations for the  $s$  and  $\nu$  values. As a start a wide range between  $10^2$  and  $10^{-4}$  is used as input to obtain different combinations for the fit parameters. Between each adjacent order of magnitude steps of  $\frac{1}{10}$  of the smallest order of magnitude value are taken, leading to 91 steps between two adjacent orders of magnitude. The combination of twice, 6 order of magnitudes, leads to  $(6 * 91)^2 = 298116$  combinations of  $s$  and  $\nu$  parameters. From the calculated  $\sigma_{z_0}^2$ , a minimum is obtained for a certain combination of the fit parameters, which are given by  $s_1$  and  $\nu_1$ . This combination is used to construct another set of combinations that runs from  $\frac{1}{2}s_1$  to  $\frac{3}{2}s_1$  with steps of  $\frac{s_1}{300}$ . Exactly the same is done for the  $\nu$  values resulting in another 90601 combinations. This process is repeated for all 29 depth levels.

Concluding; at each depth there are amplitudes and phases available that are obtained with the LSHA. This is a result of using an ADCP, because it measures the whole water column. As input for the model only one set of amplitudes and phases is necessary. For this set, best fit values for the fit parameters  $s$  and  $\nu$  are obtained. Having the opportunity to use amplitudes and phases of different depths result in another possibility to optimize the model. By calculating best fit values for  $s$  and  $\nu$  for each given set of amplitudes and phases and then choose the input depth level and corresponding  $s$  and  $\nu$  values for which the  $\sigma_{z_0}^2$  value is minimal. The results of this method are shown in figure (43) and method resulted in  $z_0 = 6.25m$  ( $= 10^{th}$  bin) with a slip parameter of  $s = 1.3 * 10^{-3}ms^{-1}$  and an eddy viscosity parameter of  $\nu = 1.37 * 10^{-2}m^2s$ . Note that for data sets that are too short to perform a LSHA to, this method is not qualified because the  $C\&AC$  phases and amplitudes cannot be obtained for the measurements. The model will have to be fitted in a different way, for example using the method of [29] or using the complete data set, which should than be shorter and therefore less memory absorbing. The obtained values for  $s$  and  $\nu$  can be compared with earlier work in the North Sea where values of  $s_{NS} = 2.9 * 10^{-4}ms^{-1}$  and  $\nu_{NS} = 1.4 * 10^{-3}m^2s$  are obtained [20]. The difference between their and our values is explainable. Their value for the slip parameter is lower because their velocity at the 'bottom' is lower. In this thesis the 'bottom' was chosen higher above the actual bottom leading to higher velocities at the chosen depth for the bottom leading to more slip and thus a higher velocity for  $s$ . Also the frictional effects in the North Sea are much lower than in the Wadden Sea leading to a lower value for the viscosity parameter in the North Sea.

## 5.7 Comparing the coherent velocity with the barotropic model

By inserting the obtained values for  $s$  and  $\nu$  for LSHA amplitudes and phases input depth  $z_0 = 6.25m$  in equation (182), the time dependent barotropic velocity and corresponding amplitudes and phases can be calculated. Using the  $C\&AC$  phases and amplitudes obtained with the model all other physical parameters can be calculated. In the remaining of this section the results of the model will be compared with the results of the LSHA or coherent signal.

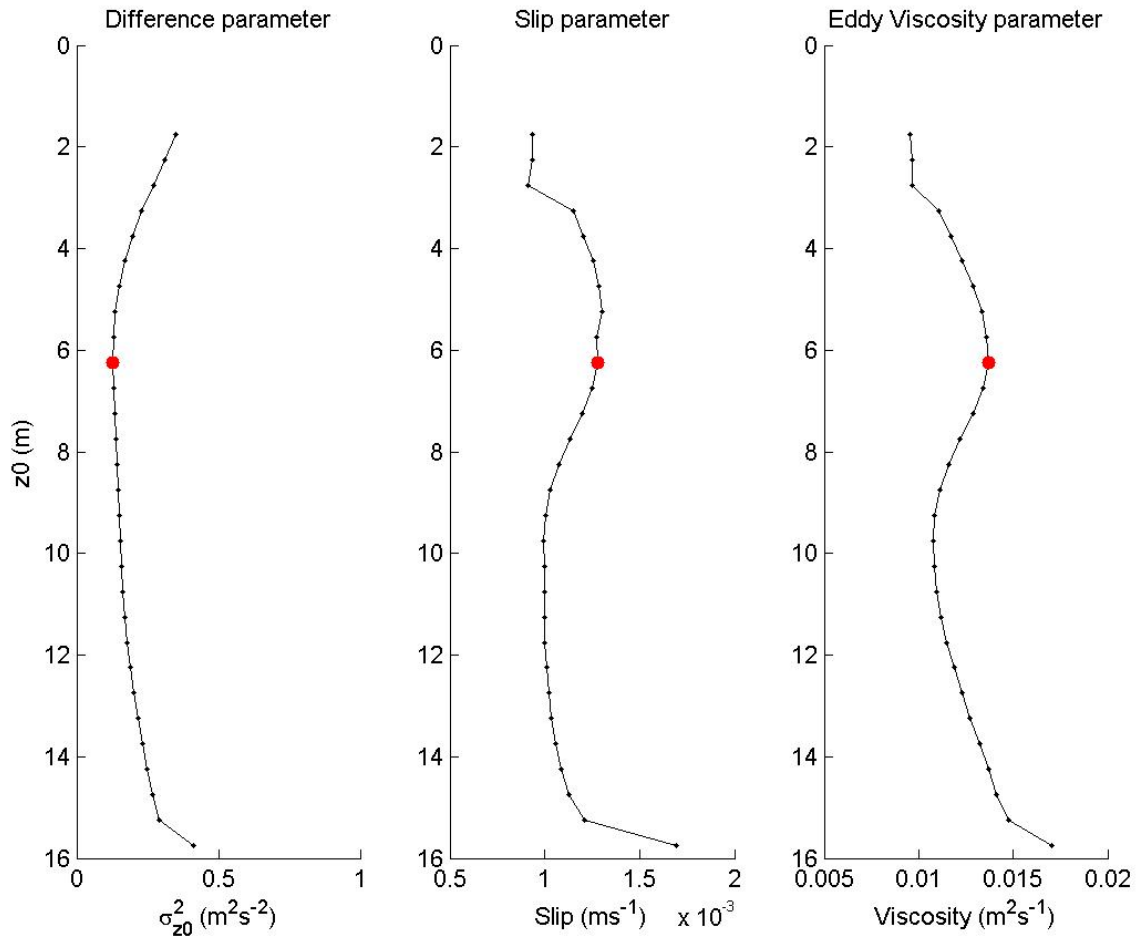


Figure 43: The left panel shows the minimum  $\sigma_{z_0}^2$  values for each  $z_0$ . The red dot indicates the minimum value. The middle and right panel are the corresponding best fit values for respectively  $s$  and  $\nu$ . The red dots are the values used for  $z_0 = 6.25\text{m}$  ( $=10^{\text{th}}$  bin).

### 5.7.1 The cross stream phase

The amplitudes and phases for all physical parameters obtained from the measurements and the model are given in figures (44) and (45) respectively. It is most convenient to start with the largest observed difference between the model and the measurements, which is the difference between the modeled and measured cross stream phase. The enormous phase difference between the bottom and the surface in the along stream direction was already noted in section (4.4). Though the differences are not exactly  $180^\circ$  the major phase lag does indicate a cross stream circulation cell with flows in opposite directions at surface and bottom. The modeled phase lag is only about  $10^\circ$  degrees which can easily be explained using the phase lag expected due to bottom friction. As a result it must be concluded that other processes than bottom friction play an important role determining the cross stream current and therefore phases and amplitudes.

Using a numerical and idealized analytical model describing tidal and residual flow in a cross section of weakly nonlinear tidally dominated estuaries, [34] showed that cross stream circulation cells as obtained are the result of the Coriolis deflection of the along stream current. This is only possible if there are boundaries, as in a coast or channel side wall. The deflected current will be blocked, as a result of continuity this leads to a set up which causes a uniform current away from the boundary. The Coriolis force is not uniform over depth (due to decreasing current towards the bottom) and therefore at the surface where the Coriolis force is strongest there will be a current towards the boundary and at the bottom there will be a current away from the boundary so that continuity is satisfied. The cross stream circulation cell due to Coriolis deflection of the along stream current can therefore only be modeled if a finite channel width is included in the model. The barotropic model in this thesis does not take this into account so that this might be the main reason for difference between the measured coherent signal and the model. All processes at tidal frequencies that cause a current in the along stream direction will result in a circulation cell due to Coriolis deflection. Several examples of processes driving these currents at the location of measurement are the different tidal species, along channel density gradients, wind, discharge and tidal rectification. Tidal rectification is a process by which a current results from advection of along channel tidal momentum by transverse tidal currents [15]. Taking into account that the cross stream current is bounded by sidewalls also processes like cross stream density gradients and wind and curvature can cause cross stream circulation cells. Some of the processes above will be coherent with tidal frequencies and some will not. Not all will cause circulation cells in the same direction causing partial cancelation of currents. Still it is concluded that all effects above will cause a circulation cell of which a part is coherent with the  $M_2$  tidal frequency. As a result these effects are found in the resulting LSHA amplitudes and phases and not in the model because it does not include a finite channel width, curvature and baroclinic processes. The effects discussed above are mainly visible in the cross stream and clockwise phases because in the along stream direction there is no Coriolis deflection and the tidal currents are too dominant.

To give an argument for the possible processes explained above it is interesting to see if the phase difference between the surface and the bottom is the same over the time series or changes due to temporal processes. By comparing the changes in the vertical phase difference with possible discharge and currents strength (spring-neap cycle) some conclusion may be drawn concerning the initiation of the cross stream circulation cells due to Coriolis deflection or baroclinic currents that might be coherent with the  $M_2$  tidal frequency. This can be done by first selecting a time span starting from the first measurement ( $t_0$ ) to exactly 4 periods of the  $M_2$  tidal frequency ( $[t_0, t = 4T_{M_2}]$ ). Perform a LSHA over this period and calculate the cross stream phase difference between the first and the 29<sup>th</sup> bin (at 1.75m and 15.75m depth). Then shift the time span exactly



one tidal cycle ( $[t = T_{M_2}, t = 5T_{M_2}]$ ) and perform the LSHA and calculate the cross stream phase difference again, etc. This way a running mean tidal phase difference (between surface and bottom) is obtained and the effect of temporal coherent signals can be seen. The results are given in figure (46) together with the current strength and discharge data of that same period. Note that full and new moon, were on respectively 9 and 25 April 2009. Related spring currents arrive two days later in the Netherlands on 11 and 27 April. Last quarter was on 17 April and the related neap currents were at 19 April. From this it can be deduced that over this period the phase difference differs between  $60^\circ$  and  $170^\circ$ . The along stream phase difference changes between  $-2^\circ$  and  $10^\circ$ , which is much smaller. Still it is interesting that the along stream phase difference is largest during spring tides which indicates the increased bottom friction effect due to higher currents and the resulting increased phase propagation from the bottom towards the surface.

The cross stream circulation cells due to the Coriolis deflection are expected to be largest during spring tides and lowest during neap tides. This is not observed. On the contrary, during neap tides the phase differences are largest. An increase in fresh water discharged from Lake IJssel and a decrease in tidal mixing strength (related to along stream tidal amplitudes) will result in cross stream and along stream density gradients resulting in baroclinic motions. Though the exact processes at the location of the deployment are hard to predict this does indicate that large discharge events lead to baroclinic motions that are temporarily (as long as there is enough discharge) coherent with the tidal frequencies. Parts of these event might be captured when performing a LSHA over the whole time series. Even though sometimes these events might be dominant all their effects discussed above will probably be present leading to a mix of processes that might explain the observed cross stream phase difference between the bottom and the surface.

### 5.7.2 All physical parameters and concluding notes

In the analytical barotropic model the bottom friction effects are partly parameterized and therefore not accurately represented at each depth. Because it is chosen to use a constant turbulent eddy viscosity parameter it can be interpreted as an average turbulent eddy viscosity over the whole water column. As a consequence the bottom friction will be underestimated near the bottom, where it is strong and overestimated near the surface, where it is of less influence. An underestimation of the bottom friction by the model near the bottom leads to an overestimation of the amplitudes near the surface. This is true for the amplitudes of all the physical parameters, except for the  $C$  rotating current. The overestimation of the  $AC$  amplitude and underestimation of the  $C$  amplitude can be better explained using equation (94). Using the best fit value for the viscosity parameter the Ekman depths for the  $C$  &  $AC$  currents are  $\delta_- = 33.7m$  ( $=C$  Ekman depth) and  $\delta_+ = 10.3m$  ( $=AC$  Ekman depth). The depth of the water column at the measurement location is approximately  $18m$ . From the amplitudes of the measurements and the discussion in section 4.4 it seems that the bottom friction effects are in the order of the height of the water column or larger. The Ekman depths are calculated using a constant viscosity while, as explained before, it changes with depth. The predicted Ekman depths by the model are therefore possibly too high for the  $C$  current and too low for the  $AC$  current. From this it can be concluded that the effect of bottom friction is underestimated (overestimated) for the  $AC$  ( $C$ ) current and therefore amplitude, resulting in larger (smaller) predicted amplitude. The effect of the bottom friction is also clearly visible in the predicted phases, which are shown in figure (45). All modeled phases show a phase advance from the bottom towards the surface as discussed in section 4.4. Except for the modeled  $C$  and cross stream phase, the modeled phase advances are in the same order as the measured phase advances. This indicates that the processes determining the cross stream phase that are

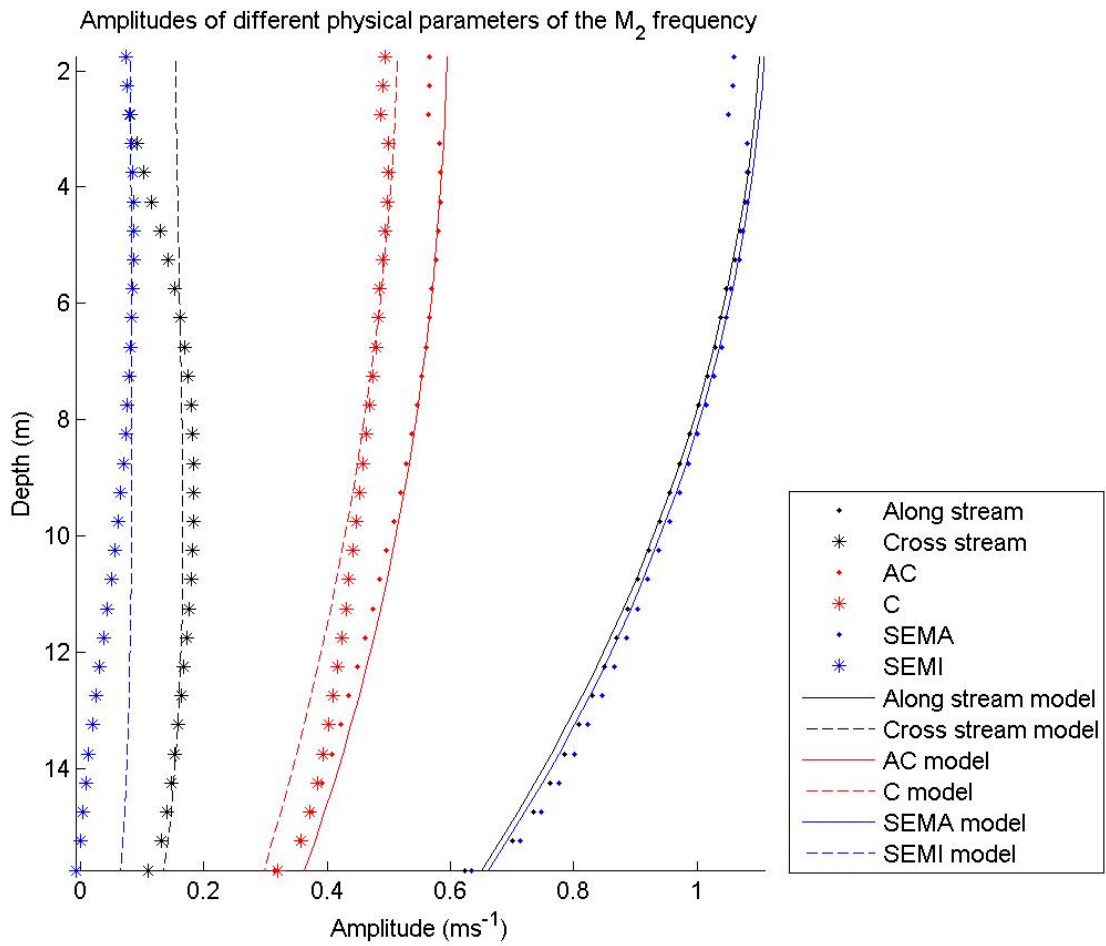


Figure 44: The amplitudes of the  $M_2$  tidal frequency of the physical parameters of the velocity triangle. The dots are derived from the LSHA that was performed on the measurements. The lines are calculated with the barotropic model using the LSHA amplitudes and phases of the 10<sup>th</sup> bin as input.

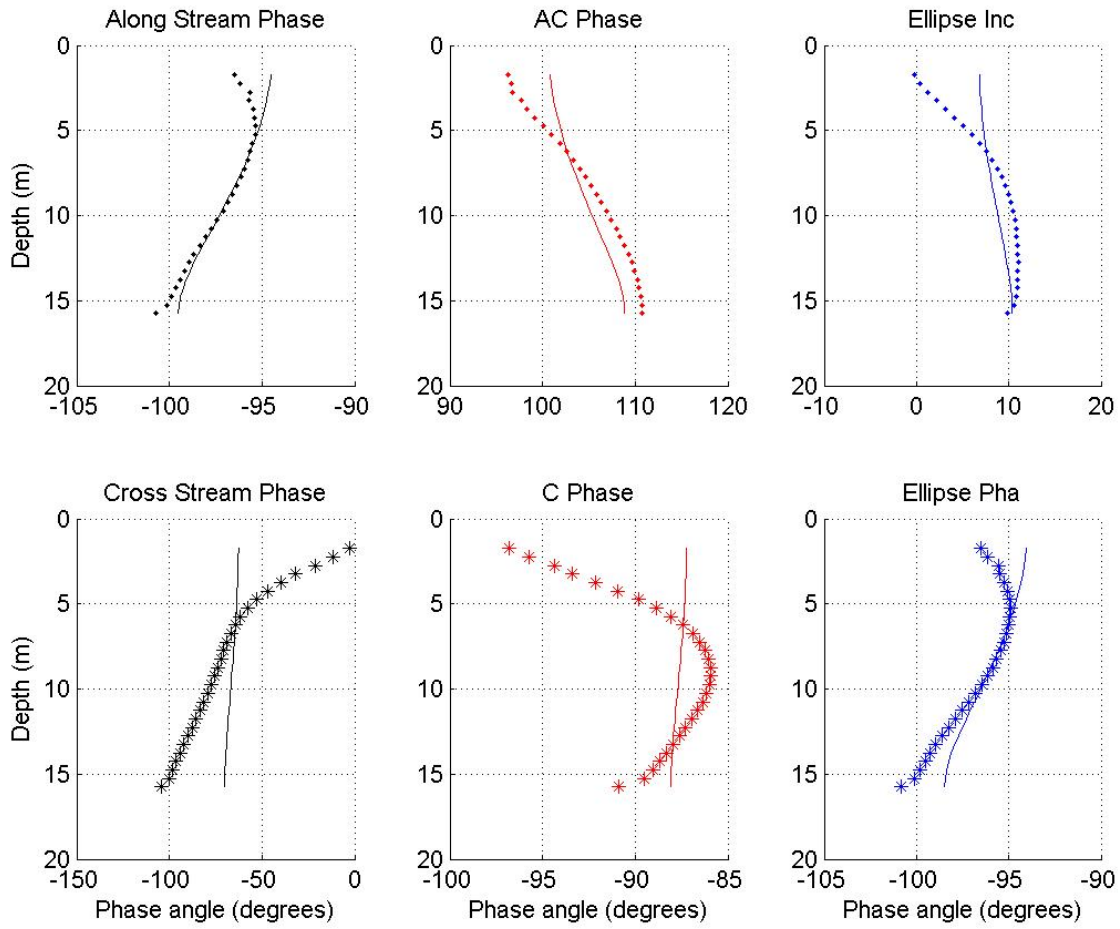


Figure 45: The phases of the  $M_2$  tidal frequency of the physical parameters of the velocity triangle. The dots are derived from the LSHA that was performed on the measurements. The lines are calculated with the barotropic model using the LSHA amplitudes and phases of the 10<sup>th</sup> bin as input.

already discussed are more pronounced in the  $C$  than  $AC$  phases.

Chain interference and wind friction is not taken into account in the model and therefore the predicted results do not show a phase advance from the surface toward the bottom, while this is often the case for the measured phases. The wind and chain effects influencing the amplitudes are not predicted either. As a result the amplitudes of the model will be too high compared to the coherent LSHA results. Near the surface the overestimation because of not taking into account the wind and chain interference is larger than the underestimation due to a constant bottom friction. For all amplitudes this leads to higher modeled than measured amplitudes.

The model is very capable of predicting the strong along stream and  $AC$  amplitudes and phases, the  $SEMA$  amplitudes and  $PHA$ . For these parameters the strong tidal currents are very dominant in determining their values and are included in the model and therefore well predicted. The eccentricity given in figure (47), is not well predicted but this is not unexpected taking into account the bad approximation of cross stream amplitudes and phases and well predicted along stream amplitudes. Even though the modeled cross stream tidal average (given in figure 48) is not as good as the along stream tidal average, this has only little effect on the predicted net currents which are almost equal for both the model and the measurements.

It is now time to end the discussion of the measurements, LSHA and the model and move on to interpret the residual signal. What is important to know is that the along stream currents are mainly dominated by tidal motion, Coriolis force and bottom friction which are also included in the model and therefore well predicted. As soon as other processes determining the current are of equal importance, than the model has a problem to predict the currents because they are not accounted for in the momentum equations. This is the case for the cross stream currents which contain much more processes which are of equal importance and captured by the coherent LSHA results and not by the barotropic model. The main processes not captured by the model are related with the lack of a finite channel width in combination with the deflection of the along stream current by the Coriolis force. It is also shown that large discharge events seem to influence the cross stream currents and the spring neap cycle is of importance for the along stream current. Some of the discussed processes mainly induce currents that are not coherent with the tidal frequency, sometimes they may (temporally) be coherent with tidal frequencies and as a result these processes affect the computed LSHA amplitudes and phases and thus create a possible source for differences between the results of the LSHA and the model. It is expected that the IWs are manifested in the incoherent currents in the measurements. The remainder of this thesis will be dedicated to the search for IWs in the residual signal obtained after subtracting the LSHA coherent signal from the measurements.

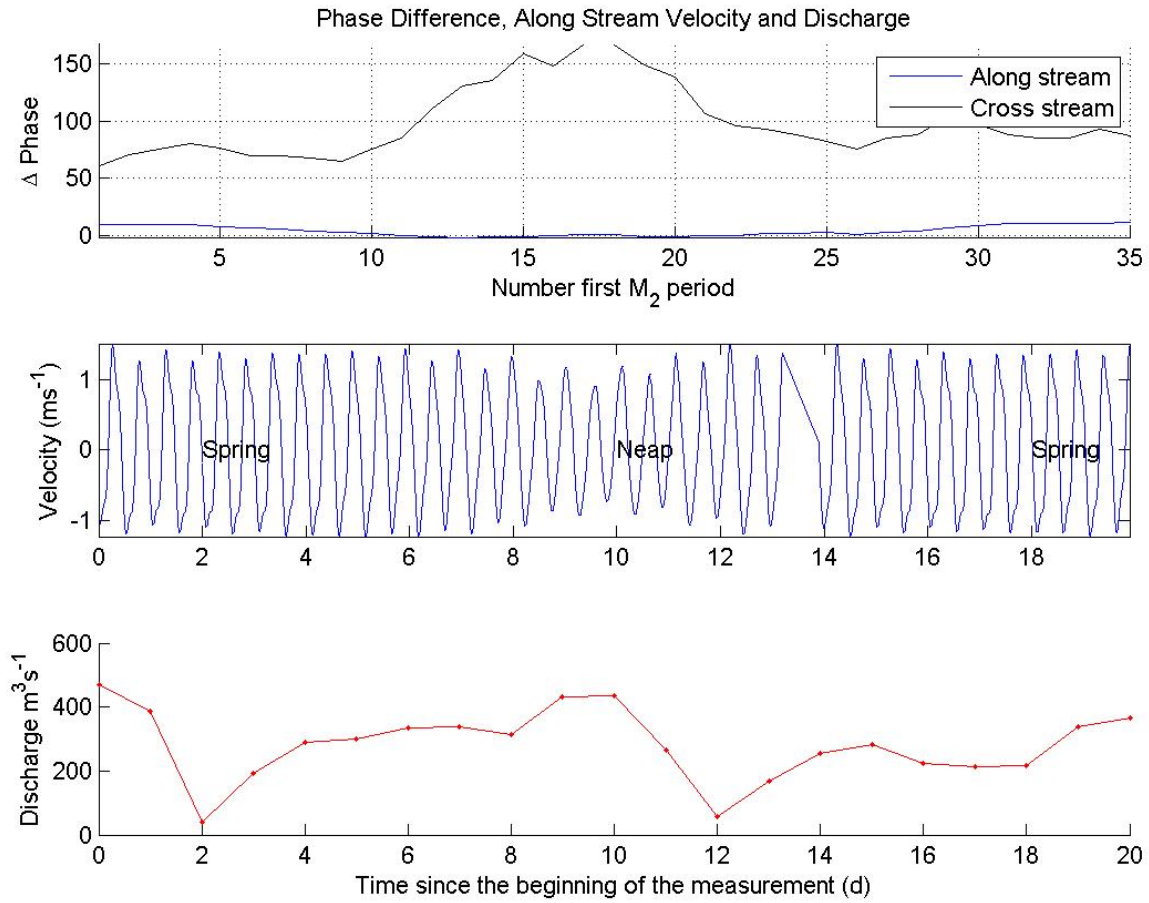


Figure 46: The upper panel shows the running phase difference of the  $M_2$  tidal frequency, between the 1<sup>st</sup> and 29<sup>th</sup> bin of the along (blue) and cross (black) velocity, predicted using a LSHA over 4  $M_2$  periods. The time span over which the phase difference is calculated, shifts one period, to obtain 35 values. These values give a good representation of the change of the phase difference in time. The middle panel shows the LSHA approximation of the 4<sup>th</sup> bin over the whole time series. The spring and neap cycle is clearly visible and indicated. The lower panel shows the amount of discharge from lake IJssel during the period over which measurements were obtained. The discharge data was delivered by Rijkswaterstaat.

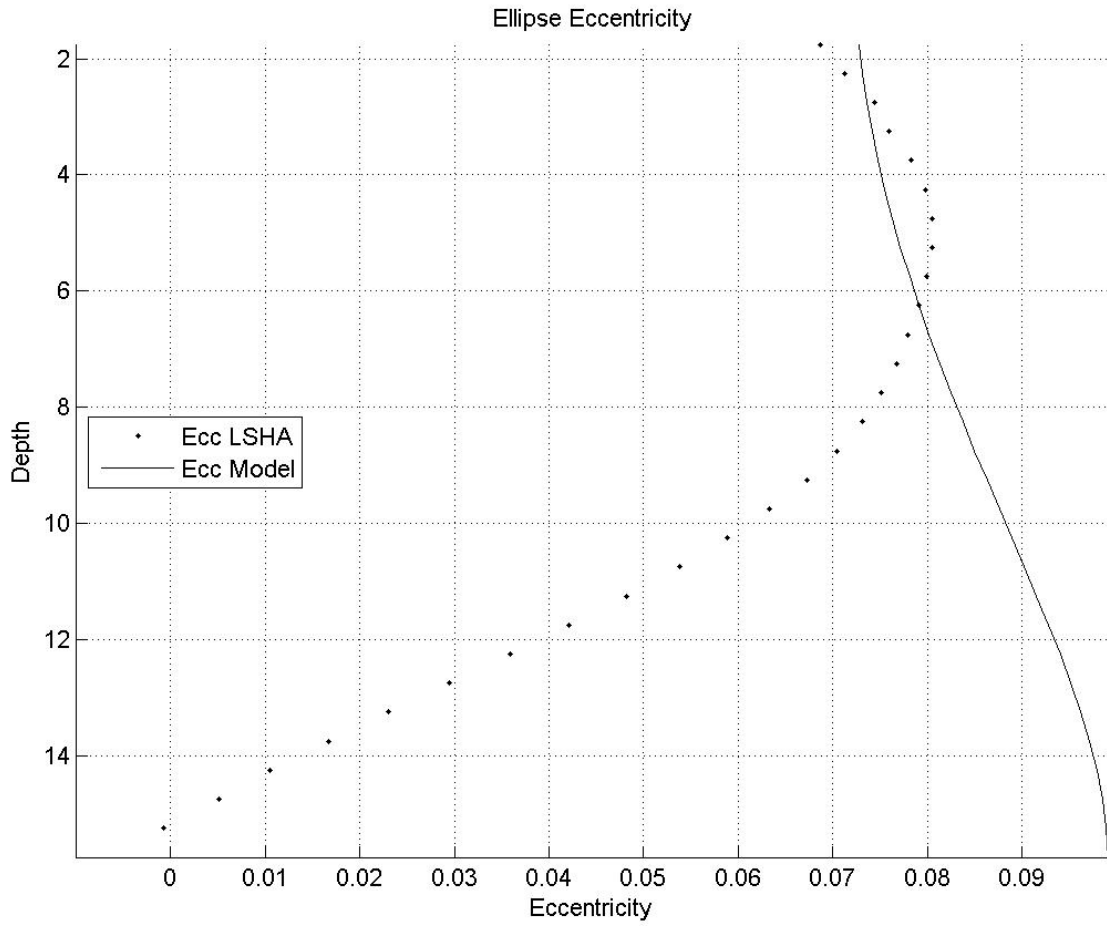


Figure 47: The eccentricity of the tidal ellipse derived from the LSHA data (dots) and calculated with the barotropic model (line).

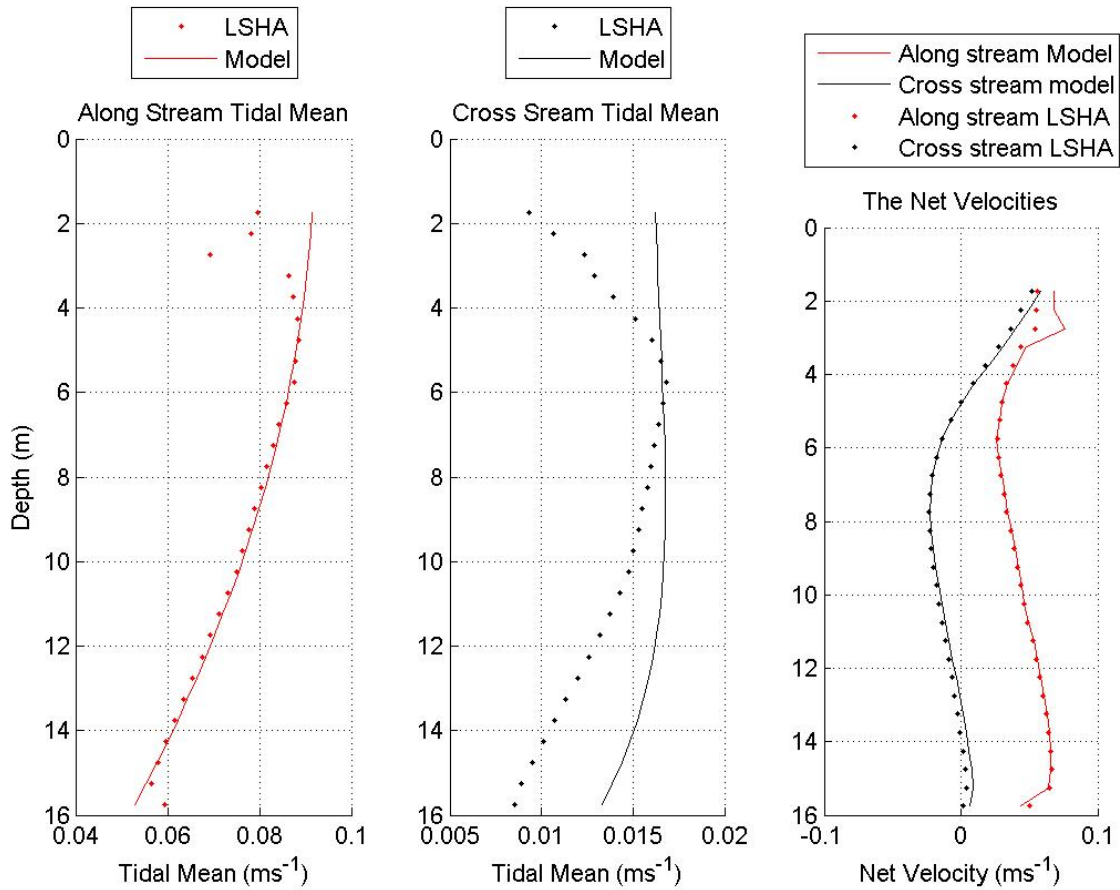


Figure 48: The left panel shows the along stream tidal mean derived from the LSHA data (dots) and calculated with the barotropic model (line). The middle panel shows the same for the cross stream and the right panel shows the net current as derived from the LSHA (dots) and calculated by the model (lines) for the along (red) and cross (black) direction.

## 6 The Residual Signal

In this section the residual signal will be discussed. The residual signal is obtained after subtracting the coherent signal (LSHA approximation) from the measurements. The remaining may be interpreted as the incoherent signal, which is incoherent on the time scale of 19.8 days over which the LSHA is determined. Events which are coherent for a few tidal cycles (for example wind induced currents) will have an influence on the LSHA approximation but not so strong that their effects are completely removed when the coherent signal is subtracted. Their effects will therefore be pronounced in the incoherent residual signal. The obtained data set contains all kind of physical processes. Limited by time and goal of this thesis only the physical processes that concern the search for IWs will be considered.

In the Marsdiep, stratification is the main ingredient needed for IWs to exist. Until now, proof of stratification in the Marsdiep has not been given in this thesis and unfortunately the deployment did not have instruments that could deliver information about the vertical structure of the density. Therefore previous measurements in the Marsdiep, obtained for a different study, are used. These data sets contain information about the vertical structure of the density during complete tidal cycles and will prove that vertical stratification may sometimes occur in the Marsdiep during some phases of the tide. Knowing this, it is tried to find physical processes in the incoherent signal from the buoy data, that indicate stratification and the possible existence of IWs.

### 6.1 Proof of vertical shear and stratification in the Marsdiep from a different source

In the measurements done for this thesis no vertical structure of temperature, salinity and/or density is measured. As a result it cannot be proven directly that there might sometimes be vertical stratification which may manifest IWs. At a different location in the Marsdiep, approximately  $2km$  from the buoy location, at different moments throughout the past years, 13 hours anchor stations (ASs) with the R.V. *Navicula* have been carried out. These ASs have revealed vertical stratification during some phases of the tidal cycle. These measurements will now be presented and discussed and will be used as an argument that stratification does occur in the Marsdiep (and likewise at the location of the buoy) and that therefore situations can occur which may manifest IWs.

#### 6.1.1 Navicula data. A general description

Six ASs, of which information is given in table (6), are used in this thesis. All ASs used a downward looking Nortek  $1.0MHz$  ADCP that is mounted at the side of the ship. The depth of the middle of the first bin is located at  $2.51m$  beneath the surface. From this depth until the bottom, the ADCP measures east, north and vertical water velocity and acoustic backscatter intensity, with a vertical resolution of  $0.99m$  and a frequency of  $1Hz$ . The accuracy of the velocity measurements is approximately 1% of its magnitude. The duration of the measurements is  $13h$  (not coincidentally a little more than the dominant  $M_2$  tidal period). During these  $13h$  every 20 minutes a CTD with Seabird sensors was lowered from the surface to the bottom. With an accuracy of  $0.004^\circ C$ ,  $0.005psu$  and a vertical resolution of  $0.05m$  it measures depth (deduced from pressure), temperature and salinity (deduced from conductivity) which can be used to calculate the density.

The main reason to use the ASs data is to indicate that (sometimes) during some phases of the tide stratification may occur and that this coincides with the existence of vertical shear of the horizontal along and cross stream velocity and strong vertical velocity. If this can be proven, then



AS	Date	Wind (Bft)	Min/Max $ms^{-1}$
49	06-04-2007	2 (Calm)	-2.01/2.00
51	28-09-2007	4-7 (Stormy)	-1.89/1.90
52	23-11-2007	3 (Calm)	-1.96/1.80
54	20-06-2008	3-6 (Moderate)	-1.76/1.71
55 <sub>1</sub> *	27-02-2009	3 (Calm)	-2.04/0.98
55 <sub>2</sub> *	02-03-2009	3 (Calm)	-2.14/1.70

Table 6: Navicula Anchor Station (AS) information. The last column gives the minimum ebb currents and maximum flood current measured during the ASs. The AS indicated with a star (\*) are *8h* surveys.

one can use the buoy data to scan for similar events that might lead to a proof of the existence of IWs in the Marsdiep.

In figure (49) the along stream velocity (upper panel) and vertical structure of the density (lower panel) of AS49, AS51, AS52 and AS54 are shown. Positive red (negative blue) along stream values indicate transport into (out) of the Marsdiep indicating flood (ebb) currents. The measured stratification and horizontal velocity shown in figure (49) are related. In general, for all four cases, one can conclude that along with the strong flood currents North Sea water and therefore relative saline and cold (=dense) water, enters the Wadden Sea through the Marsdiep. When flood currents are strong, the water mass is vertically well mixed and only horizontally stratified. During the transition between flood currents towards ebb currents (flood slack) very low velocity values are measured and the densest North Sea water has reached the Marsdiep. Because of the low velocity a little vertical stratification starts to occur with the highest densities near the bottom and less dense water near the surface. The main stratification is located near the bottom. The flood slack slowly changes to ebb currents. Meanwhile the saline North Sea water that entered the Wadden Sea has mixed with the fresh water discharged from Lake IJssel and has become less saline and therefore less dense. The effects due to heating or cooling of the North Sea water has a second order effect on the density compared to the salinity. In summer (winter) the water heats (cools) in the Wadden Sea making it less (more) dense. As a result horizontally stratified water leaves the Wadden Sea towards the North Sea. When the ebb currents increase, vertical mixing increases and the water column again becomes vertically well mixed and only horizontally stratified. In the following ebb slack (low currents between the transition from ebb to flood) the most freshest Wadden Sea water passes through the Marsdiep. Due to decreasing currents a little vertical stratification starts to form once again, with the strongest stratification found near the surface and in general the complete water column is fresher than during flood slack. When the flood current starts to increase the process starts all over again.

The stratification found during the ebb and flood slacks are often minor ( $\Delta\sigma < 0.001kgm^{-3}$ ) and the observed slacks are as one would typically expect for a current with a dominant barotropic signal. The slack starts at the bottom and propagates towards the surface resulting in a smooth curved transition. Fortunately there are a few examples where the stratification is relatively intense ( $\Delta\sigma > 0.002kgm^{-3}$ ) and also the measured slacks have a different form than expected from barotropic currents, indicating that other processes are dominant during that phase of the tide. This is especially the case for the flood slack of AS49 and the ebb slack of AS51. Stratification during these phases is relatively strong, and worth looking at into in more detail.

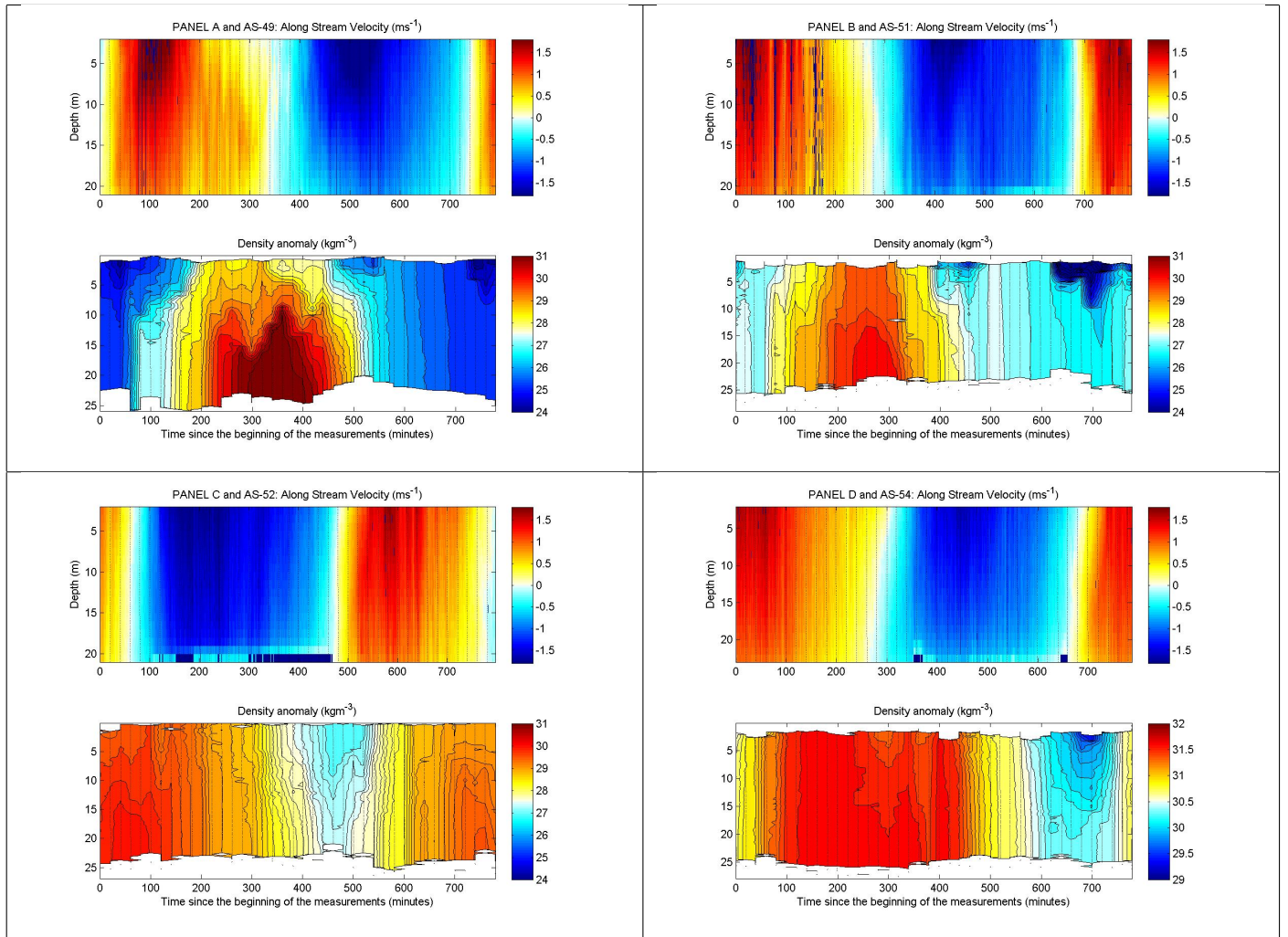


Figure 49: Observations for AS49, AS51, AS52 and AS54. Of each panel (A,B,C and D indicated in the titles of the figures) the upper figure shows the along stream velocities and the lower figure shows the density. As for the buoy data, positive red (negative blue) along stream values indicate a flood (ebb) current into (out of) the Wadden Sea. The density anomaly scale is given as the measured density minus  $1000\text{kgm}^{-3}$ . Note that the scale of AS54 is different than that of the other ASs. The vertical dashed lines indicate the times at which measurements of the vertical structure of the density are obtained.

### 6.1.2 Navicula data. The search for shear, using the barotropic model

To study the incoherent currents of AS49 and AS51, it is convenient to subtract the coherent signal given by the LSHA approximation. The ASs data are short term measurements but just long enough to be able to perform a LSHA, as described in section 4.1. This results in a LSHA approximation using four tidal frequencies including the dominant  $M_2$  frequency. Because of the short duration of the period over which the LSHA is performed it is expected that, when present, baroclinic effects are also included in the coherent approximation. By subtracting the coherent currents from the measurements, also baroclinic currents are subtracted and will not be available in the incoherent signal for further analysis. Therefore the amplitudes and phases obtained with the LSHA, are used to feed the barotropic model predicting the barotropic currents. When the barotropic model is subtracted from the measurements, the resulting incoherent signal will contain currents that are induced by for example baroclinic motions (when present). The barotropic model is fitted in the same manner as for the buoy data explained in section (5.6.2). The resulting values for the eddy viscosity and slip parameter and the depth level used as input for the model are given in table (7).

For the discussion of the measurements of AS49 and AS51, important variables are shown in figure (50). From the top panel to the lowest panel the along and cross stream incoherent velocity and vertical velocity are shown. The incoherent cross stream and along stream measurements of both ASs shows circulation cells. In this case a circulation cell is used as an indication that the water column is divided into two parts on top of each other of which both have currents in a different direction (opposite sign). There can be Negative or Positive Circulation Cells (NCCs or PCCs). A NCC (PCC) circulation cell has negative (positive) currents at the surface and positive (negative) currents near the bottom (and are thus directed in the opposite direction). Both cross and along stream incoherent signals show NCCs and PCCs. For some reason, with exception of the period around slack, the vertical velocity is in general directed towards the bottom (negative). This indicates that when there are (strong) currents, there are local effects resulting in a dominant downward vertical velocity which is stronger than the vertical velocities expected due to rising and fall of the sea surface due to tides. During some slack phases the vertical velocity is positive and as will be indicated, seems to be ordered in a way that is very typical for vertical motion associated with a passing IW. Therefore it seems to be worthwhile to focus especially at the slacks where there seems to be stratification, circulation cells and interesting vertical motion.

In figure (51) three variables are shown for four different slacks, two slacks for both AS49 and AS51. The variables shown are the along stream incoherent and vertical velocity and the acoustic backscatter intensity. The acoustic backscatter intensity is shown in the lowest panel accompanied by a black line representing the 'interface'. The acoustic backscatter interface is depth at which the acoustic backscatter intensity is equal to the average over the shown period. The interface gives a good visual representation of the general behavior of the acoustic backscatter intensity. Because currents are weak around slack, this period of the tidal cycle contains no turbulent eddies that cause vertical mixing which alters the height of the acoustic backscatter interface. As a result, there is a rather clear interface that rises (falls) under influence of positive (negative) uniform vertical velocity caused by processes as for example a propagating IW. The acoustic backscatter interface is therefore interpreted as a proxy for the shape of the isopycnals (lines of equal density). When looking at figure (51) again, it is concluded that the ebb slack (second slack) of AS49 and the flood slack (first slack) of AS51 does not seem to have IW motion within. On the other hand, the flood slack (first slack) of AS49 does show signs of IWs in all three variables. In the along stream incoherent signal there is a clear wave feature, visible as shear currents, starting at

AS	$M_2(ms^{-1})$	$M_6$	$M_4$	$3MS_8$	$\sigma_t^2(\%)$	$z_0$	$\nu(m^2s)$	$s(ms^{-1})$
49	1.58	0.33	0.25	0.04	99.3	7	$9.53 * 10^{-2}$	$15 * 10^{-3}$
51	1.56	0.32	0.20	0.12	98.7	7	$15.68 * 10^{-2}$	$9.6 * 10^{-3}$
52	1.65	0.30	0.16	0.08	98.6	8	$10.6 * 10^{-2}$	$8.9 * 10^{-3}$
54	1.45	0.30	0.14	0.01	99.3	9	$5.7 * 10^{-2}$	$4.9 * 10^{-3}$

Table 7: Information obtained for the different R.V. Navicula ASs after performing a LSHA to the data. The results are used to calculate and fit the barotropic model. In the 1<sup>st</sup> column the number of the ASs are given. The next columns are the amplitudes ( $ms^{-1}$ ) of the tidal frequencies obtained when performing the LSHA. The 6<sup>th</sup> column gives the goodness of fit value. The 7<sup>th</sup> column gives the depth from which the amplitudes and phases of the LSHA are used. The 8<sup>th</sup> and 9<sup>th</sup> column give the slip and eddy viscosity best fit parameters. Note that these are rather high.

approximately 330 minutes after the first measurement. As indicated with the black lines, when the vertical motion is zero, the waves reach their maximum or minimum, leading to a 90° phase difference between the elevation of the acoustic backscatter interface and the vertical velocity, which is typical motion associated with a passing wave.

During AS51 stormy weather conditions were present in the morning and changed into rather calm condition towards the evening. Still a little stratification is found during flood and flood slack, but the main stratification is found during ebb slack when the weather conditions relaxed and there was less mixing due to wind. The second slack (ebb to flood) of AS51 shows a little motion that indicates passing waves. At approximately 680 minutes after the first measurement all three variables shows related motion: negative/positive vertical currents and fall/rise of the acoustic backscatter interface. At the same time the incoherent along stream signal a water mass moving up and down through the water column is visible trough shear (it is stronger than its surroundings). The wave motion is on the same time scale as AS49 but seems to be spread over the whole water column instead of only at the middle as in AS49. When comparing the results with figure (3) than the 'half a sine' shape of the vertical velocity and resulting motion of the acoustic backscatter interface, suggests that during the first (flood) slack of AS49 and the second (ebb) slack of AS51 a first mode IWs are detected.

### 6.1.3 Navicula data. Anchor Station 55, a special case

With the help of AS49, AS51, AS52 and AS54 events with stratification and shear have been shown. Another example to strengthen the conclusion that stratification in combination with shear events and strong vertical velocity exist, is given by AS55-1 and AS55-2. These are two 8h ASs measured on separate days. Both days were calm and showed clear signs of stratification that fits the same general description as AS49, AS51, AS52 and AS54.

In figure (52), representing AS55-2, the left panels shows the density and the along stream velocity measurements. The right panels show the along stream measurements and incoherent currents, vertical velocity and acoustic backscatter intensity during (flood) slack. Less strong but similar features as for AS49 are seen. Shear in the along stream velocity (between  $t = 160$  and  $t = 220$  minutes) moving in wave like motion. During the same time, strong uniform vertical velocity that rapidly changes in sign for a few times, is also observed. Even motion of the acoustic backscatter interface, corresponding with the vertical velocity, seems to be present. Though this example does not convincingly show IWs, it does show strong shear and stratification.

More interesting is what happened during AS55-1, which is shown in figure (53). Though

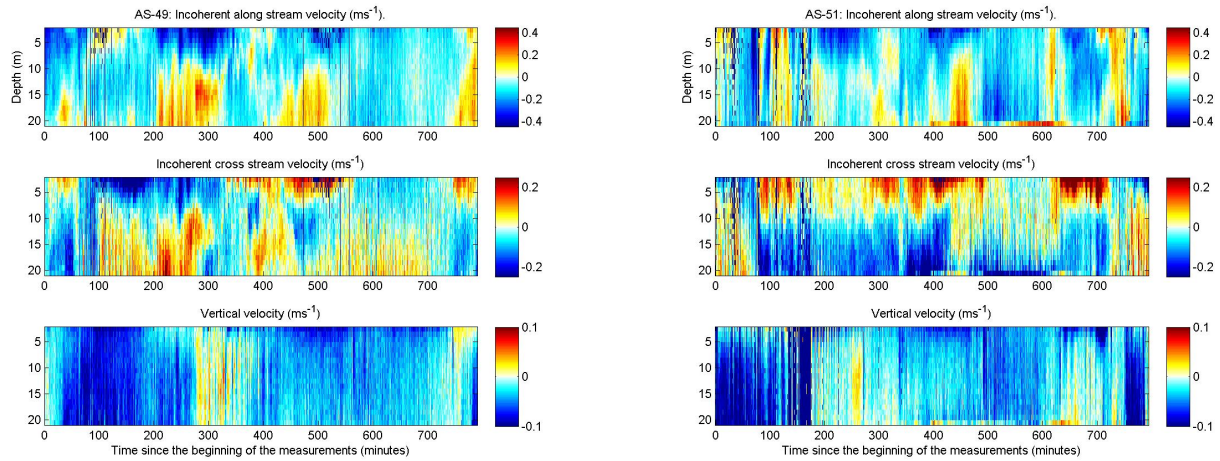


Figure 50: Shown are the incoherent along stream velocity (upper panels), incoherent cross stream velocity (middle panels) and measured vertical velocity (lower panels) of AS49 (left) and AS51 (right). Because the barotropic model is subtracted from the measurements, red (blue) values in the incoherent velocity indicate an under estimation (over estimation) of the measured currents by the model. As for the buoy data, positive red (negative blue) vertical velocity values indicate up ward (down ward) motion.

no photo was taken, lines as shown in figure (1), were visible at the sea surface and passed the Navicula during AS55-1. When this happened the ship itself seemed to move under influence of the currents that accompanied the wave. This was a very strong indication of a possible passing IS and therefore the CTD was continuously moving up and down for 10 minutes. The results are shown in figure (54) and make visible that during this time the isopycnals (lines of equal density) moved up and down. At the same time strong positive (upward) vertical motion was measured and (strong) shear occurred in the (in)coherent along stream velocity. The acoustic backscatter interface shows the same motion as the isopycnals. This strengthens the assumption that the acoustic backscatter interface is a good proxy for the shape of the isopycnals. This is quite convincing evidence of a passing IS. As can be deduced from figure (53), which shows the same as figure (52) but than for AS55-1, the whole process was accompanied by strong stratification. Peculiar is that, when comparing the currents during the time that the IS past with the rest of the signal, the incoherent along stream shear and vertical velocity are stronger than 'average', but not very abnormal and show the same vertical structure as before. So even though it was quite sure that an IS passed the Navicula, it would have hardly been noticed when searching in the data and not informed beforehand.

## 6.2 Residual Buoy signal

From all the R.V. Navicula ASs it is very clear that (strong) vertical stratification of the water column is possible during some phases of the tide. During these stratification events, strong vertical velocities accompanied by vertical shear of horizontal velocity has been observed. As a result it is concluded that the Marsdiep might manifest IWs.

Taking this into account, it is likely that the buoy data will contain physical processes indicating the passing of IWs. By searching for shear events in the horizontal velocity, accompanied by strong events of vertical velocity and the movement of the acoustic backscatter interface of the

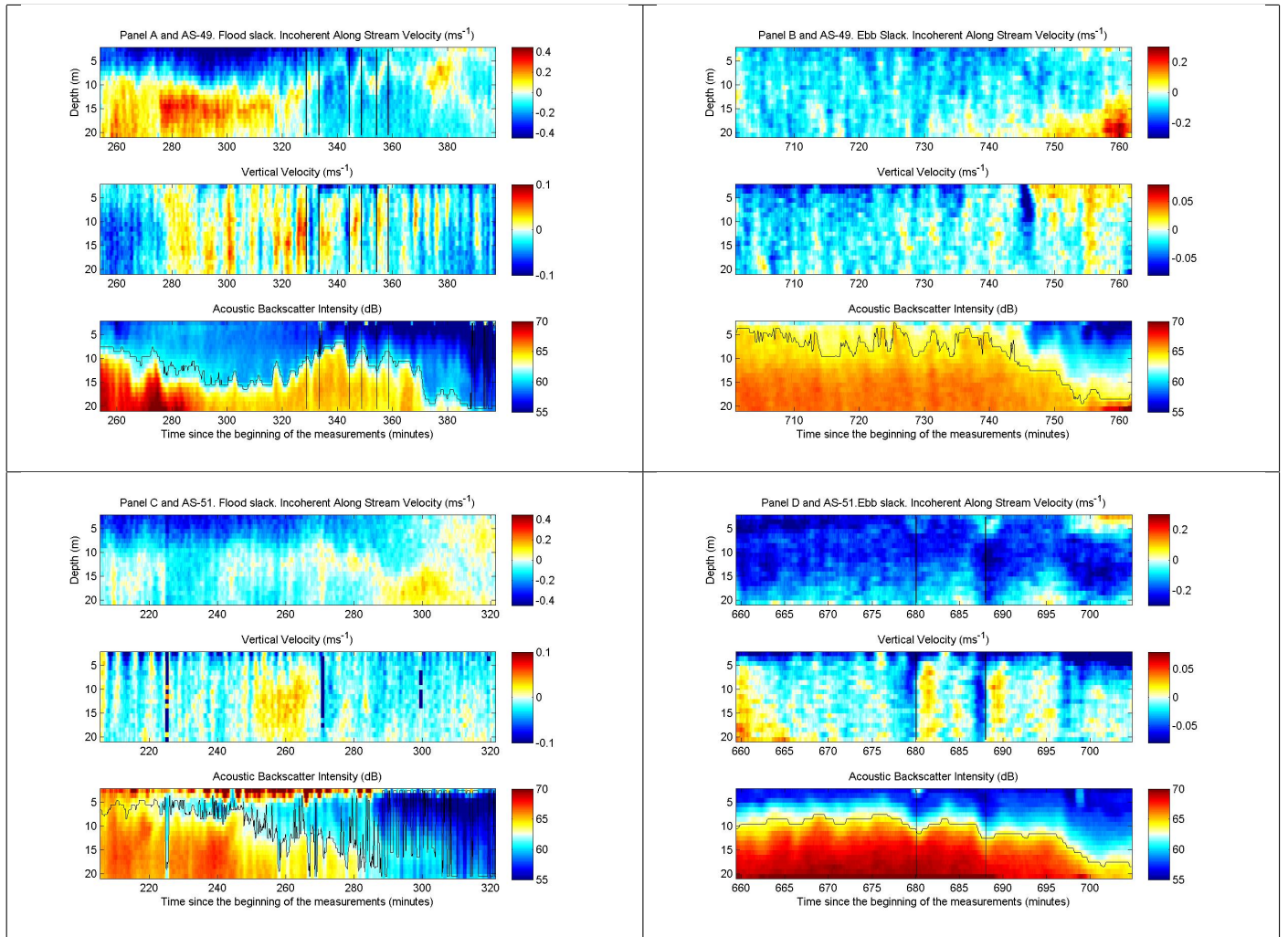


Figure 51: Observations for AS49 and AS51 during slack tide. Of each panel (A,B,C and D indicated in the titles of the figures) the upper figure shows the along stream incoherent velocity, the middle figure shows the vertical velocity and lowest figure shows the acoustic backscatter intensity and its interface (black line) as defined in section 6.1.2. Panel A shows the flood slack of AS49. Panel B shows the ebb slack of AS49. Panel C shows the flood slack of AS51 and panel D shows the ebb slack of AS51. Colors indicate motion in directions as explained in figure (51). Black vertical lines in Panel A and D are used to indicate positions of zero vertical velocity.

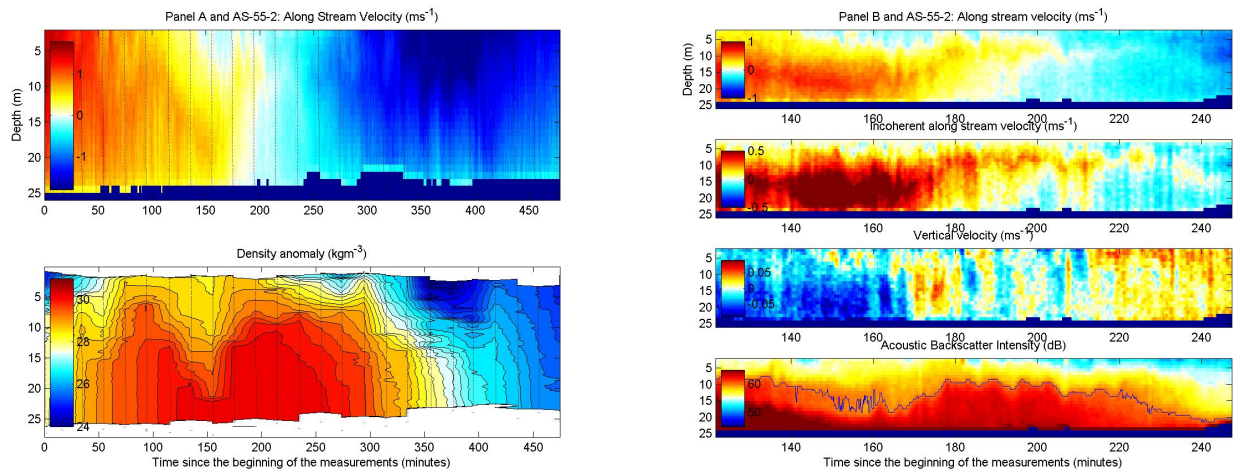


Figure 52: Observations for R.V. Navicula AS55-2 are shown in panel A and B (indicated in the titles of the figures). Panel A contains two figures. The upper figure shows the along stream velocity and the lower figure shows the measured density anomaly as in figure (6). Panel B contains four figures. Shown from top to bottom are the measurements during flood slack of the along stream velocity, incoherent along stream velocity, vertical velocity and acoustic backscatter intensities and its interface (black line) as defined in section 6.1.2. Colors indicate motion in directions as explained in figures (49) and (51). The vertical dashed lines indicate the times at which measurements of the vertical structure of the density are obtained.

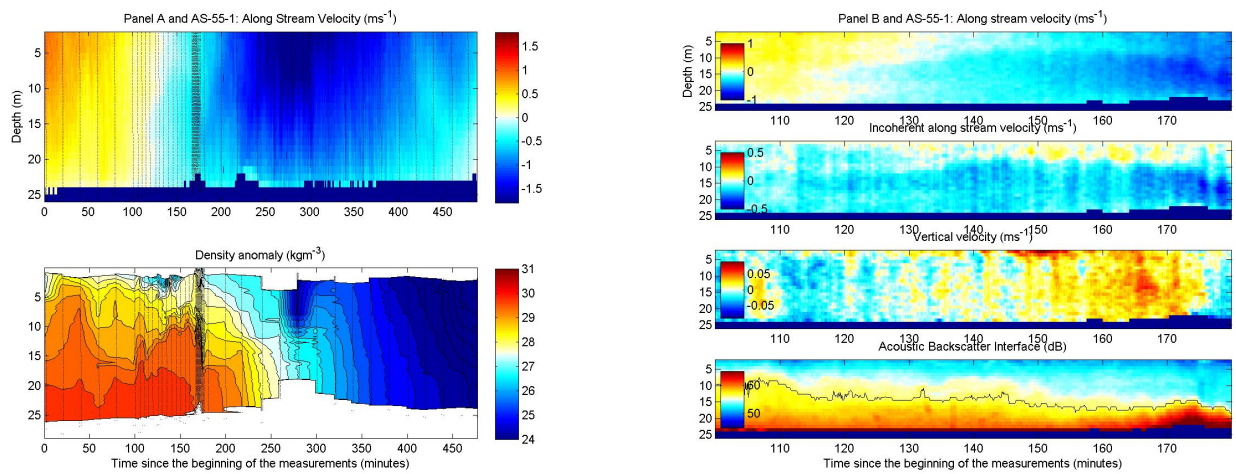


Figure 53: Observations for R.V. Navicula AS55-1 are shown. As figure (52) but than for AS55-1.

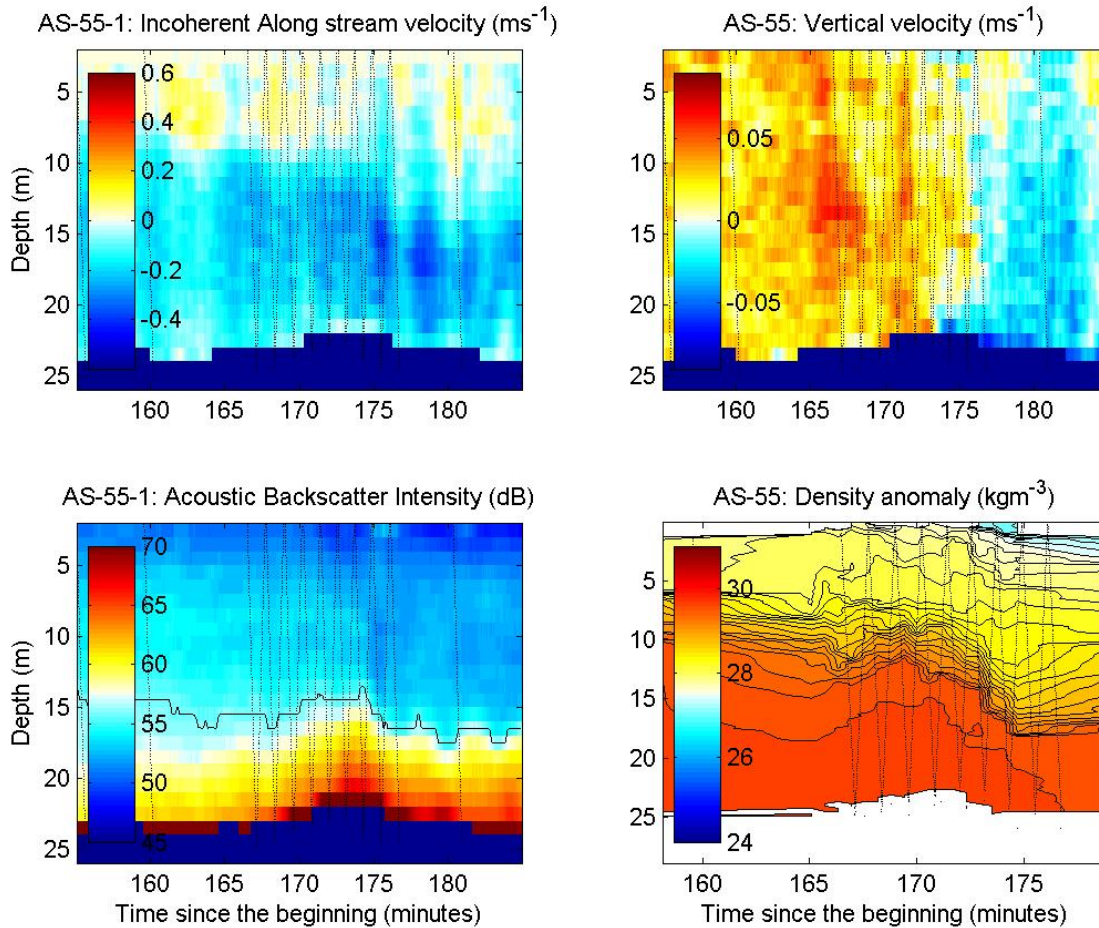


Figure 54: Observations for R.V. Navicula AS55-1 are shown during the time that a certain surface manifestation, that might have been caused by an IS, passed the ship. Titles indicated the variables that are shown and colors indicate motion in directions as explained in figures (49) and (51). The vertical dashed lines indicate the times at which measurements of the vertical structure of the density are obtained.



data collected with the buoy, it should be possible to highlight events which might concern the passing of ISs. If possible these events might be used to describe a source for the IWs, predict their occurrence and determine if they alter the acoustic backscatter intensity and therefore influence the transport of suspended matter.

A first scan of the data indicated that the main physical processes of interest are found during ebb slack. This is not unexpected because, as shown in the ASs measurements, during this phase of the tide velocities are low, therefore mixing due to vertical eddies created by the interaction between tidal currents and bottom friction is reduced and vertical stratification may develop. Though (especially) during flood slacks and possibly other phases of the tidal cycle, more processes that are of physical interest can be found within the data set, the attention will now be focused on the ebb slacks. There are 38 ebb slacks measured during the 19.8 days of data collection. Of course not all can be shown and therefore three examples will be given to illustrate typical situations observed during this phase of the tidal cycle.

### 6.2.1 Ebb slack - Example One

From the 38 ebb slacks measured by the buoy a typical example is shown in figure (55). This example is the first ebb slack measured and will be discussed in this section. This figure shows the most 'simple' observation of an ebb slack. From the along stream velocity (upper figure panel A) it is observed that, in agreement with the along stream phases obtained with the LSHA shown in figure (38), slack is first found near the bottom and propagates towards the surface. A smooth curved transition from flood to ebb is obtained, as one would be expected of a tidally dominated barotropic current. As a result the main part of the signal is explained quite accurately, leading to low currents in the incoherent along stream velocity (middle figure of panel A). Remarkable is that around slack the depth average along stream (and therefore in principle all the) velocities (black line, lowest figure of panel A), lags behind the depth average coherent current (green line). As a result the coherent current reaches slack earlier than the measured current, leading to strong negative values ( $\approx -0.5ms^{-1}$ ) in the incoherent along stream velocity. From this it can be concluded that even a signal that looks as one would expect, contains strong incoherent motion centered around slack. In the beginning of the time series the ebb slack of the along stream coherent velocity is a little in advance of (therefore generally larger than) the along stream measurements. During the time series this changes, so that in the end the coherent ebb slack lags behind the measured ebb slack. This is clear when comparing figures (55) and (57), where it is shown that in figure (57) the slacks are already at approximately the same time. This might be an artifact of missing tidal constituent with frequencies lower than that of the used tidal constituents (for example the semi-yearly constituents). As a result a similar situation in a later stadium of the measurements around slack will result in a more positive residual signal. The large differences observed during slack, do strongly suggest physical processes as a source and not the shift of the phase difference between the measurements and the coherent signal.

In the along stream incoherent nor the measured velocities (top and middle figure Panel A), (strong) shear events are observed. On the contrary this is observed in both the cross stream incoherent and measured velocity (top and middle figure Panel B). During the main part of the shown ebb phase a strong negative velocity (thus directed towards Den Helder), which is more or less uniform in the vertical, is observed. At a certain moment ( $t = 0.14d$ ), quite sudden (order of 2 minutes) a NCC occurs for approximately 90 minutes.

At the same instant that the cross stream NCC occurs there is also a relatively sudden and large drop visible in the acoustic backscatter interface shown in the upper figure of panel C. The

sudden drop of the intensity interface is unexpected because one would normally expect a gradual decrease of the acoustic backscatter interface towards slack due to the slow decrease of the ebb current towards a value beneath the settling velocity for the suspended matter in the water. When currents start to increase and reach the settling velocity the suspended matter is again distributed height into the water column. These processes are more gradual than the drop at  $t = 0.14d$  shown in the acoustic backscatter intensity measurements. Therefore it is expected that this drop is due to a different process. The new depth level to which the acoustic backscatter interface drops  $z \approx 10m$ , is the same height as the interface between the positive and negative currents of the NCC. The reason for the sudden transition toward a NCC is not exactly known, but a possible mechanism will now be described.

During the occurrence and existence of the NCC the along stream velocity is negative (ebb current). The cross stream velocity over the whole depth range is negative before the NCC occurs. As explained in section 3.4 and illustrated in figure (6), a positive (negative) cross stream velocity is, more or less, directed towards Texel (Den Helder). The uniform negative velocity is not visible in the incoherent cross stream velocity, so the process causing this current is coherent. It is worth mentioning that the observed negative velocity is in the opposite direction of a current expected due to the deflection of the along stream velocity by the Coriolis force. That would lead to a current directed towards Texel. There are a few explanations for a current directed towards Den Helder:

- Curvature of the channel causes a current directed towards Den Helder in case of ebb currents [5]. This effect should (later) cause a set up in negative cross stream direction (Texel to Den Helder), leading to a positive cross stream current (towards Texel). If this set up is not (yet) fully established, only a current towards Den Helder will be observed.
- In section 4 it is shown that the tidal current in the Marsdiep is governed by an AC rotating ellipse with small eccentricity. As illustrated in figure (56), this leads to negative cross stream current during the end of the ebb phase, which might explain the observed velocities.

The uniform negative cross stream current changes into a NCC. This transition is abrupt and influences the coherent and incoherent cross stream velocity and the acoustic backscatter intensity. A possible explanation is that the water mass moving towards Den Helder is restricted by a boundary, for example a coast or a different water mass which does not easily interact with other water masses. As a result the water mass is forced down, to move over the bottom back in opposite direction, resulting in a NCC. On top of this, it is also expected that the cross stream velocity in the north side of the Marsdiep basin is ordered in a NCC due to curvature [5]. Because it is not known on which side of the buoy the NCC occurs, it is not clear which of the explanations above is valid. It is clear that the NCC occurs and that the front of the NCC will, at some point, pass the buoy causing a strong and quick change in the observations.

Accompanied by the new vertical structure of the dominant currents, also the acoustic backscatter interface drastically decreases. In the first situation the measured water mass has its origin in the Wadden Sea. The water mass is forced to move due to strong ebb currents which cause a lot of bottom friction and therefore turbulence and associated vertical eddies. The column will be vertically well mixed and the suspended matter is distributed over the whole water column. In the second situation the acoustic backscatter interface is restricted to the bottom layer of the NCC (with currents directed towards Texel). It is expected that only the lowest layer will stir up sediment so that the acoustic backscatter intensity will have low values at the surface and high values near the bottom. Because friction between two water layers is (much) smaller than between

a water layer and the sea bottom, there will be less vertical eddies and associated mixing between the two water layers. As a result there is a situation that can hold for a long time in which the suspended matter is trapped in the bottom layer.

Soon after the rapid drop, the acoustic backscatter interface shows a slow decrease in height. This is the expected drop due to the decrease of the (along stream) currents caused by the incoming ebb slack. As a result the suspended matter settles and at a certain moment only relatively low acoustic backscatter intensity values are found. After a while the incoherent NCC start to weaken and slowly start to dissipate and vertical shear in the incoherent cross stream signal disappears. In the measurements shear is still present, but this must be shear due to the barotropic transition from ebb to flood, otherwise it would have also been visible in the incoherent signal.

### 6.2.2 Ebb slack - Example Two

The second example is shown in figure (57) and is the 28<sup>th</sup> measured ebb slack. The measured slack is approximately at the same time as the coherent slack. As a result a dominant red residual signal (instead of dominant blue as in the first example) is obtained. In the beginning this transition is comparable with the first example, with at  $t \approx 14.63d$  (exactly at the vertical line with rejected measurements), again the acoustic backscatter interface drops and a (very weak!) NCC cells is visible for approximately 45 minutes. Note that, even though both the drop and NCC are weaker, the observed heights of the interface of the acoustic backscatter intensity and NCC correspond once again and are located at  $z \approx 7m$ . Also the ebb slack seems to behave as in the first example, having stronger ebb currents near the surface than near the bottom due to bottom friction and the phase lag which causes the currents near the bottom to slacken first. Then, quite abrupt, at  $t \approx 14.65d$ , strong shear in the along stream velocity and a PCC in the cross stream velocity and incoherent along and cross stream velocity occurs. This lasts for approximately 60 minutes. At the same time a second drop of the acoustic backscatter interface is observed together with increased acoustic backscatter intensity near the surface. Though not very clear in this example, this often coincides with a clear negative vertical velocity resulting in an area of down welling. Due to the down welling foam and material is concentration at the surface of a location where there is down welling resulting in high acoustic backscatter intensity values near the surface. As soon as the PCC occurs, in the middle of the water column of the along stream velocity the currents seem to lag behind the surface and bottom currents. This holds on for a (short) period of approximately 55 minutes and then dissipates into a vertical structure expected for strong barotropic flood currents.

The observed shear in the along stream velocity measurements and resulting PCC in the incoherent along stream and cross stream velocity is a different vertical structure than expected from a barotropic tidally dominated current. The Coriolis effects deflects ebb currents toward Texel. When these currents collide with a boundary, a PCC occurs. Unfortunately the sudden occurrence, the short time scale and already weakening currents make it very unlikely that the Coriolis deflection causes the observed PCC. Over the 19.8 days the PCC is observed frequently with changing strength and duration. It is expected that the great variability has to do with the variability of the cross stream density gradients that are sometimes available in the Marsdiep. The water mass flowing out of the Malzwin during ebb is fresher than the water flowing out of the Texelstroom. This can be attributed to higher concentration of fresh water discharged from Lake IJssel in the Malzwin than in the Texelstroom. As a result, cross stream density gradients, of which the strength depends on the amount of discharged water from Lake IJssel, are easily established in the Marsdiep [38, 5].

As illustrated in figure (58) a cross stream density gradient will, in first instance, lead to a

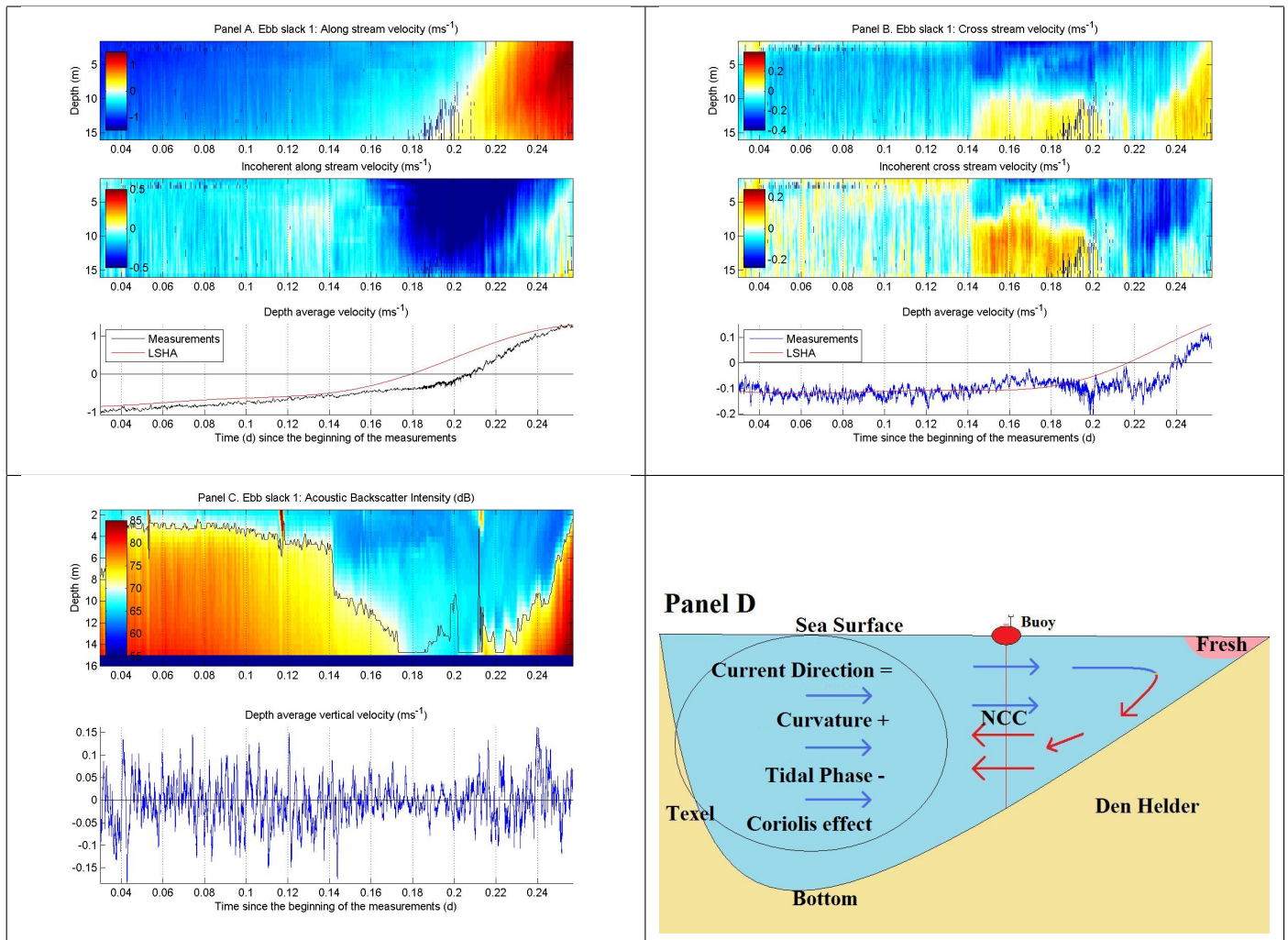


Figure 55: Observations for ebb slack 1. Panel A (indicated in the titles of the figures) show 3 figures. The upper figure shows the along stream velocity, the middle figure shows the along stream incoherent velocity and the lowest figure shows the depth averaged coherent velocity (red) and depth averaged along stream velocity (black). Panel B shows the same but than for the cross stream velocity. The upper figure of Panel C shows the acoustic backscatter intensity and its interface (black line). The lowest figure shows the depth averaged vertical velocity. Panel D shows a simplistic view of the cross stream channel. One is looking from the North Sea towards the Wadden Sea, which is in positive along channel direction. The pink area on the upper right of the basin indicates a relative fresh water mass flowing out of the Malzwin. This will be discussed in more detail in section (6.2.2). Blue arrows are currents from Texel to Den Helder (as the blue colors in the measurements) and red arrows indicate currents from Den Helder to Texel. The currents inside the black circle represent the situation as measured (just) before the NCC is measured. The currents are mainly due to curvature and the phase of the tide and are weakened by a currents induced by the Coriolis force. When these currents encounter a boundary (for example a coast or different water mass, like the part indicated with fresh) than they are forced down and will create a NCC. The NCC will, at some point, pass the buoy.

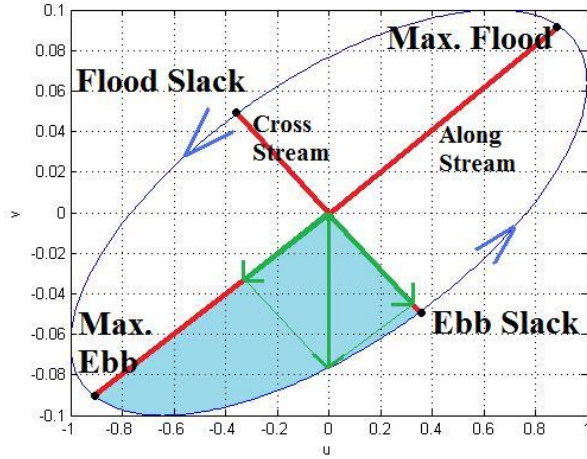


Figure 56: From the rotary currents of the  $m_2$  tidal frequency it is derived that the tidal ellipse in the Marsdiep rotates  $AC$ . The ellipse shown is not on scale but serves as an illustration. The red lines indicate the axis of the ellipse which are also the along stream and cross stream direction. The blue area indicates the phase of the tide between maximum ebb and ebb slack. During this phase, the current (for example the one indicated with the green arrow) has a component directed into the negative cross stream direction. This might cause the observed negative velocity in figure (55).

local PCC near Den Helder. This PCC might be enforced by Coriolis deflection of the Malzwin current and curvature [5]. The water flowing out of the Malzwin makes different curve than the water flowing out of the Texelstroom. As a result the effects of curvature are not the same for both water masses. Therefore the curvature effect strengthens the PCC. The Malzwin water often contains much suspended matter due to inflow of sand from tidal flats. As a result the front between the fresh water mass and the Texelstroom water is very clear due to the color differences and associated foam line. Based on personal observation verified by captains of the ferry Dokter Wagemaker, the front expands from Den Helder into the Marsdiep in the direction of Texel. The expansion or northward propagation will be forced by the PCC, on the other hand ebb currents from the Texelstroom will force the water mass to stay in position, as illustrated in figure (58). Due to slackening currents the water mass propagates in northward direction. Though it is not expected and observed that the fresh water mass will reach all the way to Texel, the front will pass the buoy at a certain moment so that the accompanied PCC will be measured. As expected, strong negative vertical velocity is measured when the front passes. In figure (58) also an attempt has been made to make clear that the front might not be directed exactly in the along stream direction and will not be a straight line. As a result the PCC will have a component and therefore be visible in both the incoherent along and cross stream velocity.

The combination of bottom and coastal friction and a tidal wave propagating from south (Den Helder) to north (Texel), that together will lead to an earlier slack near the coast of Den Helder than in the middle of the Marsdiep. In analogy with phase propagation from the bottom toward the surface due to bottom friction, the flood currents slowly propagate to the surface and the north. The (strengthening) flood currents will interfere with the PCC causing it to dissipate into 'expected' barotropic currents. The strength and duration of the PCC are expected to depend mainly on the amount of discharged water that determines the strength of the density gradients,

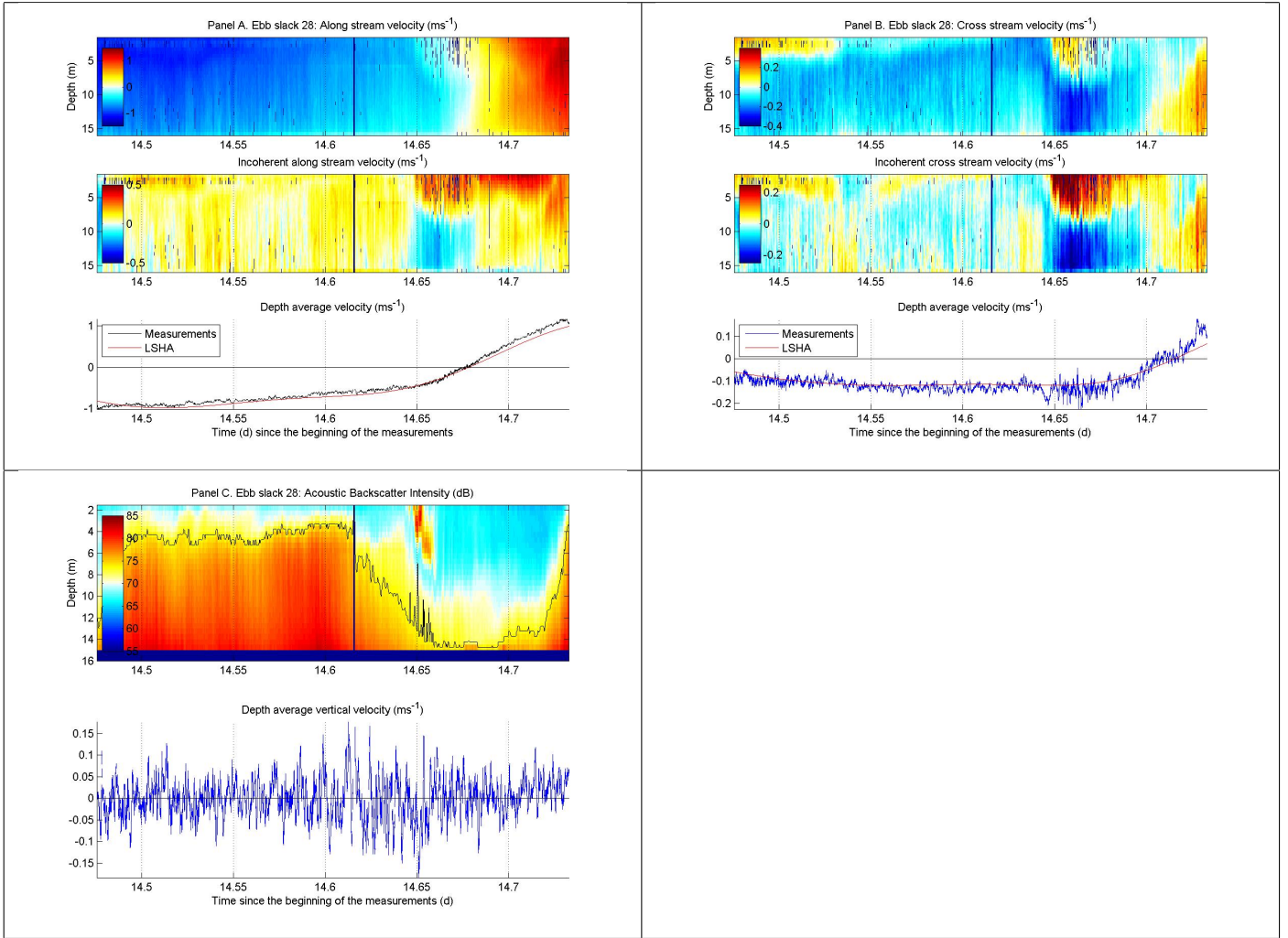


Figure 57: As figure (55) but than for ebb slack 28.

but probably also on the strength of the tidal currents (spring/neap) and the wind induced currents. Though the PCC in this example is relatively weak, stronger and longer lasting examples will be shown in this thesis.

### 6.2.3 Ebb slack - Example Three

The third example shown in figure (59) is very different from the first two examples, but also starts with an acoustic backscatter interface drop (at  $t \approx 12.53d$ ) to a height that is the same as the interface between a NCC that occurs at the same instant in the cross stream direction. This last for approximately 80 minutes. Then, like in the second example, a second drop (at  $t \approx 12.57d$ ) of the acoustic backscatter intensity signal accompanied by PCC in the cross stream direction and a current with a phase lag in the middle of the column appears abruptly. This last for approximately 25 minutes. Instead of quickly dissipating again (like in the second example) this time the lagging currents in the middle dominates the whole water column and stays stable for a long time. In the incoherent along stream velocity, starting at  $t \approx 12.6d$ , this lagging current (negative blue values) moves toward the surface accompanied with wavy motions at the interface between the lagging current and its surroundings. In short it start with situations explained in example one (figure 55),

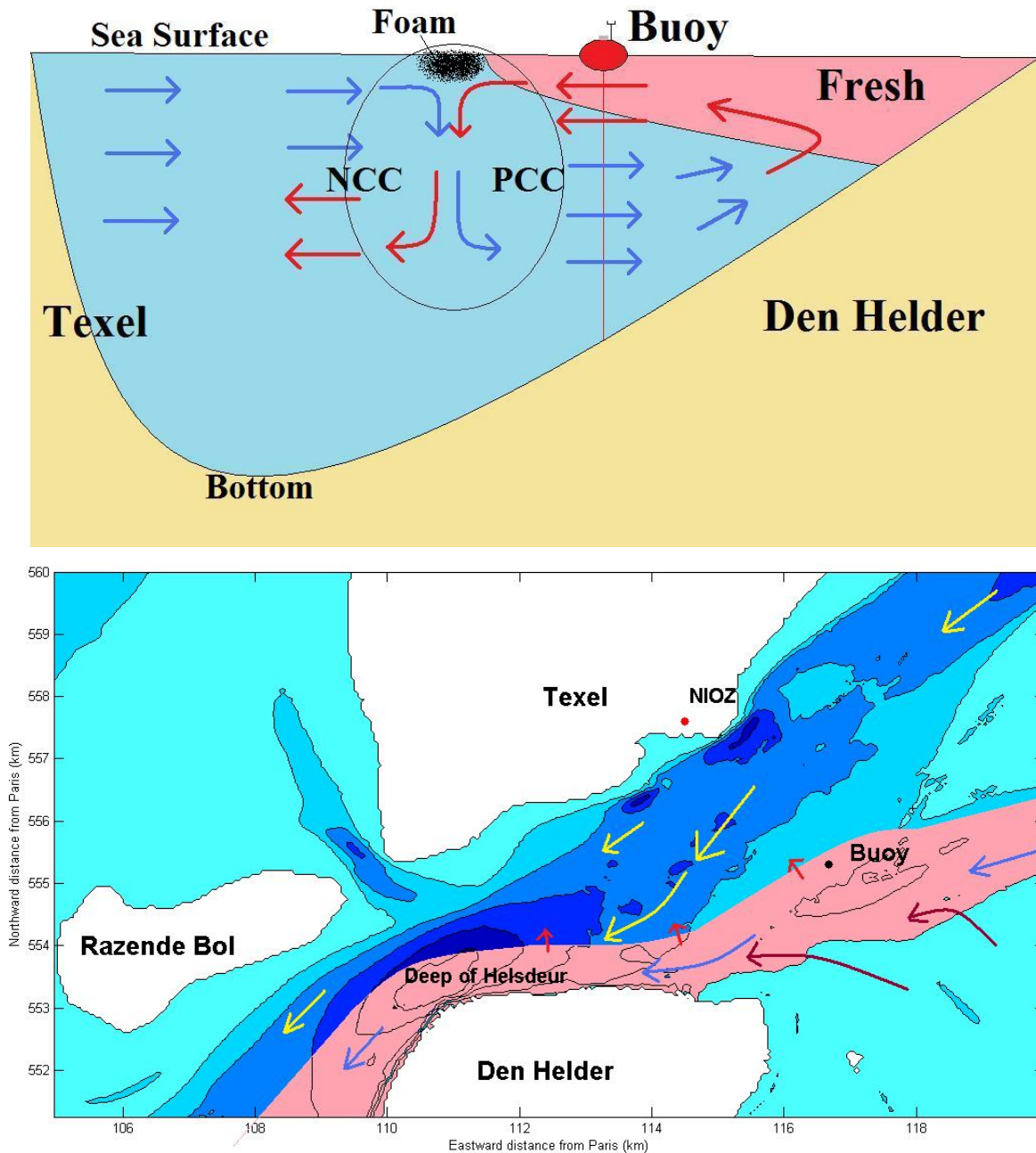


Figure 58: The upper figure shows a cross section of the Marsdiep as in Panel D of figure (55). In this example the Fresh water from the Malzwin has spread out over a large part of the Marsdiep. The density gradient due to the fresh water outflow will create a PCC as explained in section 1.3.2 and illustrated in figure (9). Under influence of the baroclinic currents, the front between fresh and more saline water and therefore the PCC, will expand towards Texel. As illustrated in part of the picture within the black circle, the point where the NCC and the PCC collide, water can only move down, resulting in strong negative vertical motion or downwelling area. At the surface of the downwelling area, foam is trapped. The lower figure is a top view of the same situation. It shows the fresh water mass (pink) flowing out of the Malzwin under influence of the ebb currents (blue arrows). Water from the tidal flats south of the Malzwin (which sometimes contain high concentrations of suspended matter), mixes with the fresh water (brown arrows). The yellow arrows indicate the direction of the currents from the Texelstroom, colliding with the fresh water mass. The red arrows indicate the propagation direction of the front.

then it changes to the PCC as in example two (figure 58). The PCC then results in wave motions which are new in this example and are to be explained.

Due to the fresh water mass from the Malzwin, (strong) vertical stratification may occur. Accompanied with the PCC an interface, between two water masses with different densities, is expected to occur. The vertical water column is stably stratified, with fresher water on top of more saline water. As explained in section 1.2, if a stratified water layer is forced by a barotropic current over bottom topography, (nonlinear) IWs are inevitable. There are many small sand dunes in the Marsdiep with amplitudes of a few meters [2], but the main and probably most influencing change in bottom topography is the Deep of Helsdeur. As shown in figure (6) and (7) this is a deep (reaching up to  $55m$ ) in the along channel direction at the south side of the basin, against the coast of Den Helder. The stratified water column is forced over the Deep of Helsdeur and as a result it is expected that the isopycnal marking the interface between the two layers, will bend downwards, forming a depression. The depression causes baroclinic pressure differences resulting in a force on the water mass. These (restoring) forces create IWs with a certain phase velocity  $c$ . As explained in section 1.2 and illustrated in figure (5), at the down current side of the depression the IWs are free to propagate away from the depression. At the up current side the barotropic ebb current ( $u$ ) prevents the waves from propagating as long as the  $c < u$ . As soon as  $c > u$  because  $u$  slackens, then the IWs will be free to propagate up current. As a result, bending of the acoustic backscatter interface (as a proxy for the isopycnals) and shear currents associated with propagating IWs, can be measured at the location of the buoy as illustrated in upper panel of figure (60). The effects of the passing IWs leave their marks in the incoherent horizontal currents, the bending of the acoustic backscatter interface and in the measured vertical velocity.

Using three examples of measurements made with the ADCP mounted on the buoy, a mechanism is proposed which allows IWs to develop and propagate in the Marsdiep. The currents accompanied with the IWs can be measured when it passes the buoy, but will be superposed on top of other currents that are due to other baroclinic events, curvature, Coriolis force, geometrical effects, wind, etc. On top of this it is possible that the IWs may not propagate exactly in the along stream direction, resulting in structures in the incoherent along and cross stream velocities that are hard to interpret.

In the mechanism proposed above it is assumed that the water mass from the Malzwin is fresher than that of the Texelstroom. Nothing is said about the stratification of the water mass flowing out of the Texelstroom. Though the water mass from the Texelstroom is fresher, it might still be stratified. The stratification will of course be less strong than that of the Malzwin water mass, but when this water mass moves over the Deep of Helsdeur, it might also produce IWs using the same mechanism as proposed for the IWs measured with the buoy data described in figure (60). A reason to note this comes from the fact that the R.V. Navicula measured less strong IW motion than the buoy and is located much more north than the buoy. Probabaly the the Malzwin water does not reach the R.V. Navicula. These problems are solved when assuming that the observed waves are due to the stratified Texelstroom.

#### 6.2.4 Ebb slacks in general

The motions described above can roughly be split into three events. The first is the transition of the ebb currents into a NCC which is accompanied by an acoustic backscatter interface drop. This event is observed in almost all measured ebb slacks. The second event is the occurrence of the PCC due to fresh water discharge from the Malzwin and the resulting baroclinic currents.



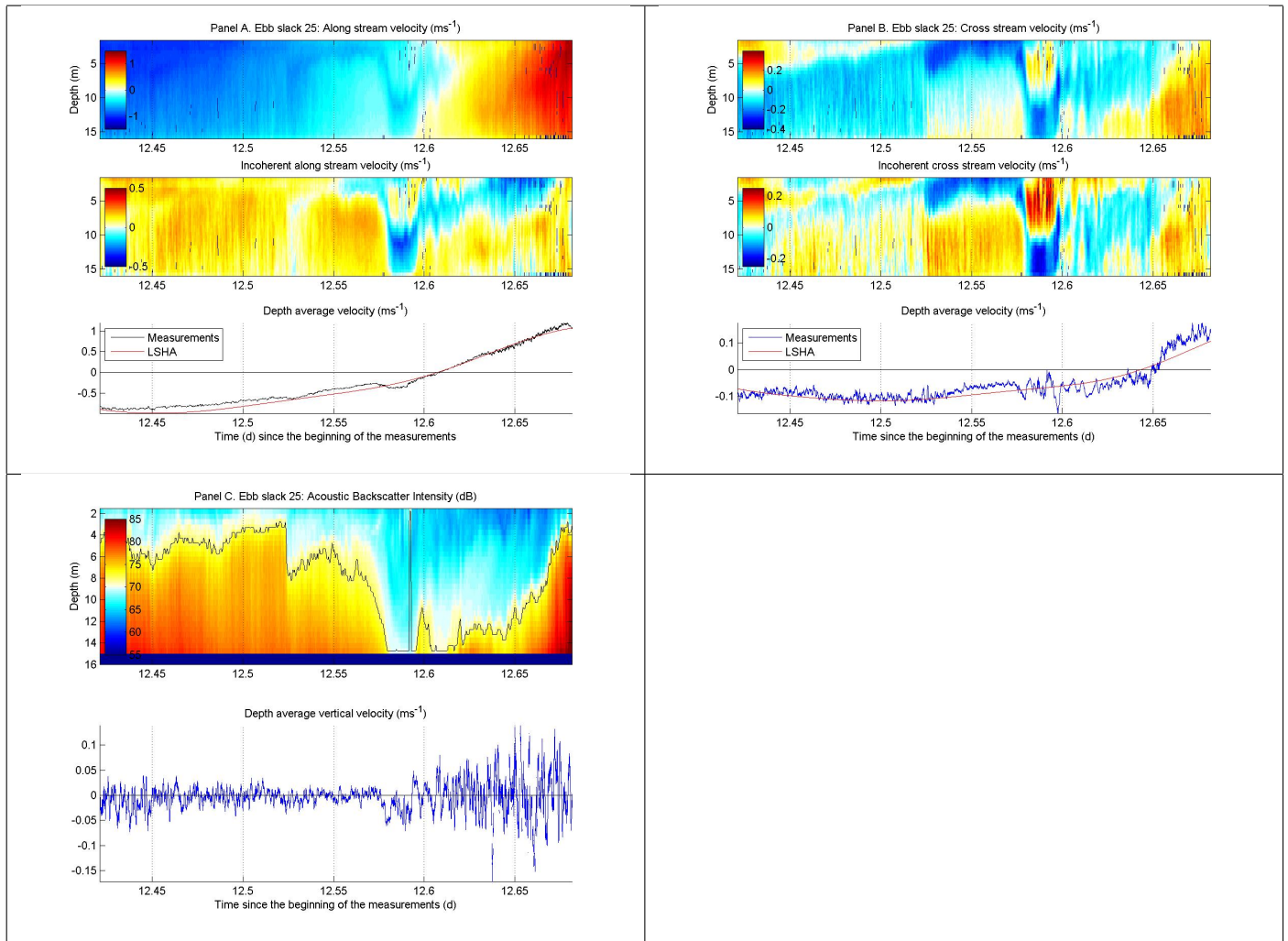


Figure 59: As figure (55) but than for ebb slack 25.

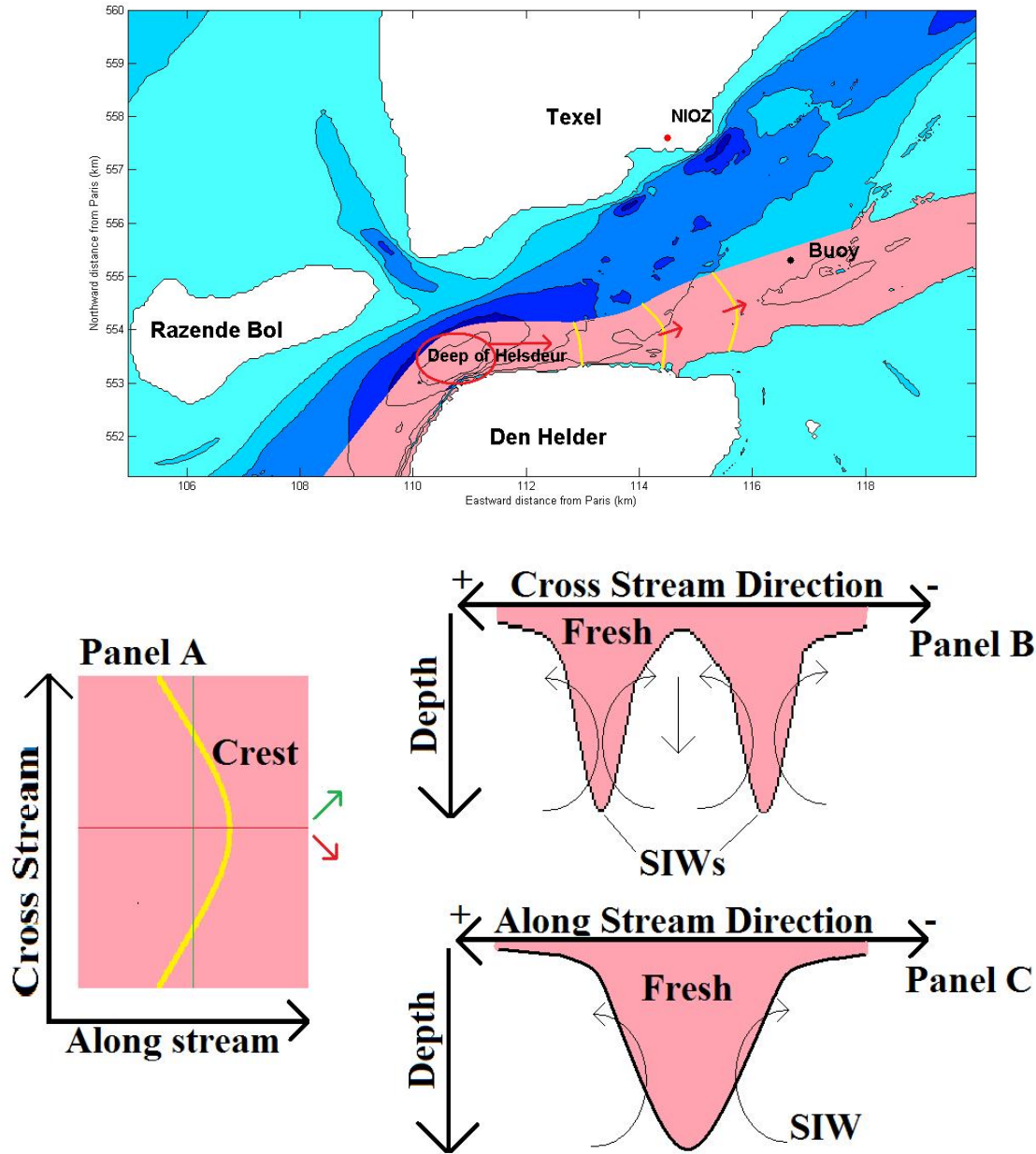


Figure 60: The upper figure shows a top view of the Marsdiep. The interface between saline water at the bottom and fresh water from the Malzwin (pink) near the surface, will form a depression above the Deep of Helsdeur (red circle). The depression will cause up current IWs when the ebb tide slackens. The red arrows indicate possible direction of propagation. The yellow lines are illustrations of wave crests propagating towards the Wadden Sea and passing the buoy. Due to interference with its surroundings it is not unlikely that the wave crests will be curved instead of straight lines. This will be noted in section 6.3.3. This has an effect on the cross stream velocity which is hard to predict and complicate the results. Panel A of the lowest figure shows a top view with an example of a curved wave crest. In the top view a red and green line is drawn which indicate intersections in the along (red) and cross (green) stream direction. Panel B shows the shape of the interface between the fresh Malzwin water at the surface and more saline water at the bottom, at the along stream intersection. Panel C shows the same for the cross stream intersection. A plus (minus) sign indicates the positive (negative) along or cross stream direction. The black arrows are the currents associated with the depression.

Category	# of times
1	10
2	8
3	6
4	9
5	5

Table 8: Number of times a certain category occurs.

The third event is the transition of the PCC into IWs. The first event is not related with the second and the third event. A PCC may occur, even when there is not a NCC. All three events, but especially the third, have strong influence on the measured vertical velocity and height of the acoustic backscatter interface.

In total 38 ebb slacks are measured. Because of the enormous amount of data not all ebb slacks can be shown. The ebb slacks have been divided into 5 categories. The first category are 'normal' slacks as in the first example (figure 55) in which only the NCC is visible. The second category contains ebb slacks with only little shear with possible a NCC and always a (weak) PCC, as in the second example (figure 57). The fifth category contains the NCC, the PCC and the wave events, specially the last two are long lasting and strong, as observed in the third example (figure 59). Slacks of the third and fourth category are in between category two and five with increasing strength and duration of the PCC and wave events. The ebb slacks are thus categorized in such a way that a higher number indicates stronger (baroclinic) events. Table (8) presents occurrences of a particular category. This is of course a very qualitative approach, but when presented using a time scale this nonetheless indicates periods of stronger or less strong events, as shown in figure (61). During the middle of the measured period strong events are observed. This is in agreement with increased phase differences between surface and bottom as explained in section 5.7.2 and shown in figure (46). It indicates that the events have a higher chance of occurrence when there is much discharge, less strong current (neap) and not too much wind (and thus mixing). These are all typical circumstances that would enhance baroclinic motions. By studying the similarities between the category five ebb slack events, one might get a more detailed impression of the physical mechanisms behind the observed structures.

### 6.3 Internal Waves or Internal Solitons?

The third example (figure 59) discussed in section 6.2.3, is a category five event. It is expected that all category five events have the same physical mechanism as proposed for the third example (figure 60). In this section the attention will be focused on discussing and understanding the incoherent velocities, vertical velocity and acoustic backscatter intensity of the category 5 events. In figure (62) the along stream incoherent velocity of respectively (from top to bottom) ebb slack number 15, 21, 22, 25 and 38 are shown. Their occurrence in time over the whole time series, can be deduced from figure (61). In figures (63) to (67) the incoherent along stream and cross stream velocity, vertical velocity, acoustic backscatter intensity are shown for the tidal phase of which the depth average along stream velocity is smaller than  $0.75ms^{-1}$  and larger than  $-0.5ms^{-1}$ . It is possible that certain occasions that are rated with a 4 would have been rated with a 5 by someone else, but the rating will be accurate enough to be able to give a detailed overview of the physical mechanism behind it. The category 5 event will now be discussed.

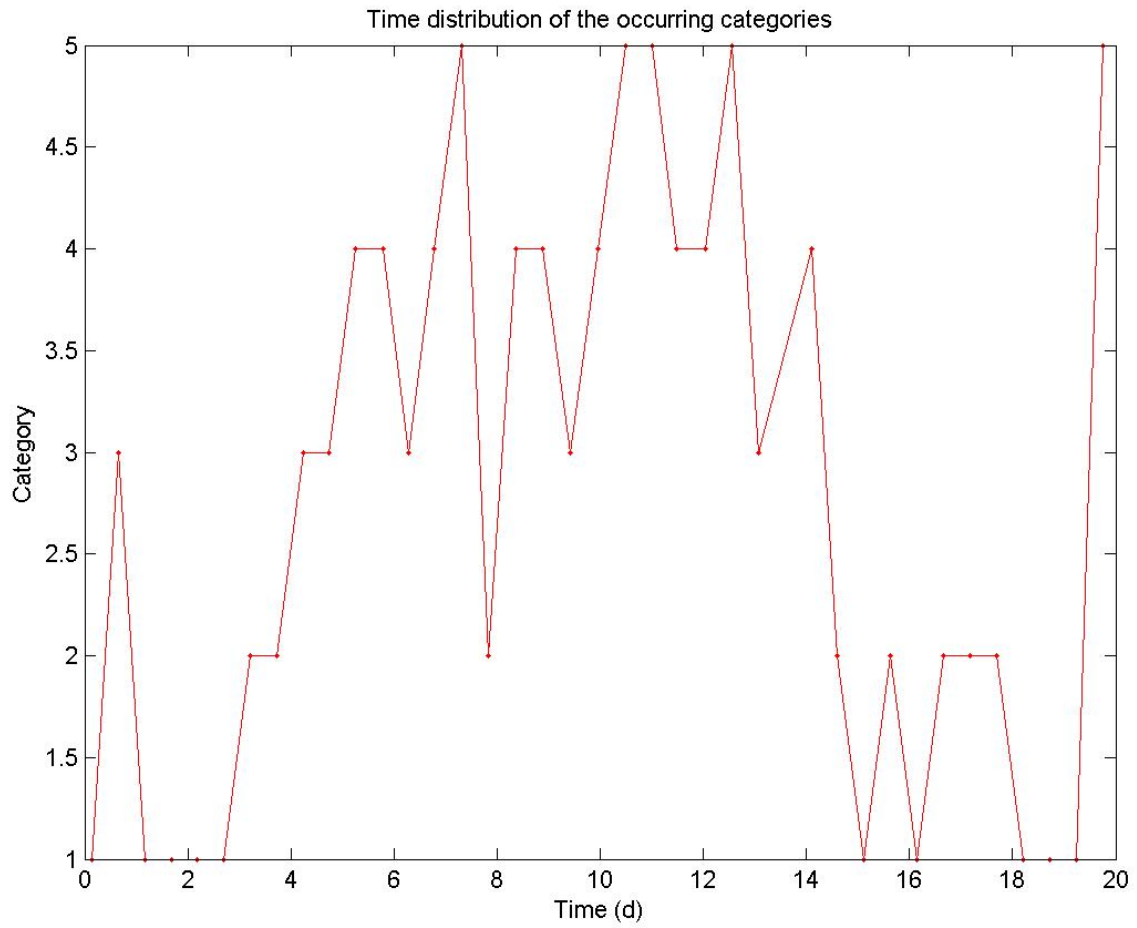


Figure 61: The time distribution of the occurring categories.

Incoherent along stream velocity ( $\text{ms}^{-1}$ ) during ebb slack. From top to bottom numbers: 15 21 22 25 and 38

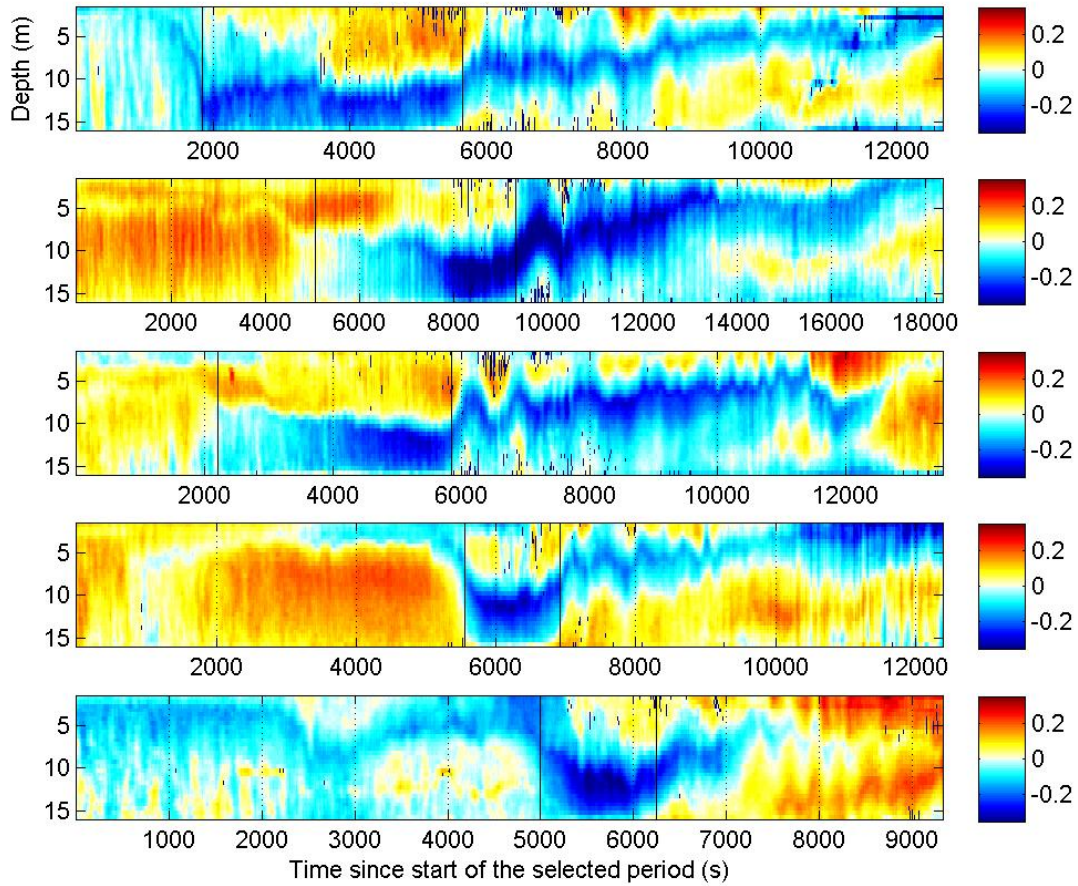


Figure 62: The 5 panels in this figure are the incoherent along stream velocity of the 5 category 5 ebb slacks. From the top to the bottom these are ebb slack number 15,21,22,25 and 38. The vertical black lines indicate the start and end of the PCCs.

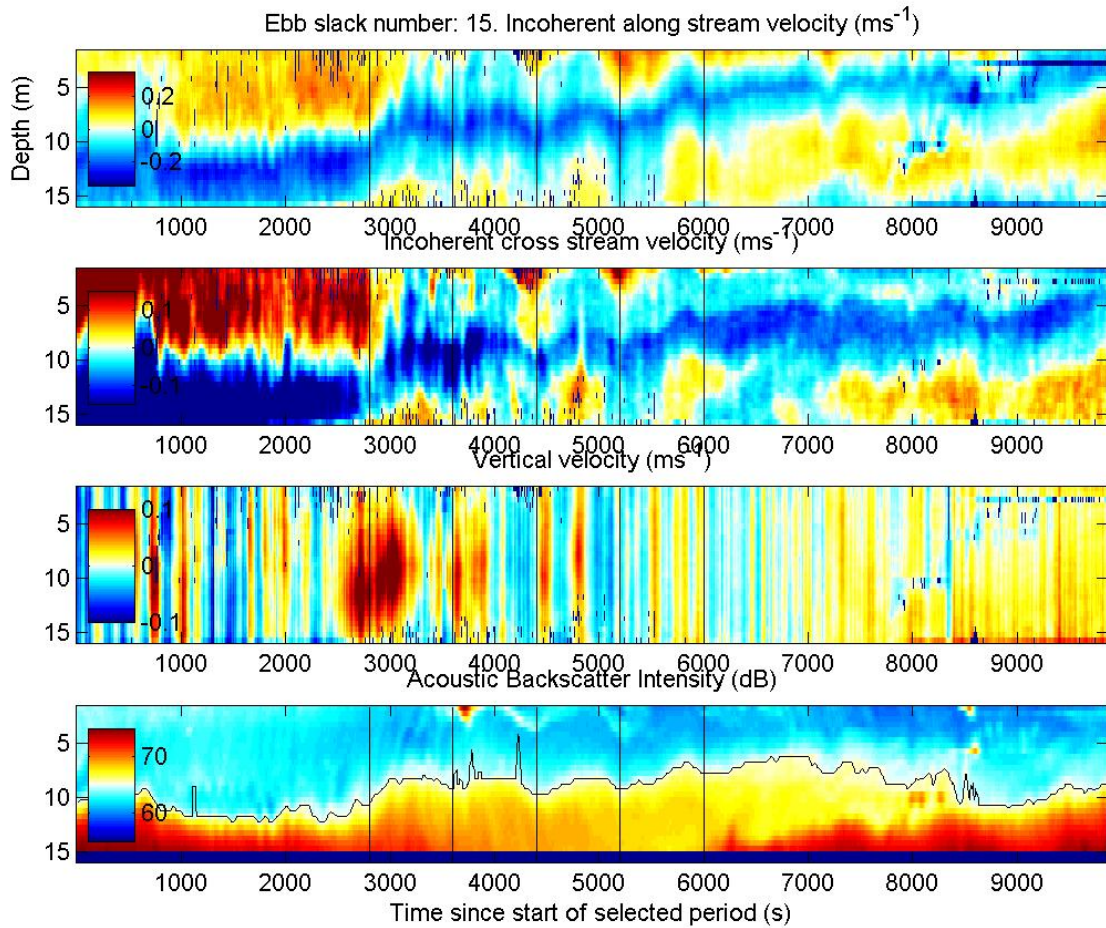


Figure 63: Ebb slack number 15 is shown, which is categorized as a category 5 event. From the upper to the lower panel respectively the incoherent along stream velocity, the incoherent cross stream velocity, the vertical velocity and acoustic backscatter intensity and its interface (black line) are shown. The vertical black lines are the crests and troughs of the waves indentified in the incoherent along stream velocity. The period that is shown is selected using measurements that are made during the period in which the depth average velocity is smaller than  $0.75\text{ms}^{-1}$  and larger than  $-0.5\text{ms}^{-1}$ .

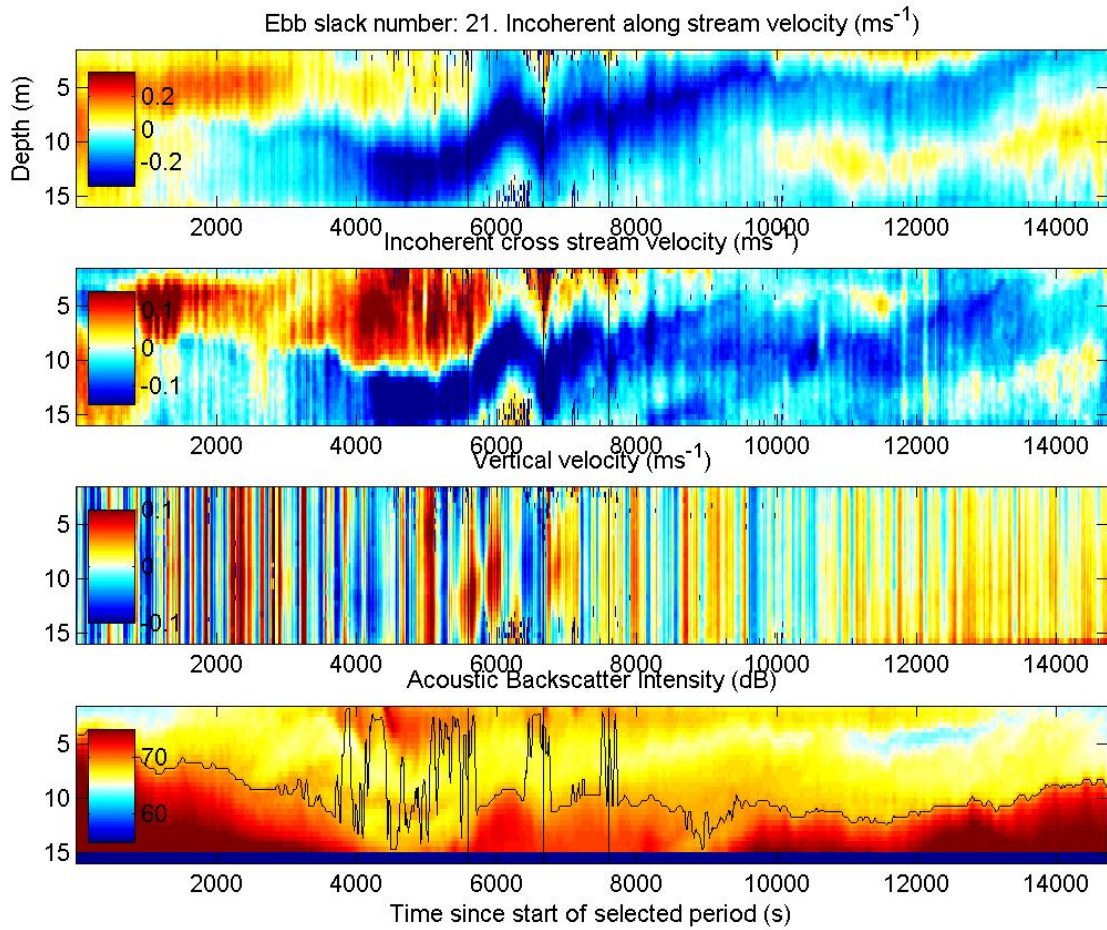


Figure 64: As figure (63) but than for ebb slack 21.

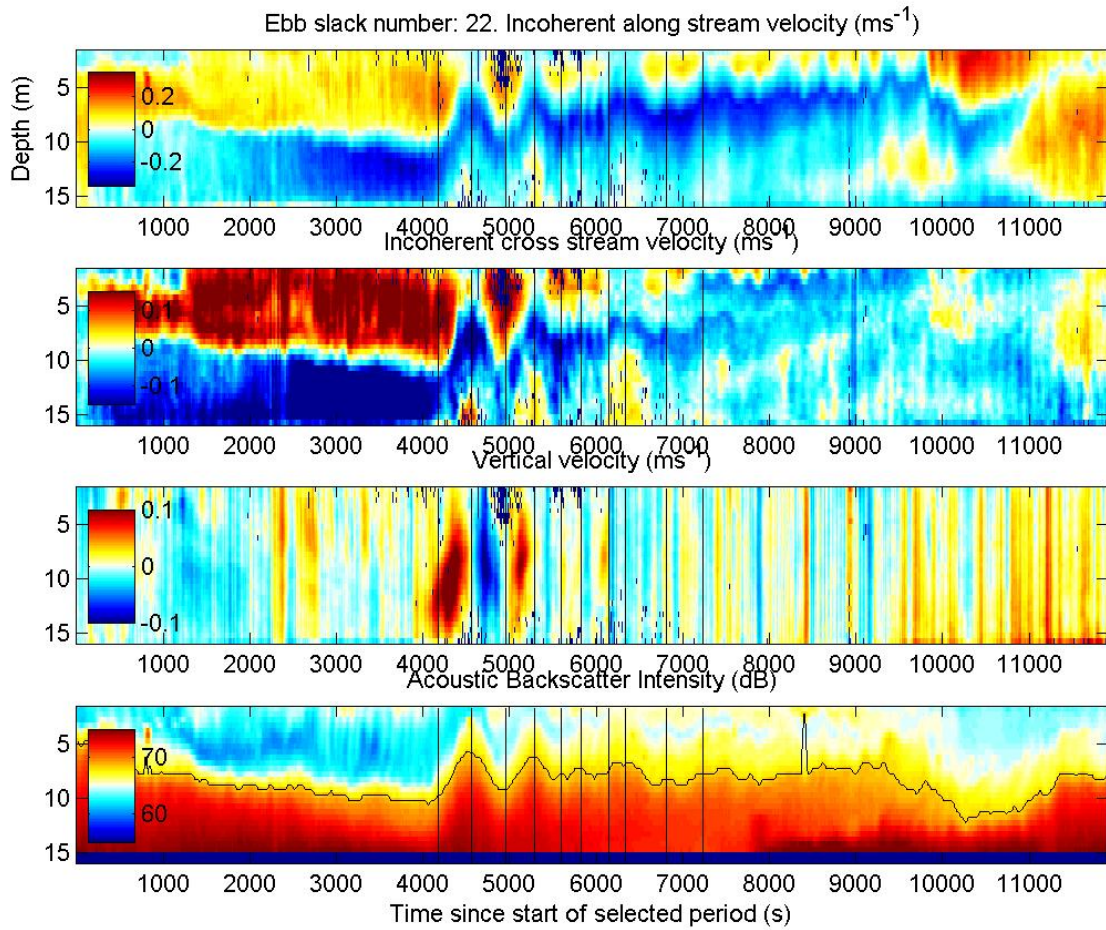


Figure 65: As figure (63) but than for ebb slack 22.



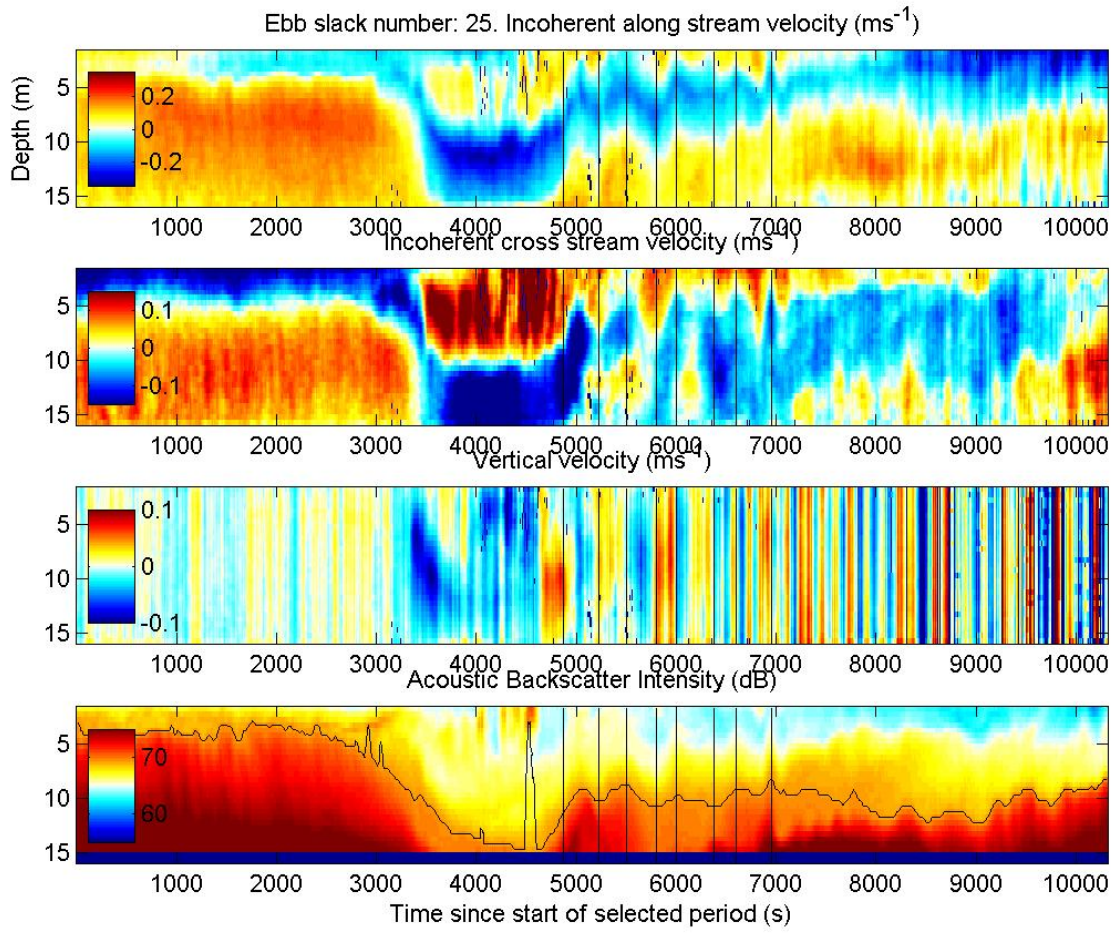


Figure 66: As figure (63) but than for ebb slack 21.

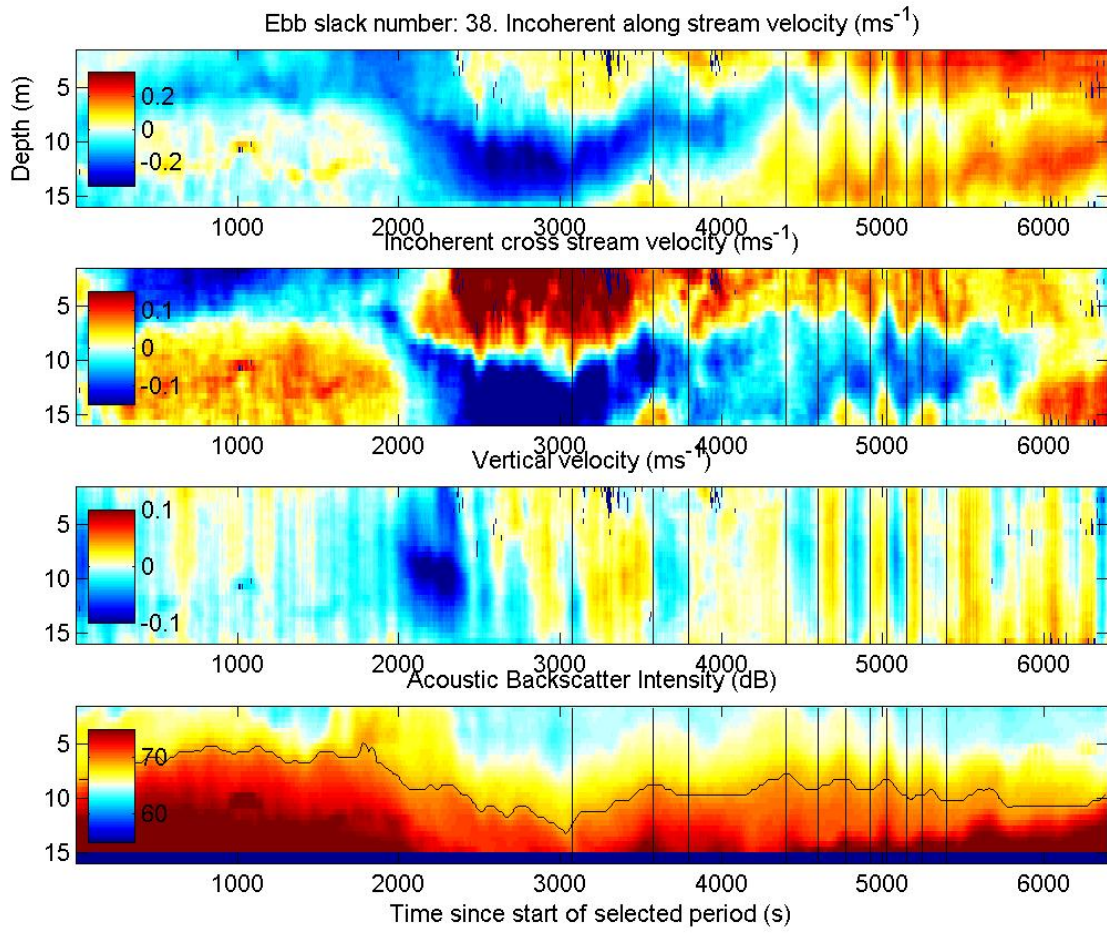


Figure 67: As figure (63) but than for ebb slack 38.

### 6.3.1 General comparison of the observed wave events

The incoherent velocities observed in figure (62) and figures (63) to (67) are not only due to baroclinic motions. As explained in the introduction of this thesis, the main forcing is the tide and secondary effects are due to the bottom and coastal friction, wind, Coriolis force, bathymetry, baroclinic currents, curvature and more. Even though some of these influences are coherent during 19.8 days with one or more of the tidal frequencies, it is expected that they are not all completely absorbed in the coherent approximation. As a result the incoherent signal is not pure baroclinic motion but will also contain currents due to other secondary effects. On top of this, even if the incoherent current would have been only baroclinic motions, it would still be complicated because the Marsdiep contains density gradients changing in strength, time and can be manifest in along stream, cross stream and vertical direction. This induces different baroclinic motions that are not all easy to separate and interpret. Therefore if there are indication of a passing IW, it must be taken into account that the motion accompanied by the IW will be superposed on top of all the motions described above that are also present in the incoherent velocity.

Fortunately, even though the signal is so complex, some coherency can be found in the incoherent velocity that indicates the phenomena observed. As can be deduced from the black lines, which are positions at crests and troughs of the along stream incoherent wave motions in figures (63) to (67), the vertical velocity can be related with the acoustic backscatter interface and incoherent along and cross stream minima. When there is a crest or trough, the vertical motion is zero. This is expected motion for a passing wave. Secondly the vertical motion is shaped as 'half a sine', with an uniform sign in the vertical and often a maximum in the middle of the water column. This is strong indication of mode 1 IWs as described in section 1.2 and shown in figure (3). In most cases (specially ebb slack 22 and 38) the waves seem to be ordered in a wave train with first the waves with the highest amplitudes followed by waves with smaller amplitudes. This is typical motion associated with ISs as also explained in section 1.2. This indicates that, in first approximation, the observed wave events are passing mode one solitary internal waves (SIWs).

### 6.3.2 Combining observations and theory.

Using the measurements a situation is sketched which can roughly be described as fresher Malzwin water on top of more saline water, resulting in a two layer stratification as illustrated in figure (58). This stratified water column flows over the Deep of Helder, so that the interface will form a depression that results in the generation of mode 1 SIWs that propagate in up current direction (from the North Sea into the Wadden Sea) during late ebb, as illustrated in figure (60). From the measurements only the amplitude and wave period can be deduced. When treating the observations as mode one IWs or pure interfacial IWs, theoretically derived equations gives the opportunity to verify the propagation direction and find the phase speeds and wave lengths of the observed waves. Of course this is only a first approximation because the reality has shown to be more complex than the theory. Use equations describing mode one IWs as already discussed in section 1.2, which is given by [12, 17, 36]:

$$w(x, z, t) = a \sin\left(\frac{\pi z}{H}\right) \cos(kx - \omega t) \quad (200)$$

$$u(x, z, t) = -a \frac{\pi}{kH} \cos\left(\frac{\pi z}{H}\right) \sin(kx - \omega t) \quad (201)$$

Where positive  $x$  is directed towards the east,  $t$  is the time,  $\omega$  is the wave frequency,  $k$  is the wave number which is positive in case of rightward propagating waves,  $z$  is the vertical coordinate

which is 0 at the surface and  $-H$  at the bottom and  $H$  is the maximum depth. The direction of propagation is given by the sign of wave number  $k$ . The wave number is part of equation (201). Because  $u$  and  $w$  are measured, the theoretical expression can be compared to the measurements to obtain the sign of  $k$  of the measurements. Before this is possible  $w$  has to be divided by  $u$  to neutralize amplitude  $a$ , which can be negative and positive. To be able to compare the theoretical signal with observations, ebb slack 22 (as given in figure 65) is used as observation example because this ebb slack has a very well defined start of the IWs starting at  $t = 4175s$ . Some assumptions are made before the measurements and theory can be compared:

- The buoy is deployed on a fixed location, therefore the spatial structure is not known. It is chosen to use  $x = 0$  as the location of the buoy.
- The constants  $\omega$  and  $H$  are positive and real. They have no further influence on the sign.
- For the calculations using equation (202), the sign of  $k$  is chosen to be positive. As a result the theoretical output will be an example for waves traveling from west to east.
- Two depth levels will be chosen to compare with measurements. These are  $z_1 = -0.4H$  and  $z_2 = -0.8H$ . Assuming an average depth during ebb of approximately  $17.5m$  (derived from figure 24), this results in  $z_1 = -7m$  and  $z_2 = -14m$ . These values are used to find the signs of  $u$  and  $w$  in the measurements.
- The variations in time are  $t \in [0, 2\pi]rad$ . Two moments in time will be chosen to compare with the measurements. These are  $\omega t_1 = \frac{\pi}{2} - \epsilon$  and at  $\omega t_2 = \frac{3\pi}{2} - \epsilon$ . Note that  $\omega$  is a constant and  $\epsilon$  is a small value. In the picture of ebb slack 22 these moments in time are just before the second and third vertical black lines assuming that the first vertical black line indicates the start of the wave.

Divide equation (200) by equation (201) and apply the assumptions:

$$\chi(z, t) = \frac{w(0, z, t)}{u(0, z, t)} = \frac{kH \sin\left(\frac{\pi z}{H}\right) \cos(\omega t)}{\pi \cos\left(\frac{\pi z}{H}\right) \sin(\omega t)} = \frac{kH \tan\left(\frac{\pi z}{H}\right)}{\pi \tan(\omega t)} \quad (202)$$

Inserting the different time and depth positions for the theoretical and measured currents, the sign of  $\chi$  can be determined. The results are given by table (9) and show that the signs of the theoretical model and observation are in agreement with each other. As a result one can conclude that the waves observed must propagate in the same direction as the theoretical waves, leading to a west-east propagation. This is the same as waves moving from the North Sea into the Wadden Sea and is in agreement with the proposed mechanism of creation of the SIWs (figure 60). Only one example is used to conclude that the direction of propagation is from into the Wadden Sea, but it is assumed that the underlying physical processes that causes the category five events are of the same and therefore this should apply to all examples during ebb slacks.

Two important variables can be directly obtained from the measurements, these are the wave period,  $T(s)$  and amplitude  $a(m)$ . Using  $\omega = \frac{2\pi}{T}$ , the frequency is calculated ( $rad\ s^{-1}$ ). Two other wave properties that would be convenient to know are the phase velocity,  $c(ms^{-1})$  and wave length  $\lambda(m)$ . These are related using:

$$\lambda = (c + \bar{u})T \quad (203)$$

Where the phase velocity is corrected for the barotropic depth averaged background current ( $\bar{u}$ ). The find  $\lambda$  the phase speed  $c$  needs to be calculated. There are two options, the first is to use the dispersion relation for mode 1 IWs which is given by [12]:

$$c_{IW} = \pm \frac{H\omega}{\pi} \sqrt{\left(\frac{N^2 - \omega^2}{\omega^2 - f^2}\right)} \quad (204)$$

Here  $N^2$  is the buoyancy frequency which is given by:

$$N^2 = -\frac{g}{\rho_0} \left(\frac{d\rho_0}{dz} + \frac{g\rho_0}{c_s^2}\right) \quad (205)$$

Where  $g = 9.81ms^{-2}$  is the gravitational acceleration,  $\rho_0$  is a reference density,  $c_s$  is the speed of sound in the water. Because the Marsdiep is shallow water it is assumed that  $\frac{d\rho_0}{dz} \gg \frac{g\rho_0}{c_s^2}$ . It is assumed that  $f^2 \ll \omega^2$ . Inserting this into equation (204) results in:

$$c_{IW} = \pm \left(\frac{2H}{T}\right) \sqrt{\frac{N^2 T^2}{4\pi^2} - 1} \quad (206)$$

The second method to calculate the phase speed is by using the phase speed of interfacial waves with an amplitude correction factor which is a result of nonlinear wave propagation which is a characteristic of ISs [24]. This is described by:

$$c_{IS} = c_0 \left(1 + \frac{a\alpha}{3}\right) \quad (207)$$

Where  $\alpha$  is a correction factor and  $c_0$  is the linear interfacial wave speed. The expressions for  $\alpha$  and  $c_0$  are:

$$c_0 = \sqrt{\frac{g(\rho_2 - \rho_1)h_1h_2}{\rho_2h_1 + \rho_1h_2}} \quad (208)$$

$$\alpha = \frac{3}{2h_1h_2} \frac{\rho_2h_1^2 - \rho_1h_2^2}{\rho_2h_1 + \rho_1h_2} \quad (209)$$

Where  $h_1, \rho_1$  and  $h_2, \rho_2$  are respectively the thickness and density of the surface and bottom layer. All variables can be obtained if first  $T$  and  $a$  are determined so that the frequency can be calculated. Several other environmental parameters have to be specified for the calculations. During ebb it is assumed that  $H = 17.5m$  (using figure (24)). Using the depth of the interface of the PCC in figure (62), the two layers are approximated as  $h_1 = 9.5$  and  $h_2 = 8$ . Using the Navicula measurements as presented in figure (49), the densities during ebb in well stratified conditions (as assumed for the category five events) are  $\rho_1 = 1024kgm^{-3}$  for the upper layer and  $\rho_2 = 1027kgm^{-3}$  for the lower layer, with an approximated average background value of  $\rho_0 = 1026kgm^{-3}$ . For the calculation of  $N^2$  a uniform stratification is assumed. In that case one should interpret this as:  $\frac{d\rho_0}{dz} = \frac{\rho_2 - \rho_1}{-H} = -\frac{3}{17.5} = -0.17kgm^{-4}$ . The values for  $H, h_1, h_2, \rho_1, \rho_2, \rho_0$  and  $\frac{d\rho_0}{dz}$  are assumed to be the same for each ebb slack and result in  $c_0 = 0.35ms^{-1}$ ,  $N^2 = 1.6 * 10^{-3}rads^{-1}$  and  $\alpha = 0.030$ . The values for  $T, a$  and  $\bar{u}$  are derived for each ebb slack separately. An overview of the results for each ebb slack is given in table (10) together with the duration of the PCC and the amount of waves the PCC dissipates into.

Time	$t_1$		$t_2$	
Depth	$z_1$	$z_2$	$z_1$	$z_2$
$u_m$	-	+	+	-
$w_m$	+	+	-	-
$\chi_m$	-	+	-	+
$\chi$	-	+	-	+

Table 9: This table is used to determine the direction of propagation of the observed SIWs. Two locations in time ( $t_1$  and  $t_2$ ) and depth ( $z_1$  and  $z_2$ ) resulting in four possible combination, have been used as an example to compare theoretical and observed values of the sign of  $\chi$ . The variables  $u_m$  and  $w_m$  are the signs obtained at a location defined by a certain combination of  $t$  and  $z$  using the measurements for the along stream and vertical velocity. These are divided as defines in equation 202 to obtain  $\chi_m$ . For the propagation to be from west to east, the sign of the theoretical value of  $\chi$ , has to be equal to the observed value of  $\chi_m$ . This is indeed the case, so it can be concluded that waves propagate to the east (into the Wadden Sea).

Ebb slack #	15	21	22	25	38
PCC (s)	3800	4250	3650	1375	1250
# Waves	4	2	4	5	5
$T$ (s)	4x800	1075/925	775/650 500/550	350/2x575 465/210	725/800/325 225/250
$a$ Range (m)	2-3	2.5-3.5	2-5	2-3	2-4
$\omega_{min}$ ( $s^{-1}$ )	$1.3 * 10^{-3}$	$1.1 * 10^{-3}$	$1.3 * 10^{-3}$	$1.7 * 10^{-3}$	$1.3 * 10^{-3}$
$\omega_{max}$ ( $s^{-1}$ )	$1.3 * 10^{-3}$	$0.9 * 10^{-3}$	$2.0 * 10^{-3}$	$4.8 * 10^{-3}$	$4.4 * 10^{-3}$
$\bar{u}$ ( $ms^{-1}$ )	-0.24 - 0.12	-0.11 - 0.10	-0.16 - 0.11	-0.15 - 0.21	-0.11 - 0.46
$c_{IW}$ ( $ms^{-1}$ )	0.22	0.22	0.22	0.21	0.22
$c_{IS}$ ( $ms^{-1}$ )	0.38	0.39	0.40	0.38	0.39
$\lambda(m)$	112/400	301/453	109/281	46/126	203/212

Table 10: The table showing the characteristics of the observed category five events. The 1<sup>st</sup> row is the number of the ebb slack. The 2<sup>nd</sup> row gives the duration of the PCC deduced from figure (62). The 3<sup>th</sup>, 4<sup>th</sup> and 5<sup>th</sup> row is obtained using figures (63) to (67) and show the number of waves produced by the PCC, the periods of the waves and the amplitude range. The 6<sup>th</sup> and 7<sup>th</sup> row are the minimum and maximum frequencies calculated using the longest and shortest period. The 8<sup>th</sup> column is the depth averaged barotropic tidal velocity at the start and end of the period in which the waves are observed. The 9<sup>th</sup> and 10<sup>th</sup> column is an indication of the phase speed calculated using equation 204 and 207. The 11<sup>th</sup> and last column is the wave length of the first and last wave, calculated using the corresponding period and depth averaged barotropic current.

### 6.3.3 Concluding discussion of the observations

A sudden occurrence of a NCC is explained using the finite width of the cross stream channel. Currents due to curvature and tidal motion are directed towards Den Helder and cause a current near the bottom in the opposite direction (figures 55 and 56). The resulting NCC passes the buoy causing rapid changes in the observed vertical incoherent current structure and acoustic backscatter interface. This event does not seem to be related with second event, the PCC. In 28 of the 38 measured ebb slacks a PCC is observed (category two or higher in table 8). The PCC is created due to a fresh water mass flowing out of the Malzwin trough the Marsdiep towards the North Sea. A fresh water mass on top of more saline water at the south side of the Marsdiep creates baroclinic currents manifested in a PCC that lasts approximately 20-70 minutes. Under influence of the resulting PCC created by the water mass itself, the fresher water propagates toward the north and (based on observations and experience from the crew of the Dokter Wagemaker) may reach up half to 2/3 of the cross stream channel width of the Marsdiep. When the front passes the buoy, the associated currents are measured (figures 57 and 58). From the stratified situation resulting from this fresh water mass, an interface is created on which mode one SIWs can propagate. The waves were categorized as mode 1 IWs due to the shape of the vertical velocity and associated bending of the acoustic backscatter interface which is used as a proxy for the shape of the isopycnals. The waves are categorized as IS because waves with higher amplitudes are observed before waves with smaller amplitudes (figures 62 to 67). The combination results in mode one SIWs. The direction of propagation is expected to be eastward because the buoy is located east of the expected source. The source is a depression of the interface that are expected to occur when the stratified water column moves over the Deep of Helsdeur. The resulting depression leads to mode one SIWs that will propagate up current (eastward into the Wadden Sea) when the slackening ebb current decreases to a value below the phase speeds of the mode one SIWs (figure 60). This idea was confirmed using a simple theoretical equation describing mode one IWs (equation 202 and table 9). Only one problem remains. The observed SIWs are waves of elevation while the source predicts wave of depression. A possible explanation for this is found in the fact that, between the Deep of Helsdeur and the location of the buoy, the depth of the water column quickly reduces. At the location of the buoy, the measurements show that, roughly, the water column seems to be separated into two layers with the surface layer ( $h_1$ ) larger than the lower layer ( $h_2$ ). It is assumed that at the Deep of Helsdeur, the surface layer must be (much) smaller than the bottom layer. As a result the SIWs propagate from a situation with  $h_1 < h_2$  to a situation in which  $h_1 > h_2$ . Using modified KdV equations [12, 24], this leads to a change in sign of the amplitude of the SIWs and therefore results in SIWs of elevation instead of depression.

From the measurements only amplitudes and periods of the measured SIWs could be deduced. Using the theoretical mode one IW equations (equation 204 and 207) an attempt has been made to find the associated phase speeds and wave lengths. Using the results given in table (10) some conclusions can be drawn. The observed number of SIWs are between 2 and 5. The wave period varies between approximately 4 and 18 minutes. In general the amplitudes of each subsequent wave is smaller than the wave preceding, which as suggested, indicates SIWs propagating with a phase speed that depends on the amplitude. Most waves are observed during a barotropic background current between  $-0.2ms^{-1}$  and  $0.2ms^{-1}$ . The phase speed calculated using linear IW theory is smaller than that calculated using the a two layer model that takes into account nonlinear effects, resulting in an amplitude depending velocity which is typical for SIWs. Though both velocities are in a realistic range, meaning that the value is lower than the barotropic background current during the main part of the ebb phase and are therefore only released when the ebb current slackens, it

is assumed that  $c_{IS}$  is the best representation for the waves phase speed because the waves seems to be (weakly) nonlinear.

The phase speed calculated is a local phase speed, because from their source toward the buoy the phase speed has changed due to changes in the total depth. As a result the depth of the bottom layer must, and that of the surface layer will probably, change. As an example a rough estimation of the phase speed at the Deep of Helder can be made assuming that the stratification, amplitude and thickness of the surface layer stays equal and that the bottom layer increases to  $h_2 = 30m$ . This results in  $\alpha = 0.21$ ,  $c_0 = 0.46$  and therefore (using  $a = 3$ ) into  $c_{IW} = 0.56ms^{-1}$ . This rough estimation shows that the original phase velocity will probably be higher. Taking this into account, the waves start propagating towards the Wadden Sea when the ebb current reaches a values lower than  $u \approx 0.56$ . During their journey from the Deep of Helder toward the buoy, the net speed of the waves ( $v = c_{IS} + \bar{u}$ ) increases due to slackening barotropic background currents and decreases due to the phase speed decrease caused by changing layer depths. The first waves reach the buoy station when the background current has already slackened to a value of approximately  $-0.2ms^{-1}$  or higher. Using  $c_{IS}$  gives an opportunity to calculate the wave length using the first and last measured wave periods (generally the longest and shortest) and associated background currents. As a result two wave lengths are given. The calculated wave lengths vary between  $46m$  and  $450m$ , with most wave lengths centered around  $200m$ . In general the wave lengths increase from the first to the last waves. This is typical for ISs and therefore another argument that the observed waves are mode 1 SIWs. Using all the information above the result can be summed up as follows:

- The Marsdiep is very complex if it comes to describing measured currents. Though a good approximation for the along stream coherent velocity is obtained using a LSHA, the resulting incoherent velocity is still complex and not only due to baroclinic motion. Secondary effects due to curvature, wind induced currents, missing low frequent tidal components, bathymetry, etc. are of great influence. Baroclinic motions are superposed on top of this and therefore not always easy to recognize.
- Measured baroclinic motions in the incoherent velocity, is not always due to passing SIWs. The stratification and associated baroclinic currents are variable in along stream, cross stream and vertical direction and change in strength and time due to influence that are not easily predicted. As a result it is hard to separate different sources of baroclinic motion from one another. Therefore the motions due to passing SIWs are hard to separate from other baroclinic motions which are already hard to separate from the secondary effects.
- The physical mechanism behind the observed NCC is not related with the mechanism behind the observed PCC and waves.
- The waves are assumed to be IWs because of the relation between the acoustic backscatter interface and the vertical velocity in combination with the measurements of the incoherent cross stream and along stream velocity.
- The waves are thought to be mode 1 IWs because of the vertical structure of the vertical velocity, which has the shape of half a sine.
- The waves are thought to be nonlinear because of the decreasing amplitude and increasing wave length of waves in measured wave trains.
- The mechanism that is used to explains the observed mode one SIW assumes east ward wave propagation. This idea is verified using equation describing mode 1 IWs.



- The interface on which the waves propagate might not be horizontal but in an angle with the horizontal leading to small variation in the currents expected due to passing mode 1 SIW.
- The front of the fresh water causing a PCC is not a straight line and does not necessarily has to be in the exact direction as the along stream current. This might be a reason why the PCC is measured in both the incoherent along and cross stream direction (see figure 58).
- The SIWs band stretching in the cross channel direction are not expected to be straight lines. At the Den Helder side of the channel it is less deep. The changes in depth might cause differences in the thickness of the surface and bottom layer resulting in different phase speeds in the cross channel direction. As a result the waves will not propagate in a straight line but will be bend, as illustrated in figure (60). This might lead to effects in the incoherent velocities that are hard to predict.
- The variations of the acoustic backscatter interface due to the passing SIWs indicate that the SIWs may transport suspended matter [33]. This would be of importance for the net budget of suspended matter transport through the Marsdiep.
- The ISs observed on the picture of figure (1) are said to propagate towards the North Sea during flood currents. This is in opposite direction than the waves described in this thesis during the ebb phase. What is important to notice is that, when stratification occurs in the Marsdiep during ebb phase, it is not unlikely that the same is possible during flood phase. An example of the possible existence of ISs during flood current is given in figure (68). It may be therefore concluded that the elongated bands of deviant surface roughness extending in cross channel direction that slowly propagate out to the North Sea are very likely surface manifestation of currents associated with ISs.

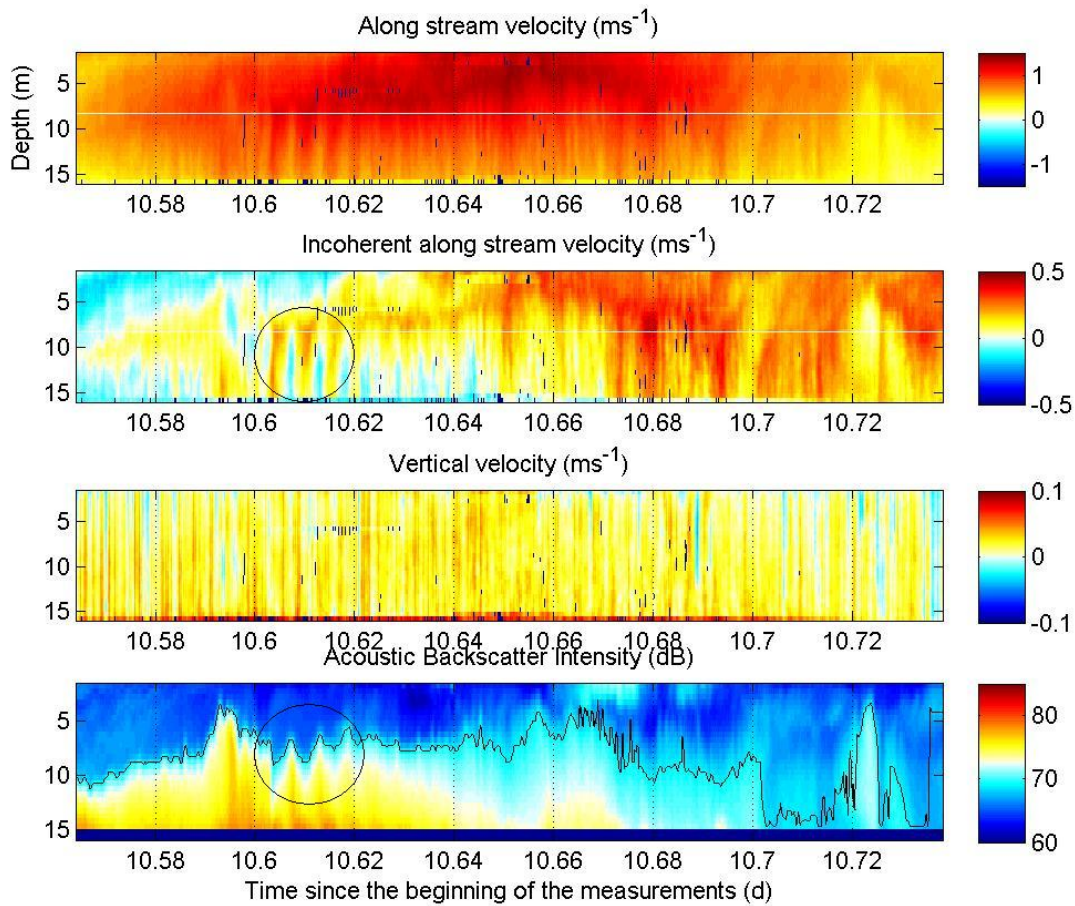


Figure 68: Flood measured after ebb slack 21 (category five event). During strong flood currents soliton like waves in the incoherent along stream velocity and acoustic backscatter intensity, is indicated with a black circle. Events like these have to be studied to determine the physical processes related with it, but it is not unlikely that they are results of ISs.

## 7 Conclusions

The goal of this thesis was to verify the hunch that the patterns in figure (1), observed at the sea surface of the Marsdiep, were the surface manifestation of currents caused by propagating ISs. In general the Marsdiep is assumed to be vertically well mixed due wind in combination with its shallowness and strong tidal motion which interacts with the bottom causing turbulence [38, 39]. Measurements obtained from the R.V. Navicula showed however, that the Marsdiep can be vertically stratified accompanied with vertical shear of horizontal currents, during slack tide. As a result, during slack tide in combination with little wind and enough discharge of fresh water from Lake IJssel, the vertical stratification might manifest IWs. Knowing this, a deployment was prepared that would measure the water velocity for three months.

The deployment was highly experimental because of the online transmission of data to NIOZ and the rough circumstances in the Marsdiep. Steep waves, possibly stormy circumstances and strong currents caused problems. The first version of the deployment had a chain that was too short, too many outlets through which water poured into the interior and was under large influence of the surface wind waves leading to strong pitch and roll events. The interior was destroyed due to leakage. The second version had a longer chain and was completely closed. Unfortunately the pole that carried the antennas that send the information to the NIOZ had fatigue problems caused by movement due to pitch and roll events which were a result of the large amount of surface waves. The pole broke down and no more data were send and therefore the experiment was ended. In total 19.8 days of data was gathered instead of 90 days. This was a pity from the data point of view, but experimentally much is learned for future deployment. Several possible improvements for future deployments are proposed in section (2).

The 19.8 days of data were used as the core of this thesis. It is expected that, if present, the ISs would be manifest in the baroclinic currents that should be present within the measured currents. To be able to separate the baroclinic current from all other currents, all other currents should be predicted and subtracted from the data set. Using a LSHA approximation good understanding of barotropic and coherent currents was obtained. It was shown that the currents in the Marsdiep are dominated by the strong tidal currents. This was in agreement with previous studies [2, 31, 38, 39, 28]. The currents rotates  $AC$ . The LSHA approximation contained 14 tidal constituent with which 95.6% of the along stream signal and 71.0% of the cross stream velocity variance was explained. The obtained signal was interpreted as a signal containing motions that are coherent during 19.8 days with frequencies equal to that of the used tidal frequencies. The coherent signal was compared with an analytical barotropic model which could predict the main tidal current using the obtained amplitudes and phases of the 14 constituents that resulted from the LSHA. The model takes into account the effects of the Coriolis force and bottom friction with partial slip and was fitted to the data set using slip parameter of  $s = 1.3 * 10^{-3}ms^{-1}$  and an eddy viscosity parameter of  $\nu = 1.37 * 10^{-2}m^2s$ .

The comparison of the model with the coherent velocity showed that the along stream signals are alike for the coherent velocity and the model. The cross stream currents showed large differences that could be explained using the Coriolis deflection of the along stream current in a channel with a finite width [34, 15]. The model uses an infinite width and uniform infinite depth. The basin has a finite width and not a uniform depth. As a result cross stream circulation cells occur that are not captured by the barotropic model but are captured in the coherent signal. The model also showed that the clockwise currents are more influenced by cross stream processes than the anti-clockwise currents.

Before studying the measured buoy data, first short term data collected with the R.V. Navicula

was studied. The Navicula data contains measurements of currents, stratification and acoustic backscatter intensity. A LSHA was applied to the Navicula current data, but because of the data's short duration (13h), the baroclinic motion within this data set were also seen as coherent and therefore incorporated in the LSHA. By using the LSHA amplitudes and phases as input for the analytical barotropic model, this problem was solved. The predicted barotropic currents were subtracted from the Navicula measurements to obtain the incoherent currents. This resulted in Navicula data showing strong stratification events, bending of isopycnals and also structures in the horizontal and vertical velocities were found that indicated possible mode 1 IWs. It was now clear that strong stratification exist in the Marsdiep and may manifest IWs.

The incoherent signal of the buoy data are the measurements from which the coherent current (LSHA approximation) is subtracted. Baroclinic currents due to IWs are expected to be manifest in the incoherent motion. Unfortunately it is expected that the incoherent motion obtained is not only due to baroclinic currents caused by IWs. Also other effects that change in strength and time will have influence on the incoherent velocity. Examples are baroclinic currents due to density gradients in any direction, wind induced currents, tides with very low frequencies and curvature effects. As a result the incoherent velocity is a superposition of several physical processes. Motions due to IWs will be superposed on top of these processes and therefore not always be as visible as clear as in the theoretical expectations.

Nonetheless the incoherent buoy data was extremely interesting during ebb slacks. In total 38<sup>th</sup> ebb slacks were measured and categorized in five groups which showed signs of increasing possibility of passing IWs. In total five events of the highest category were found and used as example to indicate the processes observed. Fresh water mass from the Malzwin causes cross stream and vertical density gradients. Under influence of the associated baroclinic current the fresh water mass expands toward Texel (the north), maximally up to 2/3 of the cross channel width. Under influence of ebb current the fresh water mass is pushed towards the North Sea and is forced over the Deep of Helsdeur. In first approximation a two layer stratification occurs and isopycnal are bend into a depression when passing over the Deep of Helsdeur. The resulting baroclinic pressure gradient causes waves to propagate up and down current away from the source. Up current (in the direction of the Marsdiep and the buoy) waves can only propagate if their phase speed is larger than the barotropic ebb current. This happens when the tide slackens. The vertical structure of the vertical amplitude suggest mode 1 IWs. The altered acoustic backscatter interface (which serves as a proxy for the shape of isopycnals) and the incoherent velocities show a decrease of amplitude and increase of wave length of incoming wave trains, indicating nonlinearity of the waves. As a result mode 1 SIWs are obtained. It is known that SIWs may act as nutrient pumps [33]. Therefore the motions of the acoustic backscatter interface due to the passing SIWs indicate that the waves influence the transport of suspended matter in the water column and therefore contribute to the net transport of suspended matter between the North Sea and the Wadden Sea through the Marsdiep. As a result the SIWs may be of interest for the ecology of the Wadden Sea.

The SIWs were ordered in wave trains consisting 2-5 waves with decreasing amplitudes between 2m-5m and a period between 4 and 18 minutes. The phase speeds at the location of the buoy was estimated to be approximately  $0.39m.s^{-1}$ . The waves are assumed to start as SIWs of depression above the deep of Helsdeur with phase velocities higher than those calculated at the location of the buoy. Because on their journey the surface layer becomes larger than the bottom layer, they turn to SIWs of elevation [24]. Using the barotropic background current at their time of arrival at the buoy and their phase speed, wavelengths between 46m and 450m have been derived.

In this thesis eventually only ebb slacks have been investigated. Quick looks have showed some signs that during flood slacks and strong flood currents (when a salt wedge accompanied with

strong stratification enters the Marsdiep) possible IW motion was visible as shown in figure (68). These and other suggestions for further research are:

- Search for IW or IS motion during flood phase.
- Determine the stability of the buoy used for the deployment. This can be used for future deployments.
- Improve the barotropic model by including turbulence, depth depending eddy viscosity, bathymetry, finite channel width and baroclinic currents.
- Try to measure IWs that should be found at the down current side of the Deep of Helsdeur to validate the suggested source for the SIWs.
- Compare the measured SIW with theoretical models
- Obtain measurements with a longer duration, simultaneously at different locations, to be able to better estimate propagation speed and direction. Also the LSHA and therefore barotropic model will be of better quality because more constituents can be used. These measurements may lead to a prediction method for the occurrence of the IWs and to a quantitative estimation of their influence on the transport of suspended matter between the North Sea and Wadden Sea. The data could also be used to verify the proposed change in sign of the amplitude of the observed SIWs.
- The enormous amount of data (being) gathered by the ADCPs mounted under the hull of the TESO ferries: The Dokter Wagemaker and Schulpengat, must have measured passing SIWs and can be analyzed to verify this.

In the end it may be concluded that the research described in this thesis was a success. A new deployment technique is tested from which much is learned and it is shown that the surface roughness differences shown in figure (1) are likely the surface manifestations of passing SIWs.

### *Acknowledgment*

*I thank Rijkswaterstaat for the discharge data of Lake IJssel. Many people of the NIOZ put their trust in me and worked with me to complete the research described in this thesis. Many of them are named in the appendix. But a special thanks go's out for my supervisor Leo Maas. Without him this thesis would have been impossible to complete.*

## 8 Appendix

### 8.1 Velocity triangle calculations

The first step shown in figure (29) is calculating the rotary components using the LSHA amplitudes and phases. This is done in equations (73),(74),(75) and (76). Step #2, calculating the ellipse parameters from the rotary currents is given by equation (88),(82),(83) and (78). The last step that is already given is step #5. In equations (92),(93),(90) and (91) the rotary currents are determined from the ellipse parameters. This is the opposite of step two. There are now three steps remaining. The easiest step, step #4, is to calculate the ellipse parameters directly from the LSHA amplitudes and phases. This can be done by inserting equations (73),(74),(75) and (76) into equations (88),(82),(83) and (78) resulting in:

$$\psi_P = \frac{1}{2} \left[ \arctan \left( \frac{U \sin(\phi_u) + V \cos(\phi_v)}{U \cos(\phi_u) - V \sin(\phi_v)} \right) - \arctan \left( -\frac{U \sin(\phi_u) - V \cos(\phi_v)}{U \cos(\phi_u) + V \sin(\phi_v)} \right) \right] \quad (210)$$

$$U_{Ma} = \frac{1}{2} \left[ \sqrt{U^2 + V^2 + 2UV \sin(\phi_v - \phi_u)} + \sqrt{U^2 + V^2 - 2UV \sin(\phi_v - \phi_u)} \right] \quad (211)$$

$$\psi_I = \frac{1}{2} \left[ \arctan \left( \frac{U \sin(\phi_u) + V \cos(\phi_v)}{U \cos(\phi_u) - V \sin(\phi_v)} \right) + \arctan \left( -\frac{U \sin(\phi_u) - V \cos(\phi_v)}{U \cos(\phi_u) + V \sin(\phi_v)} \right) \right] \quad (212)$$

$$U_{Mi} = \frac{1}{2} \left[ \sqrt{U^2 + V^2 + 2UV \sin(\phi_v - \phi_u)} - \sqrt{U^2 + V^2 - 2UV \sin(\phi_v - \phi_u)} \right] \quad (213)$$

What is left is to calculate the LSHA amplitudes and phases from ellipse and rotary currents. The easiest way to do this is to use equation (69), (70), (71) and (72) to obtain an expression for the amplitudes and phases in terms of the rotary parameters. To do so one needs to insert equation (71) into equation (69) and insert equation (72) into equation (70). This can be done in two ways. Each time replacing a different term. This results in the following 4 equations:

$$V \cos(\phi_v) = U_{ac} \sin(\theta_{ac}) + U_c \sin(\theta_c) \quad (214)$$

$$V \sin(\phi_v) = U_{ac} \cos(\theta_{ac}) - U_c \cos(\theta_c) \quad (215)$$

$$U \cos(\phi_u) = U_{ac} \cos(\theta_{ac}) + U_c \cos(\theta_c) \quad (216)$$

$$U \sin(\phi_u) = -(U_{ac} \sin(\theta_{ac}) - U_c \sin(\theta_c)) \quad (217)$$

The phases can now be found by dividing respectively equations (215) and (214) by (217) and (216):

$$\phi_v = \arctan \left( \frac{U_{ac} \cos(\theta_{ac}) - U_c \cos(\theta_c)}{U_{ac} \sin(\theta_{ac}) + U_c \sin(\theta_c)} \right) \quad (218)$$

$$\phi_u = \arctan \left( -\frac{U_{ac} \sin(\theta_{ac}) - U_c \sin(\theta_c)}{U_{ac} \cos(\theta_{ac}) + U_c \cos(\theta_c)} \right) \quad (219)$$

Category	# of times
LSHA	Least Squares Harmonic Analysis
IS(s)	Internal Soliton(s)
IW(s)	Internal Wave(s)
SIW(s)	Solitary Internal Wave(s)
AS(s)	Anchor Station(s)
INC	Inclination with angle ( $\psi_I$ )
PHA	Ellipse Phase angle ( $\psi_P$ )
SEMI	Semi minor Axis with amplitude ( $U_{Mi}$ )
SEMA	Semi major axis with amplitude ( $U_{Ma}$ )
ECC	Eccentricity with angle $e$
TESO	Texel Own Steamship Company
SSH	Sea Surface Height
FT	Fourier Transform
DTFT	Discrete Time Fourier Transform
KdV	Korteweg- de Vries
NIOZ	Royal Netherlands Institute for Sea Research

By squaring equations (214) and (215) and the same for equations (216) and (217) expressions can be obtained for the amplitudes:

$$U = \sqrt{(U_{ac} \cos(\theta_{ac}) + U_c \cos(\theta_c))^2 + (-U_{ac} \sin(\theta_{ac}) + U_c \sin(\theta_c))^2} \quad (220)$$

$$V = \sqrt{(U_{ac} \sin(\theta_{ac}) + U_c \sin(\theta_c))^2 + (U_{ac} \cos(\theta_{ac}) - U_c \cos(\theta_c))^2} \quad (221)$$

Now the Amplitudes and phases are expressed in terms of the rotary parameters. This is step #6 of figure (29). By inserting equations (92), (93), (90) and (91) into equations (219), (218), (220) and (221) the amplitudes and phases can be obtained in terms of ellipse parameters which is step #3 of figure (29). This results in:

$$\phi_v = \arctan \left( \frac{(U_{Ma} + U_{Mi}) \cos(\psi_I - \psi_P) - (U_{Ma} - U_{Mi}) \cos(\psi_I + \psi_P)}{(U_{Ma} + U_{Mi}) \sin(\psi_I - \psi_P) + (U_{Ma} - U_{Mi}) \sin(\psi_I + \psi_P)} \right) \quad (222)$$

$$\phi_u = \arctan \left( -\frac{(U_{Ma} + U_{Mi}) \sin(\psi_I - \psi_P) - (U_{Ma} - U_{Mi}) \sin(\psi_I + \psi_P)}{(U_{Ma} + U_{Mi}) \cos(\psi_I - \psi_P) + (U_{Ma} - U_{Mi}) \cos(\psi_I + \psi_P)} \right) \quad (223)$$

$$U = \frac{1}{2} \sqrt{((U_{Ma} + U_{Mi}) \cos(\psi_I - \psi_P) + (U_{Ma} - U_{Mi}) \cos(\psi_I + \psi_P))^2 + (-(U_{Ma} + U_{Mi}) \sin(\psi_I - \psi_P) + (U_{Ma} - U_{Mi}) \sin(\psi_I + \psi_P))^2} \quad (224)$$

$$V = \frac{1}{2} \sqrt{((U_{Ma} + U_{Mi}) \sin(\psi_I - \psi_P) + (U_{Ma} - U_{Mi}) \sin(\psi_I + \psi_P))^2 + ((U_{Ma} + U_{Mi}) \cos(\psi_I - \psi_P) - (U_{Ma} - U_{Mi}) \cos(\psi_I + \psi_P))^2} \quad (225)$$

## 8.2 List of abbreviations

## 8.3 People that worked on the project

Between the first idea to the last sentence, many people have helped me. They have put a lot of trust in me. I am grateful for that! Though I cannot thank everybody in the right way, I did list all the people who have been of importance to be able to come to this Master Thesis. Even if you were just doing your job, Thanks!

### **First my Parents Joop and Ria Groeskamp and girlfriend Malou Zuidema**

Helping me with everything else (and Malou with making the front of the thesis)! Thank you! Love You!

### **Leo Maas, NIOZ**

He helped with all the theoretical aspects of the thesis, gathered the permission to deploy the buoy in the Marsdiep, helped retrieving the first deployment and had time for endless amount of discussions.

### **Janine Nauw, NIOZ**

She helped planning the trips with the R.V. Navicula, delivered the R.V. Navicula ASs data, delivered Matlab scripts, ordered the LED, helped discussing the theory and helped deploying the buoy.

### **Huib de Swart, IMAU**

Thank you for your helpfull discussion!

### **Frans Eijgenraam, NIOZ**

He helped with the technical aspects to get the ADCP to work. He managed the transmitter and receiver system.

### **Theo Hillebrand, NIOZ**

He helped gathering batteries for the second deployment, bought the ADCP and beacon, helped designing the deployment.

### **Richard Koopman, TESO**

He helped with visual observations concerning the waves and fronts in the Marsdiep.

### **Yvo Witte, NIOZ**

He build the deployment, helped with deploying and retrieving the buoy and helped designing the deployment.

### **Bob Koster, NIOZ**

He helped designing the interior of the deployment and connecting all aperture. He also discussed different possible power sources.

### **Ronald de Koster, NIOZ**

He helped making a computer program that would alert us in case the deployment would drift away. Also he helped with other computer technical aspects.



**Harry de Porto, NIOZ**

He helped building the deployment, helped designing the deployment and planned the activities for the workshop.

**Jan Blom, NIOZ**

He helped building the deployment, helped designing the deployment.

**Personnel of the R.V. Navicula Cees van de star, Tony van Heerwaarden and Hein de Vries**

They helped retrieving and deploying the deployment and were very flexible.

**Theo Buijsman, NIOZ**

He Helped planning activities with the Navicula.

**Carola van der Hout, NIOZ**

Helped to retrieve along and cross stream depth transect of the Marsdiep.

**Colleagues: Anna Rabitti, Femke de Jong, Jordy de Boer, Jenny Ullgren, NIOZ**

Helping with Matlab and TeX problems and helping to relax!

## References

- [1] J. W. Book, P. J. Martin, I. Janekovic', M. Kuzmic', and M. Wimbush. Vertical structure of bottom ekman tidal flows: Observations, theory, and modeling from the northern adriatic. *Journal of Geophysical Research C: Oceans*, 114(7), 2009.
- [2] Maarten C. Buijsman. Ferry-observed variability of currents and bedforms in the marsdiep inlet. *PhD Thesis University of Utrecht*, 2007.
- [3] Maarten C. Buijsman and Herman Ridderinkhof. Long-term ferry-adeq observations of tidal currents in the marsdiep inlet. *Journal of Sea Research*, 57(4):237 – 256, 2007.
- [4] Maarten C. Buijsman and Herman Ridderinkhof. Water transport at subtidal frequencies in the marsdiep inlet. *Journal of Sea Research*, 58(4):255 – 268, 2007.
- [5] Maarten C. Buijsman and Herman Ridderinkhof. Variability of secondary currents in a weakly stratified tidal inlet with low curvature. *Continental Shelf Research*, 28(14):1711 – 1723, 2008.
- [6] Thomas B. Curtin and Christopher N. K. Mooers. Observation and interpretation of a high-frequency internal wave packet and surface slick pattern. *J. Geophys. Res.*, 80(6):882–894, 1983.
- [7] K.L. Deines.
- [8] William J. Emery and Richard E. Thomson. Data analysis methods in physical oceanography. *Elsevier Publishing Company*, pages 392 – 404, 2001. Paperback Book.
- [9] David Farmer and Laurence Armi. The generation and trapping of solitary waves over topography. *Science*, 283(5399):188–190, 1999.
- [10] David M. Farmer and J. Dungan Smith. Tidal interaction of stratified flow with a sill in knight inlet. *Deep Sea Research Part A. Oceanographic Research Papers*, 27(3-4):239 – 246, IN5–IN10, 247–254, 1980.
- [11] L.-L. Fu and B. Holt. Internal waves in the gulf of california: Observations from a spaceborne radar. *J. Geophys. Res.*, 89(C2):2053–2060, 1984.
- [12] T. Gerkema and J.T.F. Zimmerman. An introduction to internal waves. *Lecture Notes, Royal NIOZ and Utrecht University*, 2008.
- [13] Yasuda H. Vertical structure of the tidal current ellipse in a rotating basin. *Journal of Oceanography*, 43(5):309 – 318, 1987.
- [14] B. A. Hughes and H. L Grant. The effect of internal waves on surface wind waves 1. experimental measurements. *J. Geophys. Res.*, 83(C1):443–454, 1978.
- [15] K. M. H. Huijts, H. M. Schuttelaars, H. E. de Swart, and C. T. Friedrichs. Analytical study of the transverse distribution of along-channel and transverse residual flows in tidal estuaries. *Continental Shelf Research*, 29(1):89–100, 2009.
- [16] R. A. Kropfli, L. A. Ostrovski, T. P. Stanton, E. A. Skirta, A. N. Keane, and V. Irisov. Relationships between strong internal waves in the coastal zone and their radar and radiometric signatures. *J. Geophys. Res.*, 104(C2):3133–3148, 1984.

- [17] P.H. LeBlond and L.A. Mysak. Waves in the ocean. *Elsevier, Amsterdam (1978) 602pp.*, 1978. Book.
- [18] M. D. Levine, C. A. Paulson, M. G. Briscoe, R. A. Weller, H. Peters, H. M. Van Aken, J. M. Huthnance, G. Siedler, and E. D. R. Shearman. Internal waves in jasin [and discussion]. *Philosophical Transactions of the Royal Society of London. Series A, Mathematical and Physical Sciences*, 308(1503):389–405, 1983.
- [19] H.A. Lorentz. Verslag staatscommissie zuiderzee 1918–1926. *Algemene Landsdrukkerij, Den Haag.*, 1926.
- [20] L. R. M. Maas and J. J. M. Van Haren. Observations on the vertical structure of tidal and inertial currents in the central North Sea. *Journal of Marine Research*, 45:293–318, 1987.
- [21] A.L. New and R.D. Pingree. Large-amplitude internal soliton packets in the central bay of biscay. *Deep Sea Research Part A. Oceanographic Research Papers*, 37(3):513 – 524, 1990.
- [22] C. B. Officer. Physical oceanography of estuaries (and associated coastal waters). *A Wiley-Interscience publication*, 1976. Book.
- [23] A. R. Osborne and T. L. Burch. Internal solitons in the andaman sea. *Science*, 208(4443):451–460, 1980.
- [24] L. A. Ostrovsky and Yu. A. Stepanyants. Do internal solitons exist in the ocean? *Rev. Geophys.*, 27(3):293–310, 1989.
- [25] B.B. Parker. The relative importance of the various nonlinear mechanisms in a wide range of tidal interactions. *Tidal Hydrodynamics*, John Wiley and Sons, New York:237 – 268, 1991.
- [26] R. D. Pingree and A. L. New. Downward propagation of internal tidal energy into the bay of biscay. *Deep Sea Research Part A, Oceanographic Research Papers*, 36(5):735–758, 1989. Cited By (since 1996): 48.
- [27] R.D. Pingree and G.T. Mardell. Solitary internal waves in the celtic sea. *Progress In Oceanography*, 14:431 – 441, 1985.
- [28] H. Postma. Hydrography of the dutch wadden sea. *PhD Thesis University of Groningen*, 1954.
- [29] M.J.D. Powell. A Method for Minimizing a Sum Of Squares of Non-linear Functions Without Calculating Derivatives. *Computer Journal*, 7(4):303–307, 1965.
- [30] D. Prandle. The vertical structure of tidal currents and other oscillatory flows. *Continental Shelf Research*, 1(2):191 – 207, 1982.
- [31] H. Ridderinkhof. Tidal and residual flows in the western dutch wadden sea i: Numerical model results. *Netherlands Journal of Sea Research*, 22(1):1 – 21, 1988.
- [32] H. Ridderinkhof. Tidal and residual flows in the western dutch wadden sea ii: An analytical model to study the constant flow between connected tidal basins. *Netherlands Journal of Sea Research*, 22(3):185 – 198, 1988.

- [33] H. Sandstrom and J. A. Elliott. Internal tide and solitons on the scotian shelf: A nutrient pump at work. *Journal of Geophysical Research*, 89(C4):6415–6426, 1984.
- [34] G. P. Schramkowski, K. M. H. Huijts, H. E. de Swart, and H. M. Schuttelaars. A model comparison of flow and lateral sediment trapping in estuaries. In DohmenJanssen, C.M. and Hulscher, S.J.M.H., editor, *River, Coastal and Estuarine Morphodynamics: RCEM 2007, Vols 1 and 2*, Proceedings and Monographs in Engineering, Water and Earth Sciences, pages 413–420. Taylor & Francis LTD, 2008. 5th IAHR Symposium on River, Coastal and Estuarine Morphodynamics, Enschede, Netherlands, Sep 17-21, 2007.
- [35] R. L. Soulsby. The bottom boundary layer of shelf seas. *Physical oceanography of coastal and shelf seas*, pages 189–266, 1983.
- [36] C. Wunsch and A. E. Gill. Observations of equatorially trapped waves in pacific sea level variations. *Deep-Sea Research and Oceanographic Abstracts*, 23(5):371–390, 1976.
- [37] Xu Z. Ellipse parameters coversion and vertical velocity profiles for tidal currents. *Ocean Science Divison, Fisheries and Oceans Canada, Bedford Institute of Oceanography.*, 2000. Available on the internet, not published.
- [38] J.T.F. Zimmerman. Mixing and flushing of tidal embayments in the western dutch wadden sea, part i: Description of salinity distribution and calculation of mixing time scales. *Netherlands Journal of Sea Research*, 10(2):149 – 191, 1976.
- [39] J.T.F. Zimmerman. Mixing and flushing of tidal embayments in the western dutch wadden sea, part ii: Analysis of mixing processes. *Netherlands Journal of Sea Research*, 10(4):397 – 439, 1976.
- [40] J.T.F. Zimmerman. The tidal whirlpool: A review of horizontal dispersion by tidal and residual currents. *Netherlands Journal of Sea Research*, 20(2-3):133 – 154, 1986.